SAND77-0587
Unlimited Release

Surface Roughness Effects on the Hypersonic Turbulent Boundary Layer

Dale E. Berg

Prepared by Sandia Laboratories, Albuquerque, New Mexico 87115
and Livermore, California 94550 for the United States Energy Research
and Development Administration under Contract AT(29-1)-789

Printed September 1977

Sandia Laboratories

SF 2900 Q(7-73)

DISCLAIMER

Issued by Sandia Laboratories, operated for the United States Energy Research & Development Administration by Sandia Corporation.

Printed in the United States of America

Available from
National Technical Information Service
U. S. Department of Commerce
5285 Port Royal Road
Springfield, VA 22161

Price: Printed Copy ~~$7.75~~ 6.50 Microfiche $3.00

SAND77-0587
Unlimited Release
Printed September 1977

SURFACE ROUGHNESS EFFECTS ON THE HYPERSONIC TURBULENT BOUNDARY LAYER*

Dale E. Berg
Experimental Aerodynamics Division 1334
Sandia Laboratories
Albuquerque, New Mexico 87115

*This work was supported jointly by the Energy Research and Development Administration and the U.S. Army Research Office. This work was performed at the Graduate Aeronautical Laboratories, California Institute of Technology, Pasadena, California.

ACKNOWLEDGEMENTS

It is impossible to name here all those who have contributed to the successful completion of this task. I must content myself with naming but a few, hoping that those who are not specifically named will not feel slighted.

My sincere thanks are extended to Professor Toshi Kubota who has guided the course of this research and my graduate education here at GALCIT. His constant availability for discussions, patience and understanding in the presence of a student's errors and ability to ask penetrating questions have contributed greatly to this task and to my own enlightenment.

I am grateful to the members of my committee for their investment of time and effort, especially to Professors Edward E. Zukoski and Anatol Roshko for their valuable contributions to this research; to the staff of the Aeronautics shop, especially George Lundgren and Bob Seguine, for the countless hours spent conferring on design problems and fabricating the hardware required for this work; to the staff of the Aeronautics electronics shop for their invaluable assistance in maintaining the electronic equipment used; to Betty Wood for the preparation of the figures in this thesis; to Virginia Conner, Liz Fox, and Jackie Beard for their excellent typing and forbearance during the preparation of this manuscript; to Florence Kovacic for her assistance in the completion of the many small but important details involved in winding up a thesis.

A special expression of gratitude is extended to Sam Roman who spent so many long, boring, and often hot nights watching control

dials instead of counting sheep during the data acquisition phase of this work. The many hours Sam spent performing the maintenance, repair, and construction work involved in this project are greatly appreciated.

The support of the present project by the U. S. Army Research Office, and the Energy Research and Development Administration through Sandia Laboratories, Albuquerque, New Mexico is gratefully acknowledged. Personal financial support was provided by Sandia Laboratories through their Doctoral Study program and I extend my thanks to Sandia for that support. I wish to express my gratitude to Drs. Kenell Touryan and Carl Peterson of Sandia for their active and continuing technical and personal support.

This thesis is dedicated to my wife, Sally, and my daughters, Lisa and Peggy. Without their encouragement, support, and stabilizing presence the completion of this work would have been far more difficult. In appreciation of hardships they have endured on my behalf during the course of this work, I extend to them my heartfelt gratitude and thanks.

ABSTRACT

An experimental investigation of the response of a hypersonic turbulent boundary layer to a step change in surface roughness has been performed. The boundary layer on a flat nozzle wall of a Mach 6 wind tunnel was subjected to abrupt changes in surface roughness and its adjustment to the new surface conditions was examined. Both mean and fluctuating flow properties were acquired for smooth-to-rough and rough-to-smooth surface configurations.

The boundary layer was found to respond gradually and to attain new equilibrium profiles, for both the mean and the fluctuating properties, some 10 to 25δ downstream of the step change. Mean flow self-similarity was the first to establish itself, followed by the mass flux fluctuations, followed in turn by the total temperature fluctuations.

Use of a modified Van Driest transformation resulted in good correlation of smooth and rough wall data in the form of the incompressible law of the wall. This is true even in the nonequilibrium vicinity of the step for small roughness heights.

The present data are found to correlate well with previously published roughness effect data from low and high speed flows when the roughnesses are characterized by an equivalent sand grain roughness height.

Existing correlations based on low speed data were found to be unsuccessful in predicting the effect of this roughness on the skin friction and velocity profile. The indiscriminate use of low speed

roughness effects correlations to predict the effects of roughness on supersonic and hypersonic flows must therefore be regarded as a procedure subject to gross errors.

Significant pressure and temperature history effects were observed throughout the boundary layer. The existence of these effects was found to create a nozzle wall boundary layer whose properties were far different than those in a boundary layer on a flat plate in the freestream, raising questions about the validity of simulating the flat plate boundary layer with the nozzle wall boundary layer.

TABLE OF CONTENTS

Table of Contents (Cont'd)

LIST OF SYMBOLS

A	constant (Eqs. 4, 6 and 7)
a	$k_w/[k_t(\ell/d)^2]$
a_1	$1 + \frac{\gamma-1}{2} M^2$
B	length of stiffened section of balance flexure (Eq. 3 and Fig. 9); constant (Eqs. 4, 6 and 7)
b	$Nu_t - i^2 r_r a_r/(\pi k_t)$
C	constant in the law of the wall (Eqs. 1 and 5); hot-wire sensitivity coefficient
C_0, C_1, C_2, C_3	constants (Eqs. 13 and A.3.1)
C_f	skin friction coefficient
C_{f_0}	smooth wall skin friction coefficient
c	specific heat; $\frac{\bar{i}^2 r_r}{\pi \bar{k}_t \bar{\eta} \bar{T}_t} [1+a_r(\bar{\eta} T_t - T_r)]$; $\sqrt{\frac{2EI}{F}}$
D	constant in the law of the wall (Eqs. 2, 5 and 8)
d	hot-wire diameter
E	modulus of elasticity of balance flexure material (Fig. 9)
e	$\frac{\bar{i}^2 r_r a_r}{\pi \bar{k}_t}$; base of natural logarithms; hot-wire fluctuation voltage
F	force acting on the balance (Eq. 3 and Fig. 9)
$g(S_1)$	tabulated function
H	δ^*/θ - shape factor

List of Symbols (Cont'd)

$\dot{H}$	$\frac{100}{\delta^*} \int \frac{\rho u}{\rho_e u_e} (1 - T_t/T_{t_e})dy$ - enthalpy flux coefficient
h	heat transfer coefficient (Eq. A.2.1)
I	polar moment of inertia of stiffened section of balance flexure (Fig. 9)
i	hot wire current
j	$\sqrt{-1}$
K	$\rho_w c_w d^2/(4k_t)$, wire property
k	roughness height; thermal conductivity; balance scale factor; slope of $\overline{R}_{wm}$ vs $\overline{i}^2\overline{R}_{wm}$ plot
k_c	balance beam coil scale factor
k_s	equivalent sand grain roughness (Eqs. 9 and 11)
k^+	$k u_\tau/\nu_w$
k_s^+	$k_s u_\tau/\nu_w$
L	length of free balance flexure (Eq. 3 and Fig. 9)
ℓ	wavelength of roughness (Fig. 5); hot wire length; characteristic length in Reynolds number of roughness
ℓn	natural logarithm
M	Mach number
m	$d\ell n\, \mu_t/d\ell n\, T_t$
$\dot{m}$	ρu, mass flux
Nu	$\frac{hd}{k}$, Nusselt number
n	$d\ell n k_t/d\ell n\, T_t$
p	pressure (static unless noted otherwise)
Pr	$\mu c_p/k$, Prandtl number

List of Symbols (Cont'd)

q	heat flux
R	hot wire resistance
$R_{\dot{m}\,T_t}$	$\overline{\dot{m}'\,T_t'} \,/\, \left(\sqrt{\overline{\dot{m}'^2}}\sqrt{\overline{T_t'^2}}\right)$, mass flux-total temperature correlation coefficient
r	recovery factor (Eq. 7); wire resistance per unit length
Re	$\rho\, u\, \ell/\mu$ Reynolds number
$S_{\dot{m}}, S_{T_t}$	hot wire sensitivity coefficients
S_1	$(\frac{\gamma}{2})^{\frac{1}{2}}\, M$
T	temperature (static unless otherwise noted)
u	streamwise component of velocity
u_τ	$\sqrt{\frac{\tau_w}{\rho_w}}$, friction velocity
u^*	Van Driest transformed velocity (Eq. 4)
Δu	change in velocity due to wall roughness
v	component of velocity normal to the wall
W	effective weight of balance element (Eq. 3)
w	wake function (Eq. 5)
x	streamwise coordinate, distance from the throat
y	distance normal to the wall; displacement of balance beam (Eq. 3)
y^+	$y\, u_\tau/\nu_w$
y_0	effective origin for rough surface
z	correlation exponent (Eq. A.6.5)

List of Symbols (Cont'd)

a	b/a; energy accomodation coefficient
a_r	temperature coefficient of resistivity
β	$L/c = \sqrt{FL^2/(2EI)}$ (Eq. 3 and Fig. 9)
γ	c_p/c_v, ratio of specific heats
δ	boundary layer thickness (determined from correlation, Eq. 8)
δ^*	$\int_0^\delta (1 - \frac{\rho u}{\rho_e u_e})dy$ = displacement thickness
η	recovery factor
κ	Karman constant in the law of the wall
λ	ℓ/k-roughness wavelength-to-height ratio
ψ_N	Nusselt number ratio
μ	fluid viscosity
ν	μ/ρ, kinematic viscosity
$\overline{\pi}$	wake strength parameter in the law of the wall (Eq. 5)
ρ	fluid density (static unless otherwise noted)
τ	shear stress; nondimensional temperature
θ	$\int_0^\delta \frac{\rho}{\rho_e}\frac{u}{u_e}(1 - \frac{u}{u_e})dy$ - momentum thickness
ω	angular frequency
ω_o	$\frac{\tanh \sqrt{a_o}}{\sqrt{a_o}}$

Superscripts

'	fluctuation quantity
—	time average or nondimensional quantity
*	nondimensional quantity

List of Symbols (Cont'd)

Subscripts

aw	adiabatic wall
awm	measured adiabatic wall quantity
c	continuum flow
e	boundary layer edge conditions
f	free molecular flow
H	hypersonic limit
i	ideal hot wire quantity
ℓ	local value
m	measured
r	reference property
s	hot-wire support
t	total conditions
w	wall or wire property
wm	measured wire quantity
∞	free stream conditions; infinite frequency

LIST OF TABLES

LIST OF FIGURES

List of Figures (Cont'd)

List of Figures (Cont'd)

INTRODUCTION

The effect of surface roughness on the characteristics of flow over a surface has long been of interest, especially to those people who are involved in the design of vehicles which operate in or on the water or within the atmosphere. It is well known that the presence of surface roughness can significantly alter the drag and heat transfer characteristics of a surface and can even cause considerable modification of the flow-field about a body, compared to the smooth wall case. Quantitative knowledge of these roughness effects, and insight into the physical phenomena which give rise to these effects is essential for the realistic design of new vehicles, regardless of their speed range or medium of operation. Without such knowledge, vehicle performance cannot be adequately predicted and considerable overdesign is mandatory to insure that the vehicle will satisfy the design criteria. Ship hulls, aircraft, reentry vehicles, and the space shuttle are but a few areas in which the design is influenced heavily by the knowledge or lack of knowledge of roughness effects.

One of the earliest extensive studies of roughness effects was that of Nikuradse,[1] in which the effects of Reynolds number and relative roughness heights were investigated. This work was carried out using dense sand grain roughness in pipe flow. He discovered that for Reynolds number based on roughness height below a certain critical value, the roughness had no discernible effect on the flow, i.e., the surface was "hydraulically smooth." For roughness Reynolds numbers above this critical value and below a second critical value, the effect of the wall roughness on the boundary layer properties

was dependent on flow Reynolds number and roughness density, k/d (k is the roughness height, and d is some characteristic length of the flow, such as the pipe diameter for Nikuradse's work). These flows were termed "transitional." Flows with roughness Reynolds numbers above the second critical value were found to depend only on the roughness density and were termed "fully rough."

Moore,[2] in 1951, investigated a zero pressure gradient boundary layer over a roughness consisting of square bars placed normal to the flow with a ratio of pitch to height of 4. Moore found that a similarity defect law correlated his boundary layer profiles, and the law was identical with the smooth-wall law, provided the origin for measuring y and δ (the boundary layer thickness) was located some distance below the crest of the roughness elements.

Hama,[3] in 1954, conducted an extensive investigation which showed that the Clauser[4] form of the logarithmic velocity distribution for rough wall flows

$$\frac{u}{u_\tau} = \frac{1}{\kappa} \ell n \left(\frac{y u_\tau}{\nu}\right) + C - \frac{\Delta u}{u_\tau} \qquad (1)$$

where

u_τ = $\sqrt{\tau_w / \rho_w}$

κ and C = universal constants

τ_w = wall shear stress

ρ_w = fluid density at the wall

$\frac{\Delta u}{u_\tau}$ = a roughness function which is zero for smooth walls and which depends on the roughness Reynolds number

and the Clauser[4] form of the roughness function for fully rough flows

$$\frac{\Delta u}{u_\tau} = \frac{1}{\kappa} \ell n \left(\frac{k u_\tau}{\nu} \right) + D \qquad (2)$$

are both universal for a given roughness geometry in pipe, channel, and zero pressure gradient boundary layer flow. The constant D is found to depend upon the free stream pressure gradient.

More recently, the work of Betterman,[5] Morris,[6] Liu et al.,[7] and Perry et al.[8] have included the effects on the constant D of the element density. Perry and Joubert[9] have investigated the effect of an adverse pressure gradient on the roughness function. All of these works were for either a sand grain roughness[1, 3] or a transverse square bar type of roughness,[2, 4-9] while Streeter and Chu,[10] Sams,[11] Ambrose,[12] and Corrsin and Kistler,[13] have investigated different types of roughnesses.

Antonia and Luxton,[14] Liu et al.,[15] and Logan and Jones[16] are among those who have studied the turbulent properties of incompressible fluid flow over rough surfaces. They have found that the velocity fluctuation magnitudes in the outer part of the rough wall boundary layer are significantly higher than those on the smooth wall. The fluctuation profiles were also found to assume a self preserving shape.

Using the information obtained in these investigations, Van Driest[17] has constructed a mathematical model of incompressible fluid flow over a rough wall which has met with considerable success when used to compute the mean properties of such a flow.

Dvorak[18] utilizes the correlation of Betterman,[5] extends it to other roughness densities, and incorporates the universal rough surface law of the wall into a procedure for computing incompressible rough wall turbulent boundary layer profiles.

Considerably less progress has been made in determining the effects of surface roughness on compressible turbulent boundary layers. One of the first investigations was that of Goddard[19] who studied the effects of sand grain roughness at Mach numbers of 2 to 4.5. Wade[20] at about the same time determined the effects of "screw thread" roughness at Mach number 2.5. Fenter,[21] Young,[22] Shutts and Fenter,[23] Mann,[24] Reda,[25] and Monta et al.[26] have also investigated this phenomenon at Mach numbers varying from 2 to 5.

With the added phenomenon of compressibility, it is no longer possible to directly correlate the boundary layer profiles in the law-of-the-wall form as was done for incompressible flow. Even compressible smooth wall turbulent boundary layers, at different Mach numbers or wall-to-stagnation temperature ratios, cannot be directly correlated by the law of the wall. Several transform methods[27-37] have been proposed, based on either theoretical analysis or experimental data. These methods are designed to transform compressible velocity profile data into an "equivalent" incompressible form which can then be correlated by the incompressible law of the wall.

Spalding and Chi,[34] Hopkins et al.,[38] Miles and Kim,[39] and Hopkins and Inouye[40] have compared several of the theories with available data and conclude that while some of them work

quite well for a wide variety of data, many of them perform adequately only for data which were acquired under certain conditions such as limited Mach number range, limited wall temperature range, etc. Since only the immediate wall region of the compressible turbulent boundary layer is affected by the presence of wall roughness, it seems likely that the smooth wall transform methods will work for the rough wall case as well, and Fenter,[21] Young,[22] and Reda[25] have verified this.

Dvorak[41] and Chen[42] have developed computational procedures based on a combination of empirical laws and theoretical equations which purport to predict the compressible rough wall boundary layer development in a pressure gradient. The agreement with the limited amount of data is quite good, but Dvorak specifically deplores the availability of suitable test data.

The earliest comprehensive investigation of the fluctuating properties of the compressible turbulent boundary layer was performed by Kistler[43]. He found that in the Mach number range of 1.7 to 4.7, the mass flow and total temperature fluctuation intensities increased throughout the boundary layer with increasing Mach number. The velocity fluctuation profile was observed to be generally similar in shape to low speed fluctuation profiles. Subsequent to Kistler's work, Owen and Horstman[44] and Laderman and Demetriades,[45, 46] have investigated smooth wall turbulent boundary layer flows at Mach numbers of 7, 8, and 9 with adiabatic and cold walls. Laderman and Demetriades[46] conclude that the fluctuation intensity is strongly dependent on the wall temperature

to stagnation temperature ratio.

An investigation of the response of a hypersonic turbulent boundary layer to a step change in roughness was seen as serving several purposes; it would provide information on the distance required to achieve equilibrium rough wall flow in hypersonic flow--essential for future roughness work; it would yield information on the equilibrium rough wall boundary layer flow downstream of the transition region, creating additional test data for the existing computational procedure; and it would serve as a preliminary step for possible later investigations of a turbulence production dominated region of flow, designed to gain further understanding of the mechanisms involved in turbulence. In addition, comparison of the data with the existing low speed results of Antonia and Luxton[14] would reveal the Mach number dependence of the boundary layer response to sudden perturbations.

DESCRIPTION OF THE EXPERIMENT

Facility

This work was performed in Leg II of the Graduate Aeronautical Laboratories, California Institute of Technology (GALCIT) hypersonic wind tunnel. The tunnel is a closed circuit, continuously operating facility utilizing heated air as the test gas. A schematic of the tunnel circuit is shown in Fig. 1. Compression is accomplished by five stages of sliding vane, rotary compressors and either one or two stages of reciprocating compressors, depending on the required compression ratio. A silica gel dryer is used to remove moisture from the air, and a 5μ nominal size pleated-paper filter removes the large particles from the airstream prior to its entering the electric heater and test section. More detailed descriptions of the wind tunnel are given by Kubota[47] and Baloga and Nagamatsu.[48]

Leg II has a two dimensional, flexible nozzle which may be contoured to produce Mach numbers in the range of 6 to 9. The side walls of the tunnel diverge to compensate for boundary layer growth in the flow direction. For this work, a half nozzle configuration as shown in Figure 2 was contoured to produce a nominal free stream Mach number of 6.0. This resulted in a total test section height of approximately 2.8 inches, with an inviscid core approximately 0.8 inches in height by 5.0 inches in width.

The nominal tunnel operating conditions for this work were chosen to give the highest possible Reynolds number consistent with good quality flow and safety conditions. These conditions were p_t = 228 psia and T_t = 770° R which resulted in a free stream Reynolds

number of $Re_\infty \approx 4x10^5$/in. Operating conditions varied slightly from run to run, but for a given run the conditions were constant within ± 0.5% for the temperature, and ± 0.2% for the pressure.

Experimental Apparatus

The bottom flexible nozzle wall of the tunnel was removed and replaced by an assembly consisting of a permanent 0.625 inch thick steel plate (base plate) upon which removable surface plates 0.35 inch thick were mounted. The base plate itself was 48.8 inches long and the removable surface element length was 46.3 inches. The plate assembly is illustrated in Figures 3 and 4. The plate assembly was leveled using a surveyor's transit and a straight edge and was estimated to have been flat and level within ± 0.010 inch over the 48 inch length. The surface plates were tapered to match the side-wall divergence. Sealing was accomplished by means of inflatable tubing, both against the side wall, where nitrogen at 150 psi was used to inflate the tube and achieve a seal, and between the surface plates where the tubing was injected with uncured Eccofoam FP. The curing foam created significant pressures on the inside of the tubing, forming an effective, permanent seal between the plates.

Four sets of surface plates were fabricated, one of which was left smooth to serve as a reference condition, while the others were machined to different surface roughness.

Each set of surface plates was ground to the proper thickness and then hand finished while installed in the base plate to minimize the steps in the surface, both at the junction with the throat block

and between the plates themselves. All joints on the smooth surface set had steps of less than 0.0001 inch.

The surface roughness chosen for this study was a transverse square bar type as illustrated in Figure 5. This configuration was chosen because it has been extensively studied in low speed flow (Moore,[2] Antonia and Luxton,[14] Perry, Schofield and Joubert,[8] Betterman[5]) and it may be readily characterized by a height and a wavelength. The wavelength to height ratio used was 4, and the grooves were recessed into the surface, leaving the top of the roughness elements level with the smooth wall upstream of the roughness. Roughness heights of 0.0125, 0.0250 and 0.050 inch were used, which, using the data of Betterman,[5] correspond to incompressible sand grain roughness heights of 0.04, 0.09, and 0.18 inch yielding nondimensional roughness values $k_s^+ (= \frac{k_s u_\tau}{\nu_w})$ of approximately 19, 40, and 85.

To reduce the heat loss from the flat plate to the room, a continuous flow of low speed (< 40 ft/sec) heated air was maintained in a channel formed by the base plate and the tunnel side walls. The bottom of this open channel was closed and flexible ducting connected it to a blower and electric resistance heater. A sketch of this system is shown in Figure 6. The heater current was controlled by means of a Powerstat auto-transformer, so that any desired heater output temperature from ambient to about 300° F could be set, with an accuracy of ± 2° F.

Further reductions in heat loss were accomplished by placing a two inch layer of fiberglass insulation on the outside of each

sidewall to reduce the plate conduction losses to these structures, and by inserting a micarta section of nozzle wall just downstream of the test section to reduce heat conduction to the unheated downstream section of the nozzle wall.

Instrumentation

The mean flow properties of the boundary layer were computed from data acquired during Pitot pressure and total temperature surveys. A limited amount of static pressure data was obtained, the main concern being the verification of the standard assumption of constant static pressure across the boundary layer. Direct measurements of wall temperature and pressure were made via instrumentation in the tunnel wall, while the wall shear stress was determined using a skin friction balance which could be installed at either of two axial locations. A constant current hot wire anemometer was used to obtain fluctuation data from which the turbulent properties of the boundary layer could be deduced.

The Pitot and static pressure probes used were of conventional design. The Pitot probe was fabricated from 0.065 inch O.D. stainless steel tubing with the tip flattened and filed to about 0.010 inch by 0.08 inch with an opening height of 0.004 inch. The probe tip was pitched down at an angle of 10° to insure that it contacted the flat plate before any other portion of the probe touched. Fernandez[49] and Peterson and George[50] have shown that the flattened tip Pitot probe is insensitive to angle-of-attack variations of ± 10° for subsonic and supersonic flow.

The static pressure probe was fabricated from 0.032 inch O.D. stainless tubing. The tip was sealed and sharpened to a cone with an 8°-10° semi-vertex angle. Four holes of 0.007 inch diameter were drilled 90° apart some 12 probe diameters behind the shoulder of the probe in the region of full pressure recovery.

Pitot pressures were measured using a Statham pressure transducer (PA-208TC-10-350, 0-10 psia). Static pressures were measured using a Datametric electronic barometer, type 1014A. Pitot pressure readings are estimated to be accurate to within ±1%.

The total temperature probe shown in Figure 7 was based on the design of Behrens[51] and consisted of a micarta body and wedge shaped micarta supports 0.5 inch apart. A butt welded 0.005 inch Chromel-Alumel thermocouple was suspended between the supports with 0.001 inch Chromel and Alumel wires spot welded to the appropriate wires and leading from the support tips back to the probe body. A 0.001 inch spot welded Chromel Alumel thermocouple was epoxied to one support to monitor the support temperature. The 0.005 inch thermocouple proved to be very sturdy, capable of withstanding considerable handling without breaking, and the 0.001 inch lead wires (which were protected by epoxy and thus not subject to breakage) minimized heat loss from the supports.

Two traverse mechanisms were used in this experiment. One traverse was window mounted and permitted cross stream as well as vertical and axial movement, while the other was a top mounted unit which utilized a more rigid support system for the

axial moving sting (0.50 inch O.D., 0.375 inch I.D. SS tube) and permitted only axial and vertical movement. Both mechanisms were located at the aft end of the test section ($\approx$ 52 inches from the throat), and when the probe was extended forward this cantilever support system resulted in increased vibration problems and decreased position accuracy. Estimates of the probe position (with respect to the flat plate) accuracy under tunnel operating conditions vary from $\pm$ 0.002 inch at the aft end of the test section to $\pm$ 0.005 inch at the maximum probe extension of 28 inches.

The smooth surface plate sections were instrumented with static pressure taps and thermocouples. The taps consisted of a 0.067 inch diameter hole drilled from the back surface of the surface plate to within 0.025 inch of the front surface with a 0.014 diameter inch hole through the surface. A short piece of 0.063 inch O.D. by 0.045 inch I.D. stainless steel tubing was epoxied into the back of the plate, and 0.060 inch I.D. Saran tubing was used to connect to a silicone oil manometer bank. The ports were all leak checked under tunnel operating conditions and the outgassing of the connecting tubes was found to be negligible. These static pressure readings are estimated to be accurate to within $\pm$ 1 mm silicone oil (0.0013 psi) or $\pm$ 1% or less of the minimum wall pressure sensed. The thermocouples were installed as shown in Figure 8. A 1/8 inch diameter hole was drilled from the back side of the plate to within 0.05 inch of the plate surface and two 0.012 inch diameter holes were then drilled through to the surface. Copper constantan thermocouple wire was stripped and one wire threaded through each hole to the surface

where they were soldered to the surface and then finished flush with the surface. The resulting junction thus incorporated the outer 0.05 inch of the plate surface and effectively measured the surface temperature of the plate. The outputs of all of the surface thermocouples were monitored on a self balancing strip chart recorder, and the accuracy of the thermocouples based on calibration was± 1°F.

Location of the wall pressure taps and thermocouples are given in Table I.

Provisions were made for mounting a skin friction balance at two axial locations, 27.9 and 47.9 inches from the throat. The surface elements of the balance could be interchanged in the same manner as the rest of the flat plate surface sections. Roughness elements for the balance were machined to match the various plate roughnesses with no interruption or discontinuity. The roughness heights were such that an integral number of roughness wavelengths would be present on the balance element (1, 2, and 4λ for k = 0.050, 0.025, and 0.125 inch, respectively).

The balance itself was a floating element, null return instrument based on the design of Coles.[52] A section view of the balance is shown in Figure 9, and a photograph of the balance assembly is shown in Figure 10. Basically, the balance consisted of a fixed balance table four inches in diameter containing a slot 0.20 inch by 1.5 inches with the small dimension parallel to the flow; from this table the rectangular element, which was 0.002 inch smaller in each dimension than the slot, was supported within the slot by two pairs of stiffened flexures. The two pairs of flexures were joined by a balance beam

which was fixed, through a micrometer, to the balance table. The balance was constructed so that when the element was centered in the slot, the step between the element surface and the surface of the surrounding table was less than 0.0001 inch for the smooth surface and 0.0002 inch for the rough surface. The results of O'Donnell and Westkamper[53] indicate that the error in the measured skin friction due to this misalignment would be less than 0.5% for the smooth wall and less than 1% for the rough wall. Two small dashpots filled with 1000 centistoke silicone oil were incorporated into the inner flexure system to reduce vibrations of the element.

Locations of the floating element and the balance beam were monitored with Schaevitz Linear Variable Differential Transducers[54] (LVDT's). The LVDT basically consists of an annular primary coil flanked by two annular secondary coils with a magnetic core positioned on the coil centerline free of contact with the coil itself. The primary coil is excited by an ac power source, and the differential voltage induced in the secondary coils is directly proportional to the displacement of the core. Since the core does not contact the coil physically, no friction is involved, and this property uniquely suits the LVDT to this type of application.

Installation of the instrument in the flat plate was accomplished by means of 16 leveling screws located near the outer edge of the balance table which were alternately tapped into the table and into the base plate. Discontinuity in surface level between the balance table surface and the surrounding plate surface was held to less than 0.0001 inch for the smooth flat plate and less than 0.0002 inch for the rough plates.

The balance was operated as follows:

1) With no air flow, the element was positioned in the center of the table slot by means of the micrometer attached to the balance beam. The positions of both the element and the beam were determined via the LVDT's.

2) Flow was established over the floating element, causing deflection of the inner flexure unit and movement of the element in the flow direction.

3) The element was returned to the center of the gap, as determined by the element mounted LVDT, using the micrometer, and the movement of the balance beam measured via the LVDT attached to it.

4) The distance the balance beam traveled was determined and multiplied by the balance spring constant to find the skin friction on the element.

Power supply and signal conditioning for the LVDT's was accomplished through use of a Schaevitz CAS-200 module for the floating element LVDT (ML-10 unit), and a CAS-025 module for the beam LVDT (010-MHP unit). Both CAS units supply 3-5 V rms power to the LVDT's, and perform the necessary signal conditioning to the LVDT output to produce a dc output directly proportional to the displacement of the core of the LVDT. The CAS-025 unit, however, supplies the power to the LVDT at 7.5 KHz, while the CAS-200 unit operates at 20 KHz, resulting in increased sensitivity, but also increasing the noise.

The element mounted LVDT and CAS-200 combination produced a dc output signal of approximately 0.12 V for an element movement of 0.001 inch, while the balance beam mounted LVDT

and CAS-025 combination resulted in an output of approximately 0.10 V for a beam movement of 0.001 inch. Movements on the order of $1x10^{-6}$ inches could easily be measured with this instrumentation.

As a result of this extremely sensitive instrumentation, any conditions which might cause erroneous readings, such as particles or oil in the gap between the element and the table, contact of a core with its coil, contact of the dashpot dampers with their case, stray magnetism, or balance chamber pressure leaks, could readily be spotted.

Typical traces of voltage output from the floating element coil versus the voltage output of the balance-beam mounted LVDT are shown in Figure 11. The location of the gap center was determined by fitting a straight line through the data within the gap region, excluding that close to the gap edges, and determining the gap edges as the points of intersection of this straight line with the straight line fairings of the data with the element pinned against the gap edges. The gap center was then picked as being midway between the two edges. This technique is illustrated in Figure 11. Determination of the gap center in this way eliminates the possibility of obtaining an incorrect balance load due to a single bad data point, and makes it very easy to spot balance malfunctions. Also, when the balance is subject to vibration, as it was during actual use, causing continual element vibration which could not be damped out (see Figure 11 for a typical data trace), this technique enables one to achieve a much higher degree of accuracy than could be obtained by taking data only at the gap center.

In order to analyze the balance and obtain an analytic expression for the calibration constant, several assumptions were made:

1) Since the outer flexures are fixed through the micrometer to the balance table, for purposes of analysis the balance is equivalent to the floating element supported above a fixed base by two stiffened flexures (see Figure 9).

2) The two flexures carry equal amounts of horizontal and vertical load.

3) A stiffened flexure is equivalent to a rigid strut with a flexure at each end.

4) The unstiffened portions of the flexure undergo small deflections and hence can be analyzed using beam theory.

5) The floating element is idealized as a point at the end of each flexure subjecting the flexure to a vertical force W/2 (W is the effective weight of the element) and a horizontal force F/2 (F is the skin friction force).

6) All flexure ends are assumed to be ideally clamped.

Using these assumptions, one may obtain for the spring constant

$$k = F/y = \frac{W}{B\left[-\left(1+\frac{2L}{B}\right)+\frac{\cos\beta+\frac{2L}{B\beta}\sin\beta}{\cos\beta-\frac{B\beta}{2L}\sin\beta}\right]} \qquad (3)$$

where the quantities B, L, and β are as defined in Figure 9, and y is the total horizontal distance traveled by the element.

The problem that arose in using the expression for the spring constant was that W, the effective weight of the element, was not known. It was some combination of the true element weight, the

stiffener weight, and the flexure weight, and had to be determined from the calibration.

The method of calibration used to determine k and W was suggested by Coles[52] and consisted of loading the balance by use of the element weight. The balance was inclined at a small angle to the horizontal, and the displacement of the balance beam necessary to return the element to the gap center recorded. Since the angle was kept small, less than .03 radians, the vertical force on the flexure due to the element weight, W, remained constant, and the balance was effectively subjected to a horizontal force which was a known function of W. Use of two different angles, in theory, would be adequate to determine the two unknowns, W and k. However, to improve the calibration accuracy, several angles were used, and additional weights of 10 and 20 grams were added to the element to produce forces in the range of those expected under actual use. These data were then fit to Equation (3) above, using a non-linear least-squares procedure to determine W, k, and k_c, the scale factor for the balance beam mounted LVDT.

Since the balance was to be used at elevated temperatures in the tunnel it was calibrated in an oven at a temperature of 165° F. The elevated temperature was found to result in an increase in the spring constant, k, of about 7% and the coil scale factor, k_c, of about 6% above their values at 80° F.

Values of the spring constant and coil scale factor determined in this manner with the smooth surface floating element attached were

$k = 0.1976$ lb/in.

$k_c = 9.687 \times 10^{-6}$ in/millivolt

Using these values to calculate the calibration loads from the observed coil outputs resulted in a maximum error of .6% of the actual applied load for nine loads ranging from 0.001 lb. to 0.003 lb.

The balance was actually calibrated only with the smooth surface floating element. To determine the spring constant for any other element, the difference in weight between it and the smooth surface element was determined and Equation (3), above, was used with W and β modified to account for the weight difference.

The hot wire anemometer system used in this experiment was a Shapiro-Edwards constant current set with a half power frequency of 320 KHz.[55] The current was supplied by a low noise (0.005% output change for 10% line fluctuation) power source. The anemometer amplifier has a maximum gain of 52,000, a "floor to ceiling" ratio (ratio by which the compensation amplifier raises the wire half-power response frequency) of 420, and incorporates a compensation network which permits time constant settings of 50 μsec to 7.2 millisec. The mean hot wire voltage and current were monitored with an external circuit constructed by Gran[55] (but more thoroughly shielded) utilizing a digital multimeter. The mean square wire fluctuations were measured with a built-in thermocouple circuit of the hot wire set. The signal of this circuit was passed through an amplifier to achieve a 100 to 1 gain and monitored with a digital multimeter. Spectral measurements for the smooth plate case were made with an oscilloscope with a plug-in spectrum

analyzer unit. The amplified hot wire signal was input to the spectrum analyzer and the analyzer output was filtered to remove the high frequency noise, and recorded on an X-Y plotter. The analyzer was operated in a manual sweep mode to maximize the response.

For the rough wall data, the GALCIT Solo System was used to record the amplifier output. This is a portable system consisting of a Hewlett Packard 2100 computer, a disc unit, a tape unit, a Preston Model GMAD1-15B converter/multiplexer and associated equipment. With this unit the amplified hot wire signal was digitized at the rate of 450 KHz, and some 60,000 samples for each datum point and overheat ratio were stored on tape.

Severe problems were encountered in trying to use hot wires in Leg II. Initial attempts resulted in failure of the wire within 45 minutes to 1 hour after exposure of the wire to the air stream. The cause of the wire breakage was traced to particle impingement, and a 5 micron nominal rating, pleated, resin-impregnated-cellulose element filter was placed in the tunnel circuit upstream of the electric heater, as indicated in Figure 1. This filter is specified as removing > 95% of all particles greater than 5 microns in size and 100% of all microns greater than 13 microns.

Once the filter was installed, 0.0001 inch diameter platinum-10% rhodium hot wires with a length to diameter ratio of 180 to 200 were found to survive for several hours, although the wire would slowly stretch. This stretching was due to continued impingement of particles too small to cause wire breakage. Use of a filter with an order of magnitude smaller rating would have greatly reduced

this problem, but the cost and time required for such a modification were judged excessive. The manner in which this stretching was taken into account is discussed in the section on data reduction.

The hot wire probe design is shown in Figure 12. This design evolved from discussions with George Tenant, the "resident hot wire expert" of the Jet Propulsion Laboratory, and consideration of probe design criteria examined by Sandborn.[56] The probe body was made of brass, with the wedge strut formed from commercial 1/4 inch square brass tubing. The base plate was made of steel for rigidity, and all parts were silver soldered together. The hot wire supports were tapered jewelers' brooches made of high carbon steel and were separated from the probe body by a thin layer of Saurisen #29 ceramic cement. The same cement was used to bond the supports to the probe. Copper leads were fed through the probe body from the integral connector and joined to the supports by spot welding or silver soldering. Some probes also had 0.001 inch diameter Chromel and Alumel wires spot welded to one support within 0.005 inch of the tip to measure the support temperature. These wires were spot welded to larger leads near the aft end of the base plate and the larger leads were also fed through the probe body to the integral connector.

The probes were designed for use with 0.0001 inch diameter wire, yielding a length to diameter ratio of 180 to 200, depending on the probe and how slack the wire was when attached. This wire was chosen because it appeared to be the smallest wire which would survive the tunnel environment for a reasonable period of

time (more than six hours). The wire used was 0.0001 inch platinum-10% rhodium wire etched in concentrated nitric acid, and was spot welded to the supports with a certain amount of slack present to avoid any strain-gaging problems. All the spot welding was done by the author using a 60 power toolmaker's microscope and a conical, slightly rounded point ($\approx$ 0.005 inch diameter) copper electrode with a conventional spot welder. A jig was used to position the wire and electrode with the necessary precision.

All probes were fabricated using wire from the same spool and thus the wire properties should be very uniform. Several probes were calibrated to determine the temperature coefficient of resistivity, α_r. These probes were heated to temperatures of up to 300°F in an oven and the adiabatic wire resistance measured. The current used was 0.5 millamp--too low to cause any wire heating. No non-linear variation of resistance with temperature was found in this temperature range within the measurement accuracy.

Experimental Procedure

The nozzle contour was set with the smooth surface to provide uniform Mach 6 flow in the test section, and this contour was not altered when different surfaces were used. A nominal contour was calculated using a method of characteristics computer program and correcting for the boundary layer displacement thickness. This contour was then adjusted (while the tunnel was running at operating conditions) to minimize freestream Mach number variations in the test section. The centerline axial Mach distribution

achieved in this manner is shown in Figure 13.

Cross stream surveys were made using a Pitot probe to check the two-dimensionality of the flow. Several typical pressure traces are shown in Figure 14. It is seen that there were some small waves present in the flow, but it is believed that these were due to the tunnel throat design and they could not be eliminated. These surveys verify the two dimensionality of the flow in the tunnel, and show that within the test rhombus illustrated in Figure 13 and for a distance extending one inch on either side of the test section centerline, the free stream Mach number was $5.99 \pm \frac{1}{2}\%$. This Mach number distribution varied slightly from surface condition to surface condition; but for the worst case it was $M = 6.02 \pm 1\%$ in the above mentioned test section.

The surface plate lengths (Figure 3) were such that the leading edge of the third plate from the throat was located at $x = 25.4$ - several boundary thicknesses downstream of the intersection of the test rhombus with the wall. All step changes in surface roughness occurred at this location. For the smooth surface to rough surface configurations, the surface of the two aft surface plates consisted of the roughness illustrated in Figure 5 with one of three roughness heights ($k = 0.0125$, 0.025 and 0.050 inch). Preliminary results of the smooth-to-rough wall investigation revealed that an axial distance of some 8 inches (10δ or $20\delta^*$) was sufficient for the disturbed boundary layer to reach a new mean flow equilibrium state over the rough wall. Based on this information, the rough-to-smooth wall step change model was configured with a smooth plate immediately downstream of the throat, followed by rough surface ($k = 0.050$ inch)

second plate, with the use of two smooth surface plates downstream of x = 25.4 inches completing the surface plate set. The length of the rough wall section was 11.5 inches - considerably more than the length found necessary for the attainment of new mean flow equilibrium profiles in the absence of an axial pressure gradient. The choice of k = 0.050 inch for the roughness height was predicated on the fact that preliminary calculations indicated it would be in the fully rough regime, while the other roughness heights would fall into the transitionally rough region. The rough-to-smooth configuration is illustrated in Figure 4.

The low speed channel below the flat plate was instrumented with two thermocouples on the lower side of the base plates on the plate centerline, two on the lower side of the base plate adjacent to a side wall, and two in the low speed flow, two inches below the base plate. These thermocouples were arranged in two sets, one set at the same axial location as smooth surface thermocouple 9, and the other at the same axial location as thermocouple 12.

With the tunnel at operating conditions the low speed heater temperature was adjusted so that the temperatures indicated by the two thermocouples on the low speed side of the base plate were the same as those indicated by their respective surface thermocouples. The thermocouple readings were monitored over a period of several hours and were found to remain constant. If the low speed flow temperature were increased, a temperature gradient from the low speed flow toward the high speed surface would occur, and the plate temperature would rise toward a new state condition,

but the temperature gradient would remain. Similar results would occur for a low speed temperature decrease, but with the temperature gradient reversed.

The thermocouples near the side walls indicated temperatures within 2° F of those on the tunnel centerline, indicating negligible heat loss to the side walls. There was a somewhat more severe axial temperature gradient near the aft of the test section - some 1° F/in. between thermocouples 14 and 15. This gradient was due to the presence of the support structure for the aft end of the flat plate and could not be eliminated. The influence of this slight gradient on the plate temperature is considered to have been negligible as evidenced by the very long section of constant plate temperature shown in Figure 15.

A simple calculation based on the tunnel stagnation temperature indicates that a recovery temperature of 695° R would be expected. As shown in Figure 15, the flat plate temperature was 618° R, considerably below the anticipated value. The reason for this discrepancy is not fully understood, but it is believed to be due to a combination of heat loss from the uninsulated upper nozzle wall, and the influence of throat cooling far upstream. This will be discussed further in the Results and Discussion section, below. The heater setting determined for the smooth wall case was retained for all the surface configurations.

Prior to the acquisition of any data the flat plate was brought up to within 2-3° F of its equilibrium temperature over its entire length. This was usually accomplished by heating the flat wall with

the low speed flow (at an elevated temperature) for a period of two hours prior to tunnel startup. As the tunnel operating temperature increased after startup, the low speed flow temperature was decreased until the proper equilibrium setting was reached. The temperature distribution on the plate surface would normally level out and reach equilibrium conditions some 45 minutes to 1 hour after tunnel startup.

Pitot pressure and total temperature data were acquired using the instrumentation described above. The pressure transducer output was recorded on an X-Y plotter along with the position potentiometer output. The total temperature probe thermocouples were connected to a 32° F ice bath junction, and their outputs also recorded as a function of position. In all cases, the data were taken with the probe moving from the freestream toward the wall at a rate slow enough to prevent instrument lag. Plate contact for the Pitot probe was established by noting where the pressure ceased to decrease, while plate contact for the total temperature probe was determined by electrical contact of a portion of the probe and the plate.

The hot wire data were also taken while traversing from the freestream toward the plate. Surveys taken before the actual hot wire data were acquired were used to determine the approximate time constant of the wire as a function of applied current and wire position. The data reduction procedure could readily correct for inaccuracies in the time constant, so in the actual data acquisition an approximate time constant was determined for each location within the boundary layer at which data were to be taken, and this

value was used for each overheat current.

During data acquisition, a minimum of five overheat ratios or currents were used at each location within the boundary layer. Although three overheats theoretically would be enough for data reduction, the accuracy is increased by utilizing more, and five was chosen as a good compromise between accuracy and the time required to acquire the additional data. The currents ranged from 2 ma to either 12 ma or 10 ma depending upon the location within the boundary layer. Near the outer edge of the boundary layer, the heat transfer from the wire was greater, so higher settings were used, but as the wire approached the wall, the heat transfer decreased, and the wire temperature for a given current increased, so the maximum current was decreased. Operating experience revealed that overheat ratios of greater than 1.5 seriously weakened the wire and resulted in much shorter survival times, throughout most of the layer. Extremely close to the wall (within 0.050 inch), however, the reduced air loading and decreased particle impingement made possible the use of somewhat higher currents.

When balance data were to be taken, the balance was assembled in the plate and great care was taken to insure proper sealing of all joints. The element was traversed across the gap several times to insure that no particles or oil were present, and then the low speed channel flow was used to heat the plate until the balance reached the equilibrium temperature (as indicated by the thermocouples nearest it on the plate surface and a thermocouple mounted on the outside of the balance housing). Once the balance was up to

temperature, a pre-run zero was taken by traversing the element across the gap and recording the coil outputs. All this was done with the tunnel at atmospheric pressure. During this time, however, the compressor plant had been brought up the pressure in tunnel bypass operation. Once the zero reading was taken, the tunnel was evacuated and flow established. As soon as the nominal operating conditions and the plate equilibrium temperature were reached (normally about 15 minutes), two data traces were obtained by again traversing the element across the gap. After this was accomplished, the compressor plant was returned to bypass operation, the tunnel returned to atmospheric pressure, and a post-run zero taken. The data traces were taken as soon as possible after the tunnel start due to the presence of considerable oil vapor in the air flow which manifested itself as an oil film that gradually worked its way from the throat area aft. This film would be removed before each data run, but within 35 to 40 minutes of tunnel startup it would again reach the vicinity of the balance. If the oil did reach the balance element, it would cause the element to remain pinned to the side of the slot, and the only possible procedure was to shut the tunnel down and carefully clean the balance to remove the oil.

Pre- and post-run zeroes were taken with the tunnel at atmospheric conditions because tunnel leaks (outside of the test section) made it very difficult to maintain a uniform vacuum in the test section with the compressor plant in bypass operation. Any change in the pressure level would cause air to bleed into or out of the balance chamber through the gap around the element, causing

an erroneous reading. In addition, the extreme rigidity of the base plate insured that it, and thus the balance level, would not shift due to the existence of a pressure differential across the plate. Therefore, no error should be introduced by using atmospheric zeroes rather than evacuated zeroes.

The operation of the compressor plant causes considerable vibration of the entire wind tunnel structure and the balance was thus subjected to a rather severe vibration environment. The use of dashpots on the element reduced the element vibrations to the point where meaningful data could be obtained, but did not completely eliminate it. A typical data trace taken with 1000 centistoke silicone oil in the dashpots is shown in Figure 11. The change from the 50 centistoke oil originally used to the 1000 centistoke oil resulted in a very small decrease in the vibration amplitude, so it was concluded that the amplitude could not be decreased significantly by increasing the fluid viscosity further.

Except when balance data were actually being taken, the balance insert locations in the plates were filled with dummy balances which were solid plates the same size as the actual balance and machined to match the surface roughness pattern.

Wall temperature and pressure were monitored periodically throughout the test. Surfaces other than the smooth contained no pressure taps, but did contain thermocouples located at the same axial locations as the smooth surface, positioned some 0.050 inch below the surface.

DATA REDUCTION

Pressure Data

The free stream Mach number was computed from the free stream total pressure to stagnation pressure ratio assuming an isentropic expansion from the throat to the final flow conditions. The static pressure corresponding to this Mach number and stagnation pressure was then computed (using isentropic, perfect gas relations) and assumed to be constant across the boundary layer (a static pressure traverse established the validity of this approximation). The local measured Pitot pressure, corrected for Reynolds number effects using the results of Ramaswamy,[57] was used in conjunction with this static pressure to compute the local Mach number from the Rayleigh Pitot formula.[58]

Total Temperature Data

The local total temperature was determined using the theory of Behrens.[51] Basically, the wire recovery factor was computed from equation (A.6.5) and the flow total temperature was then computed from

$$T_t = \eta T_A$$

where

T_A = measured total temperature corrected for end loss effects

The wire end loss and radiation loss effects were computed and found to be negligible for flow conditions throughout the boundary layer. Due to the probe construction, it was not possible to acquire data within 0.030 inch of the wall, so a linear variation of total

temperature between the last measured data point and the wall temperature was assumed. Adiabatic, perfect gas relations were used to compute the local static temperature.

Hot Wire Data

Quantitative information on the fluctuating flow properties was obtained from the hot wire measurements utilizing the techniques developed by Kovasznay,[59] Morkovin,[60] Kistler,[43] Laufer,[61] and Gran.[55] The reduction of both mean and fluctuating flow hot wire data, including the end loss correction, is given in a condensed form by Gran.[55] For completeness, the theory is presented as Appendix A.

The hot wire support temperature was measured for both smooth and rough wall conditions at several locations within the boundary layer, and the data were found to be represented within 2 or 3% by

$$\frac{T_s - T}{T_t - T} = 0.94$$

Since the data reduction was found to be quite insensitive to small changes in this ratio, a constant value of 0.94 was used to reduce all the data. The manufacturer's specifications for wire diameter, d, and resistance per inch, r_r, were used. The thermal coefficient of resistivity was determined for several probes and was found to be $0.00094/^{\circ}R$ which is very close to that found by Dewey[62] for similar wire. Since all the probes were constructed with wire from the same spool, it was assumed that all probes had the same coefficient.

Significant problems were encountered during the test due to particle impingement on the hot wire. The filter located in the wind tunnel circuit, as stated above, had a nominal 5 micron rating and an absolute 13 micron rating while the wire size was 2.5 microns, so there still existed particles in the free stream which were considerably larger than the hot wire diameter. Although direct hits by large particles seldom occurred (wire breakage would immediately result), the wires would continually stretch while data were being obtained. In order to reduce the data, it was necessary to compensate for the resultant change in the resistance of the wire in still air (reference resistance). This was accomplished by determining, for each location within the boundary layer, the reference resistance which would yield a calculated total temperature equal to the measured total temperature. This resistance was then used to reduce the data at that location.

Once the fluctuating hot wire voltages had been corrected for wire thermal lag and the sensitivity coefficients had been computed, the mass flow and total temperature fluctuations were separated by using the mode diagram techniques of Kovasznay[59] and Morkovin.[60]

RESULTS AND DISCUSSION

Profile Data

Mean flow Pitot pressure and total temperature data were obtained throughout the boundary layer at least every two inches axially throughout the test section, Near the step change in roughness, profile data were obtained at one inch axial spacings. The results of these surveys are presented in Figures 16, 17, 18 and 19. The Mach number profiles presented in Figure 19 are representative of those for all the configurations. These profile data were extrapolated to wall conditions ($M = 0$, $u = 0$, $T = T_t = T_w$) at $y = 0$ in order to determine the displacement thickness (δ^*), momentum thickness (θ) and nondimensional enthalpy flux ($\dot{H}$).

Smooth Wall

Comparison of the smooth wall velocity profiles as presented in Figure 20 reveals that the smooth plate boundary layer is very nearly self preserving downstream of $x = 25.4$. A small amount of adjustment in the shape is seen to occur between $x = 25.4$ and $x = 29.4$, followed by very nearly identical profiles downstream to $x = 35.4$. However, the velocity profile suddenly becomes more "full" near the wall at $x = 37.4$. Although no data downstream of $x = 37.4$ are presented on the overlay plot, the profile data remain self-similar downstream to $x = 47.4$. The velocity profiles for all the step change configurations exhibit similar behavior in the vicinity of $x = 37.4$. Comparable perturbations are present in the density data. The profile integral data (to be discussed later) in Figures 24, 25, 26 and 27 also exhibit sudden shifts in level in the vicinity

of x = 37.4.

An examination of the typical freestream Pitot pressure distribution (Fig. 13) offers some insight into the cause of these anomalies. Small pressure peaks are seen to be centered in the freestream (y = 1.1 inches) near x = 33 and x = 48. This spacing is compatible with the existence of a weak pressure wave which is reflected off the upper nozzle wall such that it intersects the lower wall boundary layer near x = 33, reaches the wall near x = 40 and reflects back into the freestream near x = 47. Static pressure from widely dispersed smooth plate boundary layer surveys indicate that such a pressure wave does exist, although it is weak--maximum pressure variation across the boundary layer was observed to be some 7% at axial location 33.4.

Since all the data were reduced assuming $\frac{dp}{dy} = 0$, a question arises as to whether the observed effects of the pressure wave are real or due to the method of data reduction. Reduction of the smooth plate profile data at x = 33.4 and 39.4 utilizing the measured static pressure distributions produced velocity and density profiles which were very similar between the two locations. The effect of the wave was observed to be a slightly fuller velocity profile close to the wall at x = 33.4 as compared to x = 39.4. The effect of this wave on the profile integral data will be discussed in a later section. Thus, even though the pressure variation across the boundary layer was small, the assumption $\frac{dp}{dy} = 0$ is the major cause of the non self-similar boundary layer profiles. The presence of the pressure wave does affect the profiles, but only slightly. Use of the measured static

pressure data was precluded by the limited amount obtained (some four axial locations, all on the smooth plate), so the constant pressure assumption was utilized to produce the data reported here.

Comparison of the profile data for the various configurations was predicated on the fact that although strictly similar profiles could not be attained for an extended axial distance due to the pressure wave, the effect of this wave on the profile should be independent of configuration.

Roughness Effects

The step change configuration profile data are also presented in Figures 16, 17, 18 and 19 with representative profiles featured in more detail in Figures 21, 22 and 23. A cursory examination of the profile data reveals that the step change in roughness does, as expected, introduce significant changes into the various profiles and results in new equilibrium or self-similar profiles some distance downstream.

The development of the disturbed boundary layer may readily be observed from overlays of profile data at progressively greater distance downstream of the throat (Fig. 21, 22 and 23). The smooth-to-rough wall development as seen in these figures is representative of all the smooth-to-rough configurations. An increase or decrease in roughness size simply causes a corresponding increase or decrease in the magnitude of the observed effects. The influence of the step change in roughness is seen to spread rapidly across the entire layer, causing progressively larger changes as the layer

continues downstream, until a new equilibrium profile is assumed.

Analysis of the smooth-to-rough configuration profiles reveals that, for all quantities presented, the attainment of a new equilibrium profile is accomplished in approximately the same axial distance, regardless of the roughness height. The new profiles are definitely established 33 inches downstream of the throat, corresponding to some 10 boundary layer thicknesses (δ) or 20 displacement thicknesses (δ^*) downstream of the step change.

The boundary layer appears to take a slightly greater distance to adjust to the rough-to-smooth step change, but even in this case the new equilibrium profile is definitely established 37 inches downstream of the throat, some 14δ or 26δ^* downstream of the step change. Thus, although the boundary layer adjusts to the rough-to-smooth step change somewhat more slowly than to the smooth-to-rough step change, the difference in distance involved is only some 30% in terms of δ^*, or 40% in terms of δ.

Jacobs[63] performed his low speed work in fully developed channel flow on a two-dimensional roughness comprised of transverse rectangular bars. He found that the rough-to-smooth surface change resulted in a new equilibrium state within 17 channel half heights, while the rough-to-smooth change took some 25 channel half heights, an increase of 50%. Antonia and Luxton,[14, 64] working with the same type of roughness as used here in a low-speed boundary layer, found that less than 20 boundary layer thicknesses were required for the flow over the smooth-to-rough step to adapt to the change, while after 16 boundary layer thicknesses the profiles were "far from

self preserving" for the flow over the rough-to-smooth step. The present data, when δ^* is regarded as the thickness of the compressible boundary layer, are consistent with the results of both investigations.

Comparison of the profile data for the smooth wall case and the rough-to-smooth step change case (as presented in Figure 23) reveals that although the flow over the step change does attain new equilibrium profiles, they are not the same as the profiles for the smooth wall. The velocity, density and Mach number profiles for the rough-to-smooth configuration are found to be considerably less full throughout the boundary layer than the corresponding smooth plate configuration profiles. Much smaller differences are noticeable in the total temperature data. Thus the presence of the rough wall seems to give rise to some non-reversible changes in the boundary layer flow.

Rotta[65] and Bertram and Neal,[66] have suggested that non-equilibrium or upstream history effects may account for the differences observed in nozzle wall and flat plate boundary layers.

Feller,[67] Voisinet, et al.,[68] Sturek[69] and Bushnell, et al.[70] have investigated the effects of upstream conditions on the boundary layer. Their findings indicate that the properties of the nozzle-wall boundary layers are indeed very sensitive to changes in the upstream wall temperature and freestream pressure gradients. The effect of the upstream favorable pressure gradient was found by Bushnell, et al. to result in increased fullness of the velocity profile while not significantly affecting the total temperature profile. They

quote the data of Feller and Jones in the Langley Mach 6 high Reynolds number tunnel as revealing a tendency to relax from the characteristic tunnel wall quadratic total temperature-velocity variation to the usual flat plate linear relationship some 60 boundary layer thicknesses downstream of the nozzle exit. If the data of Feller and Jones could be applied to this work, this relaxation tendency would become evident some three feet downstream of the end of the test section.

If the subjection of the boundary layer to the rough wall section followed by the readjustment to smooth wall conditions produced a large enough perturbation to destroy or significantly decrease these upstream pressure and temperature effects, the anticipated result would be a somewhat less full velocity profile and a more nearly Crocco temperature-velocity variation. The observed velocity profile difference supports such a hypothesis, as do the temperature-velocity relationships presented in Figure 28. Further indications that the upstream wall temperature effects were destroyed by the rough wall sections are discussed in Appendix B.

Profile Integral Data

The following boundary layer parameters were computed from the profile data at each traverse:

$$\delta^* = \int_0^\delta \left(1 - \frac{\rho u}{\rho_e u_e}\right) dy$$

$$\theta = \int_0^\delta \frac{\rho u}{\rho_e u_e} \left(1 - \frac{u}{u_e}\right) dy$$

$$H = \delta^*/\theta$$

$$\dot{H} = \frac{100}{\delta^*} \int_0^\delta \frac{\rho u}{\rho_e u_e} \left(1 - T_t/T_{t_e}\right) dy$$

These data are tabulated in Table II and presented graphically in Figures 24, 25, 26 and 27. Trapezoidal integration of the appropriate quantities utilizing the data presented in Figures 16, 17 and 18 was used to determine these quantities. The profile data were extrapolated to the wall conditions ($M = 0$, $u = 0$, $T = T_t = T_w$) at $y = 0$ for these calculations. The effect of replacing the measured velocity profile for $y^+ = \frac{yu_\tau}{\nu_w} < 50$ (where the data would be most susceptible to probe interference effects) with data computed from Coles[52] tabulation of the incompressible law of the wall was found to be negligible.

As discussed earlier, the flow in the test section where these measurements were obtained was characterized by a freestream Mach number of $6.02 \pm 1\%$ where the variations in the Mach number were found to be caused by the presence of a weak pressure wave. The effect of this wave on the profile data was discussed earlier with respect to the consequences of utilizing the assumption $\frac{dp}{dy} = 0$ for the boundary layer reduction. The effect of this assumption on the integral data is illustrated in Figures 24, 25, 26 and 27 where the summary parameters resulting from the use of the measured static pressure profile at two axial locations on the smooth wall are plotted.

The $\frac{dp}{dy} = 0$ assumption is observed to be the major reason for the anomalous behavior of the momentum thickness near $x = 35$. This assumption, however, has little effect on the displacement thickness and enthalpy flux, implying that their sudden shift in level in the vicinity of $x = 33 \rightarrow 37$ is due to the presence of the

weak pressure wave in the test section.

The momentum integral equation for a two dimensional, zero pressure gradient flow such as this may be written

$$\frac{d\theta}{dx} = \frac{\tau_w}{\rho_e u_e^2} = \frac{C_f}{2}$$

The skin friction was directly measured (through use of the skin friction balance) for three configurations (smooth plate and smooth-to-rough wall with k = 0.025 and 0.050 inch) at x = 27.9 and 47.9. These data are included in Table III. The data at x = 47.9 were used in the above equation to determine the anticipated streamwise variation of θ for the various configurations. Lines with the appropriate slopes are faired through the data downstream of x = 37 (where the presence of the pressure wave has little effect on the data) in Figure 25. The actual streamwise variation of θ is seen to be in good agreement with the calculated value for all configurations.

Examination of the data in Figures 24-27 with the effect of the wave on the data in the vicinity of x = 33-37 in mind reveals no sudden changes due to the existence of a step change in roughness. The parameters are observed to adjust gradually to the change and to approach new equilibrium behavior in the vicinity of x = 37, just as the mean flow profiles do.

Transformation and Correlation

As mentioned in the introduction, there exist a multitude of transformation techniques for casting compressible velocity profile data into an equivalent incompressible form, but several recent papers including Lewis, et al.,[71] Keener and Hopkins,[32] and Kemp and Owen[72] have found that the Van Driest I[29] method accomplishes

this task as well as any of the others, and perhaps better than most. This occurs in spite of the fact that it was one of the earliest developed, is based on a less firm "theoretical" foundation, and is simpler to use than most.

Briefly, the Van Driest I transformation starts with the assumption of a Crocco temperature distribution through the boundary layer, i.e.

$$\frac{T_t - T_w}{T_{t_e} - T_w} = \frac{u}{u_e}$$

and uses the Prandtl mixing length theory to determine the Reynolds stress in the flow. The result is a transformation of the compressible velocity, u, into an "incompressible" velocity u^* via the equation

$$\frac{u^*}{u_e} = \frac{1}{A}\sin^{-1}\frac{2A^2(u/u_e)-B}{(B^2+4A^2)^{\frac{1}{2}}} + \frac{1}{A}\sin^{-1}\frac{B}{(B^2+4A^2)^{\frac{1}{2}}} \qquad (4)$$

where

$$A^2 = \frac{\frac{\gamma-1}{2}M_e^2}{T_w/T_e}$$

$$B = \frac{1+\frac{\gamma-1}{2}M_e^2}{T_w/T_e} - 1$$

Van Driest deduced that this velocity would be correlated by

$$\frac{u^*}{u_\tau} = \frac{1}{\kappa}\ell n\frac{y u_\tau}{\nu_w} + \Gamma$$

where

$u_\tau = \sqrt{\tau_w/\rho_w}$

κ = 0.4 - Karman's constant

ν_w = kinematic viscosity at the wall temperature

F = constant dependent only on the boundary conditions (i.e. freestream pressure gradient and wall conditions)

The similarity of this equation and the law of the wall immediately suggests the use of the law of the wall to correlate the transformed velocities. The form of the law of the wall to be used in this work is[73]

$$u^+ = \frac{1}{\kappa} \ell n\, y^+ + C + \frac{\overline{\pi}}{\kappa} w(y/\delta) - \frac{\Delta u}{u_\tau} \qquad (5)$$

where

$u^+ = u^*/u_\tau$

$y^+ = \frac{y\, u_\tau}{\nu_w}$

C = 5.0 - universal constant

$\overline{\pi}$ = wake strength parameter dependent on the free-stream pressure gradient

$w(y/\delta) = 2 \sin^2 (\frac{\pi y}{2\delta})$ - "wake function" suggested by Coles[73]

$\frac{\Delta u}{u_\tau}$ = Clauser's[74] rough wall velocity defect

$= \frac{1}{\kappa} \ell n \frac{k\, u_\tau}{\nu_w} + D$

D = a constant dependent only on the wall conditions

As stated above, the Van Driest transformation is based on the assumption of a Crocco temperature profile. The temperature profile most often used to estimate temperature distributions in boundary layers are

(a) Crocco

$$\frac{T_t - T_w}{T_{t_e} - T_w} = u/u_e$$

which leads to

$$\frac{T}{T_w} = 1 + A\, u/u_e - B(u/u_e)^2 \qquad (6)$$

where

$$A = (1 + \frac{\gamma-1}{2} M_e^2) T_e/T_w - 1$$

$$B = \frac{\gamma-1}{2} M_e^2 \, T_e/T_w$$

and

(b) Walz[75] or quadratic

$$\frac{T_t - T_w}{T_{t_e} - T_w} = \frac{T_r - T_w}{T_{t_e} - T_w} u/u_e + \frac{T_{t_e} - T_r}{T_{t_e} - T_w} (\frac{u}{u_e})^2$$

$$(= (u/u_e)^2 \text{ for } T_r = T_w)$$

which leads to

$$\frac{T}{T_w} = 1 + A(u/u_e) - B(u/u_e)^2 \qquad (7)$$

where

$$A = (1 + r\frac{\gamma-1}{2} M_e^2) T_e/T_w - 1$$

$$B = r\frac{\gamma-1}{2} M_e^2 \, T_e/T_w$$

Comparison of these formulae with the experimental data for two sample cases is made in Figure 28 where it is evident that while the trend of the temperature-velocity relation is represented by both profiles, neither is a good approximation. Also shown is a least squares quadratic curve fit to the data for each case.

Since the Crocco distribution is such a poor fit to the data, doubt is cast on the validity of the transformation for the velocity data. It is readily verified, however, that the Van Driest transformation may be altered to utilize the coefficients of the curve fit to the actual data in place of the A and B in equation (4). Both the Crocco and empirical temperature distributions were used in an attempt to correlate the data. The transformation of the velocity data via the "modified" Van Driest relationship resulted in a better correlation (in the sense that the deduced skin friction was closer to the measured value) for the smooth plate data at x = 47. This procedure yielded a skin friction within 1% of the measured value while the use of the standard Van Driest transformation resulted in a skin friction value some 8% lower. The modified form of the transformation has been used exclusively in the results discussed below.

Examination of equation (5), above, reveals that, for the general case of a rough wall, there exist four parameters to be determined by application to the data, u_τ, $\bar{\pi}$, δ and $\frac{\Delta u}{u_\tau}$. A value for δ may be determined by examination of each velocity profile before it is correlated, but it was felt that this is a very imprecise method, so it was determined as one of the correlation parameters. These four parameters are not independent, however, as may be seen by evaluating the law of the wall at the edge of the boundary layer:

$$\frac{u_e^*}{u_\tau} = \frac{1}{\kappa} \ell n \frac{\delta u_\tau}{\nu_w} + C - \frac{\Delta u}{u_\tau} + \frac{2\bar{\pi}}{\kappa}$$

Here u_e^*, ν_w, C and κ are known, so there exist only three independent parameters. In the case of the smooth wall, $\frac{\Delta u}{u_\tau} = 0$ was assumed to

apply as for the incompressible case, leaving only two parameters to be determined from the correlation.

Following the application of the modified Van Driest transformation, a non-linear least square parameter estimation computer routine was used to determine the values of u_τ, $\bar{\pi}$, δ, and $\frac{\Delta u}{u_\tau}$ which best fit the data. In all the correlation parameter fits, only data which satisfied the criteria

$$y^+ \left(= \frac{(y+y_0)}{\nu_w} u_\tau\right) > 50 \quad (y_0 = \text{effective origin, see below})$$

and

$$u/u_e < 0.98$$

were utilized. The rationale for these criteria is that for $y^+ < 50$, the influence of the viscous sublayer is present and equation (5) is known to be inapplicable in this region, while for $u/u_e > 0.98$, the law of the wall is not expected to hold since these data are essentially in the freestream.

The composite law of the wall was fit to all of the data satisfying the above criteria for each velocity profile rather than trying to cast the data in velocity defect form and fit the logarithmic section first to determine $\frac{\Delta u}{u_\tau}$, followed by a fit to all the data with $\frac{\Delta u}{u_\tau}$ fixed to determine u_τ and $\bar{\pi}$. It was felt that such a procedure would be quite imprecise because of the very short logarithmic section present in these data.

As indicated above, for the smooth plate data, the required two parameter fit was found to be a very stable procedure. In the case of a step change in roughness, however, the situation was

considerably more complicated. There is some evidence (Antonia and Luxton[14]) that the law of the wall does not correlate incompressible velocity profile data immediately downstream of a step change in surface roughness. The applicability of the correlation to the data reported here will be determined from the correlation results. Assuming that the correlation is applicable for all the step change data, several factors made its use more difficult than in the smooth wall case. First, unlike the smooth plate case, $\frac{\Delta u}{u_\tau}$ was not known. Second, $\frac{\Delta u}{u_\tau}$, although anticipated constant for the fully developed profile case, will certainly change in some manner from its value for the pre-step surface condition to its equilibrium value for the post-step surface condition. In addition, Perry et al.[8] and Antonia and Luxton[14] have found that the flow over a rough wall may be correlated with the smooth wall form of the law of the wall only if an effective origin (which falls somewhere between the crest and the valley of the roughness) is used. The exact location is that origin displacement which results in the logarithmic portion of the velocity data acquiring a slope of $1/\kappa$. The precise determination of this effective origin has been found to be very elusive, but for this type of roughness it is thought to be in the range of 0.5 to 0.66 of the roughness height below the roughness crest.

A systematic variation of y_0 (the effective origin distance below the crest) was performed for the fully developed rough plate flows, using ten equally spaced increments to go from the crest to the valley. $y_0 \approx 0.5k$ was found to most consistently produce the best fit (in the least squares sense) to the data in the fully developed

region of flow. Visual inspection of the results of using this y_0 verified the existence of a $1/\kappa$ slope. In the transition region downstream of the step, the proper value of y_0 was found to be very elusive. For the smooth to rough change, $y_0 = 0$ for a distance of two inches downstream of the step usually resulted in the best fits. This was then followed by a distance of 10 to 12 δ in which y_0 changed from 0 to 0.5k. The rough to smooth case yielded a less well behaved y_0. y_0 changed very quickly subsequent to the surface change, but seemed to oscillate before acquiring the downstream value of 0 some 14δ downstream of the step. The effect of changes in y_0 on the correlation results was found to be quite small. A change from $y_0 = 0.5k$ to $y_0 = 0.25k$ produced a 1% or smaller change in the computed τ_w.

Even with the value of y_0 established, however, the correlation of the step change velocity data retained a fair amount of difficulty. One of the parameters had to be fixed before the parameter fit became a stable procedure. Although it has been argued that the wake strength parameter is independent of wall conditions, the freestream pressure distribution varied enough from one configuration to the other to cause changes, for Lewis, et al.[71] have shown $\bar{\pi}$ to be very sensitive to changes in pressure gradients. The existence of skin friction data for some of the configurations provided a means whereby this difficulty could be overcome.

The measured skin friction (Table II) was used to correlate the velocity obtained adjacent to the aft balance location. This yielded values of $\bar{\pi}$ and $\frac{\Delta u}{u_\tau}$ (and thus δ) for that location. In addition, it was assumed that for the flow upstream of the step change $\frac{\Delta u}{u_\tau} = 0$ for the

smooth to rough configurations. This then yielded a second value of $\overline{\pi}$. Values of $\overline{\pi}(x)$ for $24 < x < 48$ were then estimated, using these values as reference points and following the general trend of the smooth wall $\overline{\pi}(x)$. No balance data were available for the k = 0.0125 smooth-to-rough wall, so $\overline{\pi}(x)$ for k = 0.025 in. was used. A similar procedure was utilized for the rough-to-smooth step change data, assuming that the value of $\Delta u/u_\tau$ determined at the aft balance station for the k = 0.050 in. rough wall would apply upstream of the rough-to-smooth wall step. Examination of the sensitivity of the correlation to the assumed value of $\overline{\pi}$ indicated that the effect of a change in $\overline{\pi}$ was reflected by an inversely proportional change in the computed skin friction.

Figure 29 presents the results of two correlations, both at x = 47.4 inches from the throat. The correlation of the smooth wall data was computed, as indicated earlier, assuming $\Delta u/u_\tau = 0$ while the rough wall correlation was based on the measured skin friction at that location. A comparison of Coles' wake function with the actual data is made in Figure 30. In both figures the fit of the data is seen to be excellent.

Correlation Results

The various parameters resulting from the curvefits are presented in Table III, with graphical presentation made in Figures 31, 32 and 33. A cursory examination of these figures reveals the existence of sudden shifts in the parameter values at axial locations of 33 to 39 inches from the throat. This is the same region in which changes occurred in the profile shapes and the integral properties, indicating that these anomalies are also due to the previously

discussed pressure wave and data reduction techniques.

The wake strength parameter $\bar{\pi}$ (Fig. 31) is observed to vary between 1.1 and 1.6 for all configurations. This is significantly larger than the value of 0.61 advanced by Coles[73] as being the representative value for the incompressible, smooth, flat plate equilibrium boundary layer. Once again, the effect of the $\frac{dp}{dy} = 0$ assumption in data reduction was investigated and found to be the cause of the large change in level between x = 33 and x = 39 (Fig. 31). As stated above, only the wake strength parameters for the smooth wall case and those at x = 25.4 and 47.4 for the step change configurations were computed from the curvefit. All others were estimated from these values, as discussed in the Transformation and Correlation section.

The existence of such a large $\bar{\pi}$ parameter is in contrast to the results of Keener and Hopkins[32] at Mach 7 ($\bar{\pi} = 0.4$) and those of Lewis, et al.[71] at Mach 4 ($\bar{\pi} = 0.6$). The data of Reda, et al.[76] at Mach 2.9 yields $\bar{\pi} = 1.2$, while those of Owen, et al.[44] at Mach 7 yield $\bar{\pi} = 0.8$. Laderman and Demetriades[45] at Mach 9 report $\bar{\pi} = 1.4$. In all cases the Van Driest transformation was used to cast the velocity data into an "incompressible" form for use in the correlation. Only Keener and Hopkins have investigated the effect on the transformation of using a fit of the actual data in place of the usual Crocco distribution. They concluded, as did the author above, that the use of the measured temperature velocity relationship resulted in better correlation results and a somewhat higher value for $\bar{\pi}$, compared to the results achieved utilizing the Crocco distribution.

Laderman and Demetriades tentatively contribute their large value of π to the presence of a strong pressure gradient across the

boundary layer ($p_w = 1.5\ p_e$) in their test. The results of the present work reveal that the presence of a similar, though much smaller gradient ($p_w = 1.05\ p_e$ at $x = 39$, Fig. 31) results in essentially no change in $\overline{\pi}$.

All of the above mentioned work, with the exception of Lewis, et al. was performed on wind tunnel nozzle walls at various rates of cooling. The occurrence of larger $\overline{\pi}$ values seems to scale, to some extent, with the wall temperature ratio, but this does not explain the entire variation from test to test. The data of Lewis, et al. were acquired at adiabatic conditions in the tunnel freestream and the value of $\overline{\pi}$ was among the lowest reported. This raises the question of upstream history effects once more. As discussed earlier, the existence of the large favorable pressure gradients creates velocity boundary layers on the nozzle wall which are somewhat fuller than those formed on flat plates in the freestream. As a result, the "incompressible" velocity profiles would be expected to differ, possibly yielding different wake parameters.

The correlation skin friction results are presented in Figure 32, along with the measured skin friction. As mentioned previously the measured skin friction at $x = 47.9$ for the two smooth-to-rough wall configurations was used to determine $\overline{\pi}$ in the correlation, so any disagreement of the computed and measured values would be indicative of problems in the correlation procedure. The skin friction measurements at $x = 27.9$ for the step change configuration and at $x = 47.9$ for the smooth plate, however, were not used as inputs to the correlation. The excellent agreement of the computed skin friction with the measured values for the smooth plate and $k = 0.025$ inch

step-change configurations is conclusive evidence that the correlation procedure is valid and that it may be used in a non-equilibrium region with great success. Disagreement of the computed skin friction with that measured at x = 27.9 for the k = 0.050 inch smooth-to-rough step configuration and the behavior of the computed skin friction in the vicinity of the step indicate that the perturbation of the flow due to the large roughness height is too large for the correlation to be successful. The rough-to-smooth results, on the other hand, indicate a very smooth and relatively rapid transition to the downstream values. Although no measured values are available for comparison, these trends indicate that the correlation is applicable for this configuration, even though the roughness height is the same as that in the smooth-to-rough step where the correlation was found to be invalid.

The roughness induced velocity shift data in Figure 33 (where $\frac{\Delta u}{u_\tau}$ is from equation (5), above) tend to support these conclusions, although the scatter in the k = 0.0125 inch smooth-to-rough configuration would, by itself, give rise to doubts about the applicability of the correlation in this case. In the light of its suitability for the k = 0.025 inch configuration, however, this scatter is attributed to the use of the same $\overline{\pi}(x)$ distribution for k = 0.0125 inch as was determined for the k = 0.025 inch configuration. The significant increase in the value of $\frac{\Delta u}{u_\tau}$ immediately downstream of the step for the k = 0.050 inch smooth-to-rough case corresponds to either a significant decrease in τ_w (as seen in Fig. 32) or a significant increase in the velocity across the boundary layer. Neither of these effects would be expected and neither is observed for the other configurations,

thus substantiating doubts about the correlation's validity in the step region for this roughness. The rough-to-smooth velocity defect, however, is observed to adjust gradually to the smooth wall conditions, pausing at a somewhat low value in the vicinity of $x = 37 \rightarrow 41$ before attaining its smooth wall value of 0.

The examination of the curvefit results to this point has thus yielded the following results:

1. The assumed form of the law-of-the-wall correlates the equilibrium smooth data very well, judging by the accuracy with which the skin friction was computed.

2. The correlation is applicable in the non-equilibrium flow region immediately downstream of a step change in roughness, provided the change is not too large (what constitutes "large" cannot be deduced on the basis of these results).

3. The boundary layer adjusts gradually to the step change, assuming the properties appropriate to the new wall condition only a considerable distance downstream (the same location as that at which new equilibrium profiles are observed). This is in contrast to the finding of Antonia and Luxton[14] (for a smooth-to-rough step change) that adjustment to the rough wall condition is made within three or four boundary layer thicknesses following an initial overshoot to a level above that finally attained. Antonia and Luxton's[64] results for a rough-to-smooth change are consistent with those found here, i.e. τ_w changes gradually to the value appropriate for the smooth wall.

Quantitative Roughness Effects

One convenient method of describing any given roughness is to determine its "equivalent sand grain" roughness, which is defined as the height of Nikuradse's sand grain roughness which would be required to produce the same velocity defect. The subject roughness, however, must be "fully rough," i.e. it must have a large enough roughness Reynolds number that the law of the wall may be expressed in the form

$$u^+ = \frac{1}{\kappa} \ell n\, y/k + \frac{2\overline{\pi}}{\kappa} \sin^2 \left(\frac{\pi y}{2\delta}\right) + D \qquad (8)$$

Dvorak[41] presents tentative criteria for the upper limit of the transitionally smooth regime which indicate that the critical roughness Reynolds number for this particular roughness is $k^+ \left(= \frac{k u_\tau}{\nu_w}\right) = 30.$ Thus the k = 0.050 inch roughness ($k^+ = 33.8$ from measurements) would be considered "fully rough," while the k = 0.0125 inch and k = 0.025 inch roughness heights ($k^+ = 7.1$ and 14.9, respectively) would fall into the transitionally rough regime.

For the fully rough regime, the results of Nikuradse for incompressible pipe flow (where there is no "wake" function) may be represented by[1, 77]

$$u^+ = \frac{1}{\kappa} \ell n\, y/k_s + 8.5$$

$$= \frac{1}{\kappa} \ell n\, y^+ - \frac{1}{\kappa} \ell n\, k_s^+ + 8.5 \qquad (9)$$

where k_s is the sand grain roughness height. The smooth wall results of Nikuradse are correlated by

$$u^+ = \frac{1}{\kappa} \ell n\, y^+ + 5.5$$

Equation (9) may be rewritten as

$$u^+ = \frac{1}{\kappa} \ell n y^+ + 5.5 - \frac{\Delta u}{u_\tau}$$

where

$$\frac{\Delta u}{u_\tau} = \frac{1}{\kappa} \ell n k_s^+ - 3.0 \qquad (10)$$

which yields

$$k_s^+ = e^{\kappa(3 + \frac{\Delta u}{u_\tau})} \qquad (11)$$

As before, the effect of compressibility is to require the use of ν_w in place of ν.

The application of equation (11) to the velocity defect of the k = 0.050 inch roughness from Figure 33 ($\frac{\Delta u}{u_\tau} = 6.5$) yields $k_s^+ = 44.7$ or, since $k^+ = 33.8$, $k_s/k = 1.3$. Returning for a moment to the low speed correlation results of Dvorak and Betterman (and extended by Simpson[78] and Dirling[79] to other geometries with good results), the effect of the square bar roughness with $\ell/k = \lambda$ (wavelength-to-height ratio) < 4.7 is found to be

$$\frac{\Delta u}{u_\tau} = \frac{1}{\kappa} \ell n k^+ + 17.35\,(0.705\,\ell n \lambda - 1) \qquad (12)$$

which yields, for $k^+ = 33.8$, $\lambda = 4$

$$\frac{\Delta u}{u_\tau} = 8.4$$

The validity of this equation is limited to the fully rough regime ($k_s^+ \geq 70$); however, $k_s^+ = 45$ is close enough to this regime that no large errors are introduced ($\frac{\Delta u}{u_\tau}$ varies little from the fully rough relation--see Fig. 34). This is significantly higher than the observed value (Fig. 33) of 6.5--some 30% higher. The use of equation (11) with $\frac{\Delta u}{u_\tau} = 8.4$ yields $k_s/k = 2.8$--more than double the actual value of 1.3

calculated above. These results illustrate quite graphically the inability of the low speed correlation results of Dvorak, Betterman, Simpson and Dirling to correlate the present hypersonic data.

For transitional roughness, Dvorak suggests the use of an equation of the form

$$\frac{\Delta u}{u_\tau} = C_0 + C_1 \ell n\, k^+ + C_2 \ell n^2\, k^+ + C_3 \ell n^3\, k^+$$

to predict the velocity defect. The constants are to be evaluated by requiring that $\frac{\Delta u}{u_\tau}$ and its first derivative match those of equation (12) at the beginning of the fully rough regime and to vanish at the hydraulically smooth limit of $k^+ = 5$. There are a number of problems with this procedure, among which are the fact that equation (12) has just been shown to be inappropriate for this roughness, and the nebulous criteria for determining when the surface becomes fully rough. Even if these difficulties are resolved, however, a new set of constants must be computed for each new roughness configuration or change in roughness effectiveness, a far from desirable situation.

The current data are presented, along with previously published data, in Figures 34 and 35. Use of the equivalent sand grain roughness Reynolds number in the abscissa effects the collapse of data for several roughness configurations and Mach numbers ranging from 0 to 6 into a single, well defined curve in both cases. The sand grain roughness, unless otherwise noted, was computed for each set of data by choosing a value of $\frac{k u_\tau}{\nu_w}$ in the fully rough regime and utilizing the associated value of $\frac{\Delta u}{u_\tau}$ in equation (11) above. This value of k_s was then used to plot all data points for that configuration.

When presented in this manner, a single curve is sufficient to describe the data in Figure 34. For $k_s^+ > 70$ the appropriate equation is $\frac{\Delta u}{u_\tau} = \frac{1}{\kappa} \ell n\, k_s^+ - 3.0$. An equation of the form suggested by Dvorak may be used to describe the trend of the data in the transitionally rough regime. Such an equation is presented in Figure 34. The velocity defect and its first derivative were specified to vanish at $k_s^+ = 3.5$ and to match the fully rough values at $k_s^+ = 70$.

The data in Figure 35 are adequately represented by the equation

$$\frac{C_f}{C_{f_0}} = 0.39(\ell n\, k_s^+ - 2.3) + 1.0$$

Thus, once the effective sand grain roughness is known, the effect of surface roughness on the skin friction and velocity defect may readily be determined. The only problem that remains is the determination of the equivalent roughness, which is basically what is accomplished by the correlations of Dirling and the others mentioned previously. However, these correlations were found to be inapplicable for these flow conditions. A brief discussion of the flow over the type of roughness is in order.

The data of Liu, et al.[7] were obtained on transverse square bar roughness with a wavelength of 4 in low speed water flow, and their results indicate an equivalent roughness of $k_s = 2 \rightarrow 2.5k$, fairly close to the value of $k_s = 2.7$ for the work of Betterman. The results of Betterman yield the following equivalent roughness for varying λ;

λ	=	$4.1 \rightarrow 4.2$	k_s/k	=	2.7
λ	=	3.3	k_s/k	=	1.1
λ	=	2.6	k_s/k	=	0.39

Thus, for λ in the vicinity of 4, the effectiveness is extremely sensitive to small changes. The visualization work of Liu, et al. revealed that in the vicinity of $\lambda = 4$, the character of the flow in the cavity between the roughness elements changes radically. For λ considerably less than 4, the flow completely bridges the cavity (the "d" type flow of Perry, et al.[8]), creating an "open" cavity, while for λ much larger than 4, the flow reattaches to the cavity floor, creating two distinct separation regions within the cavity (a "closed" cavity). The transition from one type of cavity to the other occurs for λ somewhere in the range of 2 to 8. This explains the sudden shift in slope of the correlation results of Dirling as presented in Figure 36 (from Mills and Courtney[80]). As λ increases from 2, the vortex structure within the cavity is stretched and pressure communication between the upstream and downstream faces is decreased, resulting in increased pressure drag. The maximum drag is reached very near the value of λ at which reattachment occurs, for then the pressure drag on the faces has reached the maximum and any increase in spacing simply produces less force per unit length, and, therefore, less drag per unit length. The slope change occurs at a value of λ slightly above 4, corresponding to the change between open and closed cavity flow.

Charwat, et al.[81] have investigated higher speed flow over two dimensional transverse notches and conclude that for supersonic flow over large cavities, closed cavity flow exists for $\lambda > 12$ and open cavity flow exists for $\lambda < 10$. The observation of a crossover point near $\lambda = 4$ for subsonic flow is also made, supporting the conclusions of Liu, et al.

Thus, the type of cavity flow near $\lambda = 4$ is dependent upon flow speed as well as spacing. With this fact in mind, a close examination of the results of Betterman[5] yields interesting results. Although the data for $\lambda = 4$ at velocities of 10, 20, and 30 m/s are correlated with a single curve, the actual data indicate a definite decrease in $\frac{\Delta u}{u_\tau}$ with increasing velocity, even in this speed range. An increase in velocity from 10 to 30 m/s results in a decrease in $\frac{\Delta u}{u_\tau}$ of 0.7. In light of these results all of the correlation work on equivalent sand grain roughness heights must be viewed as extremely velocity sensitive and applicable only to very low speed flows.

In conclusion, the data acquired in this work for equilibrium rough wall flow show good agreement with previously published data, when correlated with respect to Reynolds number based on the equivalent sand grain roughness height. The equivalent roughness, however, is found to be significantly altered from that for identical roughness in low speed flow. These data support the claim advanced by Mills and Courtney,[80] and others that once the equivalent sand grain roughness is determined, the effect of a given roughness on the skin friction and velocity may readily be determined (i.e. Fig. 34 and 35). The determination of equivalent sand grain roughness, however, is not a trivial matter, as demonstrated by the results of this work. In particular, the extrapolation of any low speed correlation for equivalent sand grain roughness, such as that of Dirling,[79] to higher speed flows must be viewed as highly susceptible to very large errors.

Fluctuation Data

Although the acquisition of reliable hot wire data in any hypersonic flow is difficult, the presence of large particles in the tunnel flow causes it to become a very formidable task. In this work the presence of particles ranging in size up to some five wire diameters added to the problems due to the high air loading of the wire, the high temperature environment, high frequency response requirements, and exposure of the wire to start up and shut down shocks to result in relatively short survival times for most probes. As a consequence, it was not possible to calibrate the wires prior to use because the time required for calibration would have been a large portion of the average wire lifetime. In addition, the particle impingement problem would have dictated frequent recalibrations due to the constantly changing wire length and resistance.

Preliminary analysis of the data during the acquisition phase of this work indicated that the data were of reasonable magnitude and possessed the anticipated profile shape. Later complete reduction and extensive analysis revealed that some of the data were obviously in error, but it was not possible to repeat the measurements. As a result, fluctuation data for some of the wall configurations at some axial locations were discarded and are not included in this discussion.

The fluctuation magnitudes, as discussed herein, contain rather large error bands--probably ± 10-20% on a point by point basis. However, when considered in conjunction with data at other points throughout the boundary layer, very definite trends which do not depend on the magnitude accuracy are observed. In addition, the

consistency of the observed magnitudes lends considerable credit to their validity.

Observations of the raw hot wire signal revealed properties typical of hot wire signals in high Mach number flows, i.e., high frequency components for all overheat ratios, and a one-sided signal near the outside edge of the boundary layer[43] and again near the edge of the viscous sublayer edge which was some 0.010 to 0.015 inches from the wall.[45, 72, 82] The sense of the signal one-sidedness at the viscous sublayer edge was dependent upon the overheat ratio and opposite that at the boundary layer-freestream interface, as observed by Laderman and Demetriades.[45] Within the sublayer, the signal was very similar to that in the freestream, considerably below its magnitude within the outer boundary layer. During this acquisition these very different signatures served as a handy visual means of identifying which section of the boundary layer was being surveyed at any given distance from the wall.

Kemp and Owen[72] point out that it is unlikely that large fluctuations ever reach the wall in their case (M_e = 20 - 47) due to the extreme thickness of the sublayer. The mere existence of the viscous sublayer (which is present for all turbulent smooth wall boundary layers) would significantly dissipate the fluctuations present in the outer boundary layer flow, and the effect of increasing Mach number would be to make the sublayer thicker, thereby making the dissipation more effective. Thus the observation of Kemp and Owen is simply the result of a universal property made more visible in high Mach number flows.

Typical power spectra for the smooth wall configuration at several overheat currents are presented in Figure 37. The signal is observed to remain significant up to very high frequencies which is typical of hypersonic flows.[43, 82, 83] The power is observed to become more concentrated at the lower frequencies as the overheat current is increased, indicating that the mass flux ($\dot{m}$) fluctuations (to which the wires are most sensitive at high overheats) tend to be of somewhat lower frequency and larger size than the total temperature fluctuations. The total temperature fluctuations are seen to be much more uniformly distributed over the frequency range.

Fluctuation data are presented as mass flux fluctuations $\left(\sqrt{\overline{\dot{m}'^2}}/\dot{m}_\ell\right)$, total temperature fluctuations $\left(\sqrt{\overline{T_t'^2}}/T_{t_\ell}\right)$, and the associated correlation coefficient, $R_{\dot{m}\,T_t} = \overline{\dot{m}'\,T_t'}/\left(\sqrt{\overline{\dot{m}'^2}}\sqrt{\overline{T_t'^2}}\right)$ for all wall configurations in Figures 38, 39, and 40. No smooth wall data were obtained at x = 24.4, and where data for a particular configuration have been omitted, the data were found to be in error. Some fluctuation data obtained at x = 51.4 inches downstream of the throat are presented in these figures. No mean flow data at this location have been presented because heat transfer and pressure gradient effects were present. However, the fluctuation data at this location have not yet been significantly influenced by these new flow conditions.

Here, as for the mean flow data, the profiles at various axial locations were compared to determine where the profiles ceased to show discernible change. The boundary layer downstream of this

location was then defined as an equilibrium or self preserving layer. In the case of the mean flow data, the number of axial locations and the high resolution of the data yielded fairly definitive results. For the fluctuation data, however, data were obtained at far fewer axial stations and the data scatter was much greater. As a result, the axial location at which the profiles become self similar is far more difficult to locate. Data considerably downstream of the test section would be required to verify that equilibrium profiles actually are established.

Smooth Wall

The smooth wall configuration serves as a reference for determining the roughness induced effects, and as such, will be discussed first. Examination of the mass flux ($\dot{m}$) and total temperature (T_t) fluctuation profiles reveals that both profiles become "fuller" as the axial distance increases from 27.4 to 39.4 inches from the throat and then remain essentially constant downstream to x = 45.4. Thus, although the mean flow profiles, as discussed above, indicate that mean flow equilibrium on the smooth wall is achieved near the upstream end of the test rhombus, the fluctuation properties do not achieve a self similar or equilibrium state until some distance downstream, between x = 33 and x = 39, some 14 to 20 inches (18 to 25δ) downstream of the test section boundary. It appears that the fluctuation levels characteristic of the smooth wall are suppressed in the favorable pressure gradient flow created by the nozzle and gradually relax to an equilibrium profile once free of the large gradient. The data of Rose[82] indicate that the fluctuation magnitude in a compressible flow is significantly affected by pressure gradients, with a favorable gradient causing a decrease in magnitude.

Comparison of the smooth wall data with that obtained by Kistler,[43] Laderman and Demetriades[84] and Owen et al.[85] is made in Figure 41 (replotted from Owen, et al.). The present data are observed to agree quite well with the M = 1.72 results of Kistler, in opposition to his findings that all the quantities increase with Mach number in the Mach number range of 1.7 to 4.7. Although Owen, et al. attribute the differences between Kistler's results and their own to heat transfer effects, the present data do not substantiate such a claim, for in spite of the present adiabatic nozzle wall, the data do not agree with the trends established by Kistler's results.

Smooth-to-Rough Transition

Examination of the smooth-to-rough wall configuration data (Figs. 38, 39, and 40) reveals that self-similar shapes (within the accuracy of the data) are attained for the $\dot{m}$ fluctuation profiles upstream of x = 39 inches for all roughness sizes. Equilibrium profiles for the T_t fluctuations are attained somewhat later, between x = 39.4 and x = 45.4, as verified by the available x = 51.4 data. Following the smooth-to-rough wall step change, then, a definite pattern is noted--the mean flow data are the first to attain new equilibrium profiles, followed by the mass flux fluctuation data, followed in turn by the total temperature fluctuation data. This progression is a consequence of the manner in which the roughness interacts with the boundary layer to produce the mass flux and total temperature fluctuations. The roughness actually induces velocity fluctuations which interact with the mean flow to result in mass flux fluctuations which in turn interact with the mean flow and velocity fluctuations to create total temperature

fluctuations. Thus, before the fluctuations can reach equilibrium levels, the mean flow must be in equilibrium, and since a finite amount of time is required for $\dot{m}$ fluctuations to respond to a change in mean flow conditions, there will be a time (and distance) lag prior to the establishment of $\dot{m}$ equilibrium profiles. In the same manner, the T_t fluctuations are dependent upon the interaction of the mean flow and $\dot{m}$ fluctuations, and so will reach equilibrium even later in time and further downstream.

Roughness effects (the increase in fluctuation levels with respect to those over a smooth wall) are readily apparent at x = 27.4, remain about constant in the inner half of the profile but increase in the outer section at x = 33.4, and then decrease somewhat at x = 45.4. The actual rough wall fluctuation magnitudes, on the other hand, develop to a self similar shape prior to x = 39.4. The apparent decrease in the effect of roughness (smaller amount of increase due to the roughness), then, is due not to a decrease in the rough wall fluctuation levels, but to an increase in the smooth wall levels. As discussed previously, the presence of the rough wall significantly alters the upstream history effects of the mean flow, and this, in conjunction with its increased turbulence production, leads to an earlier attainment of equilibrium. Of particular interest in the streamwise development downstream of the step is the fact that the $\dot{m}$ fluctuation level at the wall appears to first decrease upon transition to a rough wall, and then increase along with the rest of the boundary layer. The total temperature data indicate no such decrease.

Careful examination of the data reveals further insights into the manner in which the various roughness heights affect the turbulent flow structure. Turning first to the $\dot{m}$ fluctuations, consider Figure 38 in which these data are presented for all configurations. The general features of the profiles downstream of x = 27.4 are all similar, but those at x = 39.4 illustrate the trends as well as any and will be used for purposes of illustration. The largest effect is seen to be caused by the k = 0.0125 inch rough wall configuration which also exhibits a conspicuous maximum some $y/\delta^* = 0.8$ away from the wall as opposed to the more ambiguous maximum exhibited by the other configurations located at distances of $y/\delta^* = 0.5$ for the smooth wall and k = 0.050 inch rough wall and $y/\delta^* = 0.8$ for the k = 0.025 inch rough wall. The shape of the k = 0.0125 inch rough wall $\dot{m}$ profile is significantly different from that of the other configurations throughout the inner half of the boundary layer. It not only has a more definite maximum, in general, as noted above, but it also decreases in magnitude very rapidly as the wall is approached--so rapidly, in fact, that near the wall it actually falls below the smooth wall profile. The magnitude also decreases rapidly as the freestream flow is approached.

The k = 0.025 inch rough wall profile data also exhibit a peak magnitude well out in the boundary layer, as indicated above. This maximum, however, is usually less pronounced than that for the k = 0.0125 inch data, with the magnitude decreasing less rapidly as the wall is approached, achieving a value somewhat higher than the smooth wall configuration profile adjacent to the wall. Consideration

of the profile between the maximum magnitude and the freestream reveals that the magnitude drops off less rapidly than the k = 0.0125 inch profile as the freestream is approached and is larger than that of the small roughness from $y/\delta^* = 1.2$ to the freestream at $y/\delta^* = 2.0$.

Consider now the k = 0.050 inch rough wall data; it is observed that its maximum occurs much nearer the wall, in the vicinity of $y/\delta^* = 0.5$, the magnitude being very comparable to that of the k = 0.025 inch data. In fact, the behavior of the profile between this maximum magnitude point and the wall is virtually identical to that of the k = 0.025 inch profile. Going toward the freestream flow, the magnitude first drops below that of the smaller roughness configurations, and then assumes virtually the same value as the k = 0.0125 inch data from $y/\delta^* = 1.2$ to the freestream.

Thus, although the data for actual fluctuation magnitudes may be subject to considerable error, the effect of roughness size is definitely discernible. The effect of a small roughness $\left(\frac{ku_\tau}{\nu_w} \approx 7\right)$ is an increase in the $\dot{m}$ fluctuation levels throughout the boundary layer except in the immediate vicinity of the wall, where a slight decrease may occur. A very definite maximum magnitude peak is established well displaced toward the freestream compared to the smooth wall peak, with the roughness effect decreasing significantly as the freestream is approached, but not disappearing. An increase in the roughness height causes an increase in the fluctuation level relative to the magnitude peak throughout the boundary layer, with no change in peak location. As the roughness size continues to increase, the location of the magnitude peak approaches that of the smooth wall

magnitude peak and the fluctuation level between this peak and the freestream decreases somewhat but remains above the smooth wall level. In all cases the rough wall freestream fluctuation levels are about double the smooth wall freestream levels. The increased levels throughout the flow are due to the high level of velocity fluctuation production on the rough walls.

Turning now to the total temperature fluctuation data presented in Figure 39, it is apparent that significant roughness effects are present at x = 27.4 and increase in the outer portion of the boundary layer prior to x = 33.4, then decrease somewhat throughout the boundary layer between x = 33.4 and x = 39.4. Subsequent to x = 39.4, little change occurs. No definite roughness size effects are discernible in the data. In contrast to the $\dot{m}$ fluctuation data, the peak magnitude occurs at the same location for all the rough walls as for the smooth wall.

The mass flux-total temperature correlation function is presented in Figure 40. A rather consistent profile is seen to exist at all stations for all the surface conditions. The correlation function starts off with a small negative value near the wall, rapidly becomes positive, then decreases to a minimum near $y/\delta^* = 1.0$ before increasing again and approaching a freestream value of about 0.5-0.7. The smooth wall deviates from this pattern near the freestream to assume a negative value near -0.5 which is close to the value of -0.7 found by Owen, et al.[85] at M = 7 for a non-adiabatic boundary layer. The profile shape is also similar, although these correlation

functions are significantly smaller throughout the body of the boundary layer.

The k = 0.050 inch rough wall data generally are very similar to the smooth wall data, except near the boundary layer edge, while the smaller roughnesses maintain somewhat different profiles, just as for the $\dot{m}$ fluctuation profiles.

Rough-to-Smooth Transition

Only the rough-to-smooth step change fluctuation data presented in Figures 38-40 remain to be analyzed. Both the $\dot{m}$ and T_t fluctuation profiles at x = 24.4 are observed to be generally similar to those for the k = 0.050 inch smooth-to-rough configuration at x = 39 (fully developed or self similar rough wall flow). The profiles are, however, concentrated much closer to the wall, probably the result of the strong favorable pressure gradient in the nozzle. As indicated earlier, such a gradient tends to suppress fluctuation magnitudes somewhat. The correlation functions for the two configurations are very similar.

By x = 27, some 3δ downstream of the step change in roughness, the character of both fluctuation profiles has changed considerably, decreasing in magnitude at the wall and increasing in magnitude toward the freestream. This growing in the freestream direction accompanied by development of magnitude peaks near $y/\delta^* = 0.5$ is a reflection of the adjustment to a zero pressure gradient freestream, while the change in wall level is a reaction to the shift from the rough to the smooth wall. The correlation function is also seen to respond to the

absence of the favorable pressure gradient by expanding in the free-stream direction.

The profiles continue to adjust to the changes in both the freestream and wall conditions downstream of x = 27.4. A gradual increase in level on the freestream side of the profiles is observed, accompanied by a shift of the maximum amplitude peak in the same direction. Both profiles appear to be close to equilibrium at x = 39.4, but continue to change in the vicinity of the freestream between x = 39.4 and x = 45.4. A self similar profile for the $\dot{m}$ fluctuations appears to be established at x = 45.4, but the T_t profile shows evidence of continued evolvement on the freestream side. Throughout this adjustment to new surface conditions, the correlation coefficient remains essentially unchanged downstream of x = 27.4.

The large magnitude of the $\dot{m}$ fluctuations (larger than the k = 0.050 inch smooth-to-rough configuration) is due to the location of the rough plate in the nozzle. The same roughness height was used for both configurations, but the rough-to-smooth arrangement placed the upstream end of the plate in a much thinner boundary layer ($\delta^* \approx 0.2$ inch versus $\delta^* \approx 0.4$ inch for the smooth-to-rough step change). The effective roughness height was thus much greater, well within the fully rough regime, as opposed to the downstream location where it was at the very lower limit of that regime. The turbulence production caused by the roughness would therefore be considerably larger for the rough-to-smooth model. In addition, the presence of this large roughness in the strong pressure gradient section of the nozzle would significantly perturb the mean flow and exert a larger

effect on the upstream boundary history than would a similar plate in the zero pressure gradient test section.

The rough-to-smooth configuration fluctuation data are also presented in Figure 41. It is obvious that the history effects are very important and no meaningful comparison of nozzle wall data may be attempted in the absence of more detailed knowledge of these effects.

In summary, the fluctuating flow properties were found to respond to changes in the wall roughness somewhat more slowly than did the mean flow properties. This phenomenon is due to the mechanism by which the fluctuating properties are actually influenced by the surface condition. Definite roughness size effects are present in the $\dot{m}$ fluctuation data for flow over a rough wall, but none were observed for the T_t fluctuation data. Comparison of the rough-to-smooth step change data with the smooth wall data revealed upstream history effects, just as mean flow data did earlier.

CONCLUSIONS

An experimental investigation of the response of the hypersonic turbulent boundary layer to a step change in surface roughness has been performed in Leg II of the GALCIT Hypersonic Wind Tunnel. The subject boundary layer developed on the flat nozzle wall adjacent to Mach 6 freestream flow. Both mean and fluctuating flow data were acquired for several smooth-to-rouch surface step changes and a single rough-to-smooth surface step change. Use of a transverse square bar type of roughness facilitated direct comparisons with low speed data. Analysis of the data from this program has yielded the following conclusions:

1. The establishment of new equilibrium mean and fluctuating flow profiles downstream of a step change in surface roughness is accomplished in nearly the same distance (in terms of boundary layer thicknesses) as in the incompressible case. The step change smooth-to-rough configuration boundary layer attains new mean flow self similar profiles some 10δ or $20\delta^*$ downstream of the step, while the fluctuation profiles reach this state some $14\text{-}16\delta$ or $28\text{-}32\delta^*$ downstream of the step. These distances are independent of roughness height for roughnesses in the transitionally rough regime ($\frac{k_s u_\tau}{\nu_w} < 70$). The step roughness change rough-to-smooth configuration produced a somewhat slower adjustment of the boundary layer, some 14δ or $26\ \delta^*$ for mean flow equilibrium and some $20\text{-}25\delta$ or $40\text{-}50\ \delta^*$ for fluctuation equilibrium.

2. The hypersonic smooth and rough wall equilibrium profile velocity data, subsequent to a modified Van Driest transformation to "equivalent incompressible" form, are well correlated by the incompressible composite law of the wall. The use of a virtual origin for the effective surface is necessary to achieve good results for the flow over the surface roughness configurations, just as for incompressible flows. The modified form of the Van Driest transformation used incorporated a least squares quadratic curve fit to the measured temperature data in place of the standard Crocco temperature profile.

3. The above correlation is also found to be applicable in the highly non-equilibrium flow region immediately downstream of the step change in roughness, provided the roughness is not too large. A roughness height of 0.050 inch ($k_s^+ = 45$) for the smooth-to-rough step surface change was found to be too large in this sense, but the same height used in the rough-to-smooth step change configuration was not.

4. The effects of surface roughness on equilibrium or self-preserving boundary layers were found to exhibit excellent agreement with previously published data, when correlated versus equivalent sand grain roughness. When viewed in this manner, with the equivalent sand grain roughness a unique parameter for a given type of roughness in a given freestream velocity, the effect of a change in roughness height on the skin friction and nondimensional velocity (u/u_τ) profiles is found to be a universal function.

5. Existing procedures (based on incompressible data) for calculating the equivalent sand grain roughness of a given roughness configuration were found to be inapplicable in the present case, due

to velocity induced changes in the flow over the roughness. In light of this finding, the extrapolation of any low speed roughness correlation to higher velocities must be viewed very critically with the knowledge that any results of such a procedure are very susceptible to gross errors. A concentrated effort to determine the effects of compressibility and velocity on such correlations is definitely needed.

6. The investigation of the rough-to-smooth step change configuration revealed the existence of very significant pressure and temperature history effects throughout the boundary layer. The existence of these effects affords an explanation of apparent inconsistency of data obtained on wind tunnel nozzle walls with that obtained on flat plates supported in the tunnel freestream. The presence of the rough surface on the nozzle wall within the expansion region was sufficient to alter the history effects, but was not able to eliminate them. The unknown nature and extent of such history effects casts serious doubts on the validity of simulating boundary layers on freestream surfaces by use of nozzle wall boundary layers. Considerably more research is needed in this area to delineate the extent of these history effects and investigate the possibility of destroying them.

Appendix A

Derivation of the Finite Length Hot Wire Response Function and Sensitivity Coefficients

The material contained in this appendix is based on a derivation of Wilhelm Behrens, formerly at Caltech, now at TRW Systems Group, Redondo Beach, California. Gran[55] has included an abridged version in his thesis, and Ramaswamy,[57] Ikawa,[86] Behrens,[87] and Dewey[62] have all included a portion of the theory in their theses, inadvertently incorporating errors. The complete work by Behrens evidently will not be published, so it is presented here, although the author's contribution consists solely of verification of the equations and results.

A. 1 Simplifying Assumptions

In this formulation, the following assumptions are made:

1) Although all the hot wire properties vary with temperature, the thermal conductivity, heat capacity, and density are considered constant. For example, for a platinum-10% Rhodium wire, the thermal conductivity

$$k_w = 0.301\,[1 + 1.07 \times 10^{-4}\,(T-T_r)]\,\left(\frac{\text{watt}}{^{o}\text{K. cm}}\right)$$

where $T_r = 273^{o}$K (Ref. 87).

The variation of heat capacity and density with temperature is even smaller.

2) The hot wire resistance varies linearly with temperature;

$$R_w = R_r\,[1 + \alpha_r(T_w - T_r)]$$

According to Morkovin,[60] a quadratic term should be included. However, calibrations at Caltech over a range of 280°F (150°C) have consistently yielded a linear relationship within the experimental accuracy.

3) The wire length to diameter ratio is so large that the temperature may be considered independent of the radial coordinate. Thus $T = T(x, t)$ only.

4) The flow variables are functions only of time (they are not functions of wire length.

5) The Nusselt number is independent of the current overheat. Two important quantities in the hot wire problem are the logarithmic derivative of the Nusselt number with respect to the Reynolds number and the logarithmic derivative of the Nusselt number with respect to the overheat parameter. Estimates from the measurements of Laufer and McClellan[87] indicate that the derivative with respect to overheat is an order of magnitude lower than $\frac{\partial \ell n Nu_t}{\partial \ell n Re_t}$.

6) Radiation losses from the wire are neglected.

7) The hot wire support temperature is independent of time.

8) The time dependent hot wire and flow quantities are small perturbations about the local mean quantities.

A.2 Derivation of the Heat Balance Equation

Applying a heat balance to a small wire of length Δx and diameter d, with the above assumptions, the heat increase within the wire plus the heat transferred to the fluid must equal the Joule heating plus the net heat influx along the wire.

$$\text{Heat increase} = \rho_w c_w \frac{\partial T_w}{\partial t} \frac{\pi d^2}{4} \Delta x$$

$$\text{Heat transferred to fluid} = \pi dh\,(T_w - T_{aw})\,\Delta x$$

$$= \pi Nu_t k_t (T_w - T_{aw})\,\Delta x$$

$$\text{Joule heating} = i^2 r_w \Delta x$$

$$\text{Net heat influx} = -k_w \frac{\partial T_w}{\partial x} \frac{\pi d^2}{4} + k_w \left[\frac{\partial}{\partial x}\left(T_w + \frac{\partial T_w}{\partial x}\Delta x\right)\right] \frac{\pi d^2}{4}$$

Thus the heat balance yields

$$\rho_w c_w \frac{\pi d^2}{4} \frac{\partial T_w}{\partial t} + \pi Nu_t k_t (T_w - T_{aw}) = i^2 r_w + k_w \frac{\pi d^2}{4} \frac{\partial^2 T_w}{\partial x^2} \qquad \text{(A. 2. 1)}$$

where

c_w = specific heat of the wire

d = wire diameter

h = heat transfer coefficient

i = hot wire current

k_t = thermal conductivity of air at stagnation temperature

k_w = thermal conductivity of the wire

Nu_t = Nusselt number $\left(= \frac{hd}{k_t}\right)$

r_w = wire resistance per unit length

T_w = wire temperature at station x

x = distance along the wire

ρ_w = wire density

One may nondimensionalize the wire temperature, x coordinate and time according to

$$\tau = \frac{T_w - \overline{T}_{aw}}{\overline{T}_{aw}} = \frac{T_w - \overline{\eta}\,\overline{T}_t}{\overline{\eta}\,\overline{T}_t}$$

$$x^* = 2x/\ell$$

$$t^* = \left(\frac{4\overline{k}_t}{\rho_w c_w d^2}\right) t = t/K$$

where the bars denote time-independent quantities. Using these relationships and the linear wire resistance with temperature in equation (A. 2. 1), one obtains

$$\frac{\partial \tau}{\partial t^*} + \left[\frac{Nu_t k_t}{\overline{k}_t} - \frac{i^2 a_r r_r}{\pi \overline{k}_t}\right]\tau - \frac{k_w}{\overline{k}_t(\ell/d)^2}\frac{\partial^2 \tau}{\partial x^{*2}} =$$

$$= \frac{Nu_t k_t}{\overline{k}_t}\frac{(\eta T_t - \overline{\eta}\,\overline{T}_t)}{\overline{\eta}\,\overline{T}_t} + \frac{i^2 r_r}{\overline{\eta}\,\overline{T}_t}\left[1 + a_r(\overline{\eta}\,\overline{T}_t - T_r)\right] \qquad \text{(A. 2. 2)}$$

The applicable boundary conditions are $\tau = \overline{\tau}_s$ $\left(= \frac{\overline{T}_s - \overline{T}_{aw}}{\overline{T}_{aw}} = \text{constant}\right)$ at $x^* = \pm 1$ and $\frac{\partial \tau}{\partial x^*} = 0$ at $x^* = 0$. In order to solve this equation, all quantities will be assumed to consist of small sinusoidal fluctuations in time about a mean value, e. g.

$$\tau(x^*, t^*) = \overline{\tau}(x^*) + \tau'(x^*)\, e^{j\omega t^*}$$

$$Nu_t(x^*, t^*) = \overline{Nu}_t\left[1 + Nu_t'(x^*) e^{j\omega t^*}\right]$$

$$\eta(x^*, t^*) = \overline{\eta}\left[1 + \eta'(x^*) e^{j\omega t^*}\right]$$

$$T_t(t^*) = \overline{T}_t\left[1 + \tau_t'\, e^{j\omega t^*}\right]$$

$$k_t(t^*) = \overline{k}_t\left[1 + \eta\, \tau_t'\, e^{j\omega t^*}\right]$$

$$\mu_t(t^*) = \overline{\mu}_t\left[1 + m\tau_t'\, e^{j\omega t^*}\right]$$

$$i(t^*) = \bar{i}\left[1+i' e^{j\omega t^*}\right] \qquad \text{(A. 2. 3)}$$

where

$$j = \sqrt{-1}$$

$$n \equiv \frac{d\ell n\, \bar{k}_t}{d\ell n\, \bar{T}_t} \approx 0.885 \text{ for air at } 540^\circ R \ (300^\circ K)$$

$$m \equiv \frac{d\ell n\, \bar{\mu}_t}{d\ell n\, \bar{T}_t} \approx 0.765 \text{ for air at } 540^\circ R \ (300^\circ K)$$

Substituting equations (A. 2. 3) into (A. 2. 2) and separating the resulting equation with respect to the fluctuation order yields the mean temperature equation

$$\frac{k_w}{\bar{k}_t\,(\ell/d)^2}\ \frac{\partial^2 \bar{\tau}}{\partial x^{*2}} - \left(\overline{Nu}_t - \frac{\bar{i}^2 a_r r_r}{\pi \bar{k}_t}\right)\bar{\tau} + \frac{\bar{i}^2 r_r}{\bar{\eta}\,\bar{T}_t}\left[1+a_r(\bar{\eta}\,\bar{T}_t - T_r)\right]$$

$$= 0 \qquad \text{(A. 2. 4)}$$

with boundary conditions

$$\bar{\tau}\ (\pm 1) = \tau_s$$

$$\frac{d\bar{\tau}}{dx^*}\ (0) = 0$$

and the unsteady temperature equation (first order fluctuations only)

$$\frac{k_w}{\bar{k}_t\,(\ell/d)^2}\ \frac{d^2\tau'}{dx^{*2}} - \left[\overline{Nu}_t - \frac{\bar{i}^2 r_r a_r}{\pi \bar{k}_t} + \overline{i\omega}\right]\tau' =$$

$$= \left[\overline{Nu}_t(Nu'_t + k'_t) - \frac{2\bar{i}^2 r_r a_r}{\pi \bar{k}_t}\ i'\right]\bar{\tau} - \frac{2\bar{i}^2 r_r i'}{\pi \bar{k}_t \bar{\eta}\,\bar{T}_t}\left[1 + a_r(\bar{\eta}\,\bar{T}_t - T_r)\right]$$

$$-\overline{Nu}_t\,(\tau'_t + \eta') \qquad \text{(A. 2. 5)}$$

where $\bar{\omega} = \omega \frac{\rho_w c_w d^2}{4\bar{k}_t} = \omega K$

with boundary conditions

$$\tau'(\pm 1) = 0$$

$$\frac{d\tau'}{dx^*}(0) = 0$$

Let

$$a \equiv \frac{k_w}{\bar{k}_t (\ell/d)^2}$$

$$b \equiv \overline{Nu_t} - \frac{\bar{i}^2 r_r a_r}{\pi \bar{k}_t}$$

$$c \equiv \frac{\bar{i}^2 r_r}{\pi \bar{k}_t \bar{\eta}\, \bar{T}_t} \left[1 + a_r(\bar{\eta}\, \bar{T}_t - T_r)\right]$$

Then equations (A. 2. 4) and (A. 2. 5) become

$$a \frac{\partial^2 \bar{\tau}}{\partial x^{*2}} - b\bar{\tau} + c = 0 \qquad \text{(A. 2. 6)}$$

with boundary conditions

$$\bar{\tau}(\pm 1) = \tau_s$$

$$\frac{\partial \bar{\tau}}{\partial x^*}(0) = 0$$

and

$$a \frac{\partial^2 \tau'}{\partial x^{*2}} - \left[b + j\bar{\omega}\right]\tau' = \left[\overline{Nu_t}(Nu_t' + k_t') - \frac{\overline{2i}^2 r_r a_{r\,i'}}{\pi \bar{k}_t}\right]\bar{\tau}$$

$$-2ci' - \overline{Nu_t}(\tau_t' + \eta') \qquad \text{(A. 2. 7)}$$

with boundary conditions

$$\tau'(\pm 1) = 0$$

$$\frac{\partial \tau'}{\partial x^*}(0) = 0$$

A.3 Steady State Solution

The solution to (A.2.6) is dependent upon the value of $a(\equiv b/a)$

a) $a < 0$

$$\bar{\tau} = c/b + (\tau_s - \frac{c}{b}) \frac{\cosh \sqrt{a}\, x^*}{\cosh \sqrt{a}}$$

b) $a = 0$

$$\bar{\tau} = \tau_s + \frac{c}{2a}(1-x^{*2})$$

c) $a < 0$

$$\bar{\tau} = \frac{c}{b} + (\tau_s - \frac{c}{b}) \frac{\cos \sqrt{|a|}\, x^*}{\cos \sqrt{|a|}}$$

Thus, the wire temperature as a function of distance along the wire is known. However, in actual use, it is impossible to measure the spanwise temperature or resistance of the wire; only its total resistance may be measured. The relation between this measured mean resistance and $\bar{\tau}$ is given by

$$\begin{aligned} R_{wm} &= r_{wm} \ell = \ell r_r \left[1 + a_r(\bar{T}_{wm} - T_r)\right] \\ &= \ell r_r \left[1 + a_r\left(\frac{\bar{T}_{wm} - \bar{\eta}\,\bar{T}_t}{\bar{\eta}\,\bar{T}_t}\right)\bar{\eta}\,\bar{T}_t + a_r(\bar{\eta}\,\bar{T}_t - T_r)\right] \\ &= \ell r_r \left[1 + a_r\,\bar{\tau}_{wm}\,\bar{\eta}\,\bar{T}_t + a_r(\bar{\eta}\,\bar{T}_t - T_r)\right] \end{aligned} \qquad (A.2.8)$$

where $\overline{\tau}_{wm}$ is the mean measured temperature of the wire at current i and is given by

$$\overline{\tau}_{wm} = \tfrac{1}{2} \int_{-1}^{1} \overline{\tau}\, dx^{*}$$

Once again, the value of a dictates one of three equations

a) $a > 0$

$$\overline{\tau}_{wm} = \frac{c}{b} + (\tau_s - \frac{c}{b}) \frac{\tanh \sqrt{a}}{\sqrt{a}}$$

b) $a = 0$

$$\overline{\tau}_{wm} = \tau_s + \frac{c}{3a}$$

c) $a < 0$

$$\overline{\tau}_{wm} = \frac{c}{b} \; (\tau_s - \frac{c}{b}) \frac{\tan \sqrt{|a|}}{\sqrt{|a|}}$$

In general, a is greater than zero, i.e. small currents are used such that $\overline{i}^2 r_r a_r/(\pi \overline{k}_t)$ is less than $\overline{Nu}_t$. For this reason, the subsequent development will be restricted to $a > 0$.

In theory, then, $\overline{\tau}_{wm}$ could be computed directly from the appropriate equation (A.2.9), but this is not in general possible in practice due to the fact the Nusselt number, $\overline{Nu}_t$, and recovery factor $\overline{\eta}$ are not known.

Gran[55] has found that

$$\overline{R}_{wm} = \overline{R}_{awm} + k(\overline{i}^2 \overline{R}_{wm}) \qquad (A.2.10)$$

where $\overline{R}_{awm}$ is the measured adiabatic wire resistance, $\overline{R}_{wm}$ is the measured wire resistance, and k is the slope of the $\overline{R}_{wm}$ vs. $\overline{i}^2 \overline{R}_{wm}$ plot. From this equation and (A.2.8), one can show that

$$\frac{\Delta R_w}{\overline{R}_{awm}} = \frac{\overline{R}_{wm} - \overline{R}_{awm}}{\overline{R}_{awm}} = \frac{k\overline{i}^2}{1-k\overline{i}^2} \qquad (A.2.11)$$

$$\overline{\tau}_{wm} = \overline{\tau}_{awm} + \left(\frac{\Delta R_w}{\overline{R}_{awm}}\right) \frac{\overline{R}_{awm}/R_r}{a_r \overline{\eta}\, \overline{T}_t} \qquad (A.2.12)$$

and

$$\overline{\tau}_{awm} = \frac{1}{a_r \overline{\eta}\, \overline{T}_t} \left[\frac{\overline{R}_{awm}}{R_r} - 1 + a_r(T_r - \overline{\eta}\, \overline{T}_t)\right] . \qquad (A.2.13)$$

$\overline{\eta}$ may be determined from the correlation given in section 6 of this Appendix and $\overline{T}_t$ has been measured. Thus, from the known and measured quantities, (A.2.13) may be used to find $\overline{\tau}_{awm}$ which may then be used with (A.2.12) and (A.2.11) to find $\overline{\tau}_{wm}$.

Considering the mean heat balance for the entire hot wire, one obtains

$$\pi\, dh_m(\overline{T}_{wm} - \overline{T}_{awm}) = \overline{i}^2 r_r[1+a_r(T_{wm}-T_r)] \qquad (A.2.14)$$

where

$\overline{T}_{awm}$ - adiabatic wire temperature determined from $\overline{R}_{awm}$.

Normalizing quantities in the same manner as for equation (A.2.1), there results

$$\overline{Nu}_m(\overline{\tau}_{wm} - \overline{\tau}_{awm}) = \frac{\overline{i}^2 r_r}{\pi \overline{k}_t \overline{\eta}\, \overline{T}_t} [1+a_r(\overline{\eta}\, \overline{T}_t - T_r)] + \frac{\overline{i}^2 r_r a_r}{\pi \overline{k}_t} \overline{\tau}_{wm} \qquad (A.2.15)$$

or

$$\overline{Nu}_m(\overline{\tau}_{wm} - \overline{\tau}_{awm}) = c + e\,\overline{\tau}_{wm}$$

where $\overline{Nu}_m = \frac{d\,hm}{k_t}$ (measured Nusselt number)

$$e \equiv \frac{\bar{i}^2 r_r a_r}{\pi \bar{k}_t}$$

and c is as defined prior to equation (A. 2. 6). Defining

$$\psi_N \equiv \frac{\overline{Nu}_t}{\overline{Nu}_m} ,$$

$$\psi_N = \frac{\overline{Nu}_t(\bar{\tau}_{wm} - \bar{\tau}_{awm})}{c + e\bar{\tau}_{wm}}$$

Substituting for $\bar{\tau}_{wm}$ and $\bar{\tau}_{awm}$ ($\bar{i} = 0$) from equation (A. 2. 9) in this equation, one obtains

$$\psi_N = \frac{\overline{Nu}\left[\frac{c}{b} + (\tau_s - \frac{c}{b})\frac{\tanh\sqrt{a}}{\sqrt{a}} - \tau_s \frac{\tanh\sqrt{a_0}}{\sqrt{a_0}}\right]}{c+e\left[\frac{c}{b} + (\tau_s - \frac{c}{b})\frac{\tanh\sqrt{a}}{\sqrt{a}}\right]} \qquad \text{(A. 2. 16)}$$

where

$$a_0 = a\Big|_{\bar{i}=0} = \frac{\overline{Nu}_t \bar{k}_t (\ell/d)^2}{k_w}$$

Expansion of this equation in terms of $\bar{i}$ for small $\bar{i}$ and retaining only the linear terms yields, after some manipulation,

$$\psi_N = (1-\omega_0)\left\{1 + \frac{\tau_s \frac{e}{c}}{2(1+\tau_s \frac{e}{c}\omega_0)(1-\omega_0)}\left[(2\omega_0 - 1)\omega_0 - \frac{1}{\cosh^2\sqrt{a_0}}\right]\right\}$$

where

$$\omega_0 = \frac{\tanh\sqrt{a_0}}{\sqrt{a_0}}$$

Since a_0 (and thus ψ_N) is a function of $\overline{Nu}_t$, an iteration scheme is

required to determine $\overline{Nu}_t$ from the measured $\overline{Nu}_m$, (which is not yet known). Rearranging equation (A. 2. 15), and using the definitions of $\overline{\tau}_{wm}$ and $\overline{\tau}_{awm}$, one obtains

$$\overline{Nu}_m = \frac{\overline{i}^2 \overline{R}_r}{\pi \ell \overline{k}_t} \frac{\overline{R}_{wm}}{\overline{R}_{wm} - \overline{R}_{awm}}$$

but from equation (A. 2. 10)

$$\overline{i}^2 \overline{R}_{wm} = \frac{\overline{R}_{wm} - \overline{R}_{awm}}{k}$$

so

$$\frac{d(i^2 \overline{R}_{wm})}{d \overline{R}_{wm}} = \frac{1}{k} =$$

$$= \frac{i^2 \overline{R}_{wm}}{\overline{R}_{wm} - \overline{R}_{awm}}$$

Thus

$$\overline{Nu}_m = \frac{R_r \left(\frac{d(i^2 \overline{R}_{wm})}{d \overline{R}_{wm}} \right)}{\pi \ell \overline{k}_t} = \frac{R_r \, k}{\pi \ell \overline{k}_t}$$

A. 3 Solution of the Fluctuation Problem

The local hot wire fluctuation temperature must be found from equation (A. 2. 7). That equation may be rewritten using the definitions preceding equation (A. 2. 6) and following equation (A. 2. 15) as

$$(b + j\overline{\omega}) \tau' - a \frac{d^2 \tau'}{dx^{*2}} = C_1 + C_2 \frac{\cosh \sqrt{a}\, x^*}{\sqrt{a}} \qquad \text{(A. 3. 1)}$$

where

$$C_1 = 2(1 + \frac{e}{b})\, ci' + \overline{Nu}_t \left[(1 - n\frac{c}{b})\, \tau_t' - \frac{c}{b} Nu_t' + \eta'\right]$$

$$C_2 = (\tau_s - \frac{c}{b}) \left[2ei' - \overline{Nu}_t\, (Nu_t' + n\, \tau_t')\right]$$

with boundary conditions

$$\tau'(\pm 1) = 0$$

$$\frac{d\tau'}{dx^*}(0) = 0$$

The solution to (A. 3. 1) has been given by Betchov[90] as

$$\tau' = \frac{C_1}{\alpha\beta}\left(1 - \frac{\cosh\sqrt{\beta}\, x^*}{\cosh\sqrt{\beta}}\right) + \frac{C_2}{a(\beta-\alpha)}\left(\frac{\cosh\sqrt{\alpha}\, x^*}{\cosh\sqrt{\alpha}} - \frac{\cosh\sqrt{\beta}\, x^*}{\cosh\sqrt{\beta}}\right) \qquad \text{(A. 3. 2)}$$

where $\beta = \frac{b+j\overline{\omega}}{a} = \alpha(1+j\frac{\overline{\omega}}{b})$.

Since only the resistance (or voltage) fluctuation of the entire wire may be measured, the lengthwise integrated fluctuation is required, and is given by

$$\tau_{wm}' = \frac{1}{2}\int_{-1}^{+1} \tau' dx^*$$

$$= \frac{C_1}{\alpha\beta}\left(1 - \frac{\tanh\sqrt{\beta}}{\sqrt{\beta}}\right) + \frac{C_2}{a(\beta-\alpha)}\left(\frac{\tanh\sqrt{\alpha}}{\sqrt{\alpha}} - \frac{\tanh\sqrt{\beta}}{\sqrt{\beta}}\right) \qquad \text{(A. 3. 3)}$$

The derivation thus far has dealt with the response of a real wire which experiences a "thermal lag" or high frequency attenuation when responding to flow fluctuations due to the mass of the wire. The sensitivity coefficients or voltage fluctuations generated by specific flow quantities, on the other hand, are derived below for the "ideal" or massless hot wire. Thus the relationship between

the two is required.

The ideal hot wire response is instantaneous at all frequencies, and the real wire approaches this response as the frequency $\bar{\omega} \to 0$. Thus, considering equation (A.3.3) as $\bar{\omega} \to 0$, we find

$$\frac{\tau'_{wm}}{\tau'_{i,wm}} = \frac{\frac{a}{\beta}\left(1-\frac{\tanh\sqrt{\beta}}{\sqrt{\beta}}\right)+\frac{C_2}{C_1}\frac{a}{(\beta-a)}\left(\frac{\tanh\sqrt{a}}{\sqrt{a}}-\frac{\tanh\sqrt{\beta}}{\sqrt{\beta}}\right)}{\left(1-\frac{\tanh\sqrt{a}}{\sqrt{a}}\right)+\frac{C_2}{2C_1}\frac{\tanh\sqrt{a}}{\sqrt{a}}\left(1-\frac{2\sqrt{a}}{\sinh 2\sqrt{a}}\right)} \qquad \text{(A.3.4)}$$

This is a rather complicated expression. In order to obtain a simple approximation, consider the wire of "infinite" length, i.e. $\ell/d \to \infty$. In this case, one obtains from equation (A.3.4)

$$\frac{\tau'_{\infty}}{\tau'_{i,\infty}} = \frac{1}{1+j\frac{\bar{\omega}}{b}} \qquad \text{(A.3.5)}$$

This is the well known relation[91] defining the hot wire time constant

$$\bar{M}_{t,\infty} = \frac{1}{b} = K M_{t,\infty}$$

Returning now to equation (A.3.4), assume that the attenuation due to the mass of the real wire may be expressed in the form of (A.3.5), i.e.

$$\frac{\tau'_{wm}}{\tau'_{i,wm}} = \frac{1}{1+j\bar{M}_t\bar{\omega}} = \frac{1}{1+jM_t\omega} \qquad \text{(A.3.6)}$$

From this, one finds, using equation (A.3.4),

$$\left[1+(M_t\omega)^2\right]^{\frac{1}{2}} = \frac{\frac{C_1}{b}\left(1-\frac{\tanh\sqrt{a}}{\sqrt{a}}\right)+\frac{C_2}{2b}\frac{\tanh\sqrt{a}}{\sqrt{a}}\left(1-\frac{2\sqrt{a}}{\sinh 2\sqrt{a}}\right)}{\frac{C_1}{a\beta}\left(1-\frac{\tanh\sqrt{\beta}}{\sqrt{\beta}}\right)+\frac{C_2}{a(\beta-a)}\left(\frac{\tanh\sqrt{a}}{\sqrt{a}}-\frac{\tanh\sqrt{\beta}}{\sqrt{\beta}}\right)}$$

which is valid for all $\bar{M}_t$, a, and b. This may be expanded to illustrate clearly the dependence upon a and b as follows

$$[1+(M_t\omega)^2]^{\frac{1}{2}} = \frac{(\bar{\omega}^2+b^2)^{\frac{1}{2}}}{b}\left\{\frac{\left(1-\frac{\tanh\sqrt{a}}{\sqrt{a}}\right)+\frac{C_2}{2C_1}\frac{\tanh\sqrt{a}}{\sqrt{a}}\left(1-\frac{2\sqrt{a}}{\sinh 2\sqrt{a}}\right)}{1-\frac{\tanh\sqrt{\beta}}{\sqrt{\beta}}+\frac{C_2}{C_1}\left[1+\left(\frac{b}{\bar{\omega}}\right)^2\right]\left(\frac{\tanh\sqrt{a}}{\sqrt{a}}-\frac{\tanh\sqrt{\beta}}{\sqrt{\beta}}\right)}\right\}$$

If the assumptions (valid for most applications) $\bar{\omega} >> b$, $\bar{\omega} >> a$, and $M_t\omega >> 1$ are incorporated, one obtains

$$\bar{M}_t = \frac{1}{b}\left[\frac{1-\frac{\tanh\sqrt{a}}{\sqrt{a}}+\frac{C_2}{2C_1}\frac{\tanh\sqrt{a}}{\sqrt{a}}\left(1-\frac{2\sqrt{a}}{\sinh 2\sqrt{a}}\right)}{1+\frac{C_2}{C_1}\frac{\tanh\sqrt{a}}{\sqrt{a}}}\right] \qquad (A.3.7)$$

This may be expanded to give

$$\bar{M}_t = \frac{1}{b}\left(1-\frac{\tanh\sqrt{a}}{\sqrt{a}}\right)F\left(\frac{C_2}{C_1}, a\right) \qquad (A.3.8)$$

or

$$M_t = K\bar{M}_t = K\,\frac{1-\tanh\sqrt{a}/\sqrt{a}}{Nu_t - i^2 r_r a_r/\pi k_t}\,F\left(\frac{C_2}{C_1}, a\right) \qquad (A.3.9)$$

Thus the time constant is dependent upon the fluctuation properties through C_1 and C_2, but the fluctuation properties cannot be determined without knowing M_t. An iterative process is necessary, but in actual use, the value of F has been found to vary only slightly from 1, so if an iteration were used it would rapidly converge. In reality, the value of M_t is not required for the determination of the fluctuating properties, as will be seen below.

A.4 Hot Wire Sensitivity Coefficients

The ideal hot wire fluctuation response is given by equation (A.3.3) as $\omega \to 0$ and is

$$\tau'_{i,wm} = \frac{C_1}{b}\left(1-\frac{\tanh\sqrt{a}}{\sqrt{a}}\right)+\frac{C_2}{2b}\frac{\tanh\sqrt{a}}{\sqrt{a}}\left(1-\frac{2\sqrt{a}}{\sinh 2\sqrt{a}}\right) \qquad (A.4.1)$$

Using the equation for $\overline{M}_t$ given in equation (A. 3. 7), this becomes

$$\tau_{i,wm}' = \overline{M}_t \left(C_1 + C_2 \frac{\tanh \sqrt{a}}{\sqrt{a}}\right)$$

Introducing the definitions of C_1 and C_2, setting $i' \equiv 0$ (constant current hot wire system), and using equation (A. 2. 9) to define $\overline{\tau}_{wm}$, one obtains

$$\tau_{i,wm}' = \overline{M}_t \, \overline{Nu}_t \left[(1 - n\,\overline{\tau}_{wm})\, \tau_t' - \overline{\tau}_{wm}\, Nu_t' + \eta'\right] \qquad \text{(A. 4. 2)}$$

which is the response of an ideal (massless) wire of finite length. The assumptions $\overline{M}_t \, \overline{\omega} >> 1$ and $\overline{M}_t \, \overline{\omega} >> b$ are inherent in this expression.

In reality, of course, the hot wire voltage fluctuations, not the temperature fluctuations, are the measured quantities. These quantities are related to the temperature fluctuations through Ohm's law

$$\overline{e}_{i,wm} = \overline{i}\, \overline{R}_{wm,i}$$

In addition,

$$R_{i,wm} = R_r \left[1 + a_i \left(T_{i,wm} - T_r\right)\right]$$

Since this is a constant current system,

$$e_{i,wm}' = \overline{i}\; R_{i,wm}'$$

and

$$R_{i,wm}' = R_r\, a_r\, T_{i,wm}' = R_r a_r\, \overline{\eta}\, \overline{T}_t\, \tau_{i,wm}'$$

Thus one obtains

$$e'_{i,wm} = \bar{i}\, a_r R_r \bar{\eta}\, \bar{T}_t \bar{M}_t \overline{Nu}_t \left[(1-n\bar{\tau}_{wm})\tau'_t - \bar{\tau}_{wm} Nu'_t + \eta'\right]$$

$$= M_t \frac{4\bar{i}\, a_r R_r \bar{\eta}\, \bar{T}_t \overline{Nu}_t \bar{k}_t}{\rho_w c_w d^2} \left[(1-n\bar{\tau}_{wm})\tau'_t - \bar{\tau}_{wm} Nu'_t + \eta'\right]$$

$$= M_t\, C\left[(1-n\bar{\tau}_{wm})\tau'_t - \bar{\tau}_{wm}\, Nu'_t + \eta'\right] \qquad \text{(A. 4. 3)}$$

where

$$C = \frac{4\bar{i}\, a_r R_r \bar{\eta}\, \bar{T}_t \overline{Nu}_t \bar{k}_t}{\rho_w c_w d^2}$$

Following the procedure of Kovasznay[59] and Morkovin,[60] the voltage fluctuations of an ideal hot wire may be written as

$$e'_{i,wm} = -S_u u' - S_\rho\, \rho' + S_{T_t}\, \tau'_t \qquad \text{(A. 4. 4)}$$

where u', ρ', and τ'_t are the non-dimensional fluctuations of velocity (perpendicular to the wire), density, and total temperature, respectively, and S_u, S_ρ, and S_{T_t} are their sensitivity coefficients. These coefficients are found by writing equation (A. 4. 3) in terms of ρ', u', and τ'_t. It will be shown below (section A. 5) that the Nusselt number, $\overline{Nu}_t$, and the recovery factor, $\bar{\eta}$, are functions only of the local Mach number and Reynolds number, $\overline{Re}_t \equiv \frac{\bar{\rho}\bar{u}d}{\bar{\mu}_t}$. Thus

$$Nu'_t = \frac{dNu_t}{\overline{Nu}_t} = \frac{\partial \ell n\, \overline{Nu}_t}{\partial \ell n \overline{Re}_t}\, Re'_t + \frac{\partial \ell n\, \overline{Nu}_t}{\partial \ell n\, \bar{M}}\, M' \qquad \text{(A. 4. 5)}$$

$$\eta' = \frac{d\eta}{\bar{\eta}} = \frac{\partial \ell n \bar{\eta}}{\partial \ell n \overline{Re}_t}\, Re'_t + \frac{\partial \ell n \bar{\eta}}{\partial \ell n \bar{M}}\, M' \qquad \text{(A. 4. 6)}$$

where

$$Re_t' \equiv \frac{dRe_t}{\overline{Re}_t} = \frac{d\rho}{\overline{\rho}} + \frac{du}{\overline{u}} - m\,\frac{dT_t}{\overline{T}_t}$$

$$= \rho' + u' - m\,\tau_t' \qquad \text{(A. 4. 7)}$$

$$M' \equiv \frac{dM}{\overline{M}} = a_1(u' - \tfrac{1}{2}\,\tau_t') \qquad \text{(A. 4. 8)}$$

$$a_1 \equiv 1 + \frac{\gamma-1}{2}\,\overline{M}^2$$

Combining equations (A. 4. 3) through (A. 4. 8), one obtains, after some algebra

$$S_\rho = CM_t\{[B_1\overline{\tau}_{wm} - B_2] + g\,[B_2 - B_1\overline{\tau}_s]\}$$

$$S_u = CM_t\{[(B_1+B_3a_1)\overline{\tau}_{wm} - (B_2+B_4a_1)] \qquad \text{(A. 4. 9)}$$

$$+g[B_2+B_4a_1-(B_1+B_3a_1)\,\overline{\tau}_s]\}$$

$$S_{T_t} = CM_t\{[1-mB_2 - \frac{a_1}{2}B_4 + (mB_1+\frac{a_1}{2}B_3-n)\,\overline{\tau}_{wm}]$$

$$+g\,[mB_2 + \frac{a_1}{2}B_4 - 1 - (n-mB_1 - \frac{a_1}{2}B_3)\,\tau_s]\}$$

where

$$B_1 = \frac{\partial \ell n\,\overline{Nu}_t}{\partial\,\ell n\,\overline{Re}_t}$$

$$B_2 = \frac{\partial \ell n\,\overline{\eta}}{\partial\,\ell n\,\overline{Re}_t}$$

$$B_3 = \frac{\partial \ell n\,\overline{Nu}_t}{\partial \ell n\,\overline{M}}$$

$$B_4 = \frac{\partial \ell n\,\overline{\eta}}{\partial \ell n\,\overline{M}}$$

These values are determined from the relations given in section (A. 5) below.

$$n = \frac{d\ell n \bar{k}_t}{d\ell n \bar{T}_t} \approx 0.885$$

$$m = \frac{d\ell n \bar{\mu}_t}{d\ell n \bar{T}_t} \approx 0.765$$

for air at $540^{\circ}R$

$$a_1 = 1 + \frac{\gamma-1}{2} \bar{M}^2$$

$$g = \tanh\sqrt{\beta} \,/\, \sqrt{\beta}$$

- vanishes as frequency $\to \infty$ or/and $a \to \infty$ (i.e., infinite hot wire)

$$\beta = a\sqrt{1+(\bar{\omega}/b)^2}$$

$$\bar{\omega}/b = \frac{2\pi f K}{\overline{Nu}_t - \frac{\bar{i}^2 r_r a_r}{\pi \bar{k}_t}}$$

For the Mach number range encountered in this work the frequency range of the hot wire signal was found to be high enough (less than 1% of the signal below 5K Hz) that $g = \frac{\tanh\sqrt{\beta}}{\sqrt{\beta}}$ was negligible. Also, for $M > 2$, the Nusselt number and recovery factor become virtually independent of Mach number, so B_3 and B_4 go to zero. In this case, the hot wire sensitivities become

$$S_\rho = S_u = S_{\dot{m}} = CM_t\left[\left(\bar{\tau}_{wm}\frac{\partial \ell n \overline{Nu}_t}{\partial \ell n \overline{Re}_t} - \frac{\partial \ell n \bar{\eta}}{\partial \ell n \overline{Re}_t}\right)\right]$$

$$S_{T_t} = CM_t\left[1-n\,\bar{\tau}_{wm}+\left(\bar{\tau}_{wm}\frac{\partial \ell n \overline{Nu}_t}{\partial \ell n \overline{Re}_t} - \frac{\partial \ell n \bar{\eta}}{\partial \ell n \overline{Re}_t}\right)m\right]$$

These are formally the same as those for an infinite hot wire as given by Morkovin,[60] but Morkovin's measured Nusselt number, Nu_m, and recovery factor, η_m, are replaced by the "true" values $\overline{Nu}_t$ and $\bar{\eta}$ for an infinite wire without end losses. The expression for M_t also agrees with that of Morkovin as $\ell/d \to \infty$ $\left(\frac{\tanh\sqrt{a}}{\sqrt{a}} \to 0\right)$, for

rearrangement of equation (A.3.8), assuming $F(C_2/C_1, a) = 1$ gives

$$M_t \cong \frac{\rho_w c_w \pi d^2}{4i^2 r_r a_r} \frac{r_{wm} - r_{aw}}{r_{aw}}$$

and with the assumptions made in this derivation

$$\frac{r_{wm} - r_{aw}}{r_{aw}} = a'_w = A'_w$$

in Morkovin's paper. As shown above, for supersonic Mach numbers, S_ρ and S_u are found to be virtually indistinguishable. Thus it is not possible to separate the ρ' and u' fluctuations, but only to determine a mass flux quantity $(\rho u)'$ (or $\dot{m}'$).

In order to determine the fluctuation properties, the fluctuation equation (A.4.4) may be rewritten as

$$e'_{i,wm} = -S_{\dot{m}} \dot{m}' + S_{T_t} \tau'_t$$

or, forming the mean square

$$\overline{e'^2_{i,wm}} = S^2_{\dot{m}} \overline{\dot{m}'^2} - 2S_{\dot{m}} S_{T_t} \overline{\dot{m}' \tau'_t} + S^2_{T_t} \overline{\tau'^2_t}$$

or

$$\frac{\overline{e'^2_{i,wm}}}{S^2_{T_t}} = \overline{\tau'^2_t} - \frac{2S_{\dot{m}}}{S_{T_t}} \overline{\dot{m}' \tau'_t} + \left(\frac{S_{\dot{m}}}{S_{T_t}}\right)^2 \overline{\dot{m}'^2} \qquad \text{(A.4.10)}$$

and $S_{\dot{m}} = S_u \approx S_\rho$ as given by equation (A.4.9). Thus a hyperbola fitted to the $\overline{e'^2_{i,wm}}$ data obtained for 3 or more overheats (since S_{T_t} and $S_{\dot{m}}$ are dependent to different degrees on the overheat current i) is sufficient to determine $\overline{\tau'^2_t}$, $\overline{\dot{m}'^2}$ and $\overline{\dot{m}' \tau'_t}$.

A. 5 Reduction of Fluctuating Data

In the preceding sections, the response of an ideal (massless) hot wire was derived. The only measurable quantity, however, is that of a real wire which is inherently very small and is attenuated due to the wire thermal lag. The hot wire amplifier both amplifies the actual wire voltage to produce a measurable level, and compensates it for the thermal lag attenuation. The degree to which this compensation is accomplished depends on the approach of the amplifier time constant, M_A, to the actual wire time constant, M_t.

From the calibration of the amplifier and the compensating amplifier, the relation between the output of the amplifier, $E'(f)$ and the actual wire output is found to be

$$E'(f) = G_0 \, A(f) C(f) \, e'_{wm}(f) \qquad (A.5.1)$$

where

G_0 = "zero frequency" gain of the amplifier

$A(f)$ = amplifier attenuation (frequency dependent)

$C(f)$ = response of the compensating amplifier

Gran[55] found that

$$C(f) = \left[\frac{1 + (2\pi f M_A)^2}{1 + (2\pi f M_A/\kappa)^2} \right]^{\frac{1}{2}} \qquad (A.5.2)$$

where κ is the "ceiling-to-floor ratio" (ratio by which the compensation amplifier raises the wire half-power response frequency) and has a value of about 420 for the hot wire set used in this work.

Combining equations (A. 3. 6), (A. 5. 1) and (A. 5. 2), one obtains

$$\overline{e^2_{i,wm}}(f) = \frac{\overline{E'^2(f)}}{G_0^2 A(f)^2} \left[\frac{1+(2\pi f M_t)^2}{1+(2\pi f M_A)^2}\right] \left[1+(2\pi f M_A/K)^2\right] \qquad (A.5.3)$$

as the mean square voltage sensed by the "ideal" hot wire.

M_A and M_t for this work were found to vary from about 0.1 m sec to 0.6 m sec, so $(2\pi f M_A)^2 >> 1$, $2\pi f M_t >> 1$ for f > 5 Hz or so. In this case equation (A.5.3) simplifies to

$$\overline{e'^2_{i,wm}}(f) = \frac{\overline{E'^2(f)}}{G_0^2 A(f)^2} \left(\frac{M_t}{M_A}\right)^2 \left[1+(2\pi f M_A/K)^2\right] \qquad (A.5.4)$$

In general, the total mean square voltage is what is measured, rather than the spectral components. The "ideal" mean square voltage is given by

$$\overline{e'^2_{i,wm}} = \int_0^\infty \overline{e'^2_{i,wm}}(f)\, df$$

Using equation (A.5.4), this simplifies to

$$e'_{i,wm} = \left(\frac{M_t}{M_A}\right)^2 \frac{1}{G_0^2} \int_0^\infty \frac{\overline{E'^2}(f)}{A^2(f)} \left[1+(2\pi f M_A/K)^2\right] df \qquad (A.5.5)$$

In practice, M_A was, for the vast majority of the data, set between 0.2 m sec and 0.4 m sec. Based on the 0.4 m sec setting, $(2\pi f M_A/K)^2 << 1$ for f < 125K. In addition $A(f) \approx 1$ for f < 100 KHz and $A(f) \approx 0.9$ at f = 200 KHz. If one assumes $(2\pi f M_A/K)^2 << 1$ and A(f) = 1 for the frequency range of interest, equation (A.5.5) becomes

$$\overline{e'^2_{i,wm}} = \left(\frac{M_t}{M_A}\right)^2 \frac{1}{G_0^2} \int_0^\infty \overline{E'^2}(f)\, df \qquad (A.5.6)$$

It was found that the error introduced by utilizing equation (A. 5. 6) rather than (A. 5. 5) was less than 10%. It was much easier to use equation (A. 5. 6) since the hot wire set contained a built-in thermocouple circuit which was related to the mean square integrated voltage fluctuations by

$$\overline{e'^2_{i,wm}} = \left(\frac{M_t}{M_A}\right)^2 K_{tc}\, E_{tc} \qquad \text{(A. 5. 7)}$$

where

E_{tc} is the thermocouple voltage output

K_{tc} is calibration constant

Comparing equations (A. 5. 4) and (A. 5. 5) with equation (A. 4. 3), it is observed that the M_t terms in the equations may be eliminated to yield (for spectral data)

$$\int_0^\infty \frac{\overline{E'^2(f)}}{G_o^2 A(f)^2}\, \frac{1}{M_A^2}\, [1+(2\pi f M_A/\kappa)^2]\,df = \overline{[-\hat{S}_u u' - \hat{S}_\rho \rho' + \hat{S}_{T_t} \tau'_t]^2} \qquad \text{(A. 5. 9)}$$

where

$$\hat{S}_\rho = S_\rho / M_t$$

$$\hat{S}_u = S_u / M_t$$

$$\hat{S}_{T_t} = S_{T_t} / M_t$$

and S_ρ, S_u, and S_{T_t} are given by equation (A. 4. 9). Thus, the determination of the fluctuation properties (for $2\pi f M_t \gg 1$) is found to be independent of the value of M_t.

A. 6 Nusselt Number and Recovery Factor Correlations

Several correlations of experimental data for Nusselt number and recovery factor have been made, among which are those of

Dewey[92] and Kubota, as described by Batt.[93] These empirical formulas are presented here in a form suited for direct application to hot wire data reduction.

Kubota found that

$$\overline{Nu}_t = \frac{\overline{Nu}_f}{1 + \frac{\overline{Nu}_f}{\overline{Nu}_c}}$$

where $\overline{Nu}_f$ is the free molecule Nusselt number at the Mach number at which $\overline{Nu}_t$ is to be calculated and $\overline{Nu}_c$ is the Nusselt number at $M = 0$.

The free molecule Nusselt number is given by[94]

$$\overline{Nu}_f = \frac{\gamma - 1}{2\pi^{3/2}\gamma} \alpha \overline{Re}_t \overline{Pr}_t \frac{g(S_1)}{S_1}$$

where

$$S_1 = (\frac{\gamma}{2})^{\frac{1}{2}} M$$

$$\overline{Re}_t = \frac{\bar{\rho}_\infty \bar{u}_\infty d}{\bar{\mu}_t}$$

$$\overline{Pr}_t = \frac{\bar{\mu}_t c_p}{\bar{k}_t}$$

α is an energy accomodation coefficient, and $g(S_1)$ is tabulated in reference (94). For air with $\gamma = 1.4$, and $Pr_t = 0.7$, this becomes

$$\overline{Nu}_f = 0.080 \overline{Re}_t \frac{g(S_1)}{S_1} \qquad (A.6.2)$$

where α has been taken as unity.[92]

As $M \to \infty$, $\frac{g(S_1)}{S_1} \to 10.7$, and

$$\overline{Nu}_{f,H} \simeq 0.190 \overline{Re}_t \qquad (A.6.3)$$

where the subscript H indicates hypersonic speeds.

Evaluating (A. 6. 1) for $M >> 1$

$$\frac{\overline{Nu}_{t,H}}{\overline{Nu}_{f,H}} = \frac{1}{1 + \frac{\overline{Nu}_{f,H}}{\overline{Nu}_{c}}}$$

or

$$\frac{1}{\overline{Nu}_{c}} = \frac{\frac{\overline{Nu}_{f,H}}{\overline{Nu}_{t,H}} - 1}{\overline{Nu}_{f,H}}$$

Equation (A. 6. 1) may then be written as

$$\frac{\overline{Nu}_{t}}{\overline{Nu}_{f}} = \frac{1}{1 - \frac{\overline{Nu}_{f}}{\overline{Nu}_{f,H}} \left(\frac{\overline{Nu}_{f,H}}{\overline{Nu}_{t,H}} - 1 \right)} \qquad \text{(A. 6. 4)}$$

For $M > 2$, the Nusselt number $\overline{Nu}_{t}$ is found to be dependent only on $\overline{Re}_{t}$ and for $0.1 < \overline{Re}_{t} \leq 1000$, a good representation is

$$\overline{Re}_{t} = 5.26\, \overline{Nu}_{t,H} + 5.74\, \overline{Nu}_{t,H}^{2}$$

or

$$\overline{Nu}_{t,H} = \sqrt{0.174\, \overline{Re}_{t} + 0.210} - 0.458$$

Thus $\overline{Nu}_{t}$ may be calculated directly using the values for $g(S_1)/S_1$, given in reference (94). This relation (A. 6. 4) is good for $0.2 \leq M \leq \infty$ and $0.2 \leq \overline{Re}_{t} \leq 1000$. The recovery factor correlation is given by Behrens,[51] who states that

$$\overline{\eta} = \frac{\eta - \eta_c}{\eta_f - \eta_c} = 1 - \frac{1}{1 + \left[\frac{1}{0.350\, \overline{Re}_{t}} \frac{3M^{3.5}}{1+3M^{3.5}} \right]^{z}} \qquad \text{(A. 6. 5)}$$

where

$$z = 1.225 - \frac{0.3}{1 + M^4}$$

$$\eta_c = 1 - 0.050 \frac{M^{3.5}}{1.175 + M^{3.5}}$$

$$\eta_f - \eta_c = 0.21\eta \frac{M^{2.8}}{.852 + M^{2.8}}$$

$$\overline{Re}_t = \frac{\bar{\rho}\,\bar{u}\,d}{\bar{\mu}_t}$$

Logarithmic derivatives needed for data reduction were computed from these correlations using first order finite difference approximations.

APPENDIX B

Upstream History Effects on Adiabatic Wall

As discussed in the text, comparison of the smooth plate data and that for the rough-to-smooth step change configuration indicated the existence of upstream history effects, perhaps in temperature as well as pressure. Definite evidence of upstream temperature effects in the immediate vicinity of the wall were detected, as described below.

Typical wall temperature streamwise distributions for the smooth wall and the rough-to-smooth step change are presented in Figure 15. It is seen that, although the same low-speed heater setting was used in both cases, the rough-to-smooth configuration wall temperatures were significantly higher than the smooth wall temperatures, and this difference was most pronounced in the vicinity of the step (25 inches downstream of the throat). Temperature gradients from the Mach 6 wall surface to the low-speed channel were also observed for the step change configuration, indicating that the wall was far from adiabatic. In an attempt to determine the adiabatic wall temperature for this configuration, the low-speed heater temperature was increased until the gradient through the wall disappeared. After operating at this low-speed heater temperature for some four hours, the wall temperature had increased to 655°R and was still rising slowly. Use of the hot-wire probe to determine the total temperature to within 0.003 in. of the surface revealed a total temperature drop of about 8°F between the flow some 0.010-0.015 inches from the wall

and the wall.

This compares with a $32^{\circ}F$ drop in a somewhat greater distance for the colder rough-to-smooth wall configuration and the adiabatic smooth wall. The decrease in the measured total temperature gradient close to the wall is consistent with the approach to a "normal" adiabatic wall condition, indicating that the wall adiabatic temperature in this case was above $655^{\circ}R$, at least $35^{\circ}F$ above that for the smooth plate.

A careful comparison of the total temperature profiles for the two configurations in the self similar flow regime (Fig. 23) reveals small but definite differences in the distribution throughout the outer boundary layer, with very similar behavior within the inner third of the layer. Of definite interest, however, are the last few measured points near $y/\delta = 0.033$ (indicated on the figure). The smooth wall profile has already begun to decrease quite rapidly toward the wall temperature at this point, while the rough-to-smooth profile shows no such behavior. The profile shapes at $y/\delta < 0.033$ result from the assumption of a linear variation of T_t from the last measured value at $y \cong 0.030$ inch to the measured wall temperature at $y = 0$. Significant total temperature gradients, then, exist for the smooth plate case out to $y \approx 0.040$ inch ($y^+ \approx 19$) while for the rough-to-smooth case they are confined to $y < 0.030$ inch (traverses with the hot wire probe indicate they occur for $y^+ < 10$). This is in spite of nearly identical freestream and wall temperature.

The energy equation for this region of flow may be written as

($\frac{\partial T}{\partial x} = 0$, $v = 0$ in viscous sublayer)

$$0 = \frac{\partial}{\partial y}(u\tau - q) \tag{B-1}$$

or

$$u\tau - q = \text{constant} = q_w \tag{B-2}$$

For the smooth plate configuration, measurements on the wall indicate $q_w = 0$. Also, within the viscous sublayer $\tau \approx \tau_w = \mu_w \frac{\partial u}{\partial y}$. Using the standard expressions for $\tau (= \mu \frac{du}{dy})$ and $q (= -k \frac{dT}{dy})$, one obtains,

$$\mu u \frac{du}{dy} + k \frac{dT}{dy} = 0$$

Or, with $T_t = T(1 + \frac{1}{2 c_p T} u^2)$ and $\frac{\mu c_p}{k} = Pr$

$$\frac{d T_t}{dy} = - \frac{Pr}{c_p} \frac{d u^2/2}{dy} + \frac{d}{dy} \left(\frac{1}{c_p} \frac{u^2}{2} \right) \tag{B-3}$$

Assuming that $c_p \neq c_p(y)$, and performing the integration with $T_t = T_w$, $u = 0$ at $y = 0$,

$$T_t - T_w = (1-Pr) \frac{1}{2c_p} u^2$$

This may be rearranged to yield

$$\frac{T_t - T_w}{T_e} = (1-Pr) \frac{\gamma - 1}{2} M_e^2 (u/u_e)^2 \tag{B-4}$$

Now, for the smooth plate configuration at $y = 0.050$ inch, $u/u_e \approx 0.59$, $M_e = 6$, $T_e = 91^\circ R$, $T_w = 620^\circ R$. Assuming a Prandtl number of 0.85 (due to turbulent contributions, etc) one finds

$$T_t\big|_{y=0.030} = 654^\circ R$$

very close to the measured value of $651^\circ R$. Thus the low temperature of the adiabatic smooth wall is not inconsistent with the measured

temperature profile. For the rough-to-smooth configuration, however, if the total temperature gradient is taken to be within the last 0.020 inch of the wall, the total temperature corresponding to an adiabatic wall at $620^{\circ}R$ using the rough analysis would be ($u/u_e \approx 0.48$)

$$T_t\Big|_{y = 0.020} = 642^{\circ}R$$

As indicated above, estimates made with the hot wire probe indicate a total temperature of approximately $660^{\circ}R$ actually existed, implying that heat transfer to the wall was occurring.

Figure 42 illustrates quite graphically the differences in the temperature velocity relationships for the two boundary layers. The effect of the rough plate is to cause the profile to shift significantly toward the quadratic behavior which is found to be typical for many tunnel wall boundary layers[67, 95, 96] and the Crocco behavior typical of flat plate boundary layers.

The character of the equilibrium smooth wall boundary layer has obviously been radically altered by the presence of the upstream rough plate, implying that strong upstream history effects of both pressure and temperature are present in the smooth plate configuration boundary layer flow. The presence of the rough plate is sufficient to significantly alter these effects, but it definitely does not completely destroy them.

REFERENCES

1. Nikuradse, J. "Strömungsgeretze in rauken Rohren." VDI Forshungsheft no. 361, 1933. Translated as NACA TM 1292, 1950.
2. Moore, W. F. "An Experimental Investigation of the Boundary Layer Development Along a Rough Surface. Ph. D. dissertation, State Univ. of Iowa, 1951.
3. Hama, F. R. "Boundary Layer Characteristics for Smooth and Rough Surfaces." Trans. Soc. Naval Arch. Mar. Engrs., Vol. 62, pp. 333-358.
4. Clauser, F. H. "Turbulent Boundary Layers in Adverse Pressure Gradients," J. Aero. Sci., Vol. 21, pp. 91-108, 1954.
5. Betterman, D. "Contribution a l'Etude de la Convection Force Turbulente le long de Plaques Ruguenses," Int. J. Heat Mass Transfer, Vol. 9, pp. 153-164, 1966.
6. Morris, H. M., Jr. "Flow in Rough Conduits." Trans. ASCE, Vol. 120, pp. 373-397, 1955.
7. Liu, C. K., Kline, S. J. and Johnston, J. P. "An Experimental Study of Turbulent Boundary Layers on Rough Walls," Rept. MD-15, Stanford University Dept. of Mechanical Engineering, 1966.
8. Perry, A. E., Schofield, W. H., and Joubert, P. N. "Rough Wall Turbulent Boundary Layers," J. Fluid Mech., Vol. 37, Part 2, pp. 383-413, 1969.
9. Perry, A. E. and Joubert, P. N. "Rough Wall Boundary Layers in Adverse Pressure Gradients," J. Fluid Mech., Vol. 17, pp. 193-211, 1963.

References (continued)

10. Streeter, V. and Chu, H. "Fluid Flow and Heat Transfer in Artificially Roughened Pipes," Final Report Project 4918, Armour Research Foundation, 1949.

11. Sams, E. W. "Experimental Investigations of Average Heat Transfer and Friction Coefficients for Air Flowing in Circular Tubes Having Square-threads Type Roughness," NACA Res. Mem. RME S2017.

12. Ambrose, H. H. "The Effect of Surface Roughness on Velocity Distribution and Boundary Resistance," University of Tennessee, Dept. of Civil Engineering Contract N/r 811(03). Office of Naval Research, Department of the Navy, 1956.

13. Corrsin, S. and Kistler, A. L. "Free Stream Boundaries of Turbulent Flows," NASA-1244, Jan. 1954.

14. Antonia, R. A. and Luxton, R. E. "The Response of a Turbulent Boundary Layer to a Step Change in Surface Roughness. Part 1. Smooth to Rough," J. Fluid Mech., Vol. 48, Part 4, pp. 721-761, 1971.

15. Liu, C. Y., Sandborn, V. A. and Tieleman, H. W. "Turbulent Spectral Data in Large-Scale Turbulent Boundary Layers, Developed over Different Types of Boundary Roughness," Colorado State University, Research Memo No. 10, N68-29202, 1967.

16. Logan, E. Jr. and Jones, J. B. "Flow in a Pipe Following an Abrupt Increase in Surface Roughness," Trans. of ASME, J. Basic Eng., pp. 35-40, March 1963.

References (continued)

17. Van Driest, E. R. "On Turbulent Flow Near a Wall," J. Aero. Sci., Vol. 23, No. 11, pp. 1007-1011. Nov. 1956.

18. Dvorak, F. A. "Calculation of Turbulent Boundary Layers on Rough Surfaces in Pressure Gradient," AIAA J. Vol. 7, No. 9, pp. 1752-1759, Sept. 1969.

19. Goddard, F. E. Jr. "Effect of Uniformly Distributed Roughness on Turbulent Skin-Friction Drag of Supersonic Speeds," J. Aeron. Sci. Vol. 26, No. 1, pp. 1-15, Jan. 1959.

20. Wade, J. H. T. "An Experimental Investigation of the Effect of Surface Roughness on the Drag of a Cone-Cylinder Model at a Mach Number of 2.48," Rept. 34, Institute of Aerophysics, Univ. of Toronto, Toronto, Canada, Sept. 1955.

21. Fenter, F. W. "The Turbulent Boundary Layer on Uniformly Rough Surfaces of Supersonic Speeds," DRL-437. Defense Research Laboratory, University of Texas, Austin, Texas, Jan. 1960.

22. Young, F. L. "Experimental Investigation of the Effects of Surface Roughness on Compressible Turbulent Boundary Layer Skin Friction and Heat Transfer," DRL-532, Defense Research Laboratory, University of Texas, Austin, Texas, May 1965.

23. Shutts, W. H. and Fenter, F. W. "Turbulent Boundary Layer and Skin Friction Measurements on an Artificially Roughened, Thermally Insulated Plate at Supersonic Speeds," DRL-366, Defense Research Laboratory, University of Texas, Austin, Texas, August 1955.

References (continued)

24. Mann, H. W. "Experimental Study of the Compressible Turbulent Boundary Layer Skin Friction and Heat Transfer in the Fully Rough Regime," DRL-554 Defense Research Laboratory, University of Texas, Austin, Texas, Aug. 1967.

25. Reda, D. C. "Compressible Turbulent Skin Friction on Rough and Rough/Wavy Walls in Adiabatic Flow," NOLTR 74-34, NAVAL Ordnance Laboratory, February 1974.

26. Monta, W. J., Czarnecki, K. R. and Deveikis, W. D. "Drag Due to Two-Dimensional Roughness in a Turbulent Boundary Layer at Mach 3 with and without Heat Transfer," NASA TN D-4746, Sept. 1968.

27. Baronti, P. O. and Libby, P. A. "Velocity Profiles in Turbulent Compressible Boundary Layers," AIAA J, Vol. 4, No. 2, pp. 193-202, Feb. 1966.

28. Coles, D. "The Turbulent Boundary Layer in a Compressible Fluid," The Physics of Fluids, Vol. 7, No. 9, pp. 1403-1423, Sept. 1964.

29. Van Driest, E. R. "Turbulent Boundary Layer in Compressible Fluids," J. Aeron. Sci., Vol. 18, No. 3, pp. 145-160, March 1951.

30. Van Driest, E. R. "Problem of Aerodynamic Heating," Aeronautical Engineering Review, Vol. 15, No. 10, pp. 26-41, Oct. 1956.

31. Watson, P. D. and Cary, A. M. "Transformation of Hypersonic Turbulent Boundary Layers to Incompressible Form," AIAA J, Vol. 5, No. 6, pp. 1202-1203, June, 1967.

References (continued)

32. Keener, E. R. and Hopkins, E. J. "Van Driest Generalization Applied to Turbulent Skin Friction and Velocity Profiles on the Wall of a Mach 7.4 Wind Tunnel," AIAA J, Vol. 11, No. 12, pp. 1784-1785, Dec. 1973.

33. Sommer, S. C. and Short, B. J. "Free Flight Measurements of Skin Friction of Turbulent Boundary Layers with High Rate of Heat Transfer at High Hypersonic Speeds," J. of Aero. Sci., Vol. 25, pp. 536-542, 1956.

34. Spalding, D. B. and Chi, S. W., "The Drag of Compressible Turbulent Boundary Layer on a Smooth Flat Plate with and without Heat Transfer," J. Fluid Mech., Vol. 18, Part 1, pp. 117-143, Jan. 1964.

35. Clark, F. L. and Creel, T. R. Jr. "Reference Temperature Method for Predicting Turbulent Compressible Skin Friction Coefficient," AIAA J, Vol. 11, No. 2, pp. 239-240, Feb. 1975.

36. Hebbar, K. S. and Paranjpe, P. A. "Skin Friction in Turbulent Boundary Layers," AIAA J, Vol. 7, No. 4, pp. 793-796, April 1969.

37. Tennekes, H. "Law of the Wall for Turbulent Boundary Layers in Compressible Flow," AIAA J, Vol. 5, No. 3, March 1967.

38. Hopkins, E. J., Rubesin, M. W., Inouye, M., Keener, E. R., Mateer, G. C. and Polek, T. E. "Summary and Correlation of Skin Friction and Heat-Transfer Data for a Hypersonic Turbulent Boundary Layer on Simple Shapes," NASA TN D-5089, 1969.

References (continued)

39. Miles, J. B. and Kim, J. H. "Evaluation of Coles' Turbulent Compressible Boundary-Layer Theory," AIAA J., Vol. 6, No. 6, pp. 1187-1189, June 1968.

40. Hopkins, E. J. and Inouye, M. "An Evaluation of Theories for Predicting Turbulent Skin Friction and Heat Transfer on Flat Plates at Supersonic and Hypersonic Mach Numbers," AIAA J., Vol. 9, No. 6, pp. 995-1003, June 1971.

41. Dvorak, F. A. "Calculation of Compressible Turbulent Boundary Layers with Roughness and Heat Transfer," AIAA J., Vol. 10, No. 11, pp. 1447-1451, Nov. 1972.

42. Chen, K. K. "Compressible Turbulent Boundary Layer Heat Transfer to Rough Surfaces in Pressure Gradient," AIAA J., Vol. 10, No. 5, pp. 623-629, May 1972.

43. Kistler, A. L. "Fluctuation Measurements in a Supersonic Turbulent Boundary Layer," The Physics of Fluids, Vol. 2, No. 3, pp. 290-296, May-June, 1959.

44. Owen, F. K., Horstman, C. C. and Kussoy, M. I. "Mean and Fluctuating Flow Measurements of a Fully-Developed, Non-Adiabatic Hypersonic Boundary Layer," J. Fluid Mech., Vol. 70, Part 2, pp. 393-413, 1975.

45. Laderman, A. J. and Demetriades, A. "Mean and Fluctuating Flow Measurements in the Hypersonic Boundary Layer Over a Cooled Wall," J. Fluid Mech., Vol. 63, Part 1, pp. 121-144, 1974.

References (continued)

46. Laderman, A. J. and Demetriades, A. "Turbulent Fluctuations in the Hypersonic Boundary Layer Over an Adiabatic Slender Cone," The Physics of Fluids, Vol. 19, No. 3, pp. 359-361, March 1976.

47. Kubota, T. "Characteristics of Hypersonic Compressor Plant," Internal Memorandum 3, GALCIT Hypersonic Project, California Institute of Technology, May 1956.

48. Baloga, P. E. and Nagamatsu, H. T. "Instrumentation of GALCIT Hypersonic Wind Tunnels," Memorandum No. 29, California Institute of Technology, Guggenheim Aeronautical Laboratory, Hypersonic Wind Tunnel, July 1955.

49. Fernandez, F. L. "Two-Dimensional Viscous Flows with Large Distributed Surface Injection," Parts I, II, and III, Ph. D. Thesis, California Institute of Technology, 1969.

50. Peterson, C. W. and George, O. L. "Wind Tunnel Pressure Probes. New Calibrations for New Geometries and Flow Environments," SAND 75-0337, Sandia Laboratories, Albuquerque, N. M., June 1975.

51. Behrens, W. "Total Temperature Thermocouple Probe Based on Recovery Temperature of a Circular Cylinder," Int. J. Heat Mass Transfer, Vol. 14, pp. 1621-1630, 1971.

52. Coles, D. "Measurements in the Boundary Layer Flow," Ph. D. Thesis, California Institute of Technology, 1953.

53. O'Donnell, F. B., and Westkamper, J. C. "Measurements of Errors Caused by Misalignment of Floating Element Skin Friction Balances," AIAA J., Vol. 3, No. 1, pp. 163-165, January 1965.

References (continued)

54. Herceg, E. E. Handbook of Measurement and Control, Schaevitz Engineering, Pennsauken, N. J., 1972.

55. Gran, R. L. "Step Induced Separation of a Turbulent Boundary Layer," Ph. D. Thesis, California Institute of Technology, 1970.

56. Sandborn, V. A. Resistance Temperature Transducers, Meteorology Press, 1972.

57. Ramaswamy, M. A. "Experimental Investigation of the Effect of Cooling on the Near Wake of Circular Cylinders at Mach Number Six," Ph. D. Thesis, California Institute of Technology, 1971.

58. Ames Research Staff. "Equations, Tables, and Charts for Compressible Flow," NACA 1135, p. 7, eq. 100, 1953.

59. Kovasznay, L. S. G. "Turbulence in Supersonic Flow," Jour. Aero. Sci., Vol. 20, No. 10, pp. 657-674, October 1953.

60. Morkovin, M. V. "Fluctuations and Hot-Wire Anemometry in Compressible Flows," AGARDograph No. 74, November 1956.

61. Laufer, J. "Some Statistical Properties of the Pressure Field Radiated by a Turbulent Boundary Layer," The Physics of Fluids, Vol. 7, No. 8, pp. 1191-1197, August 1964.

62. Dewey, C. F., Jr. "Measurements in Highly Dissipative Regions of Hypersonic Flow," Ph. D. Thesis, California Institute of Technology, 1963.

References (continued)

63. Jacobs, W. "Variation in Velocity Profile with Change in Surface Roughness of Boundary," Translated as NACA TM 951.

64. Antonia, R. A. and Luxton, R. E. "The Response of a Turbulent Boundary Layer to a Step Change in Surface Roughness. Part 2. Rough-to-Smooth," J. Fluid Mech., Vol. 53, Part 4, pp. 737-757, 1972.

65. Rotta, J. C. "Heat Transfer and Temperature Distribution in Turbulent Boundary Layers at Supersonic and Hypersonic Flow," AGARDograph 97, Part I, pp. 41-63, May 1965.

66. Bertram, M. H., and Neal, L., Jr. "Recent Experiments in Hypersonic Turbulent Boundary Layers," paper presented at the AGARD Specialists Meeting on Recent Developments in Boundary Layer Research, Naples, Italy, May 10-14, 1965.

67. Feller, W. V. "Effects of Upstream Wall Temperatures in Hypersonic Tunnel Wall Boundary Layer Profile Measurements," AIAA J., Vol. 11, No. 4, pp. 556-558, April 1973.

68. Voisinet, R. L. P., Lee, R. E. and Yanta, W. J. "An Experimental Study of the Compressible Turbulent Boundary Layer with an Adverse Pressure Gradient," AGARD CP-93 Turbulent Shear Flows, Fluid Dynamics Panel Specialists. Meeting in London, September 1971.

69. Sturek, W. B. "Wall Heat Transfer Effects on Supersonic Nozzle Wall Boundary-Layer Temperature Profiles," BRL Mem. Rept. No. 2328, Sept. 1973.

References (continued)

70. Bushnell, D. M., Johnson, C. B., Harvey, W. D., and Feller, W. V., "Comparison of Prediction Methods and Studies of Relaxation in Hypersonic Turbulent Nozzle-Wall Boundary Layers," NASA TN D-5433, 1969.

71. Lewis, J. E., Gran, R. L. and Kubota, T. "An Experiment on the Adiabatic Compressible Boundary Layer in Adverse and Favorable Pressure Gradient," J. Fluid Mech., Vol. 51, part 4, pp. 657-672, 1972.

72. Kemp, J. H. Jr., and Owen, F. K. "Nozzle Wall Boundary Layers at Mach Number 20 to 47," AIAA J., Vol. 10, No. 7, pp. 872-879, July 1972.

73. Coles, D. "The Young Person's Guide to the Data," 1968 AFOSR-IFP-Stanford Conference on Computation of Turbulent Boundary Layers.

74. Clauser, F. H. "The Turbulent Boundary Layer," Advances in Applied Mechanics, Vol. 4, Academic Press, pp. 1-51, 1956.

75. Walz, A. Boundary Layers of Flow and Temperature, MIT Press, p. 69, 1969.

76. Reda, D. C., Ketter, F. C., Jr., and Fon, C. "Compressible Turbulent Skin Friction on Rough and Rough/Wavy Walls in Adiabatic Flow," AIAA Paper No. 74-574, presented at the AIAA 7th Fluid and Plasma Dynamics Conference, Palo Alto, Calif., June 17-19, 1974.

References (continued)

77. Schlichting, H. Boundary Layer Theory, Sixth Ed., translated by J. Kestin, McGraw-Hill, p. 582, 1968.

78. Simpson, R. L. "A Generalized Correlation of Roughness Density Effects on the Turbulent Boundary Layer," AIAA J., Vol. 11, No. 2, pp. 242-244, Feb. 1973.

79. Dirling, R. B., Jr. "A Method for Computing Rough Wall Heat Transfer Rates on Reentry Nosetips," AIAA Paper No. 73-763, presented at the AIAA 8th Thermophysics Conference, Palm Springs, 1973.

80. Mills, A. F., and Courtney, J. F. "Turbulent Boundary Layers on Rough Walls," SDL No. 76-6044, Spectron Development Laboratories, Inc., Costa Mesa, Calif., March 1976.

81. Charwat, A. F., Roos, J. N., Dewey, F. C., Jr., and Hitz, J. A. "An Investigation of Separated Flows. Part I: The Pressure Field," J. Aero. Sci., Vol. 28, No. 6, pp. 457-470, 1961.

82. Rose, W. C. "Turbulence Measurements in a Compressible Boundary Layer," AIAA J., Vol. 12, No. 8, pp. 1060-1064, August, 1974.

83. Demetriades, A. "Turbulence Measurements in an Axisymmetric Compressible Wake," J. Fluid Mech., Vol. 34, part 3, pp. 465-480, 1968.

84. Laderman, A. J., and Demetriades, A. "Advanced Penetration Problem Program. Turbulence Measurements in the Hypersonic Turbulent Boundary Layer Over a Cooled Wall," Philco Ford Publication, No. U-5079, Newport Beach, Calif., 1972.

References (continued)

85. Owen, F. K., Hartman, C. C., and Kussoy, M. I. "Mean and Fluctuating Flow Measurements of a Fully-Developed, Non-Adiabatic Hypersonic Boundary Layer," J. Fluid Mech., Vol. 70, part 2, pp. 393-413, 1975.

86. Ikawa, H. "Turbulent Mixing Layer in Supersonic Flow," Ph. D. Thesis, California Institute of Technology, 1973.

87. Behrens, W. "Flow Field and Stability of the Far Wake Behind Cylinders at Hypersonic Speeds," Ph. D. Thesis, California Institute of Technology, 1966.

88. Thermophysical Properties of Matter, Vol. 1, Thermophysical Properties Research Center, Purdue University, IFI/Plenum Press, New York, 1970, p. 739.

89. Laufer, J., and McClellan, R. "Measurements of Heat Transfer from Fine Wires in Supersonic Flows," Journal of Fluid Mech., Vol. 1, p. 256, 1956.

90. Betchov, R. "Non-linear Theory of a Hot-Wire Anemometer," Translated from the original as NACA TM 1346.

91. Kovasznay, L. S. G. "Physical Measurements in Gas Dynamics and Combustion," High Speed Aerodynamics and Jet Propulsion, Vol. IX, Princeton University Press, 1954.

92. Dewey, C. F., Jr. "A Correlation of Convective Heat Transfer and Recovery Temperature Data for Cylinders in Compressible Flow," Int. J. Heat Mass Transfer, Vol. 8, pp. 245-252, 1963.

References (continued)

93. Batt, R. G. "Experimental Investigation of Wakes Behind Two-Dimensional Slender Bodies at Mach Number Six," Ph. D. Thesis, California Institute of Technology, 1967.

94. Stalder, J. R., Goodwin, G., and Creager, M. O. "A Comparison of Theory and Experiment for High Speed Free Molecule Flow," NACA Report 1032, 1951.

95. Meier, H. U., and Rotta, J. C. "Temperature Distribution in Supersonic Turbulent Boundary Layers," AIAA J., Vol. 9, No. 11, pp. 2149-2156, Nov. 1971.

96. Meier, H. U. "Investigation of the Heat Transfer Mechanism in Supersonic Turbulent Boundary Layers," Wärme-und Stoffübertrangung, Vol. 8, No. 3, pp. 159-165, 1975.

TABLE I

Wall Thermocouple and Pressure Port Locations

Thermocouple or Pressure Port Number		Distance Downstream of Throat (Inches)
1	Surface thermocouples and ports	6.64
2		8.64
3		10.64
4		12.64
5		14.64
6		16.64
7		18.69
8		22.14
9		25.14
10		30.64
11		33.64
12		37.14
13		40.14
14		45.14
15		50.44
16	Thermocouples on back centerline of base plate	25.1
17		37.1
18	Thermocouples in low-speed flow 1-2 in. below base plate centerline	25.
19		37.
20	Low-speed flow heater output thermocouple	
21	Thermocouples on back of base plate adjacent to side walls	25.
22		37.
23		50.

TABLE II

Summary of Run Conditions and Inverse Parameters

Configuration	x (in.)	M_e	T_t (^oR)	u_e (ft/sec)	ρ_e (slug/ft^3)	δ^* (in.)	θ (in.)	H	$\dot{H}$
Smooth Plate	47.4	5.97	765.	2824.	.0001328	0.521	0.0408	12.8	-3.72
	45.4	6.03	765.	2829.	.0001270	0.486	0.0396	12.3	-4.46
	43.4	6.03	765.	2829.	.0001270	0.465	0.0380	12.2	-4.51
	41.4	6.06	765.	2831.	.0001242	0.447	0.0369	12.1	-4.73
	39.4	6.05	765.	2830.	.0001251	0.438	0.0369	11.9	-4.97
	37.4	6.05	765.	2834.	.0001248	0.431	0.0375	11.5	-5.50
	35.4	5.99	765.	2831.	.0001304	0.461	0.0384	12.0	-4.68
	33.4	5.95	765.	2828.	.0001343	0.434	0.0379	11.5	-5.31
	31.4	5.98	765.	2830.	.0001313	0.409	0.0365	11.2	-5.74
	29.4	6.04	765.	2834.	.0001257	0.384	0.0353	10.9	-6.46
	27.4	6.05	765.	2836.	.0001242	0.359	0.0355	10.1	-7.68
	25.4	6.00	765.	2835.	.0001291	0.367	0.0373	9.8	-8.03
Smooth-to-Rough k = 0.0125 in.	47.4	5.97	765.	2829.	.0001347	0.540	0.0385	14.0	-2.58
	45.4	6.02	765.	2829.	.0001302	0.495	0.0353	14.0	-2.69
	43.4	6.04	765.	2830.	.0001283	0.476	0.0344	13.8	-2.87
	41.4	6.05	765.	2830.	.0001273	0.472	0.0336	14.0	-2.77
	39.4	6.05	765.	2832.	.0001272	0.471	0.0344	13.7	-3.05
	37.4	6.08	765.	2836.	.0001243	0.457	0.0340	13.4	-3.37
	35.4	6.04	765.	2834.	.0001279	0.457	0.0344	13.3	-3.41
	33.4	6.02	765.	2834.	.0001296	0.434	0.0342	12.7	-4.01
	31.4	6.00	765.	2829.	.0001319	0.425	0.0330	12.9	-3.79
	29.4	6.07	765.	2833.	.0001253	0.391	0.0312	12.5	-4.30
	28.4	6.07	765.	2839.	.0001248	0.385	0.0323	12.0	-4.92
	27.4	6.06	765.	2836.	.0001259	0.390	0.0323	12.1	-4.78
	26.4	6.03	765.	2839.	.0001284	0.397	0.0329	12.1	-4.76
	25.4	5.98	765.	2839.	.0001328	0.401	0.0346	11.6	-5.22
	24.4	5.98	765.	2838.	.0001330	0.392	0.0340	11.5	-5.21
Smooth-to-Rough k = 0.025 in.	47.4	5.98	765.	2830.	.0001339	0.537	0.0384	14.0	-2.71
	45.4	5.98	765.	2830.	.0001339	0.497	0.0363	13.7	-2.99
	43.4	6.01	765.	2832.	.0001310	0.477	0.0354	13.5	-3.21
	41.4	6.00	765.	2833.	.0001318	0.445	0.0335	13.3	-3.39
	39.4	6.02	765.	2834.	.0001299	0.442	0.0330	13.4	-3.40
	37.4	6.03	765.	2835.	.0001289	0.441	0.0325	13.6	-3.24
	35.4	5.99	765.	2836.	.0001324	0.445	0.0338	13.2	-3.57
	33.4	5.98	765.	2834.	.0001335	0.432	0.0332	13.0	-3.76
	31.4	5.97	765.	2833.	.0001345	0.408	0.0320	12.8	-3.96
	29.4	6.03	765.	2837.	.0001288	0.381	0.0303	12.6	-4.30
	28.4	6.04	765.	2839.	.0001277	0.374	0.0308	12.1	-4.82
	27.4	6.05	765.	2838.	.0001269	0.369	0.0304	12.1	-4.78
	26.4	6.00	765.	2835.	.0001316	0.382	0.0313	12.2	-4.57
	25.4	5.99	765.	2834.	.0001326	0.370	0.0315	11.7	-5.13
	24.4	6.00	765.	2835.	.0001316	0.354	0.0306	11.6	-5.28

TABLE II (Cont'd)

Configuration	x (in.)	M_e	T_t (°R)	u_e (ft/sec)	ρ_e (slug/ft^3)	δ^* (in.)	θ (in.)	H	$\dot{H}$
Smooth-to-Rough k = 0.050 in.	47.4	6.00	765.	2827.	.0001322	0.585	0.0408	14.4	-2.55
	45.4	6.04	765.	2828.	.0001286	0.547	0.0384	14.2	-2.74
	43.4	6.03	765.	2827.	.0001295	0.522	0.0370	14.1	-2.86
	41.4	6.03	765.	2825.	.0001297	0.499	0.0354	14.1	-2.89
	39.4	6.04	765.	2828.	.0001286	0.479	0.0350	13.7	-3.22
	37.4	6.05	765.	2830.	.0001275	0.466	0.0349	13.4	-3.52
	35.4	6.04	765.	2830.	.0001284	0.473	0.0354	13.4	-3.54
	33.4	6.03	765.	2829.	.0001293	0.452	0.0343	13.2	-3.64
	31.4	6.00	765.	2827.	.0001322	0.438	0.0339	12.9	-3.85
	29.4	6.08	765.	2836.	.0001244	0.402	0.0323	12.4	-4.56
	28.4	6.10	765.	2835.	.0001228	0.390	0.0313	12.5	-4.57
	27.4	6.09	765.	2838.	.0001233	0.390	0.0321	12.1	-4.82
	26.4	6.08	765.	2836.	.0001244	0.395	0.0321	12.3	-4.60
	25.4	6.00	765.	2839.	.0001311	0.411	0.0351	11.7	-5.13
	24.4	6.00	765.	2839.	.0001311	0.391	0.0343	11.4	-5.54
Rough-to-Smooth k = 0.050 in.	47.4	6.01	765.	2843.	.0001296	0.559	0.0406	13.8	-3.02
	45.4	6.02	765.	2844.	.0001289	0.526	0.0392	13.4	-3.18
	43.4	6.01	765.	2843.	.0001298	0.514	0.0386	13.3	-3.38
	41.4	6.00	765.	2841.	.0001309	0.496	0.0373	13.3	-3.36
	39.4	6.03	765.	2842.	.0001281	0.478	0.0363	13.2	-3.58
	37.4	6.06	765.	2845.	.0001235	0.474	0.0359	13.2	-3.87
	35.4	6.07	765.	2845.	.0001244	0.487	0.0373	13.1	-3.85
	33.4	5.99	765.	2840.	.0001319	0.516	0.0400	12.9	-3.87
	31.4	6.02	765.	2842.	.0001290	0.507	0.0397	12.8	-4.13
	29.4	6.05	765.	2847.	.0001259	0.490	0.0402	12.2	-4.90
	28.4	6.05	765.	2847.	.0001259	0.477	0.0399	12.0	-5.19
	27.4	6.04	765.	2847.	.0001268	0.468	0.0388	12.1	-5.01
	26.4	6.00	765.	2842.	.0001307	0.475	0.0391	12.1	-4.92
	25.4	6.02	765.	2838.	.0001294	0.464	0.0379	12.2	-4.77
	24.4	5.96	765.	2838.	.0001348	0.467	0.0375	12.5	-4.34

TABLE III

Results of Velocity Profile Correlation

Conf.	x	y_o	$\bar{\pi}$	δ	u_τ	$\tau_w \times 100$	$\frac{\Delta u}{u_\tau}$	$\tau_w \times 100$ (meas'd*)
Smooth	47.4	0.0	1.46	1.02	134	.25	0.0	.25
	45.4	↓	1.36	0.98	138	.25	↓	
	43.4		1.34	0.94	139	.25		
	41.4		1.29	0.91	141	.25		
	39.4		1.25	0.91	143	.26		
	37.4		1.28	0.92	142	.26		
	35.4		1.45	0.93	136	.25		
	33.4		1.42	0.90	137	.27		
	31.4		1.39	0.87	139	.27		
	29.4		1.26	0.83	144	.27		
	27.4		1.12	0.83	149	.28		
	25.4		1.12	0.86	147	.29		
S → R k=0.0125	47.4	0.0063	1.34	1.01	148	.31	2.69	
	45.4	↓	1.30	0.93	150	.30	2.40	
	43.4		1.24	0.91	151	.30	2.15	
	41.4		1.30	0.90	148	.28	1.77	
	39.4		1.23	0.90	151	.30	1.96	
	37.4		1.23	0.87	149	.28	1.50	
	35.4	0.0050	1.40	0.88	140	.26	0.51	
	33.4	0.0038	1.35	0.86	143	.27	0.82	
	31.4	0.0038	1.35	0.84	145	.29	1.35	
	29.4	0.0025	1.30	0.79	142	.26	0.07	
	28.4	0.0012	1.30	0.80	142	.26	-0.15	
	27.4	0.0	1.30	0.80	138	.25	-0.80	
	26.4	↓	1.29	0.81	110	.26	-0.27	
	25.4		1.27	0.83	141	.28	-0.07	
	24.4		1.14	0.83	146	.30	0.29	
S → R k=0.025	47.4	0.0125	1.34	1.01	155	.34	3.76	.34
	45.4	↓	1.30	0.94	157	.35	3.73	
	43.4		1.24	0.90	160	.35	3.67	
	41.4		1.30	0.84	160	.35	3.77	
	39.4		1.23	0.85	163	.35	3.75	
	37.4		1.23	0.84	163	.35	3.74	
	35.4	0.010	1.40	0.84	153	.32	3.07	
	33.4	0.005	1.35	0.82	155	.34	3.21	
	31.4	0.0025	1.35	0.79	153	.33	2.66	
	29.4	0.0025	1.30	0.75	153	.31	2.01	
	28.4	0.0025	1.30	0.74	150	.30	1.44	
	27.4	0.0	1.30	0.74	145	.27	0.44	.28
	26.4	↓	1.29	0.76	146	.29	0.85	
	25.4		1.27	0.76	142	.28	0.06	
	24.4		1.14	0.75	145	.29	-0.12	

TABLE III (continued)

Conf.	x	y_o	$\overline{\pi}$	δ	u_τ	$\tau_w \times 100$	$\frac{\Delta u}{u_\tau}$	$\tau_w \times 100$ (meas'd*)
S → R	47.4	0.025	1.23	1.08	176	.43	6.55	
k=0.050	45.4	↓	1.18	1.01	178	.42	6.25	.43
	43.4		1.15	0.98	180	.43	6.22	
	41.4		1.10	0.93	188	.47	6.78	
	39.4		1.10	0.90	186	.45	6.36	
	37.4		1.10	0.89	183	.43	5.87	
	35.4		1.25	0.89	174	.40	5.45	
	33.4		1.35	0.84	168	.38	5.06	
	31.4	0.010	1.35	0.84	155	.33	3.16	
	29.4	0.0	1.30	0.79	150	.29	1.46	
	28.4	↓	1.30	0.77	146	.26	0.52	
	27.4		1.30	0.79	140	.25	-0.48	.34
	26.4		1.29	0.81	139	.24	-0.79	
	25.4		1.28	0.84	141	.27	-0.01	
	24.4		1.20	0.82	143	.28	0.15	
R → S	47.4	0.0	1.50	1.07	132	.23	-0.06	
k=0.050	45.4	↓	1.45	1.03	134	.24	-0.07	
	43.4		1.45	0.99	139	.26	1.02	
	41.4		1.43	0.96	141	.27	1.15	
	39.4		1.40	0.93	143	.27	1.22	
	37.4	0.005	1.45	0.93	142	.25	0.96	
	35.4	0.005	1.60	0.95	136	.25	0.67	
	33.4	0.010	1.55	1.00	143	.28	2.25	
	31.4	0.015	1.50	0.99	152	.31	3.37	
	29.4	0.015	1.40	0.95	158	.33	3.73	
	28.4	0.005	1.35	0.93	162	.34	3.94	
	27.4	0.015	1.30	0.92	167	.37	4.52	
	26.4	0.005	1.28	0.91	171	.40	5.14	
	25.4	0.020	1.25	0.91	177	.42	5.73	
	24.4	0.020	1.20	0.89	181	.46	6.19	

*Measurements were made only where these values are indicated.

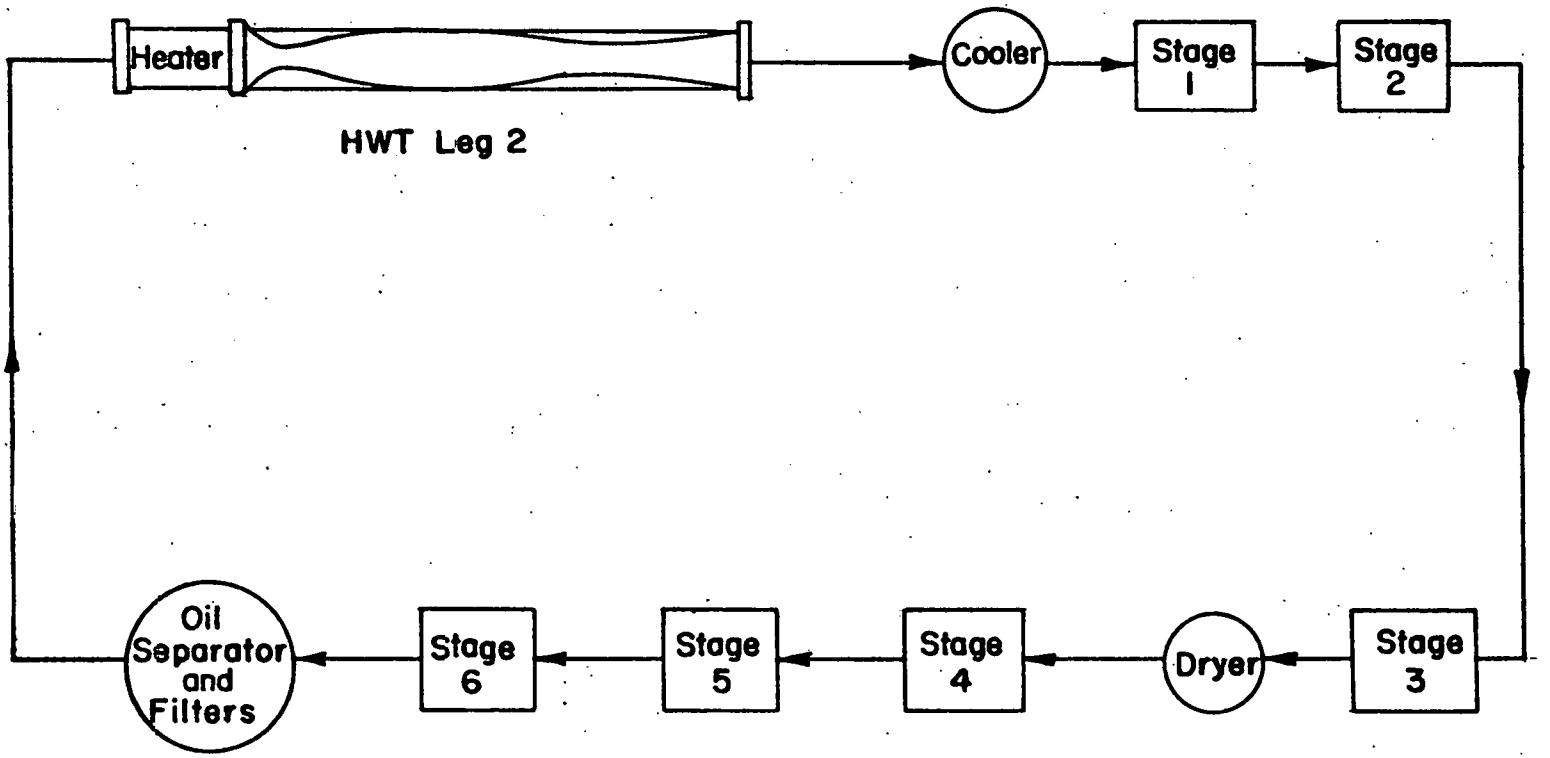

FIG. 1 WIND TUNNEL SCHEMATIC

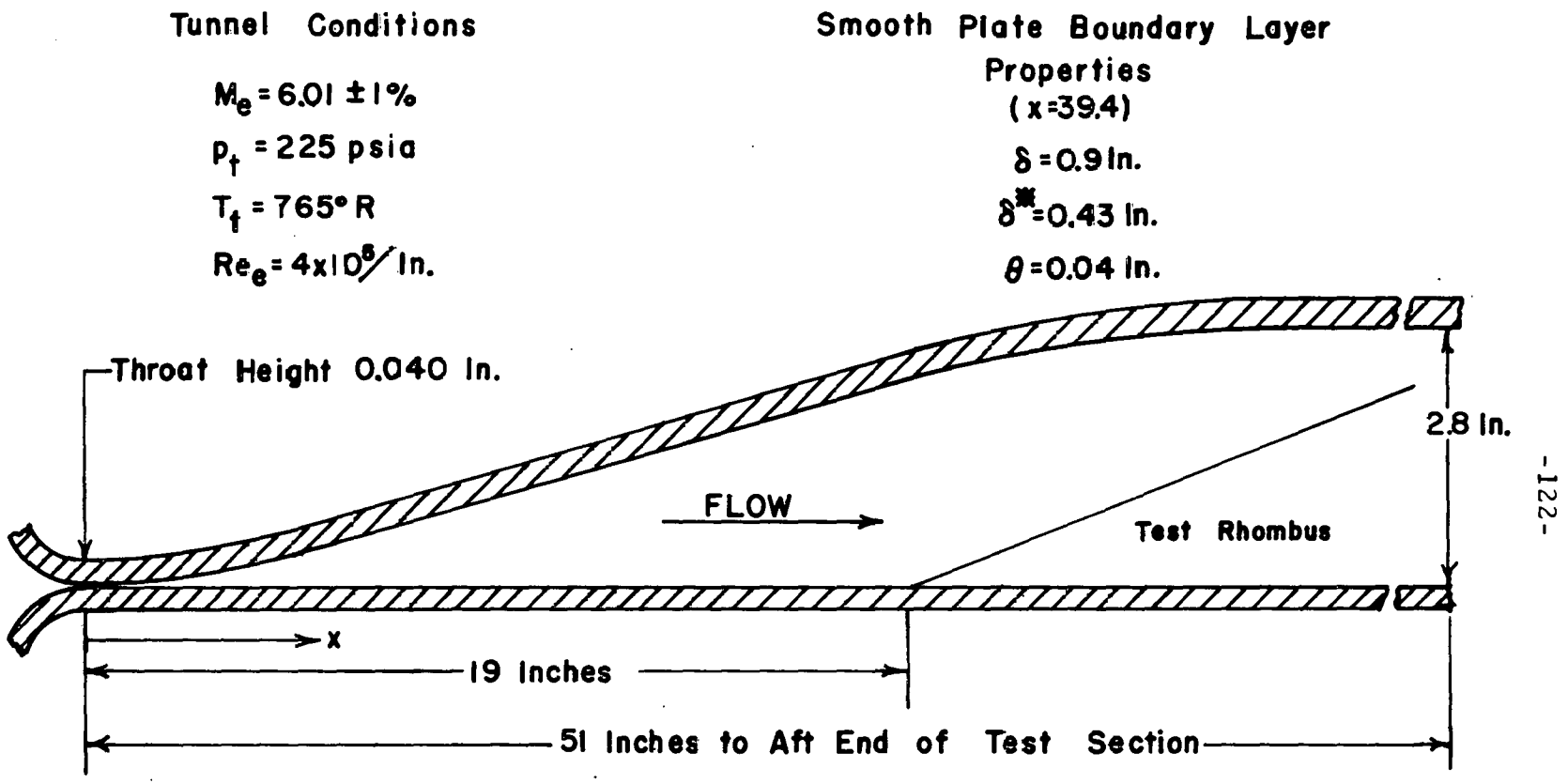

FIG. 2 WIND TUNNEL HALF-NOZZLE CONFIGURATION

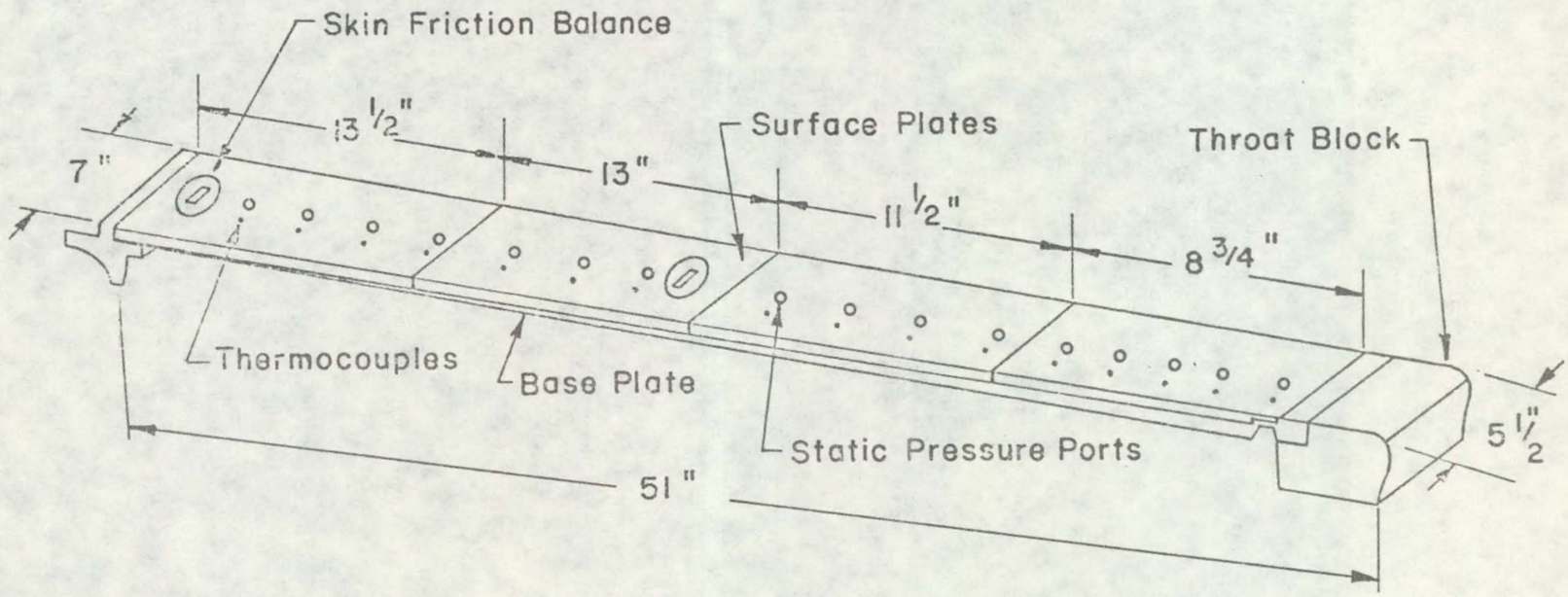

FIG. 3 EXPERIMENTAL CONFIGURATION

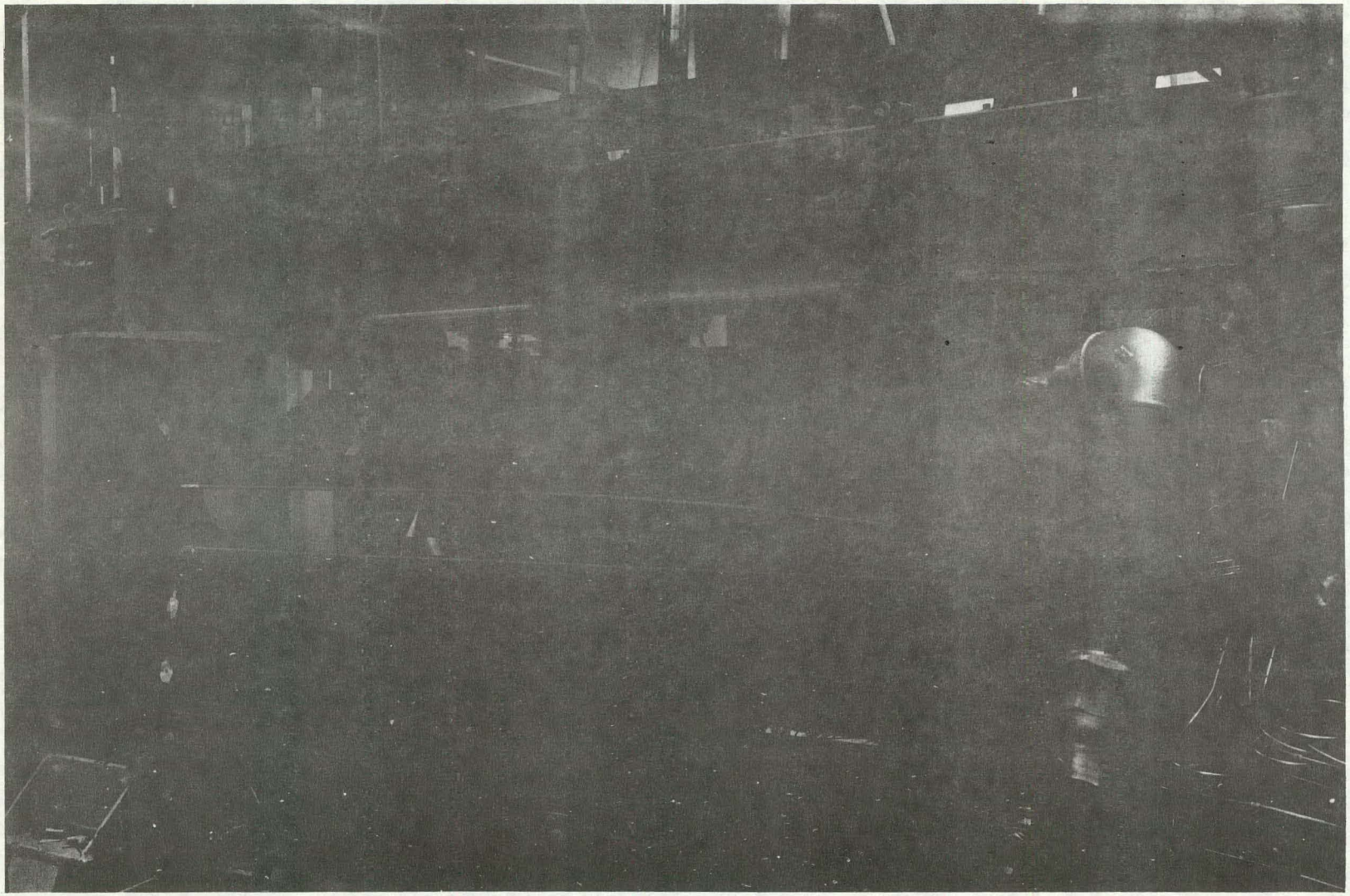

FIG. 4 EXPERIMENTAL MODEL INSTALLATION

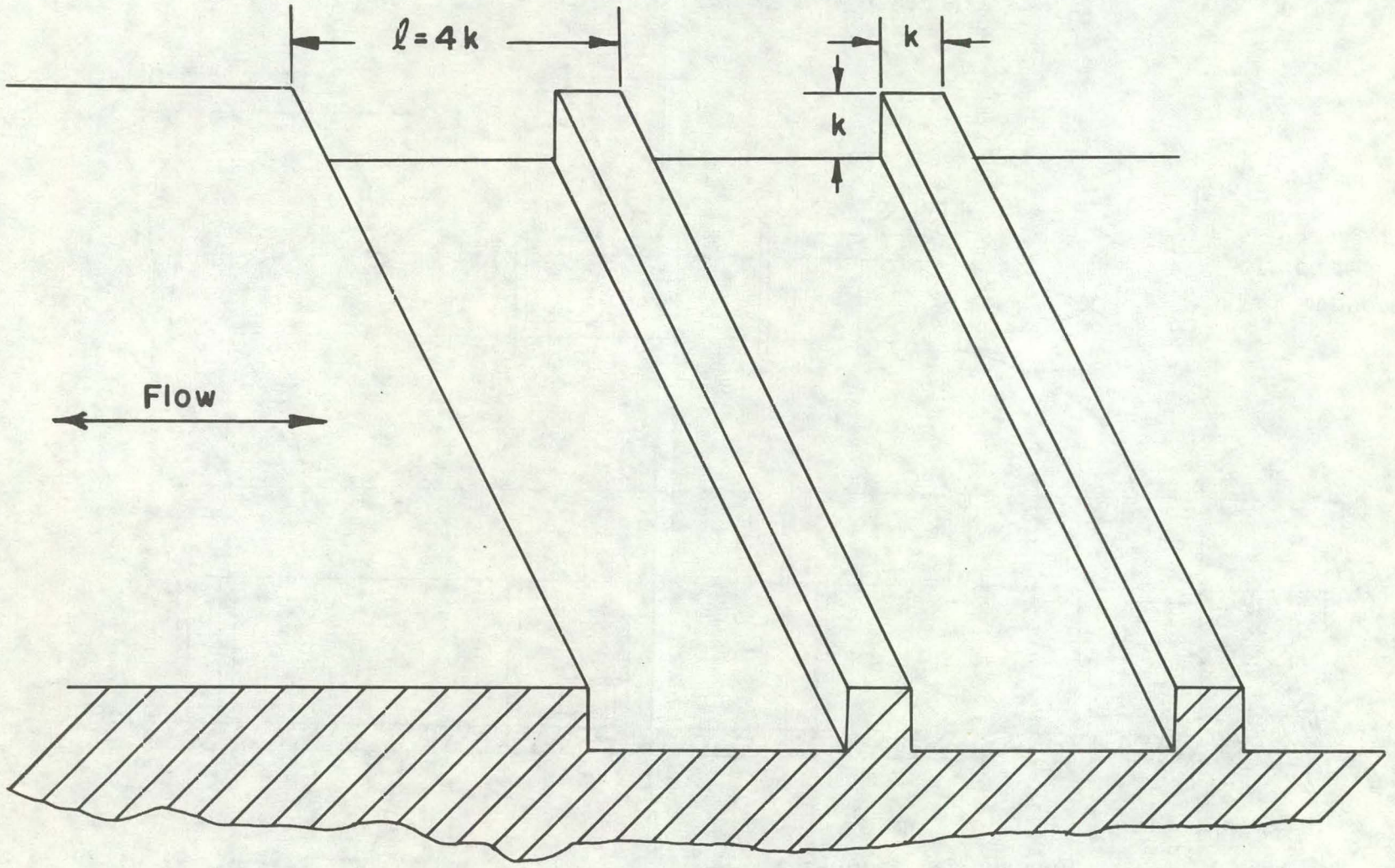

FIG. 5 SURFACE ROUGHNESS CONFIGURATION

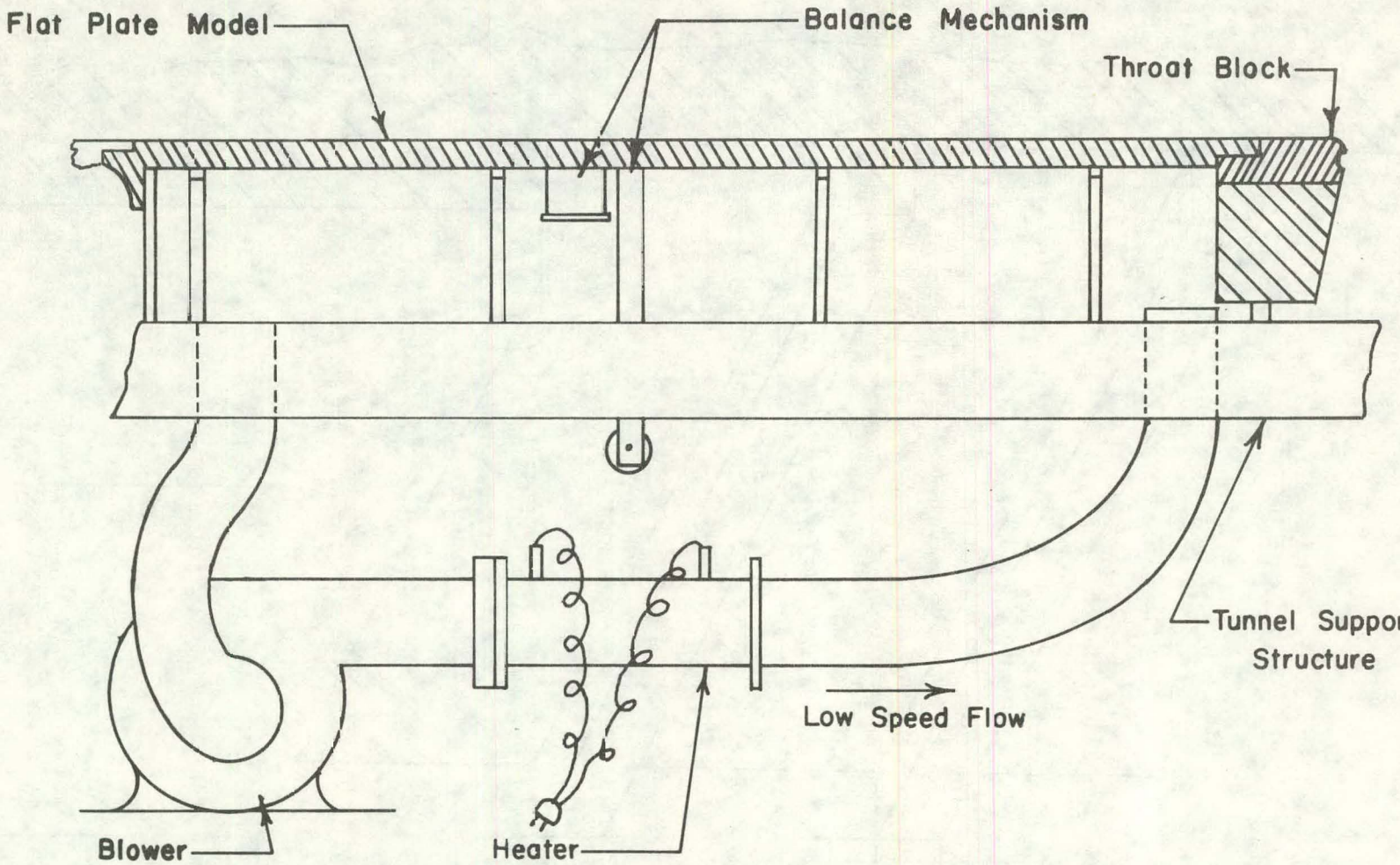

FIG.6 LOW SPEED FLOW CIRCUIT

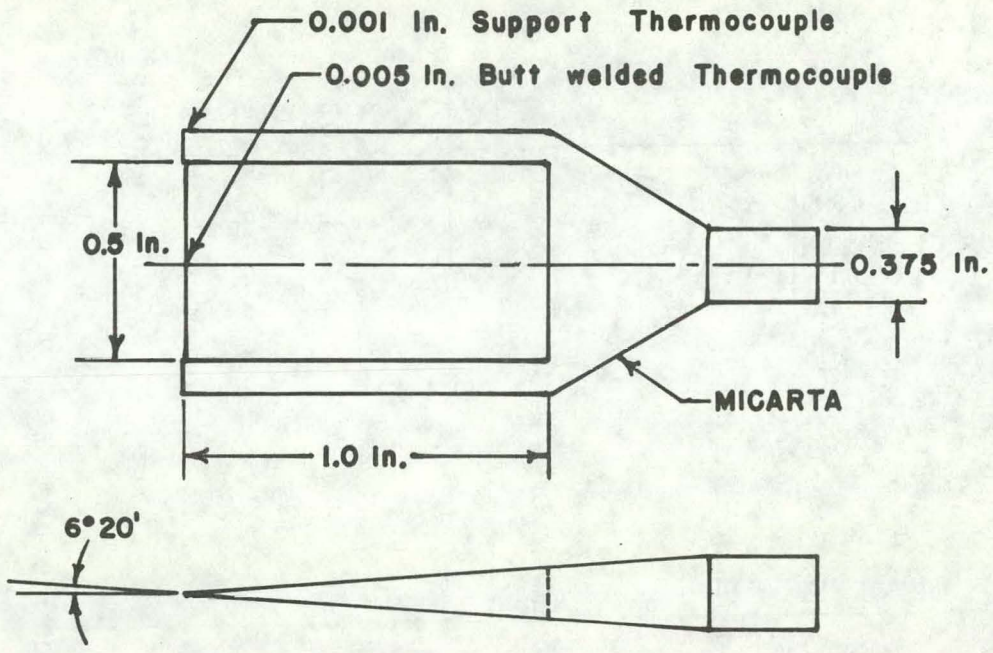

FIG. 7 TOTAL TEMPERATURE PROBE

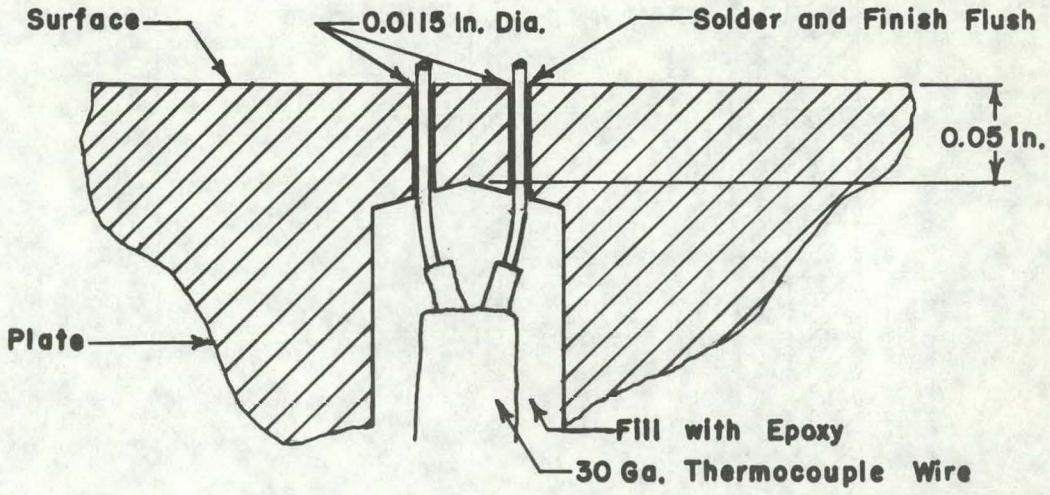

FIG. 8 WALL TEMPERATURE THERMOCOUPLE CONSTRUCTION

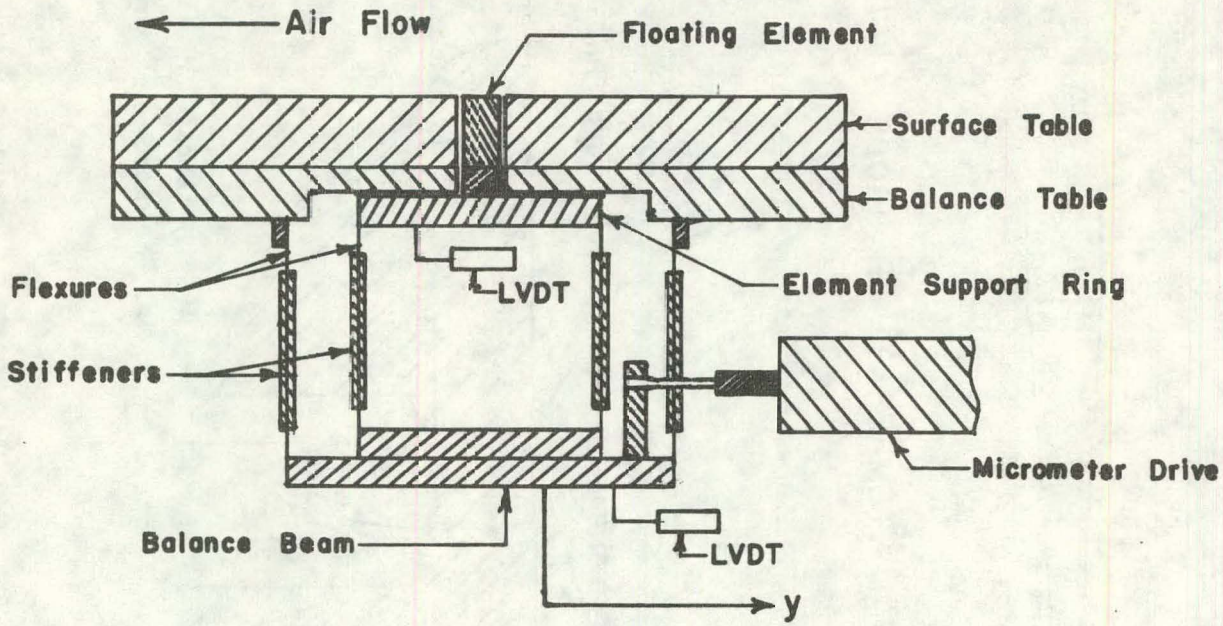

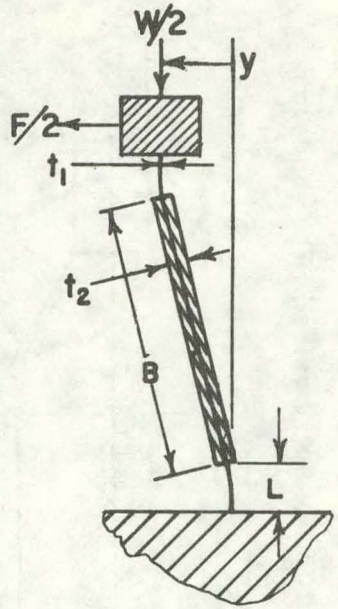

$t_1 = 0.002$ in.

$t_2 = 0.100$ in.

B = 0.825 in.

L = 0.150 in.

Flexure Idealization

$$k = F/y = \frac{W}{B\left[\frac{\cos\beta + 2L/B\beta\sin\beta}{\cos\beta - B\beta/2L\sin\beta} - (1 + 2L/B)\right]}$$

$$\beta = \sqrt{\frac{L^2 F}{2EI}}$$

E = Modulus Of Elasticity

I = Moment Of Inertia Of Free Flexure

FIG. 9 FLOATING ELEMENT BALANCE SCHEMATIC

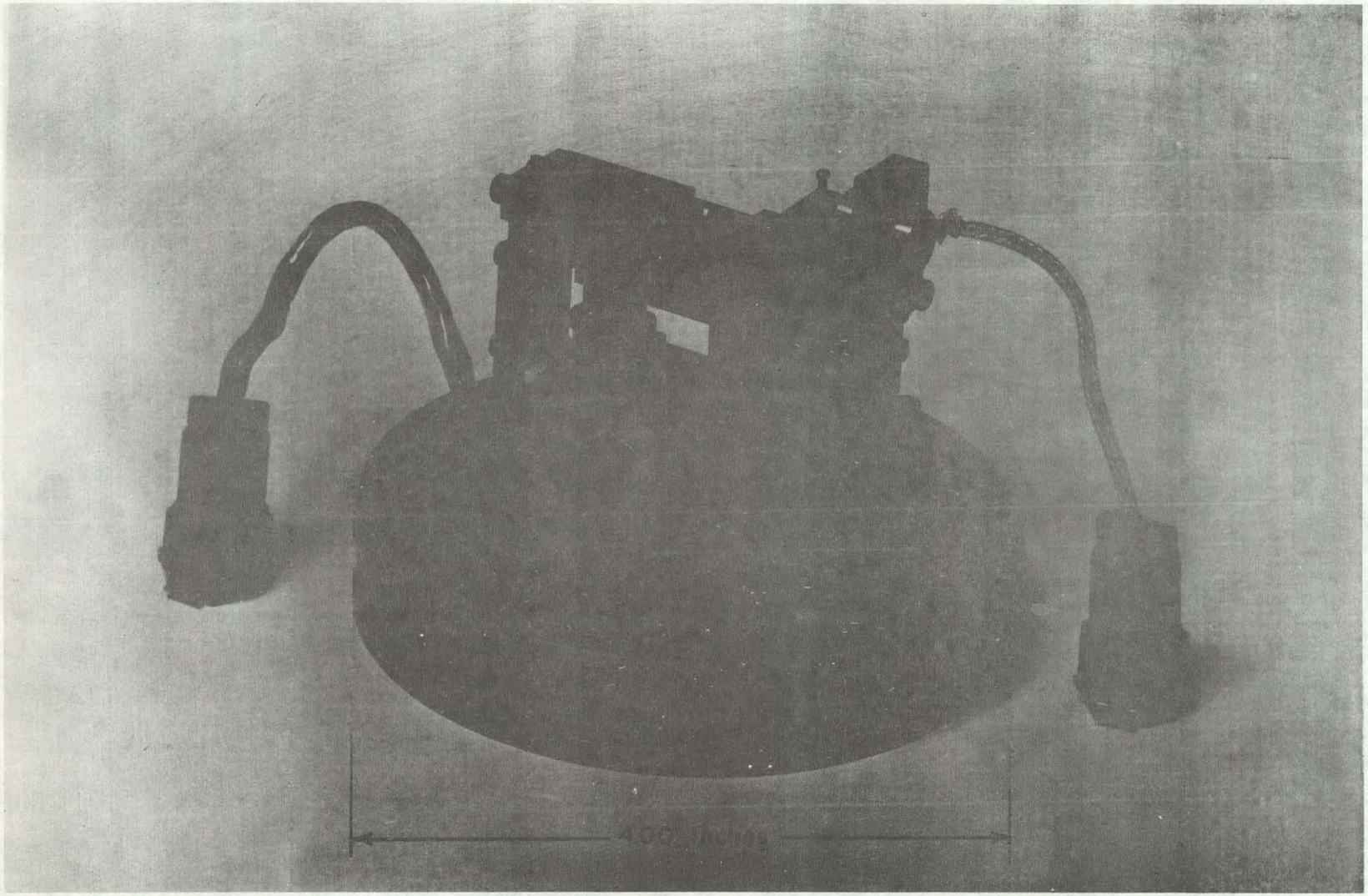

FIG. 10 FLOATING ELEMENT BALANCE

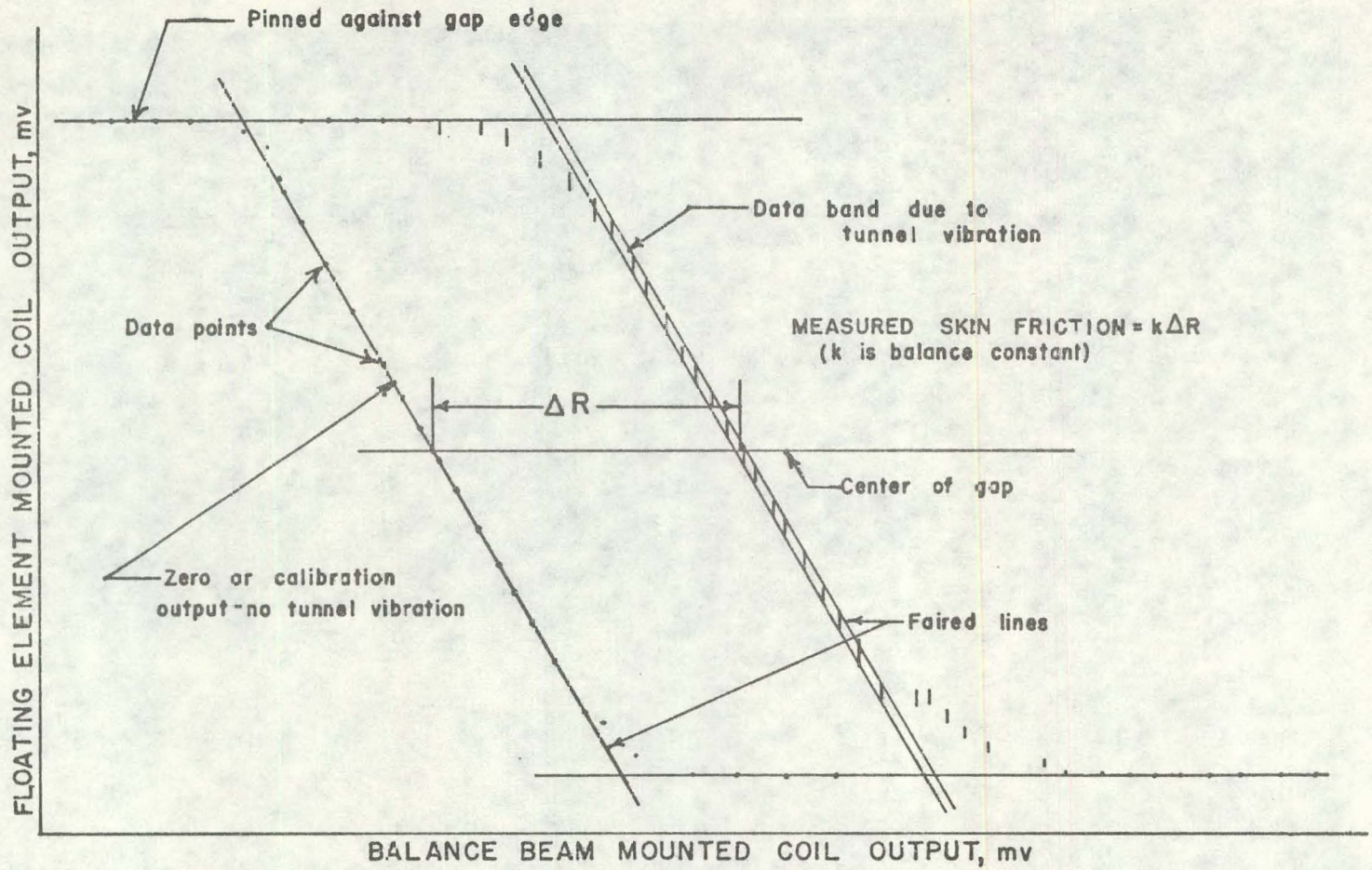

FIG. 11 TYPICAL BALANCE RAW DATA OUTPUT

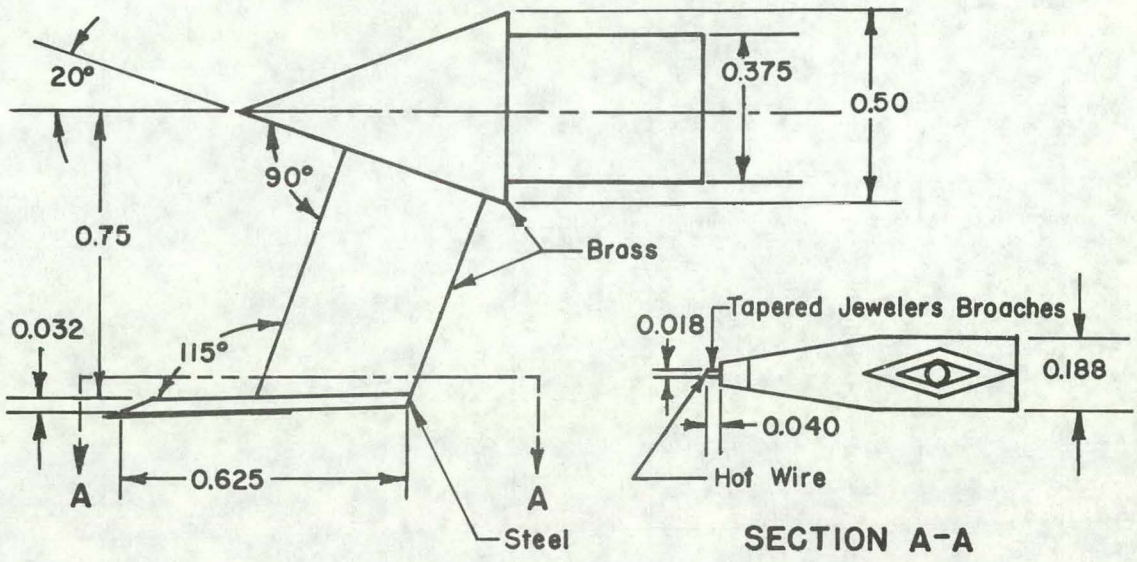

All Dimensions in Inches

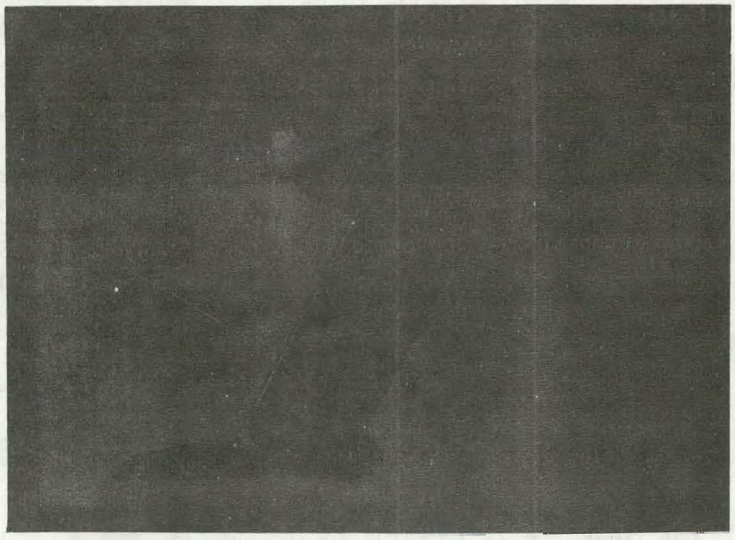

FIG. 12 HOT WIRE PROBE

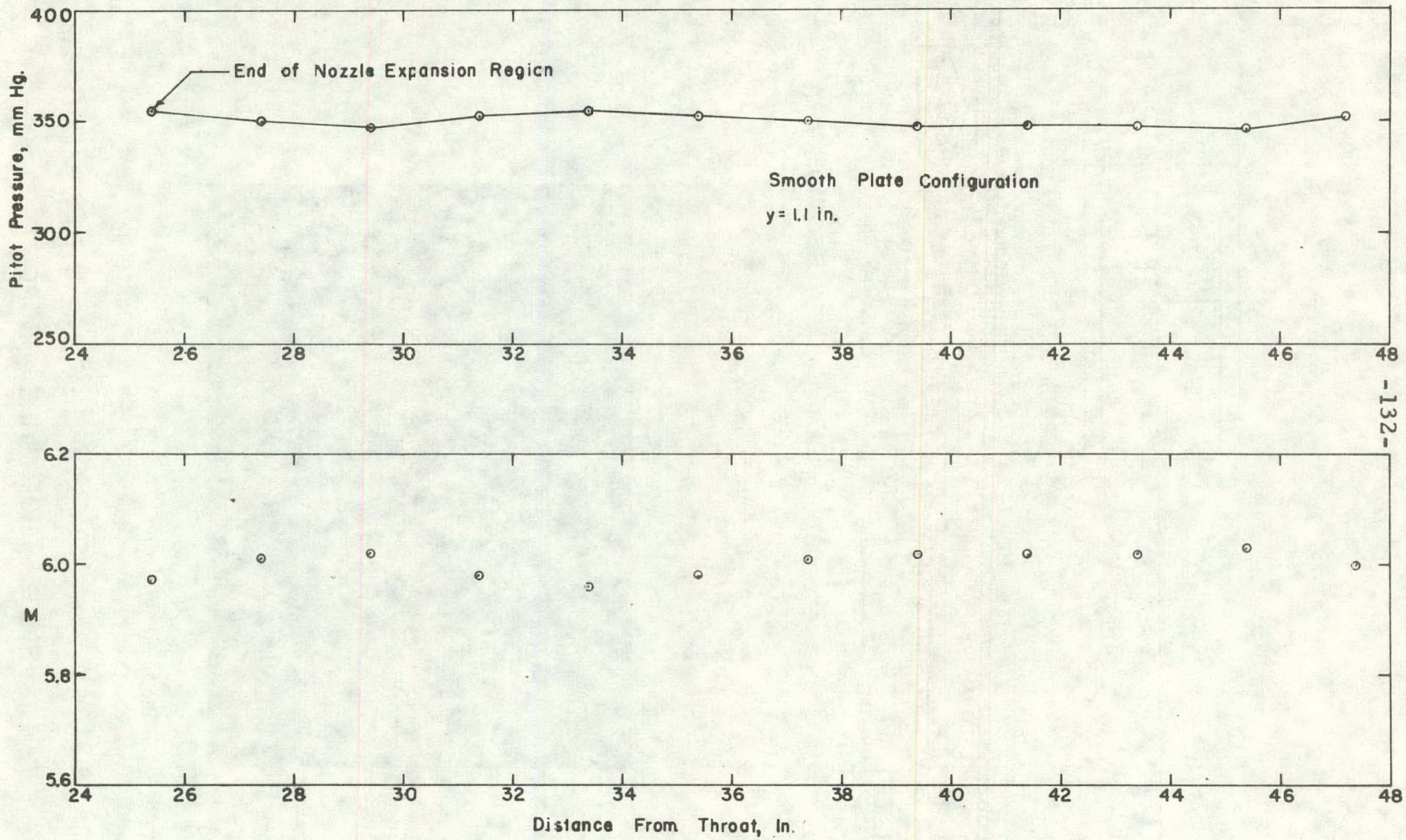

FIG. 13 AXIAL DISTRIBUTION OF FREESTREAM MACH NUMBER AND PITOT PRESSURE

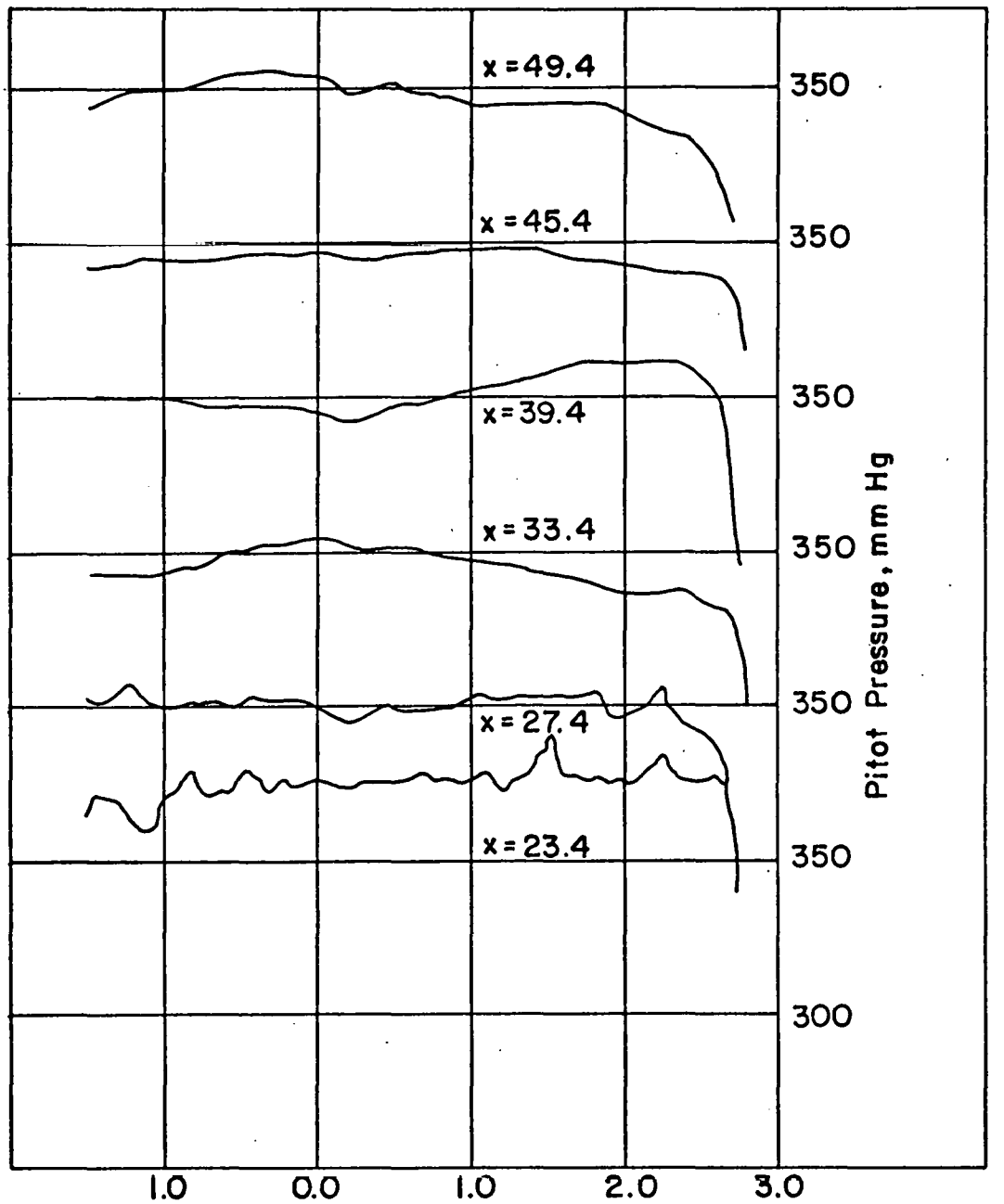

FIG. 14 CROSS STREAM PITOT PRESSURE DISTRIBUTIONS

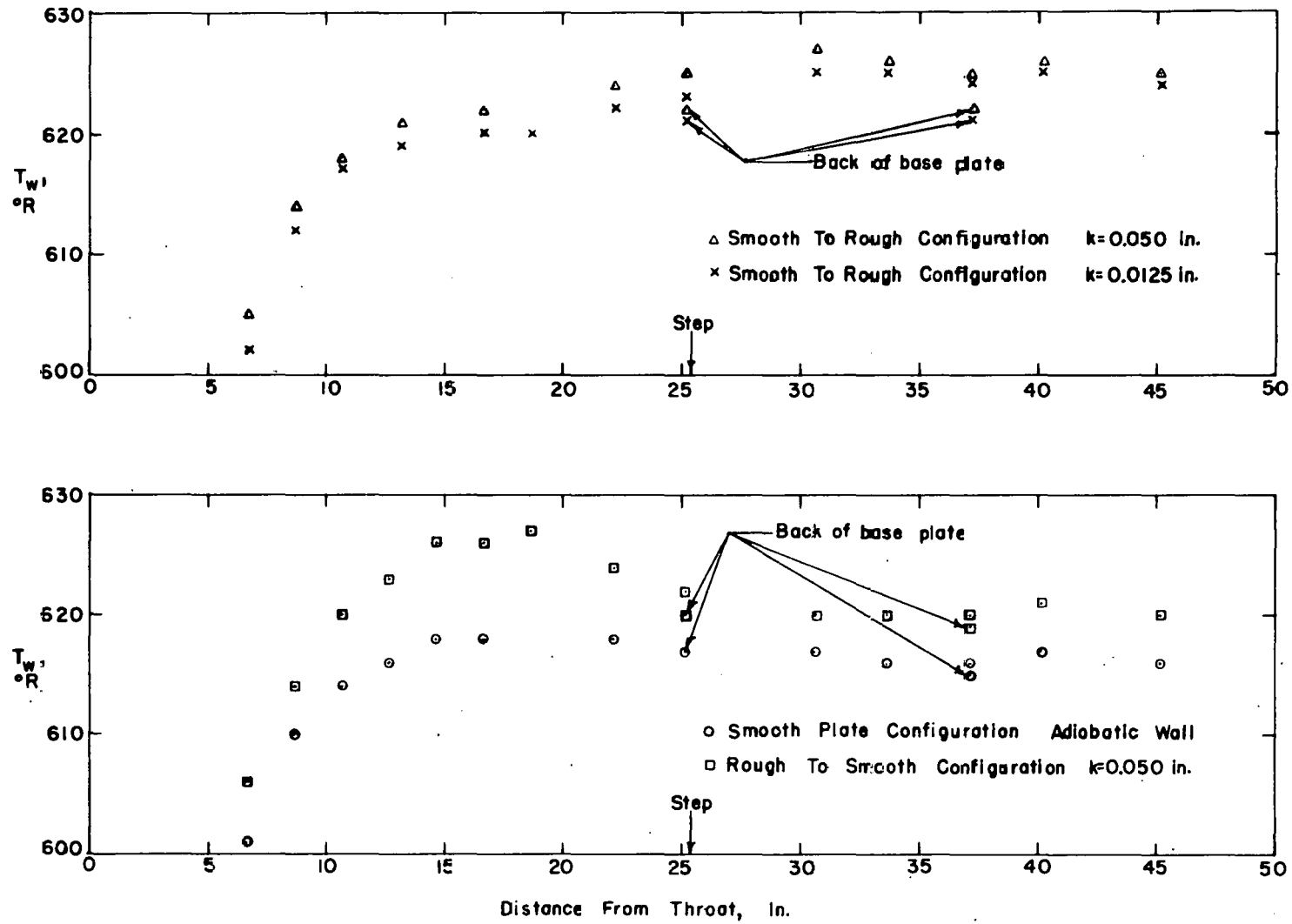

FIG. 15 AXIAL DISTRIBUTION OF WALL TEMPERATURE

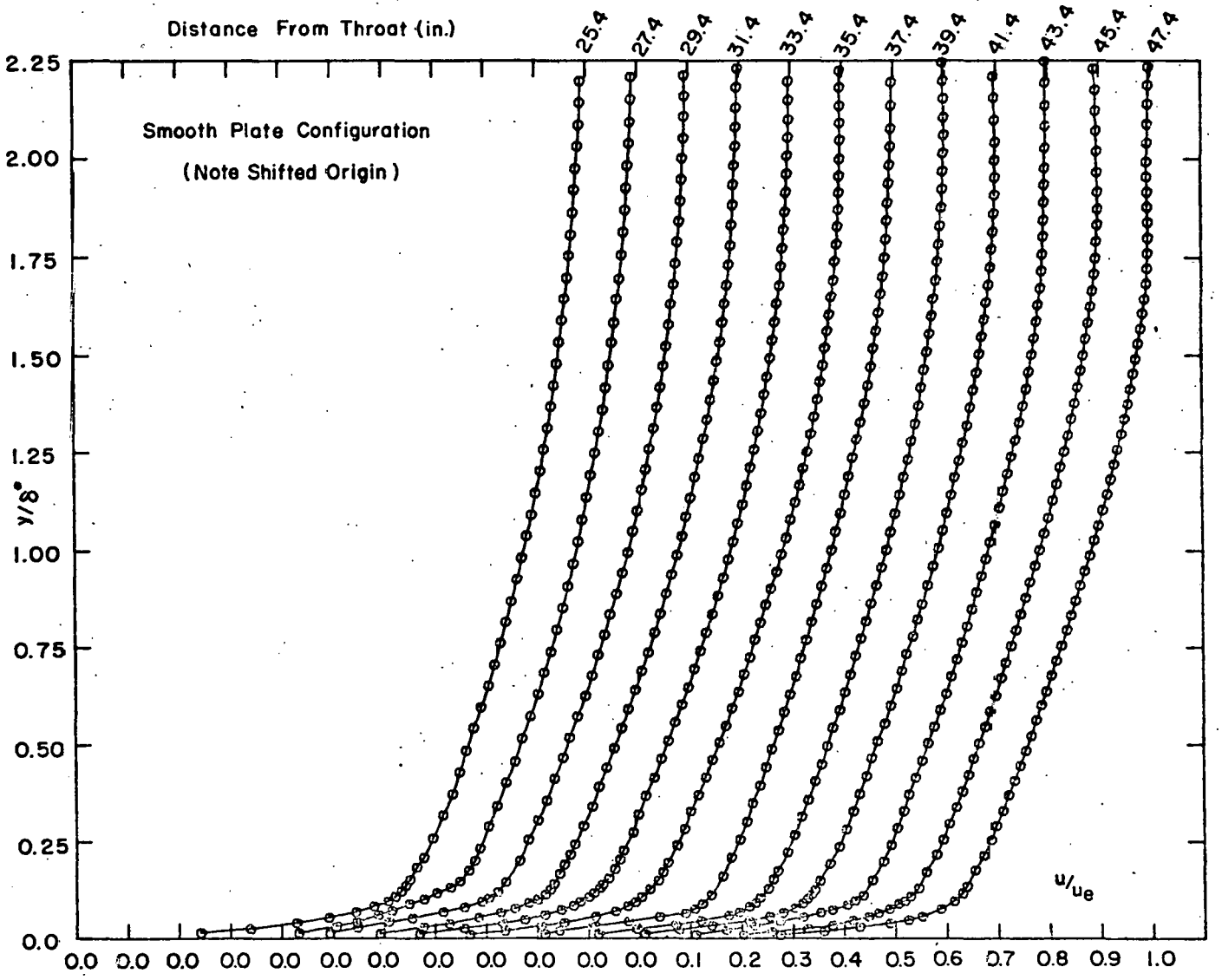

FIG. 16 VELOCITY PROFILES

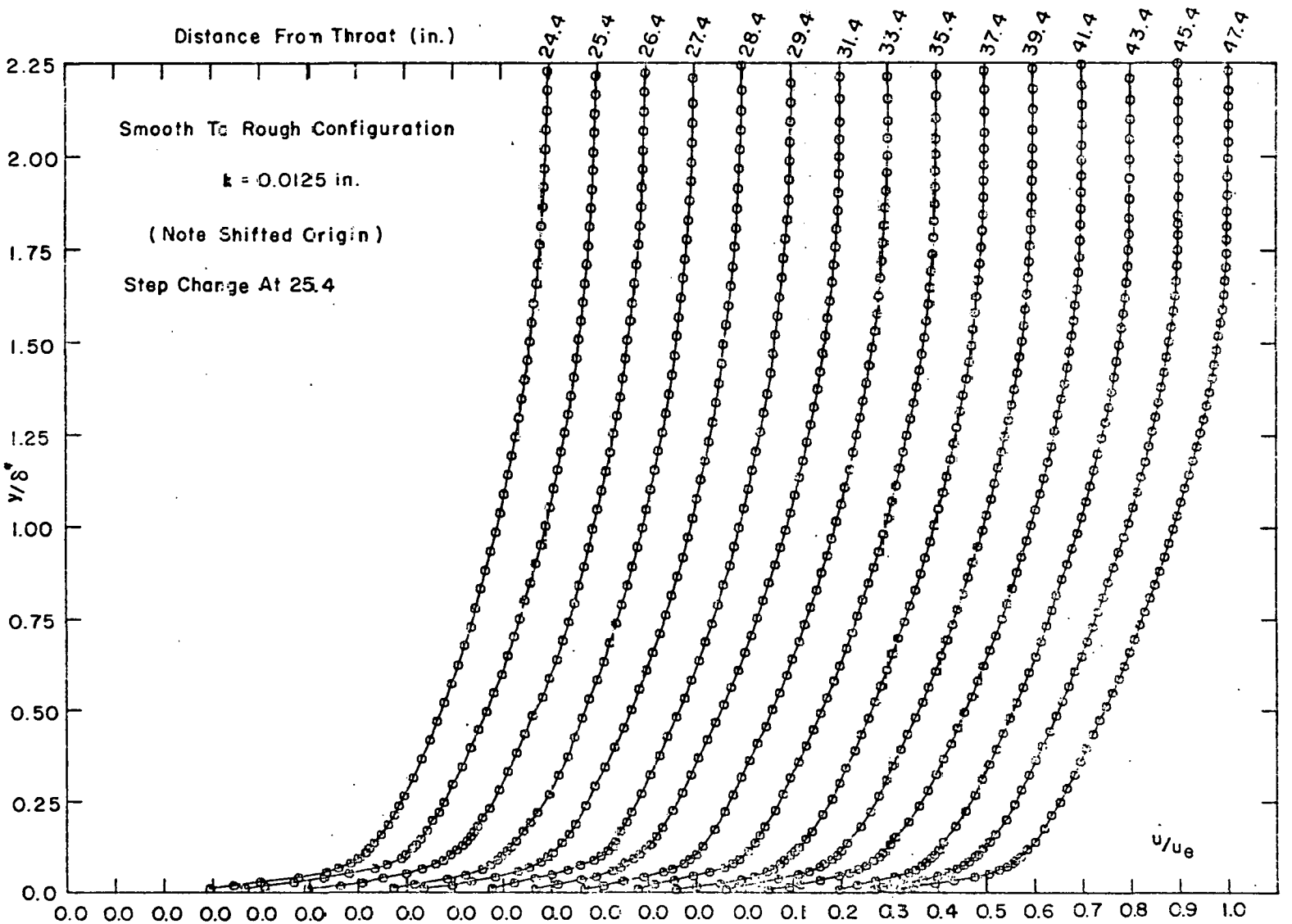

FIG. 16 VELOCITY PROFILES

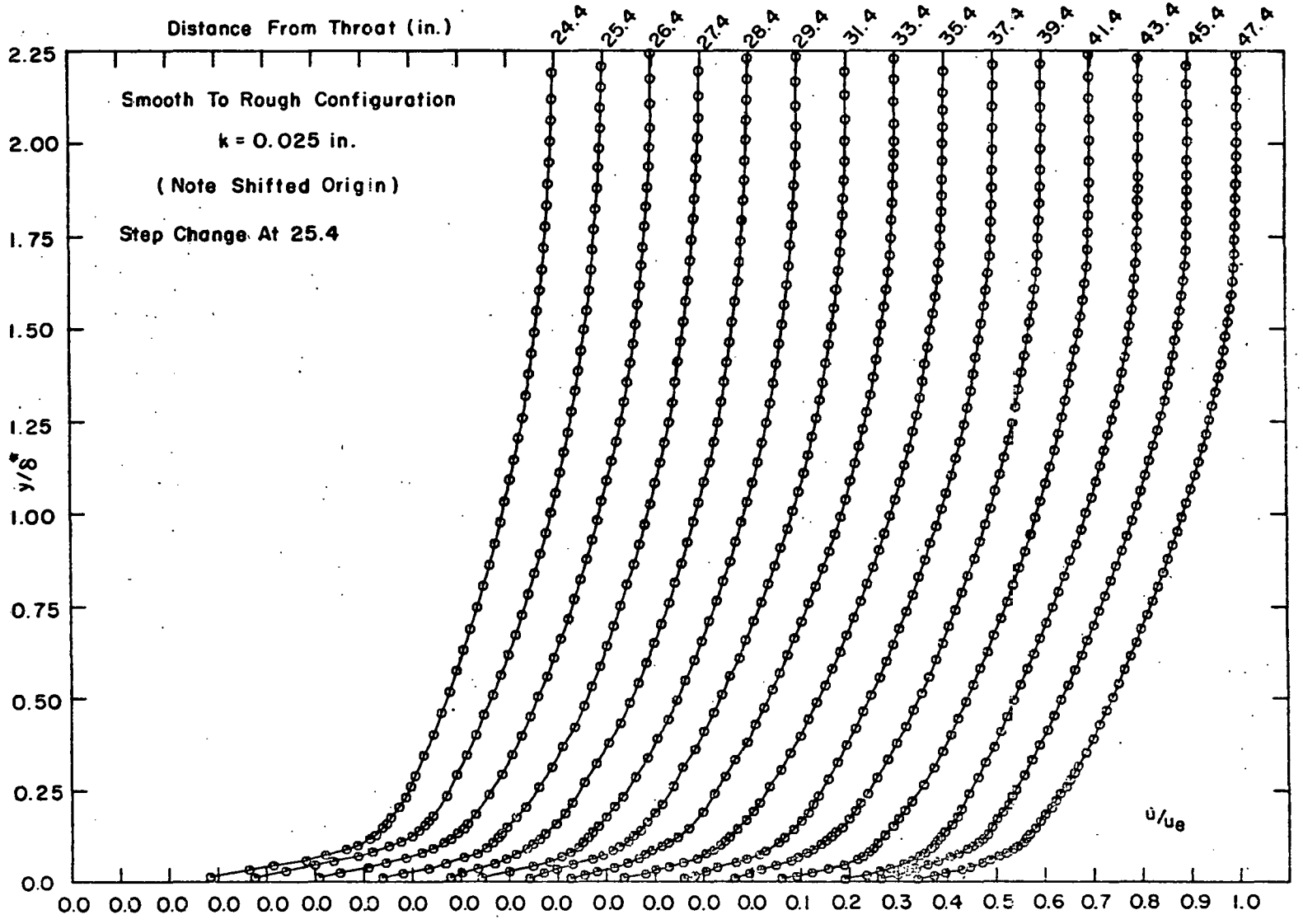

FIG.16 VELOCITY PROFILES

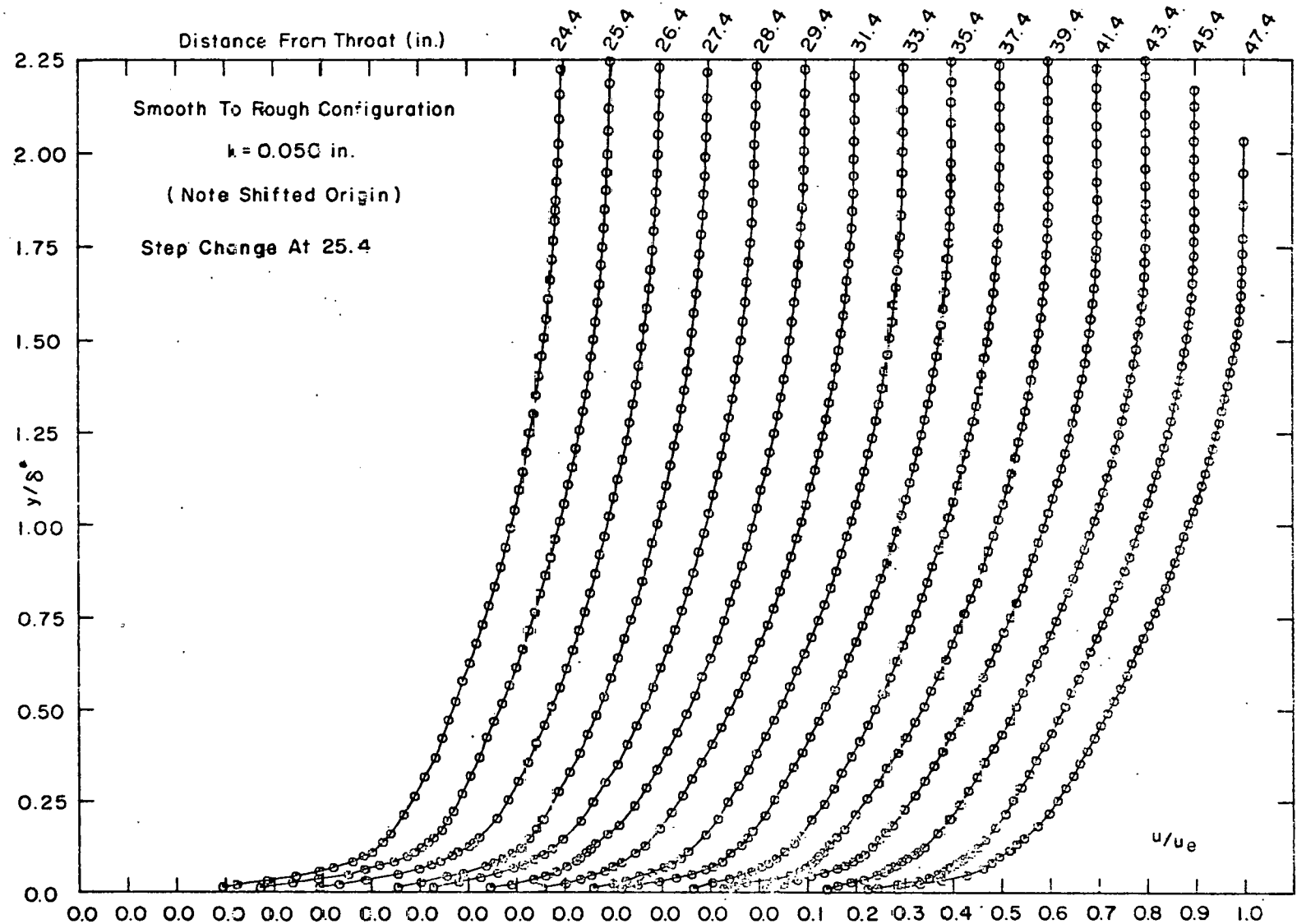

FIG.16 VELOCITY PROFILES

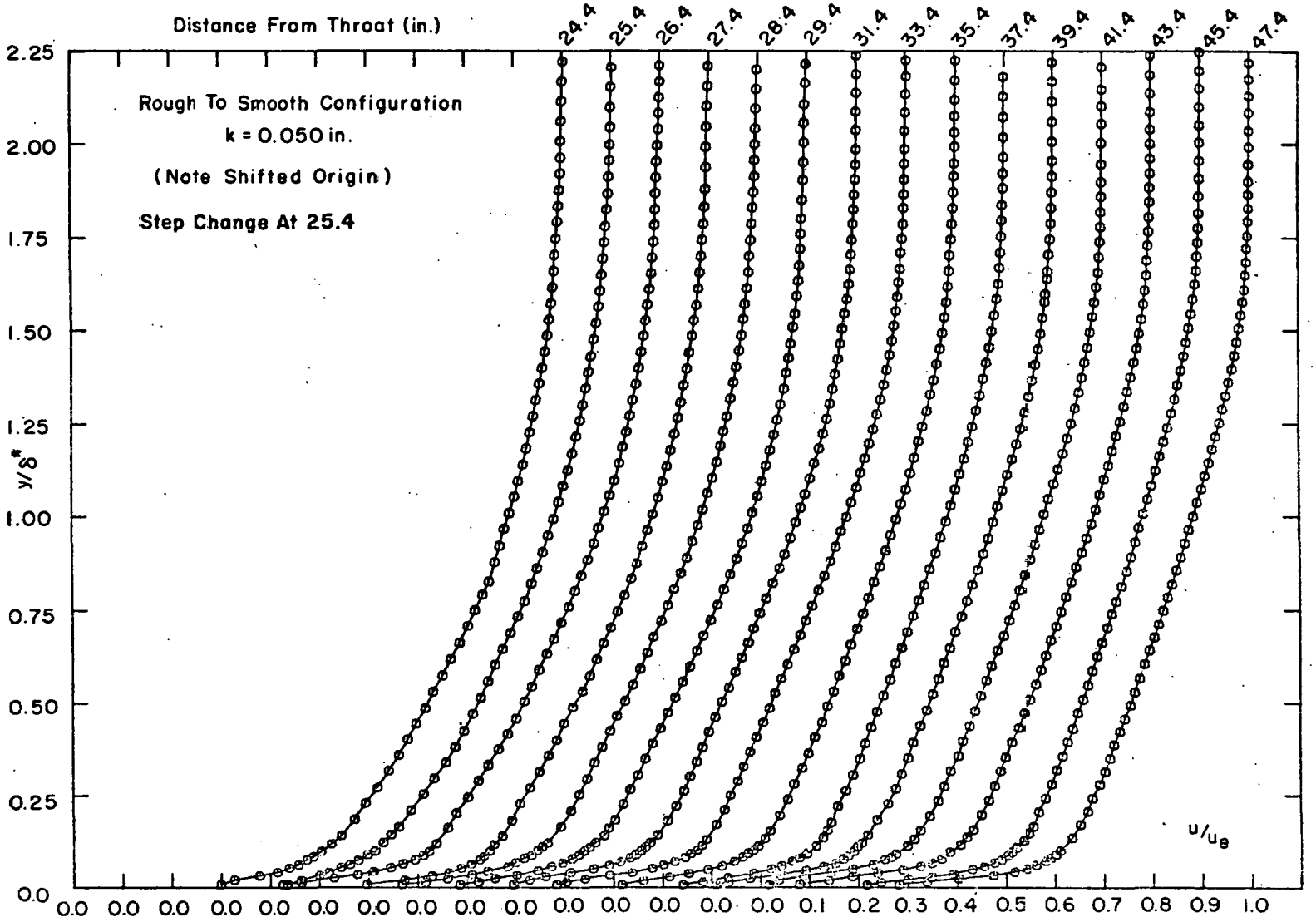

FIG. 16 VELOCITY PROFILES

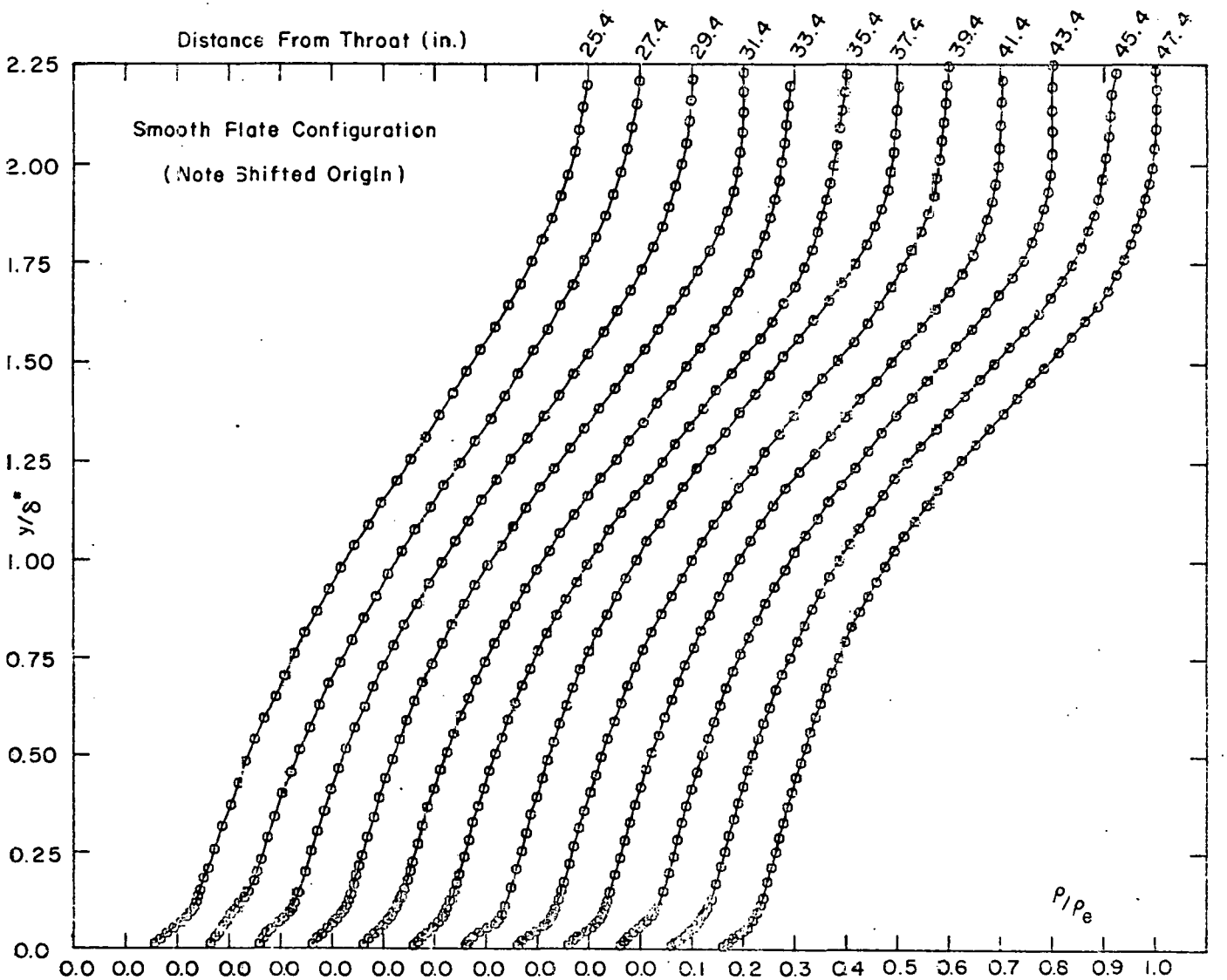

FIG. 17 DENSITY PROFILES

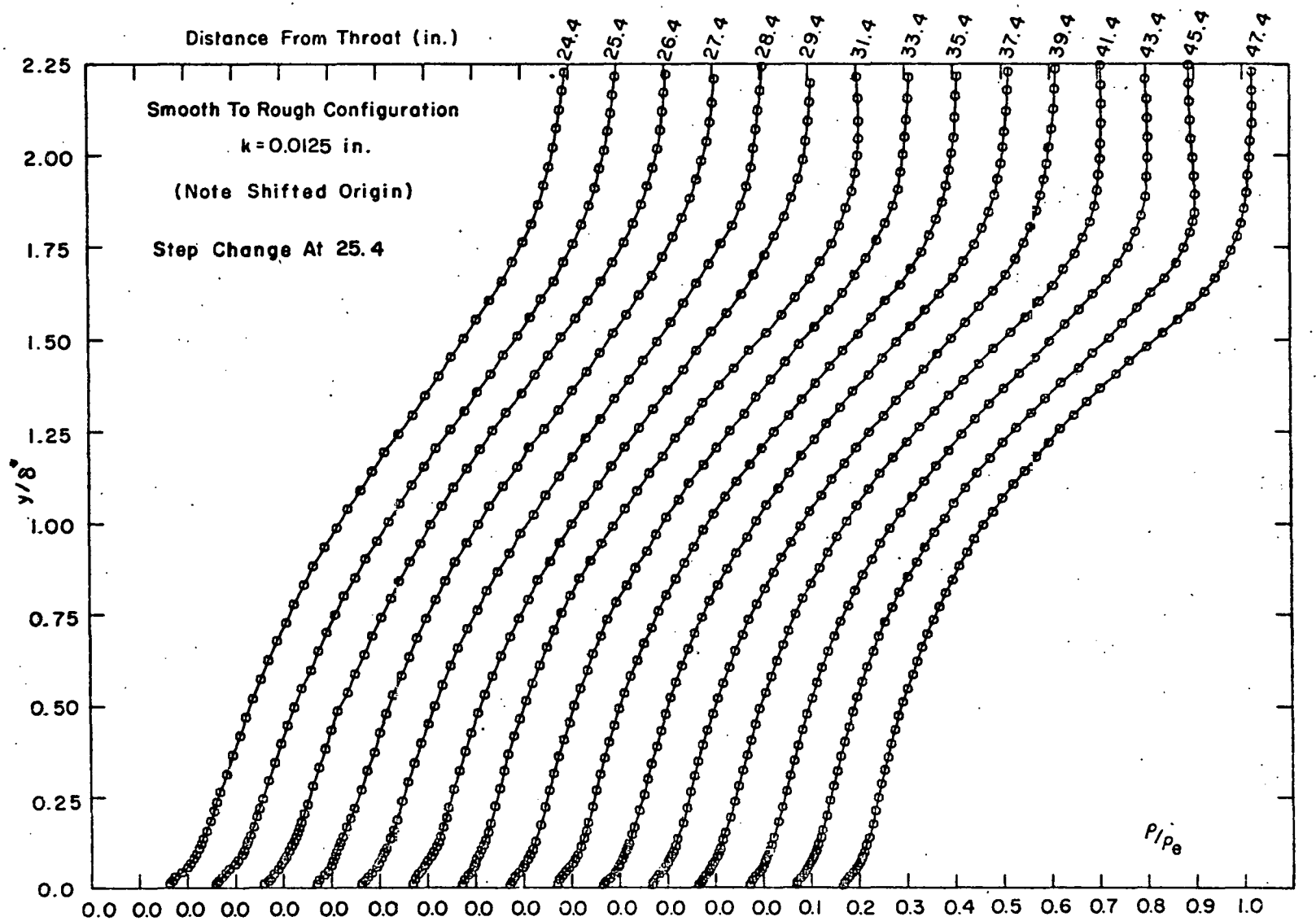

FIG. 17 DENSITY PROFILES

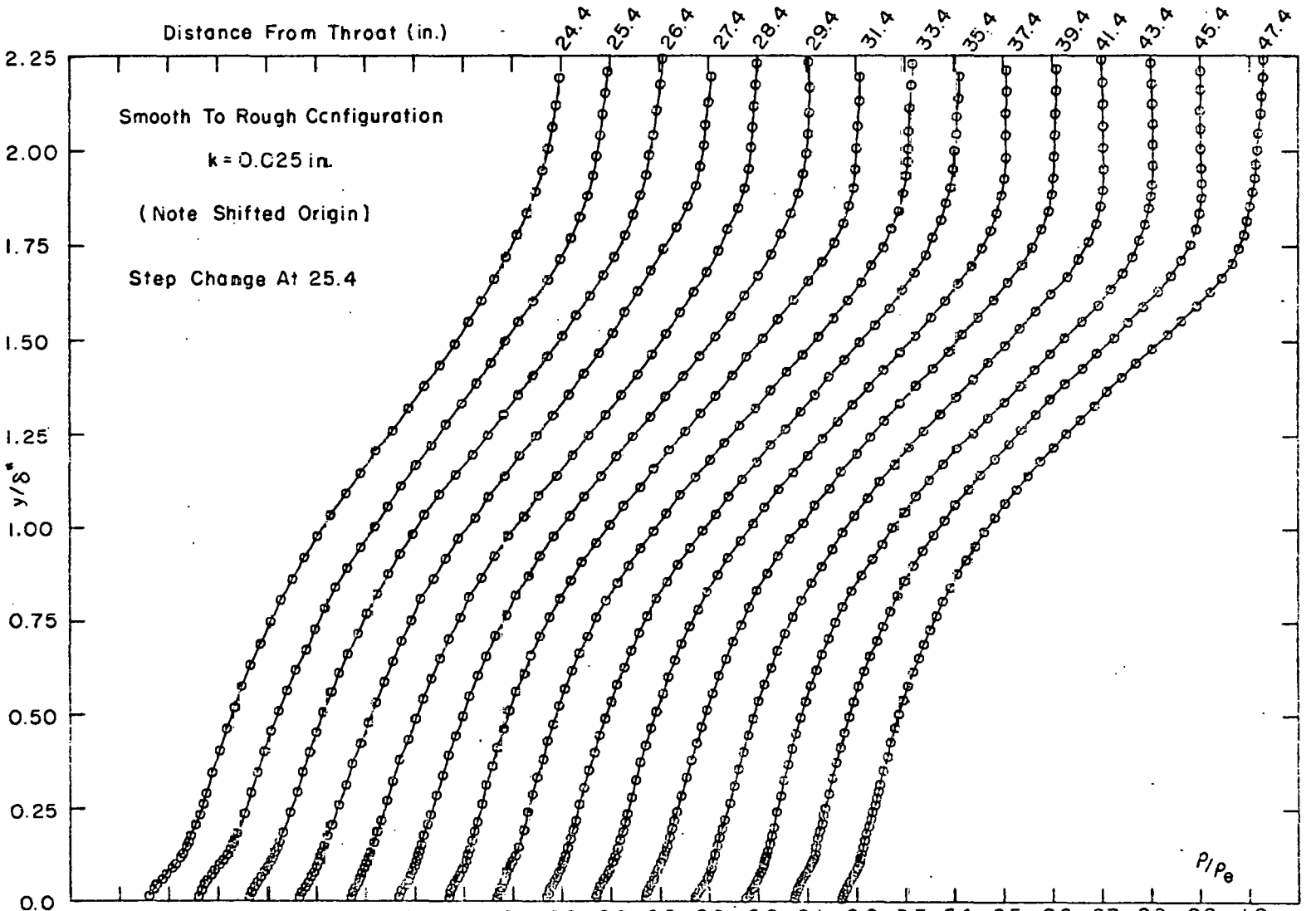

FIG. 17 DENSITY PROFILES

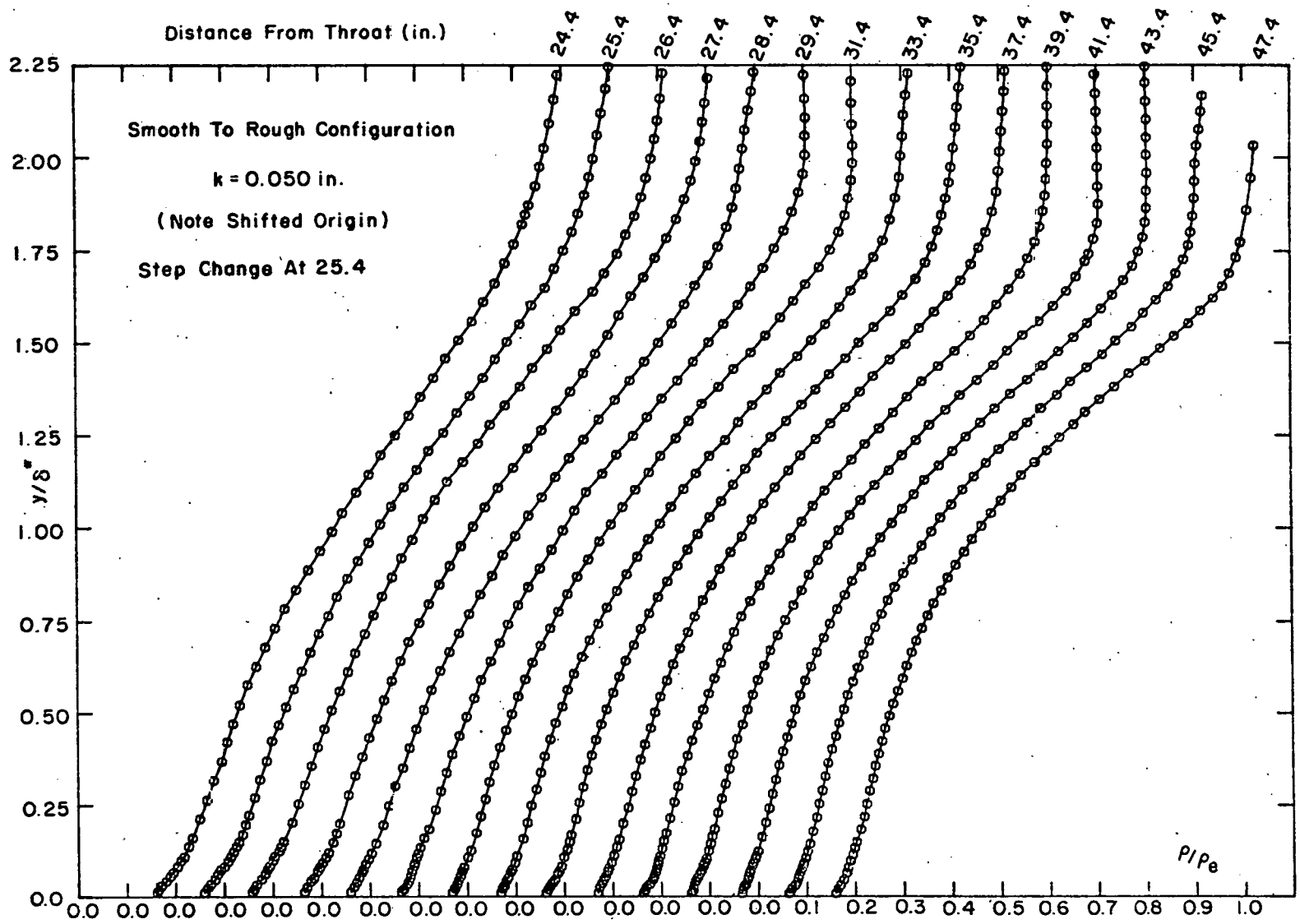

FIG. 17 DENSITY PROFILES

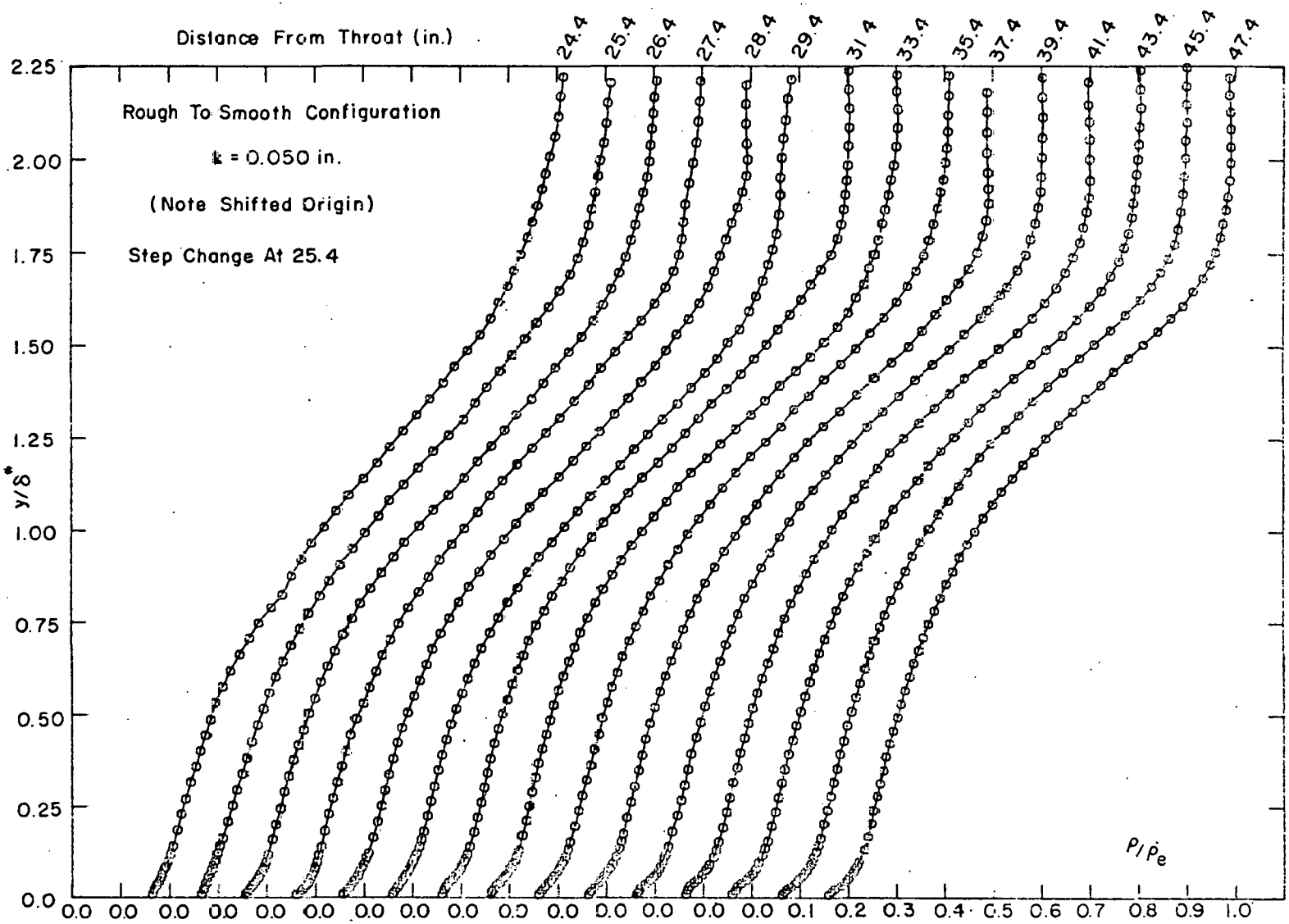

FIG.17 DENSITY PROFILES

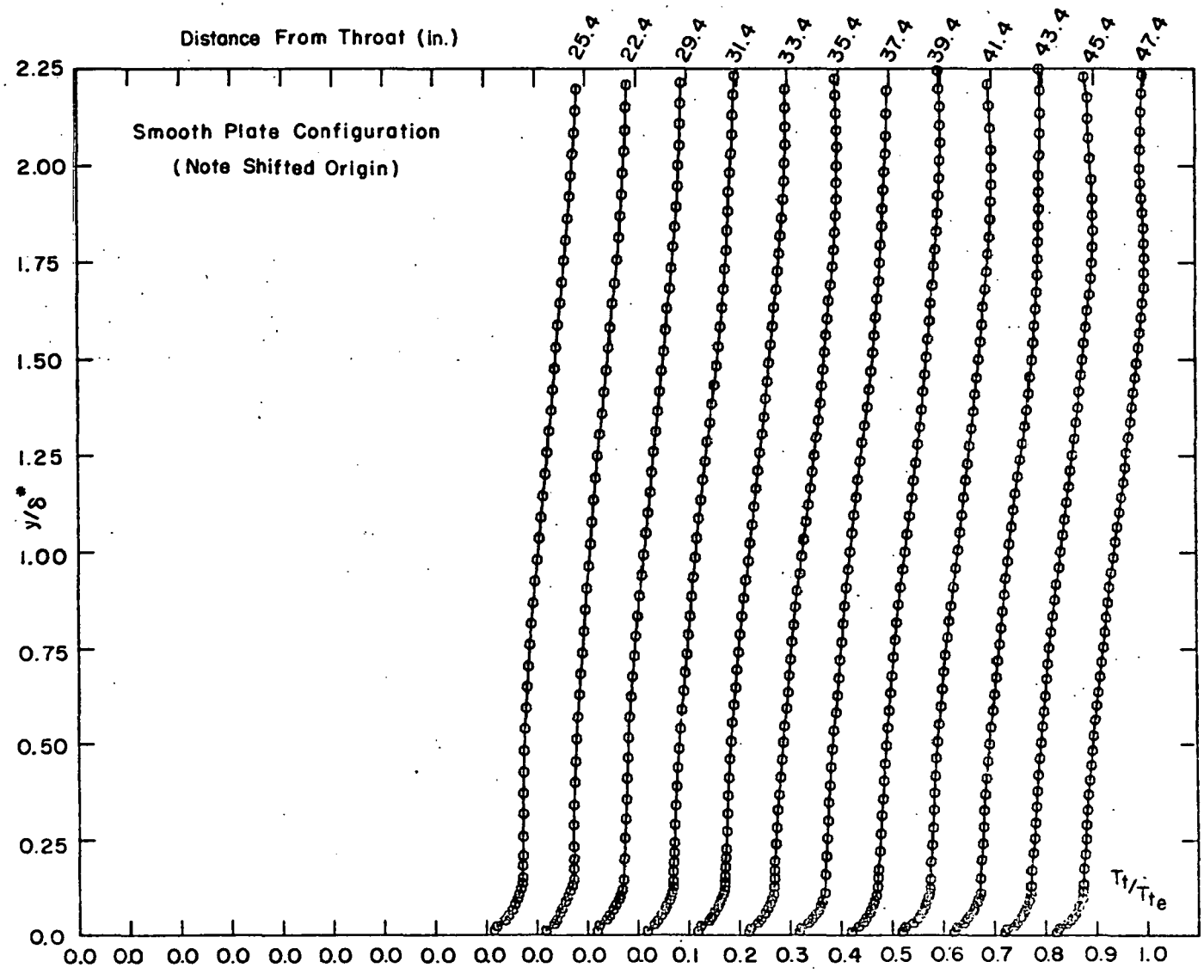

FIG. 18 TOTAL TEMPERATURE PROFILES

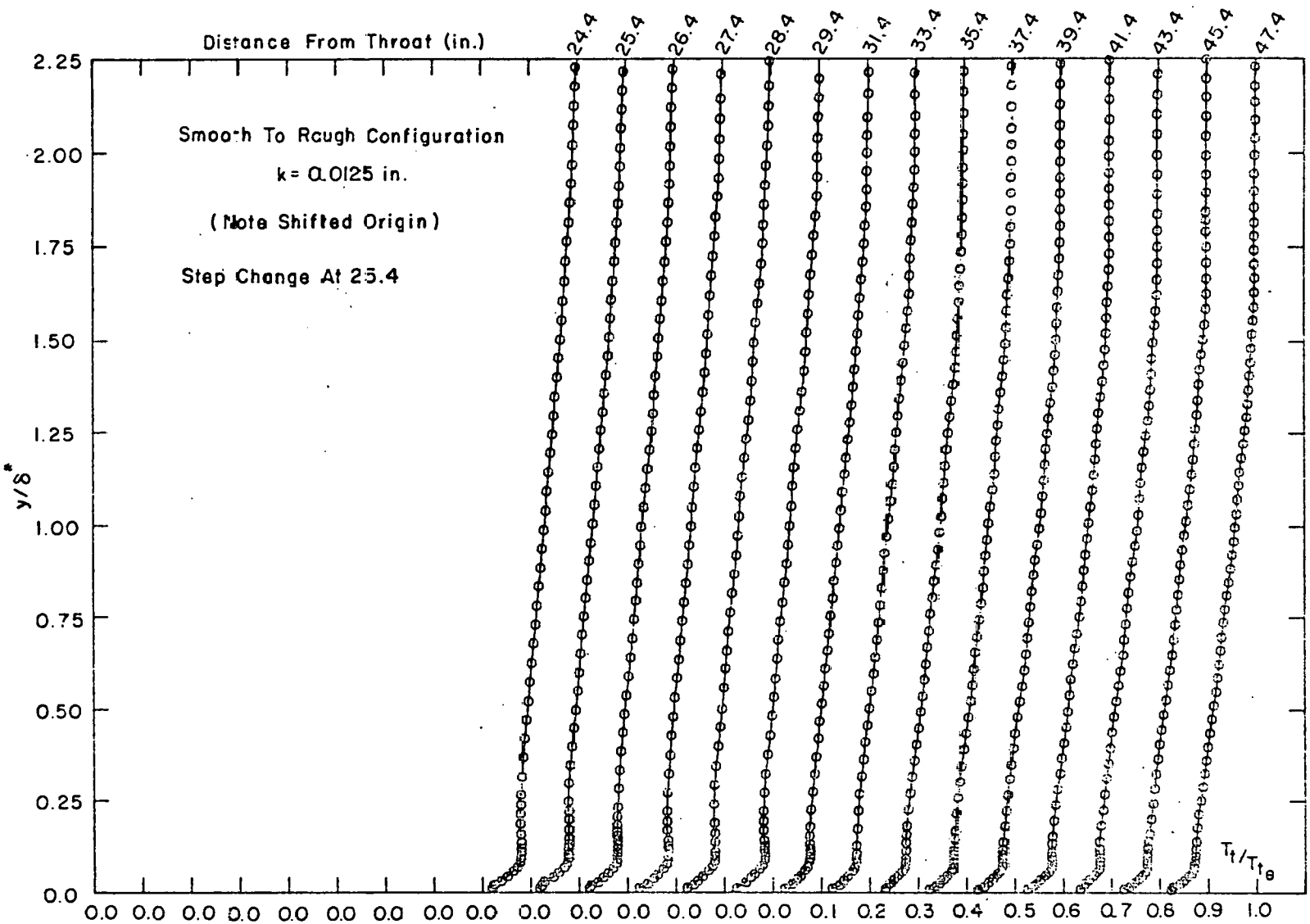

FIG. 18 TOTAL TEMPERATURE PROFILES

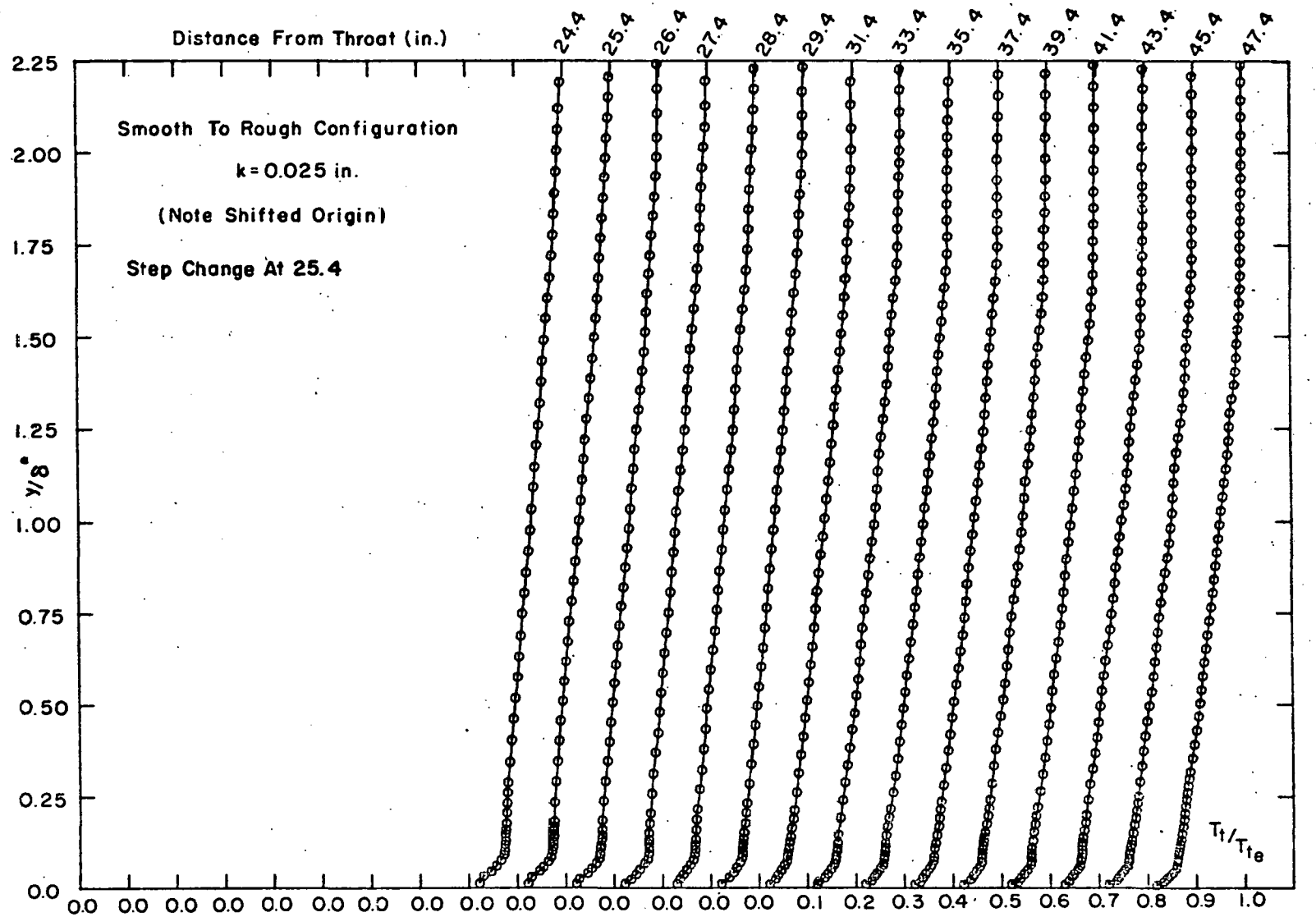

FIG. 18 TOTAL TEMPERATURE PROFILES

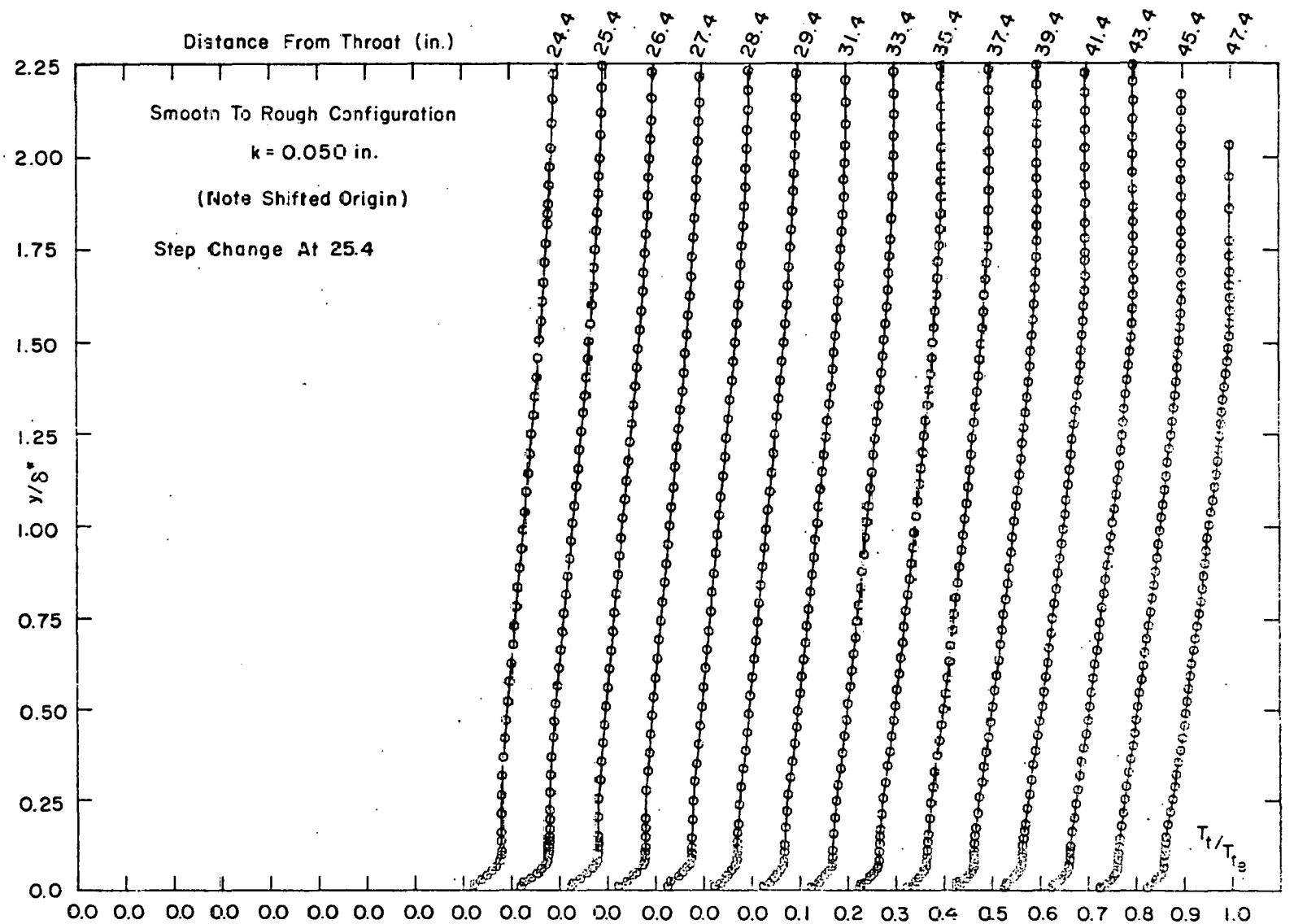

FIG. 18 TOTAL TEMPERATURE PROFILES

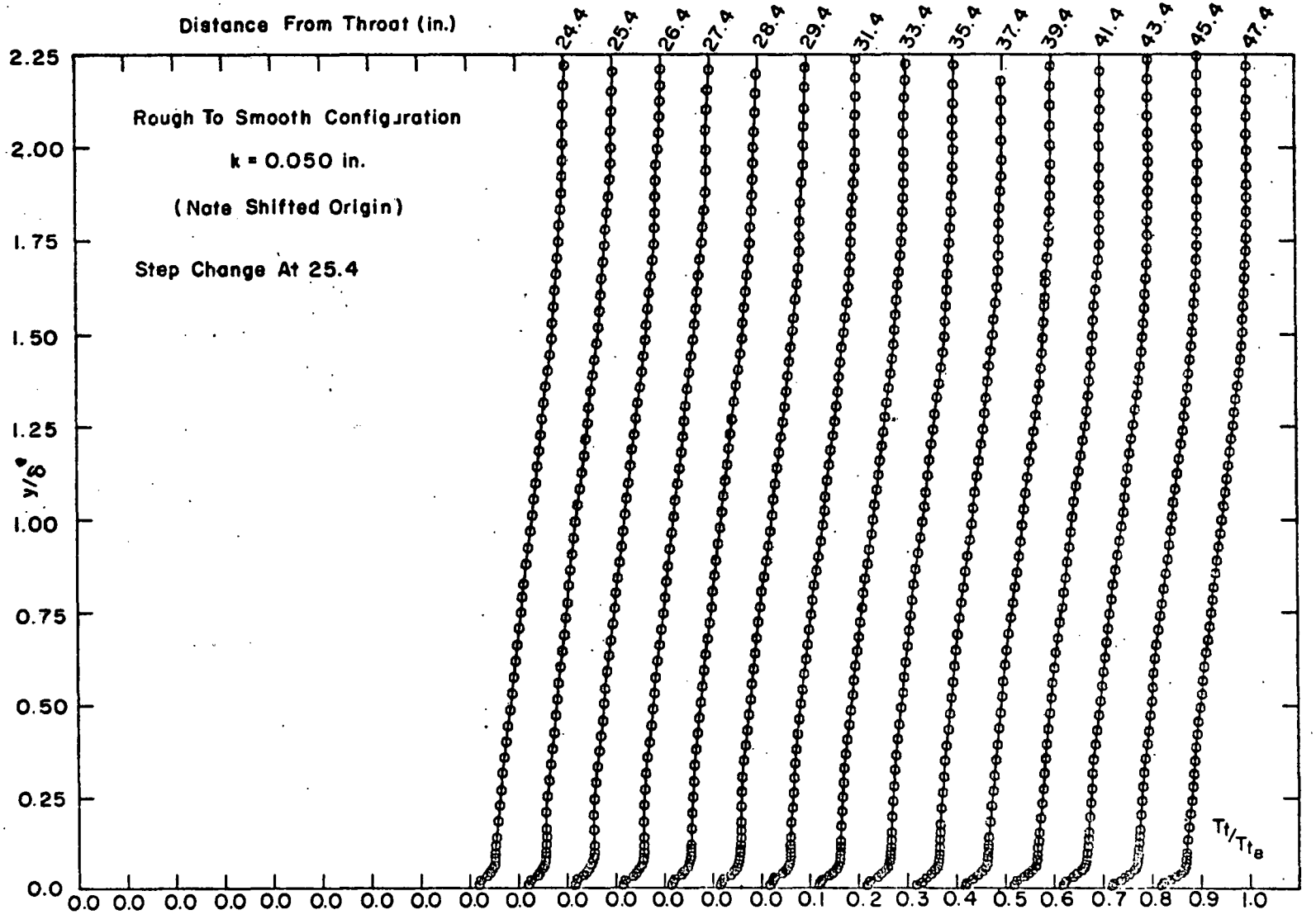

FIG. 18 TOTAL TEMPERATURE PROFILES

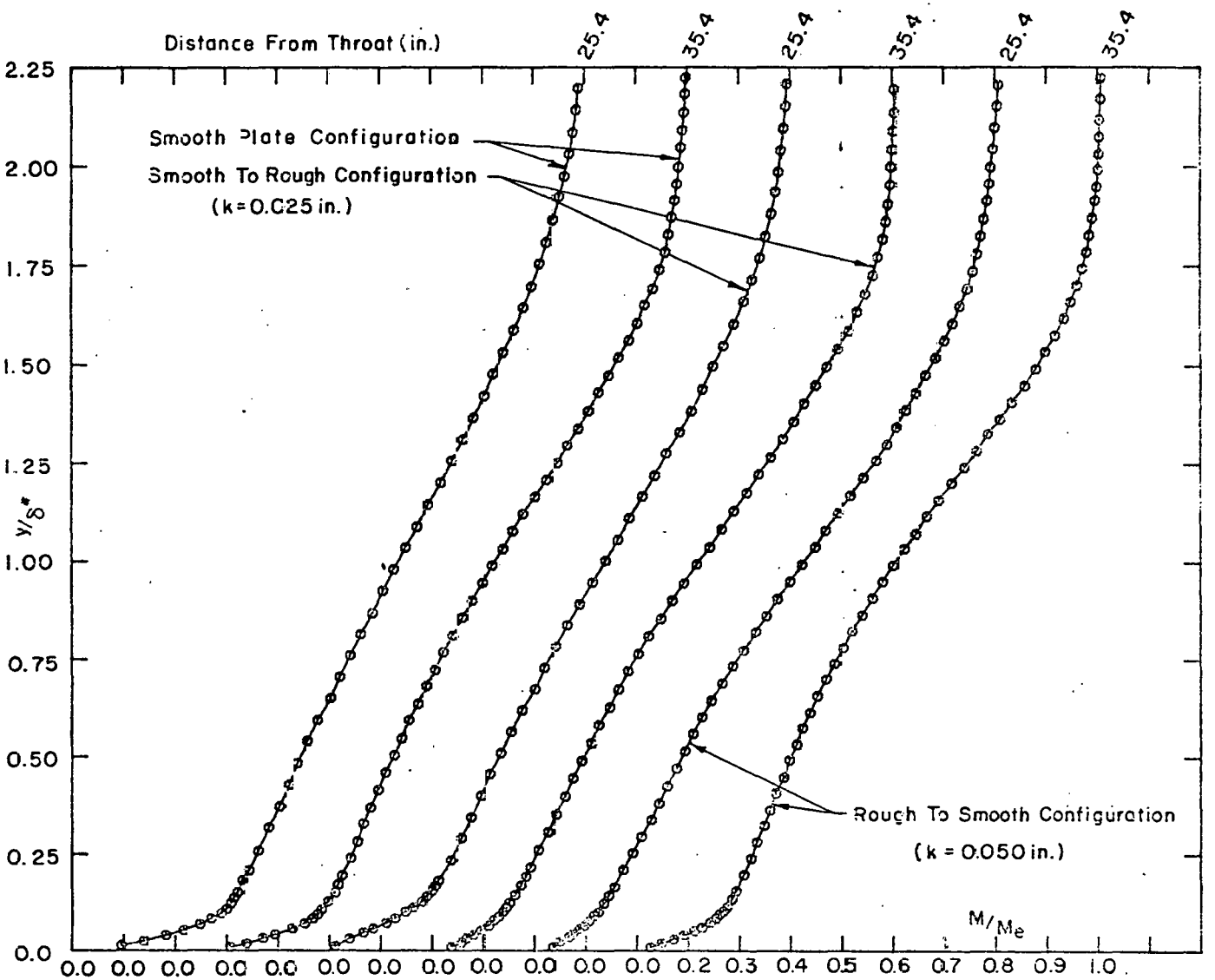

FIG. 19 MACH NUMBER PROFILES

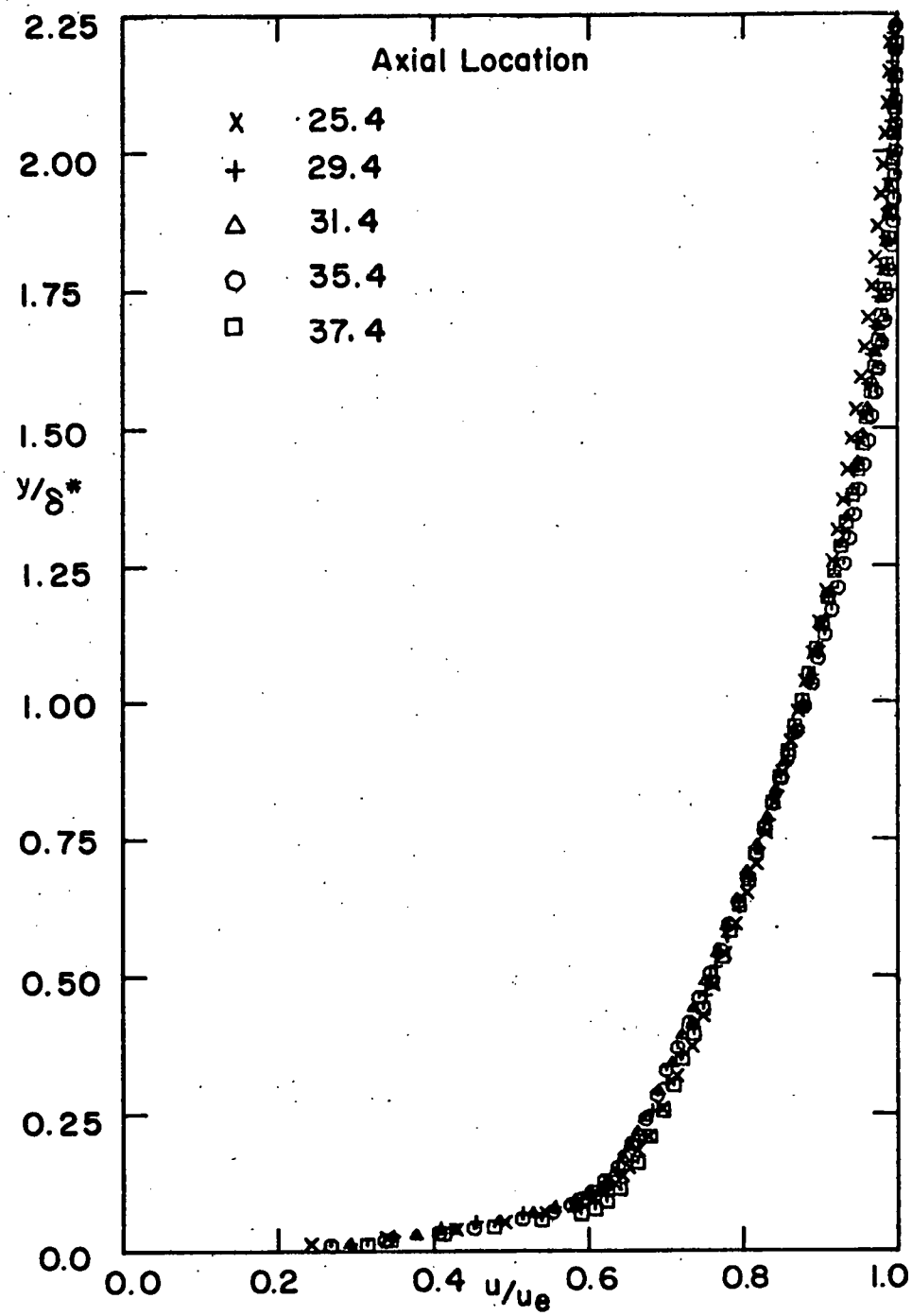

FIG. 20 SMOOTH PLATE VELOCITY PROFILES

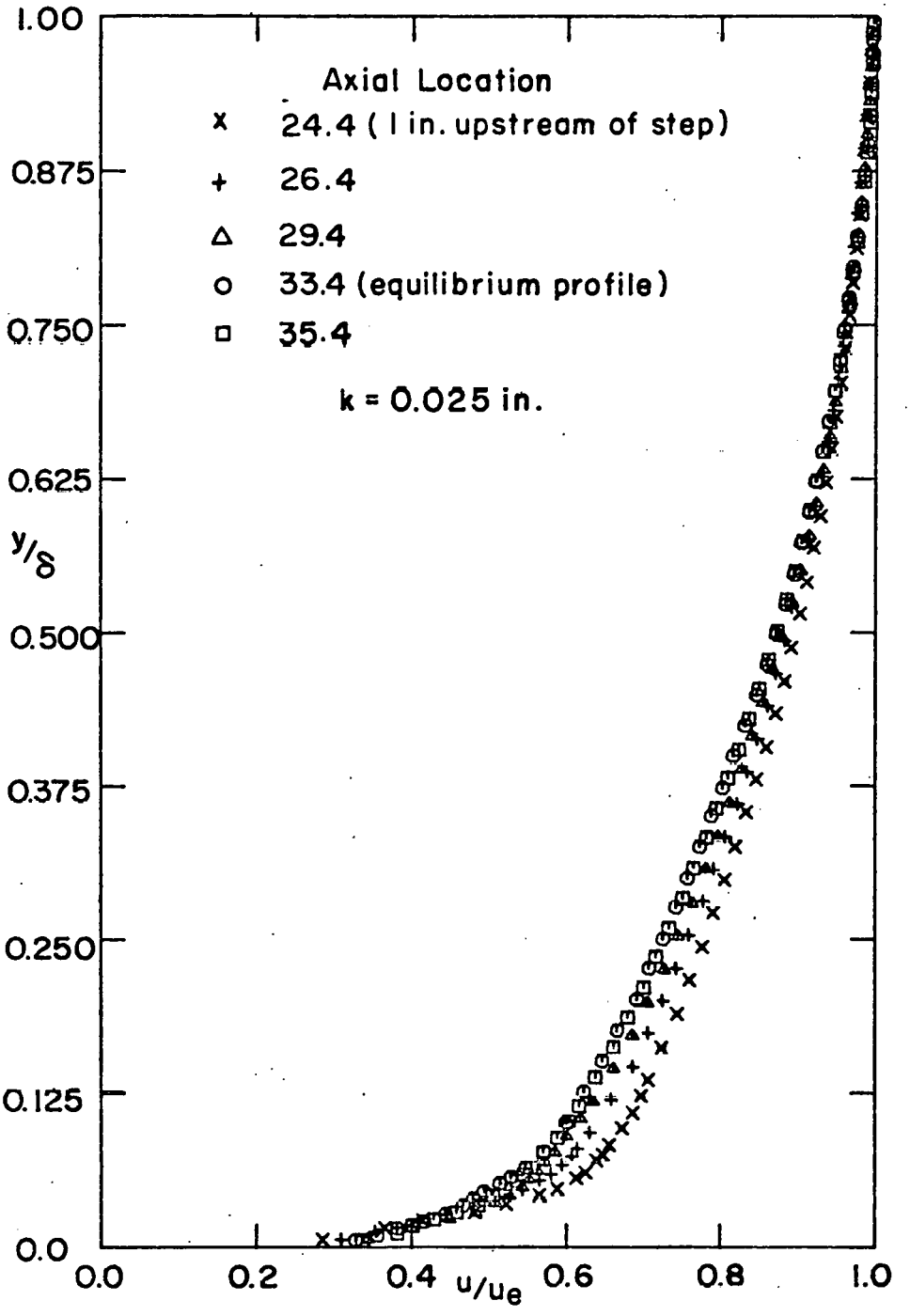

FIG.21 RESPONSE OF SMOOTH WALL BOUNDARY LAYER TO ROUGH WALL CONDITIONS (a) VELOCITY PROFILES

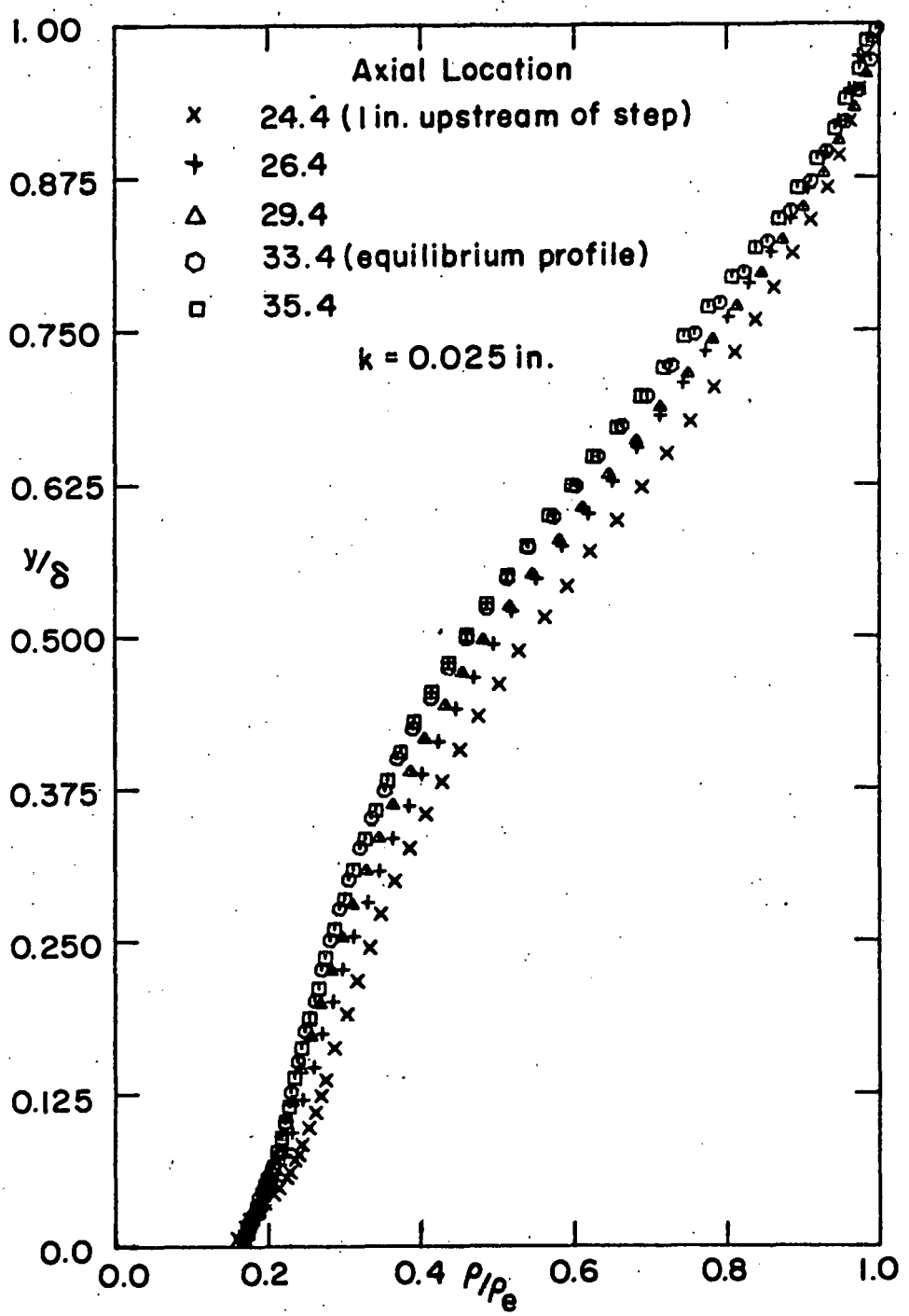

FIG.21 RESPONSE OF SMOOTH WALL BOUNDARY LAYER TO ROUGH WALL CONDITIONS(b)DENSITY PROFILES

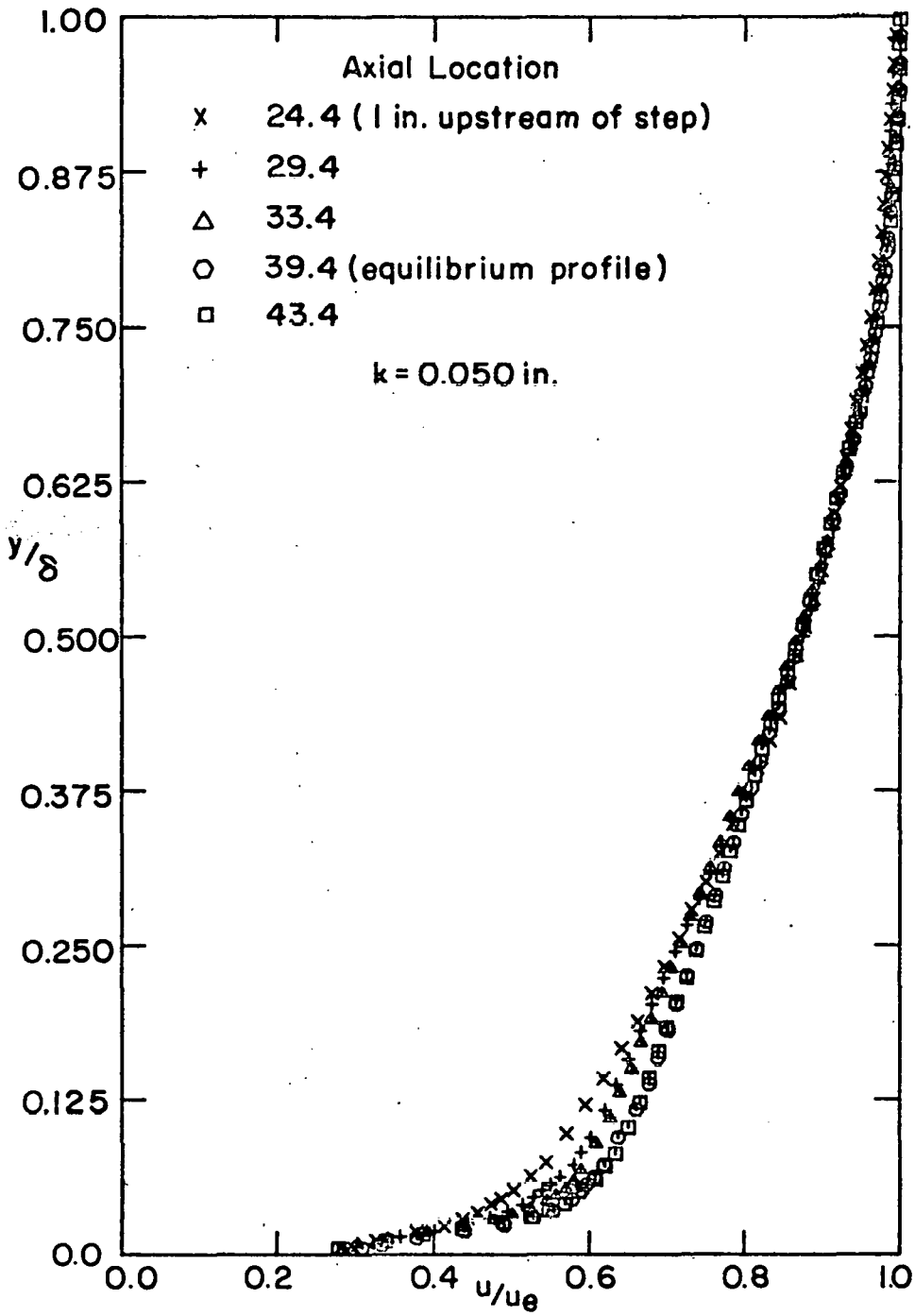

FIG.22 RESPONSE OF ROUGH WALL BOUNDARY LAYER TO SMOOTH WALL CONDITIONS (a) VELOCITY PROFILES

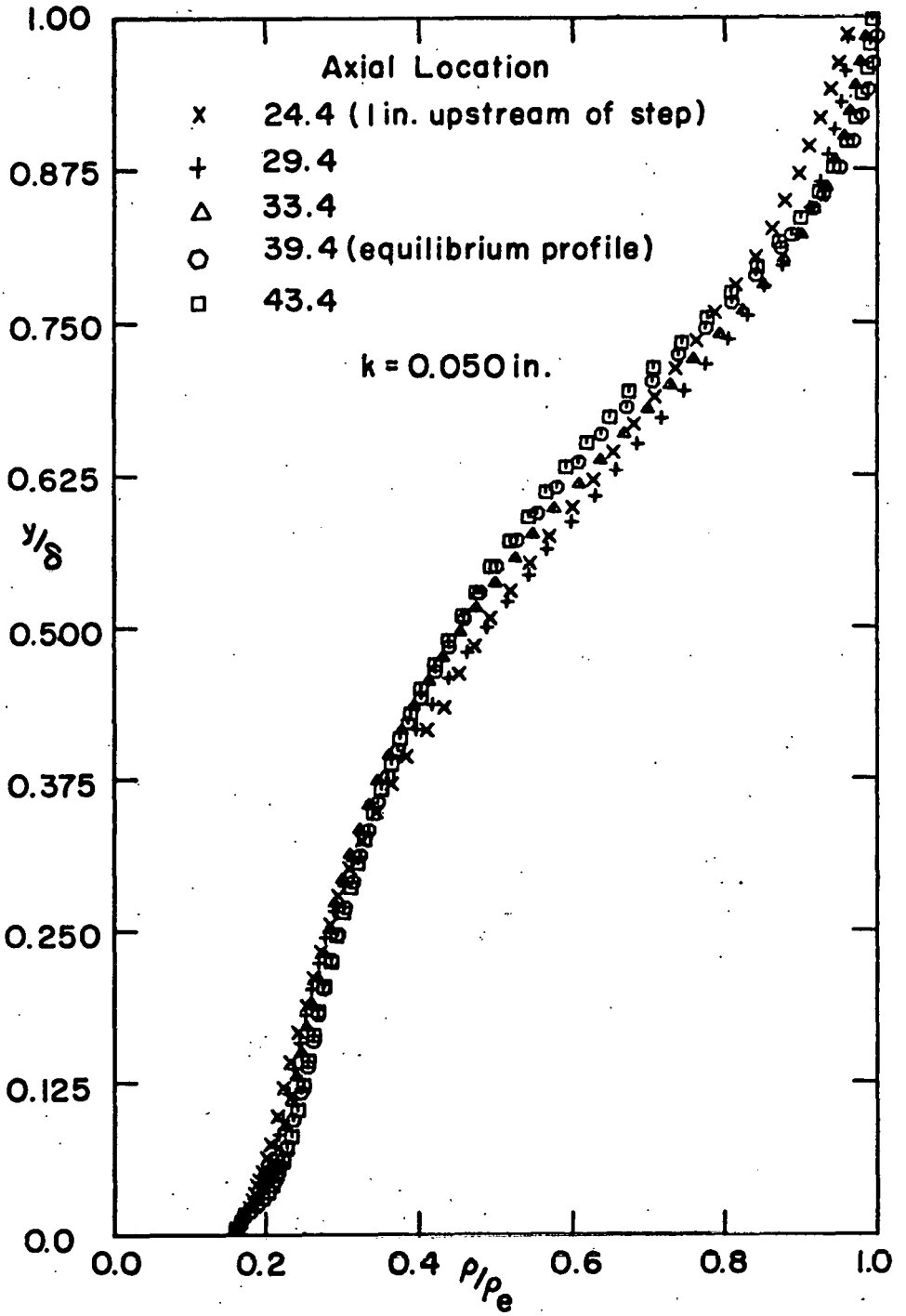

FIG.22 RESPONSE OF ROUGH WALL BOUNDARY LAYER TO SMOOTH WALL CONDITIONS (b) DENSITY PROFILES

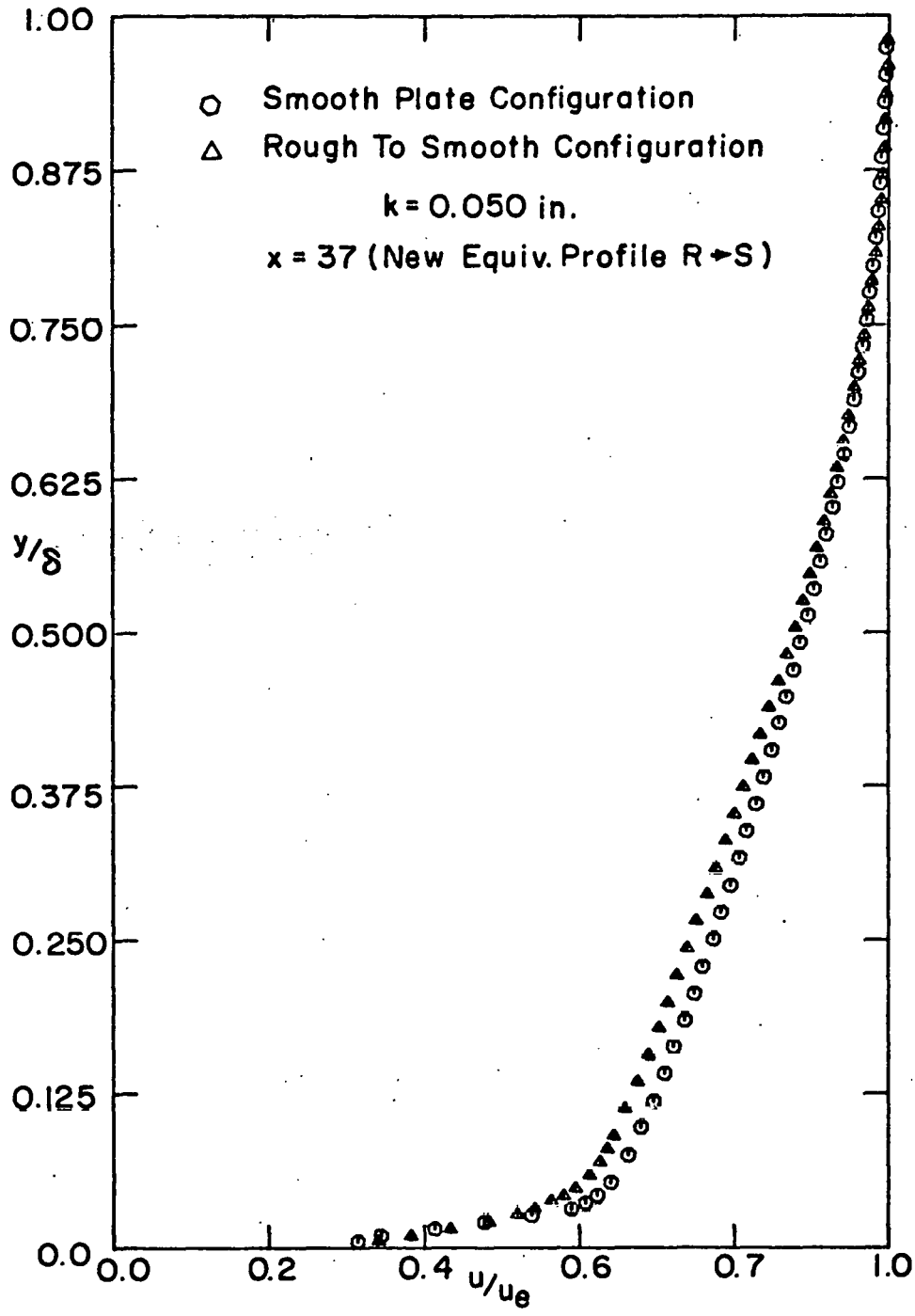

FIG.23EQUILIBRIUM SMOOTH WALL PROFILE DATA
(a) VELOCITY PROFILES

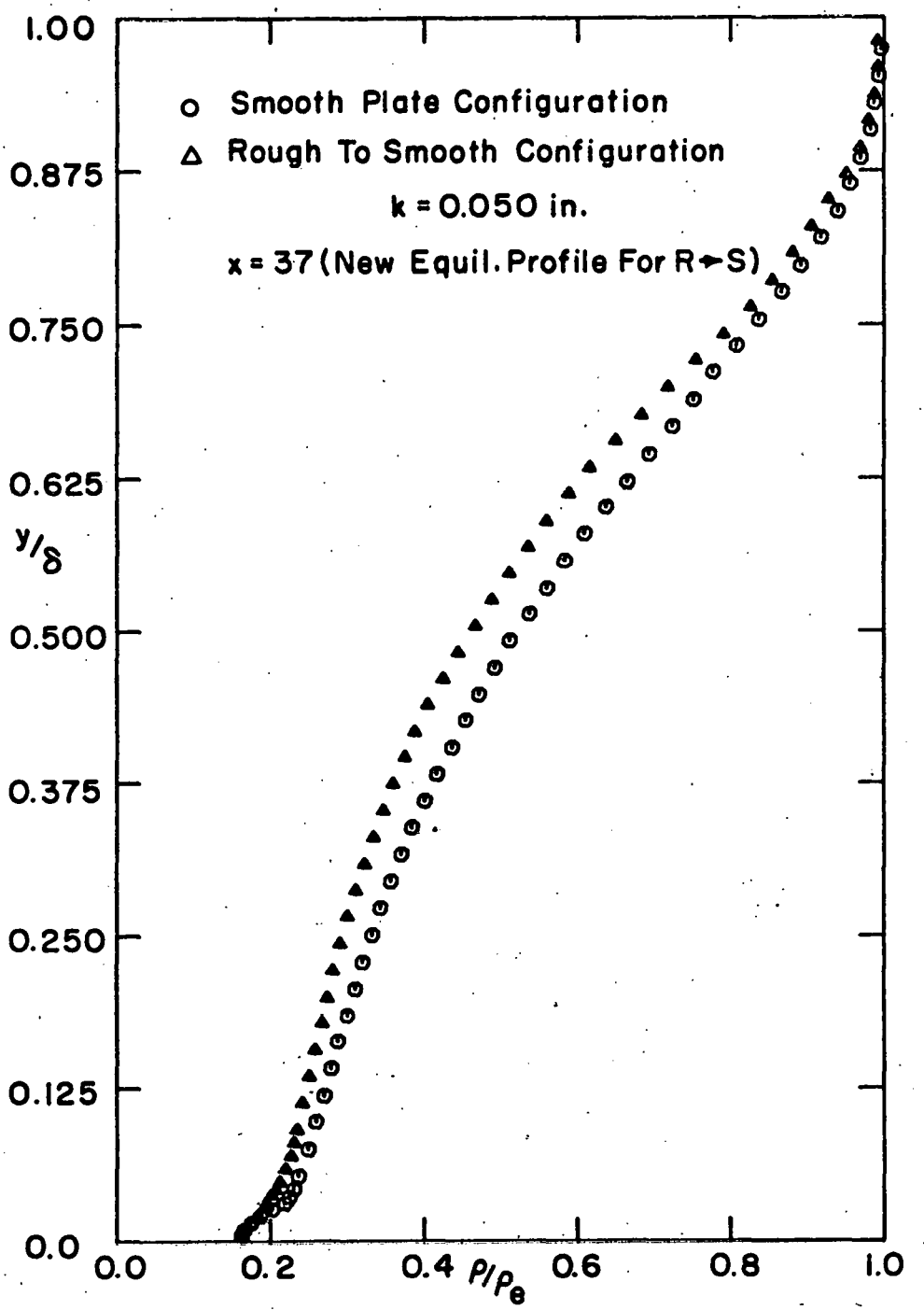

FIG.23 EQUILIBRIUM SMOOTH WALL PROFILE DATA
(b) DENSITY PROFILES

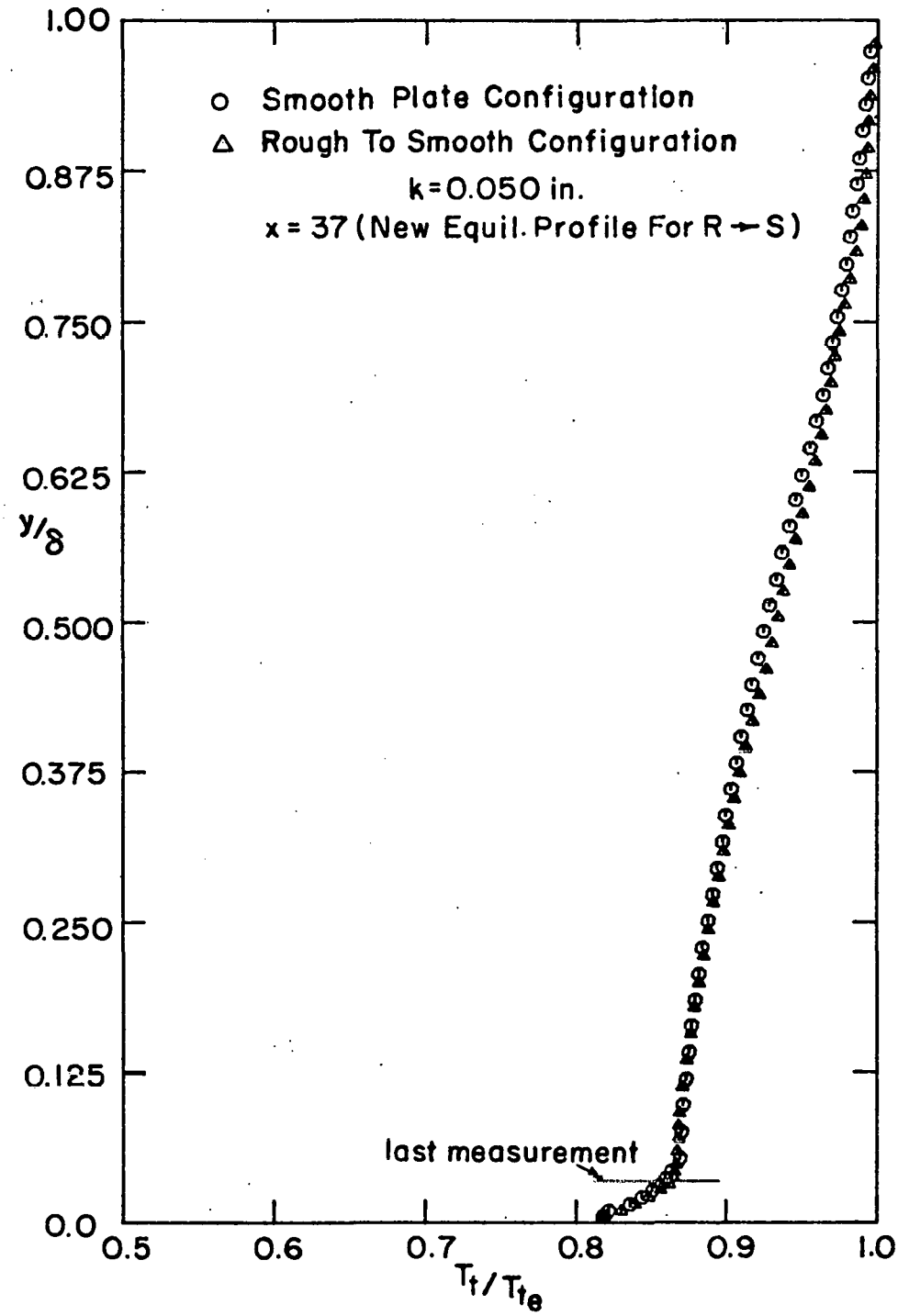

FIG.23 EQUILIBRIUM SMOOTH WALL PROFILE DATA
(c) TOTAL TEMPERATURE PROFILES

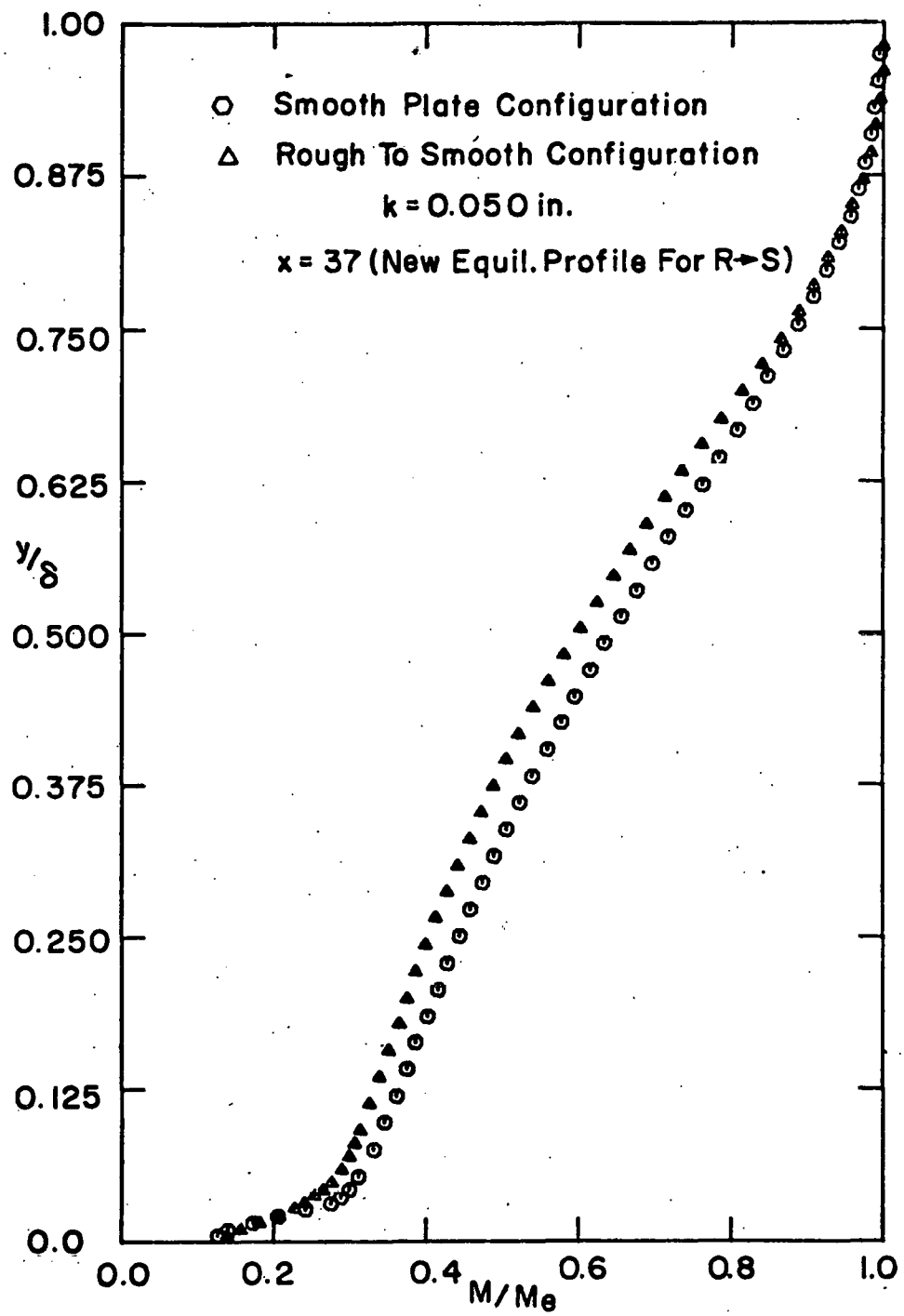

FIG.23 EQUILIBRIUM SMOOTH WALL PROFILE DATA
(d) MACH NUMBER PROFILES

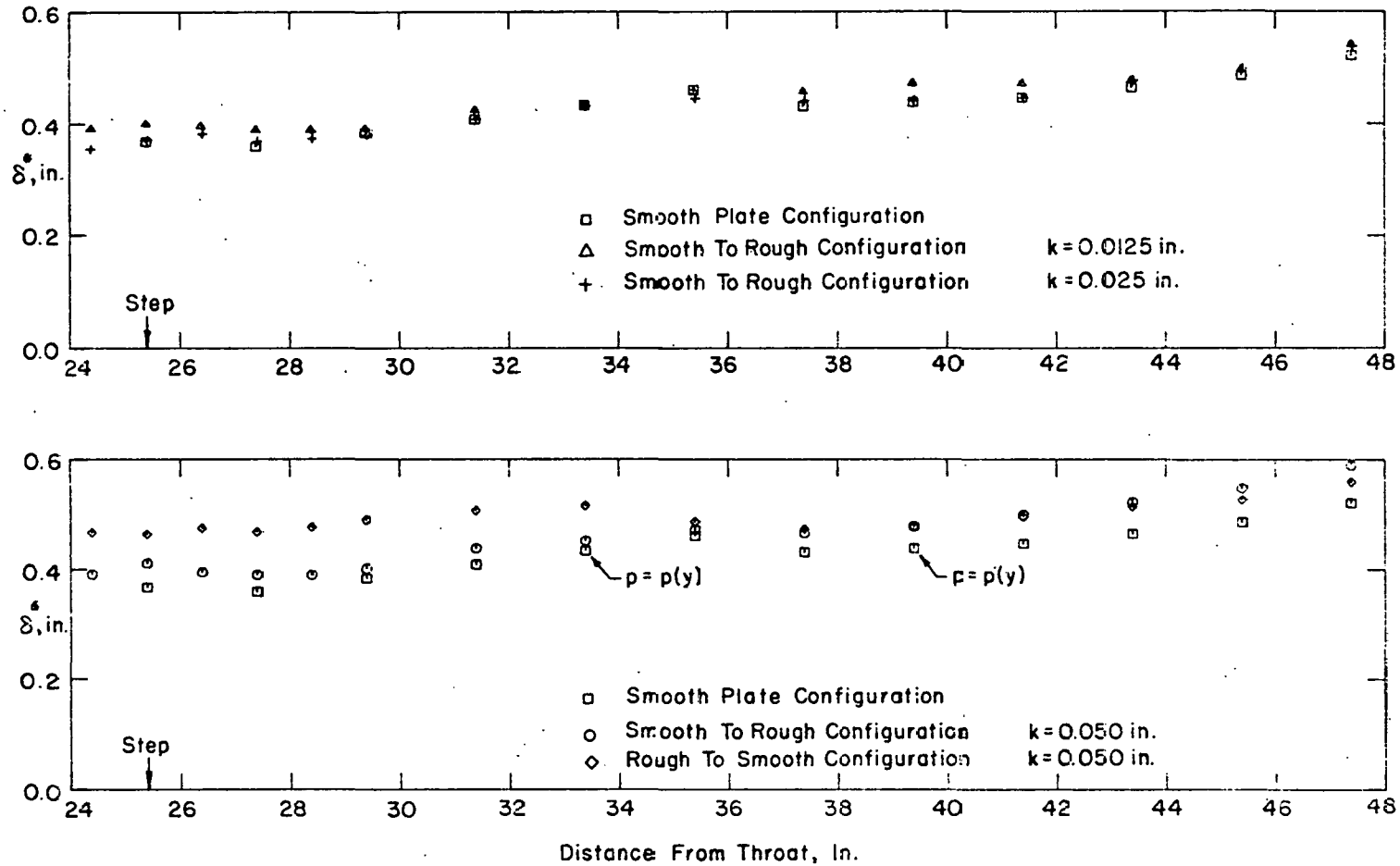

FIG. 24 AXIAL DISTRIBUTION OF DISPLACEMENT THICKNESS

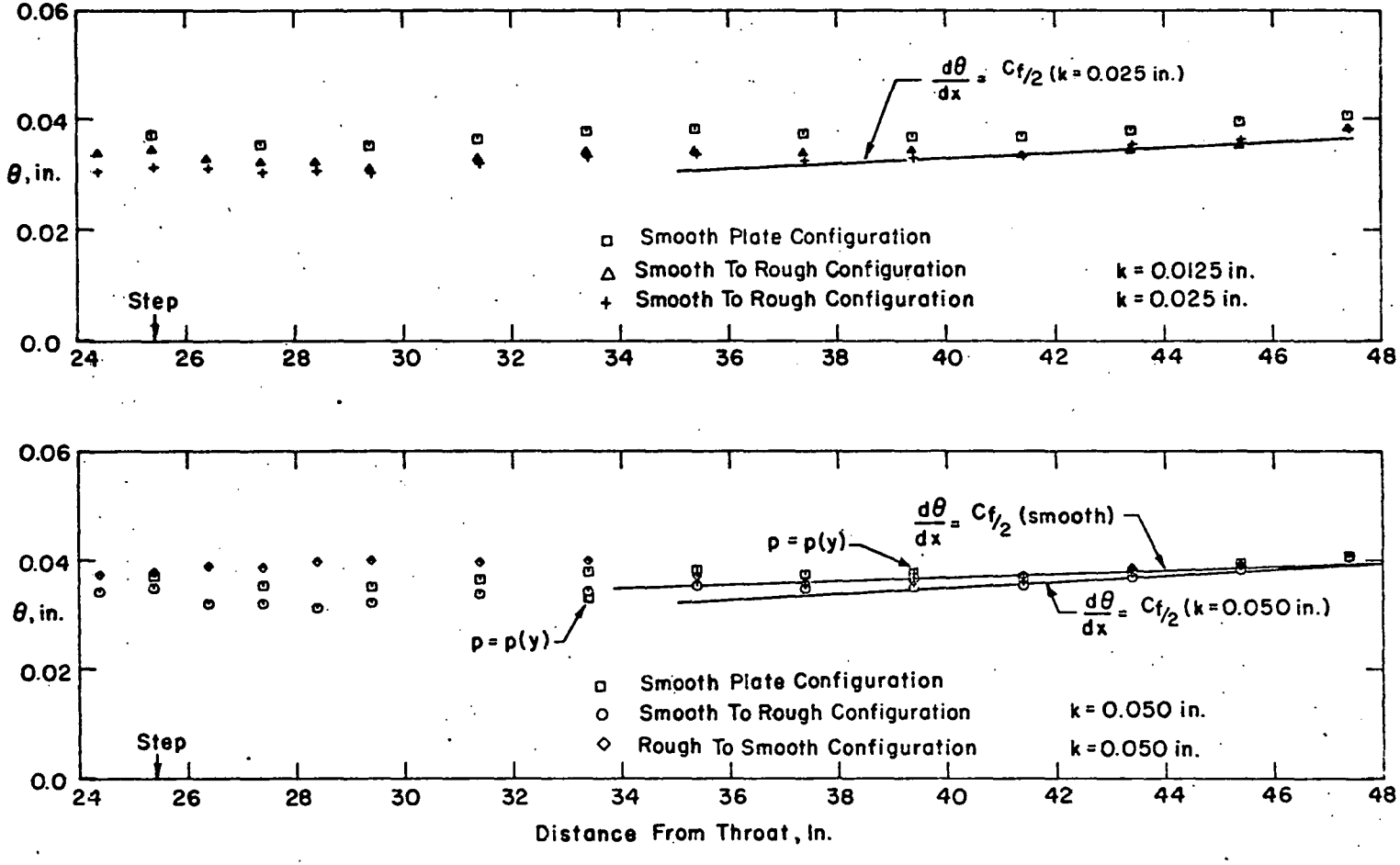

FIG. 25 AXIAL DISTRIBUTION OF MOMENTUM THICKNESS

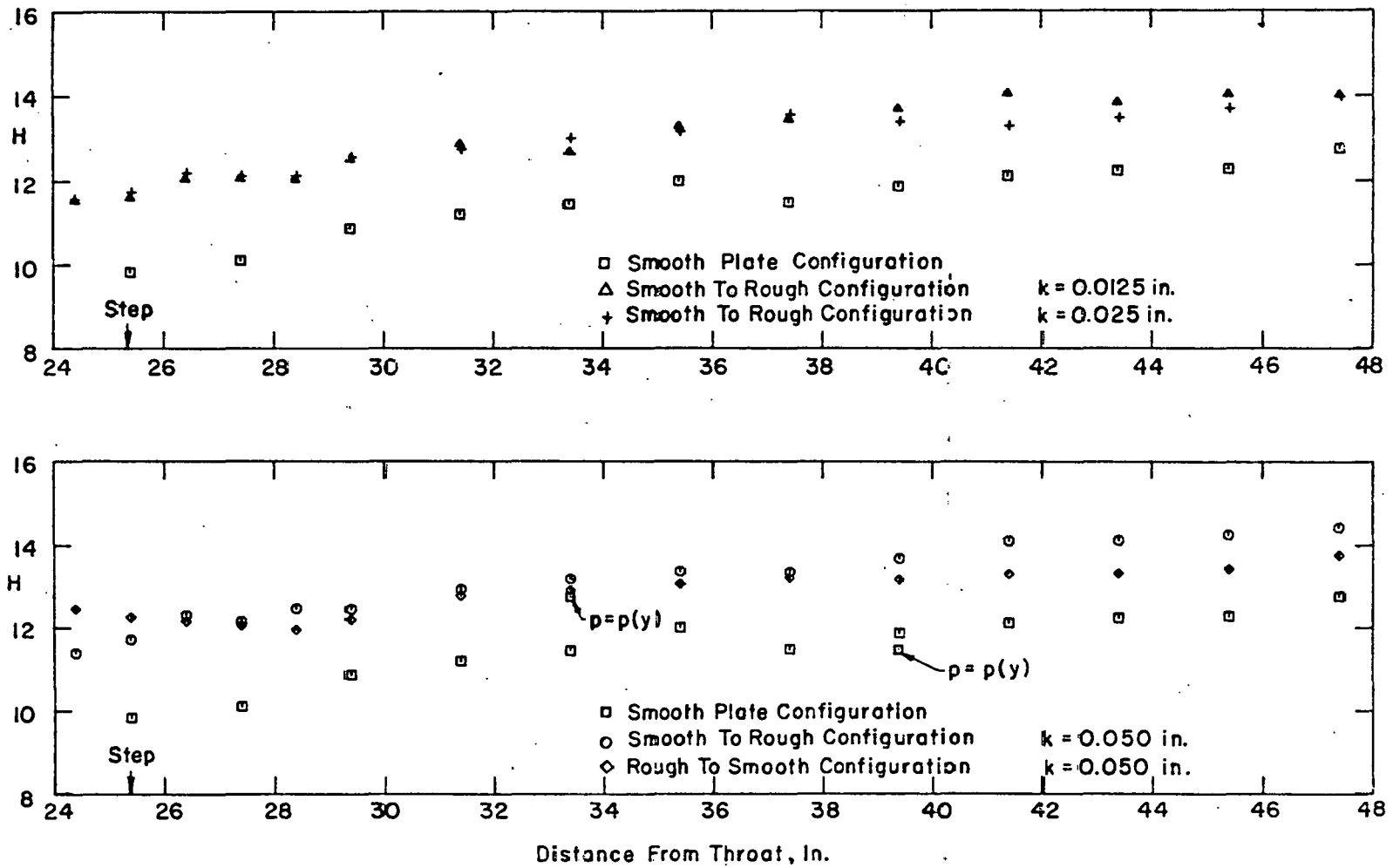

FIG. 26 AXIAL DISTRIBUTION OF SHAPE FACTOR

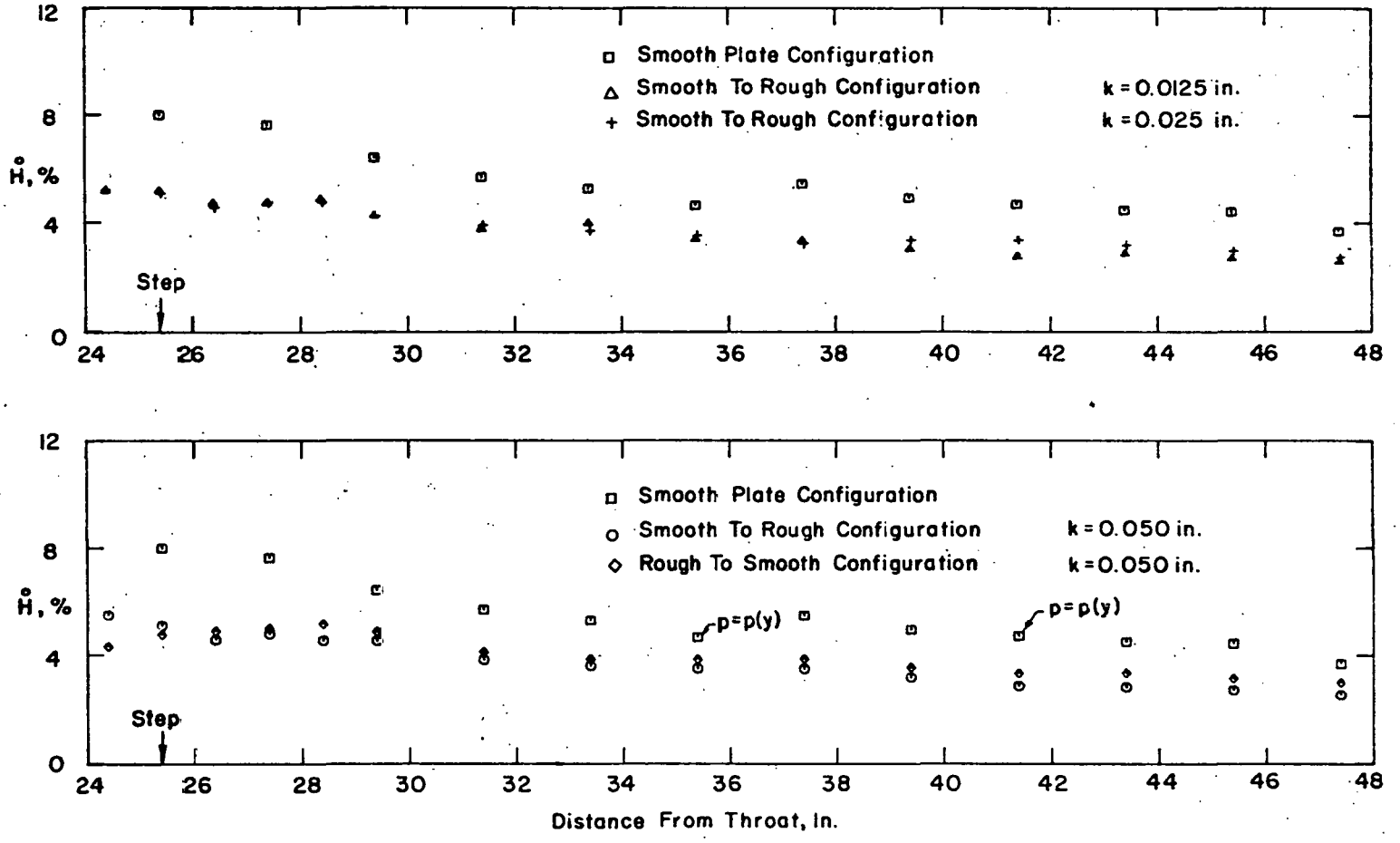

FIG.27 AXIAL DISTRIBUTION OF ENTHALPHY FLUX

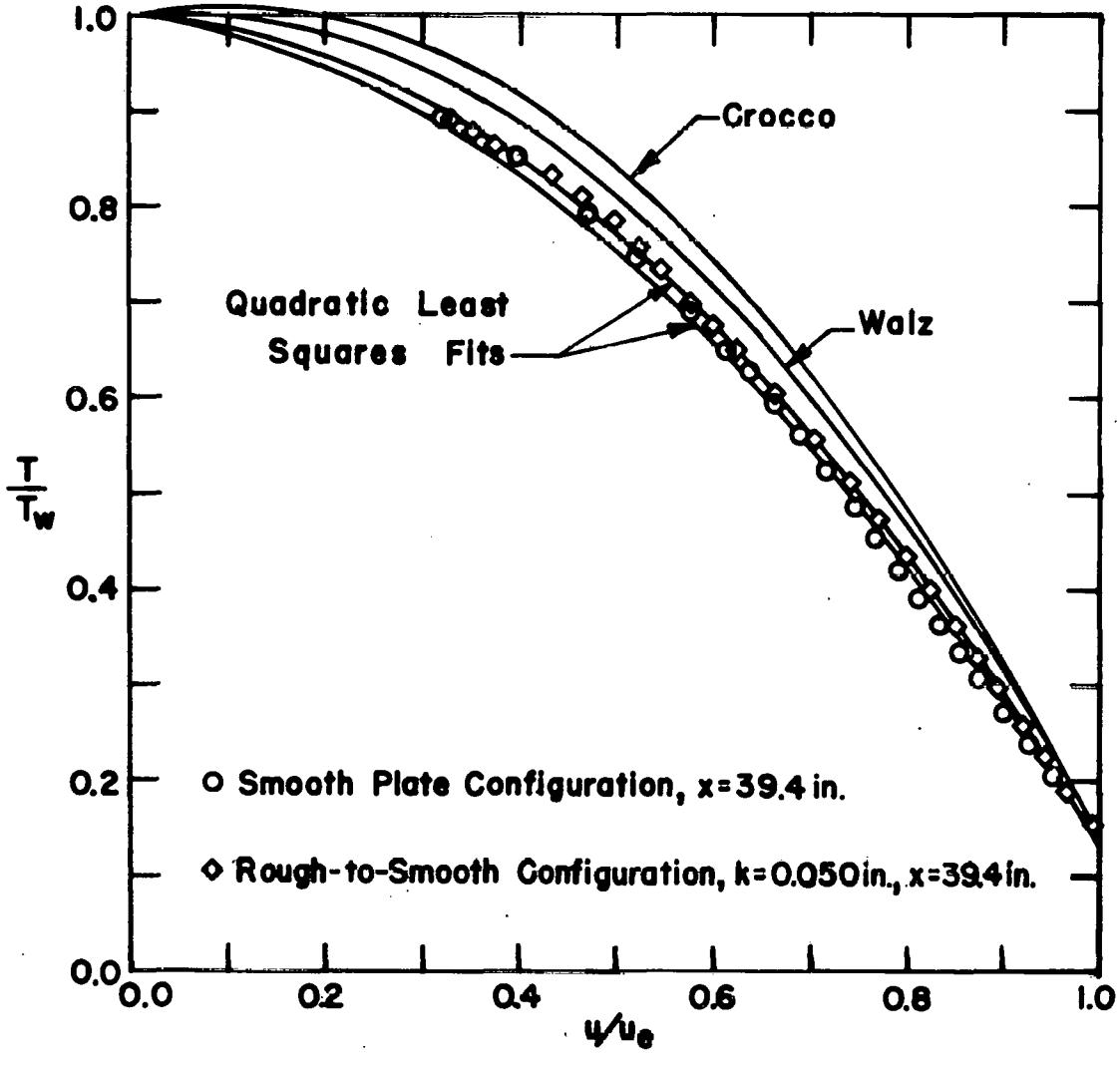

FIG. 28 TEMPERATURE–VELOCITY RELATIONSHIP

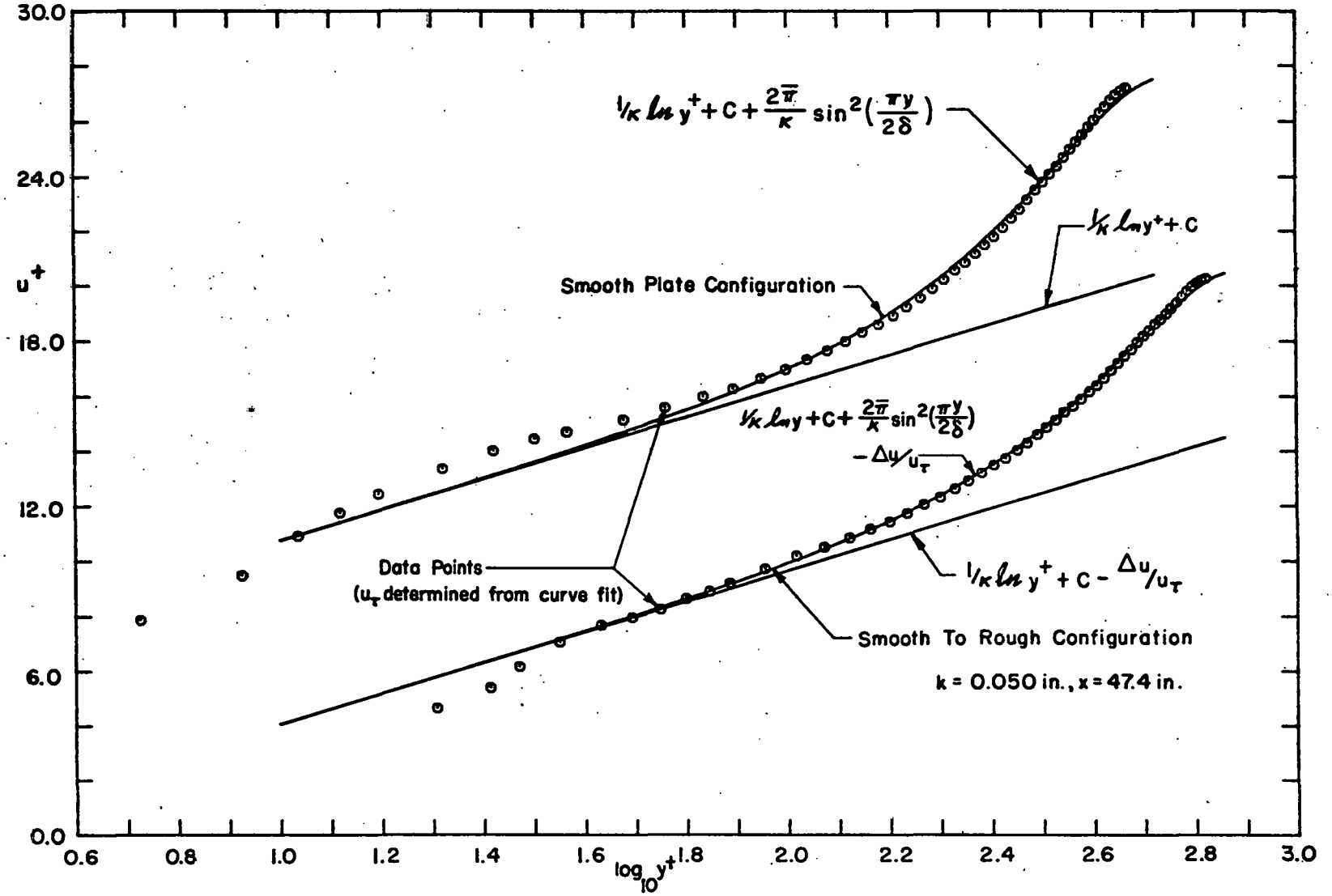

FIG. 29 FIT OF TRANSFORMED VELOCITY DATA TO THE LAW OF THE WALL

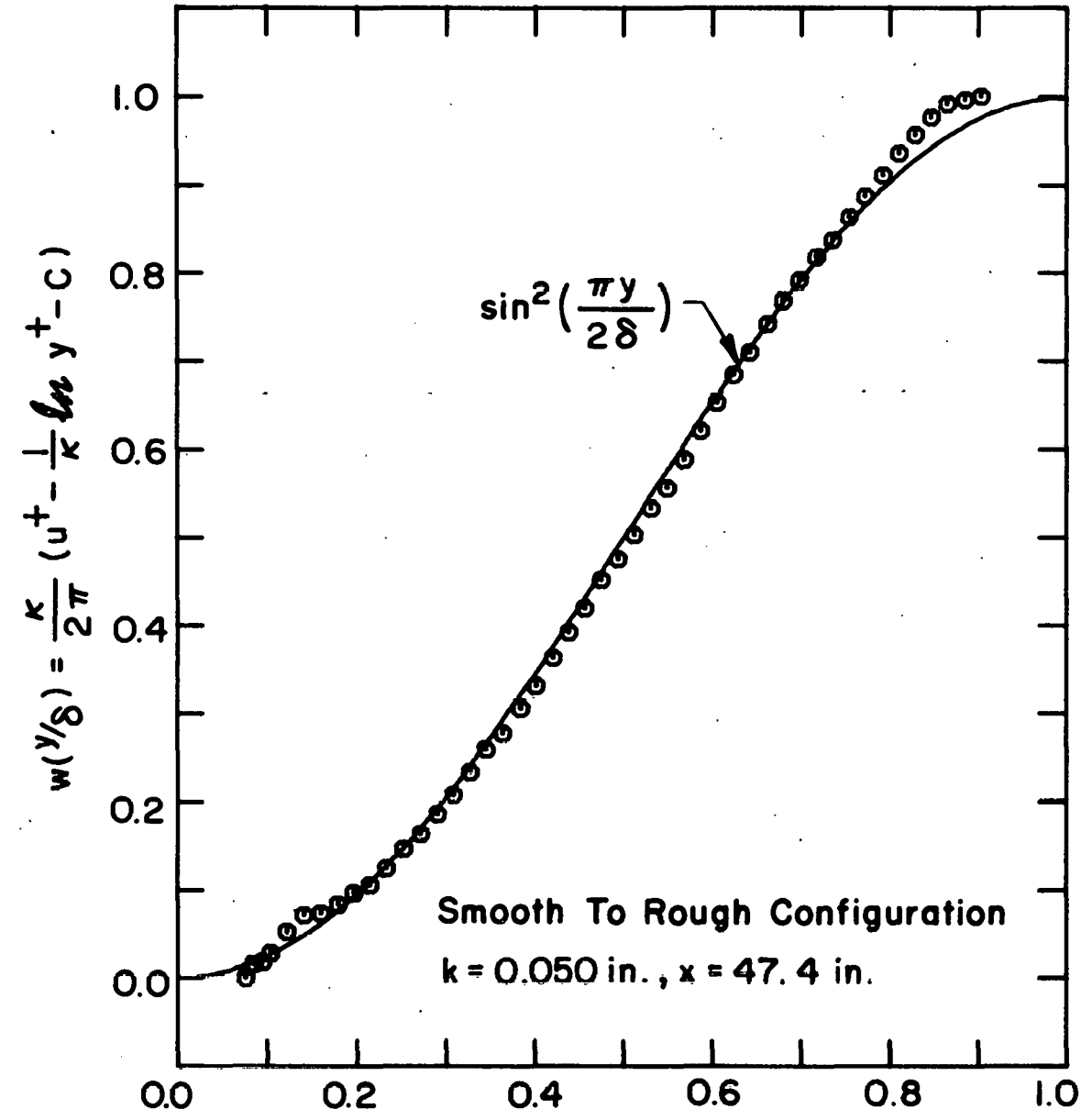

FIG. 30 FIT OF COLES' WAKE FUNCTION TO THE TRANSFORMED VELOCITY WAKE DATA

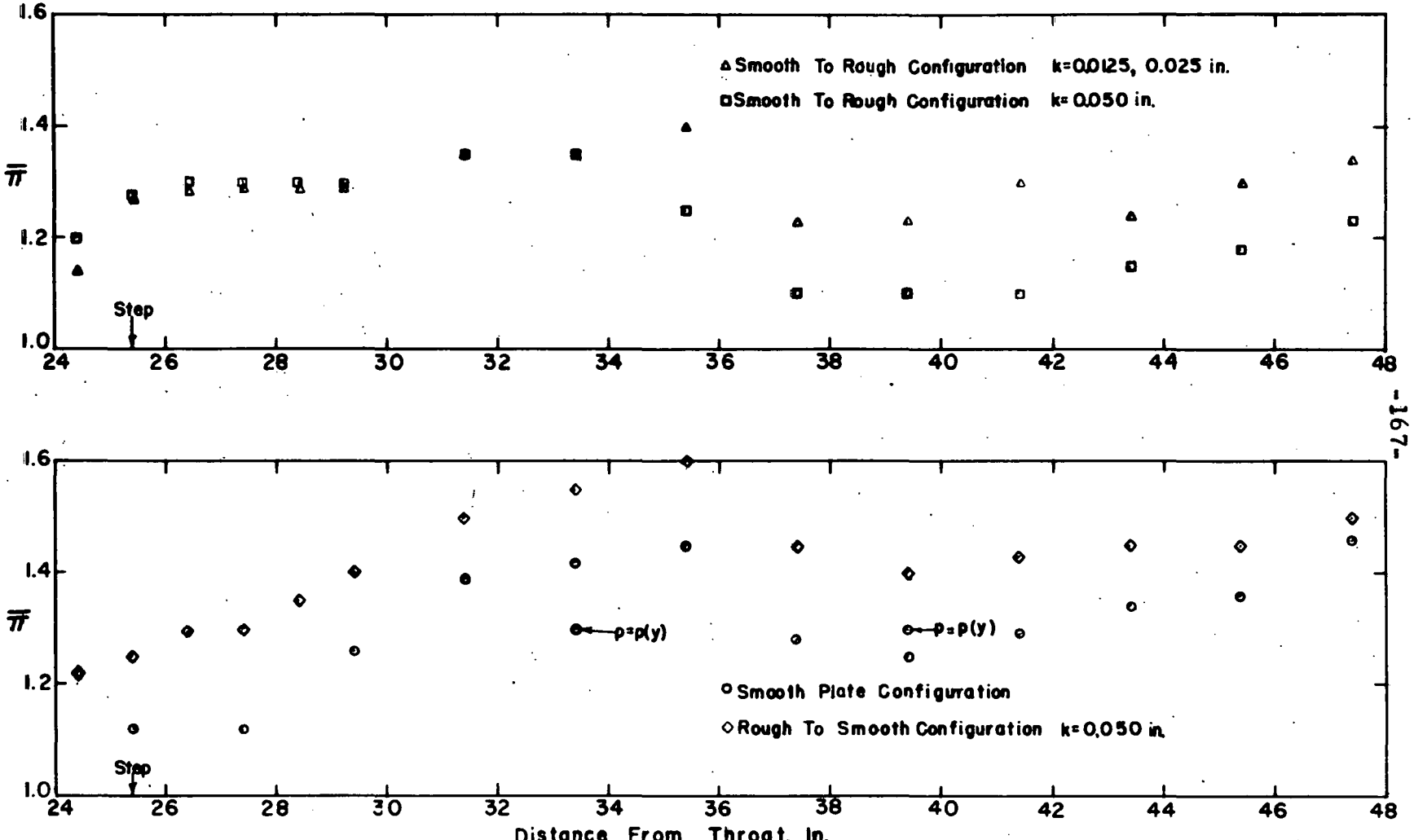

FIG. 31 AXIAL DISTRIBUTION OF WAKE STRENGTH PARAMETER

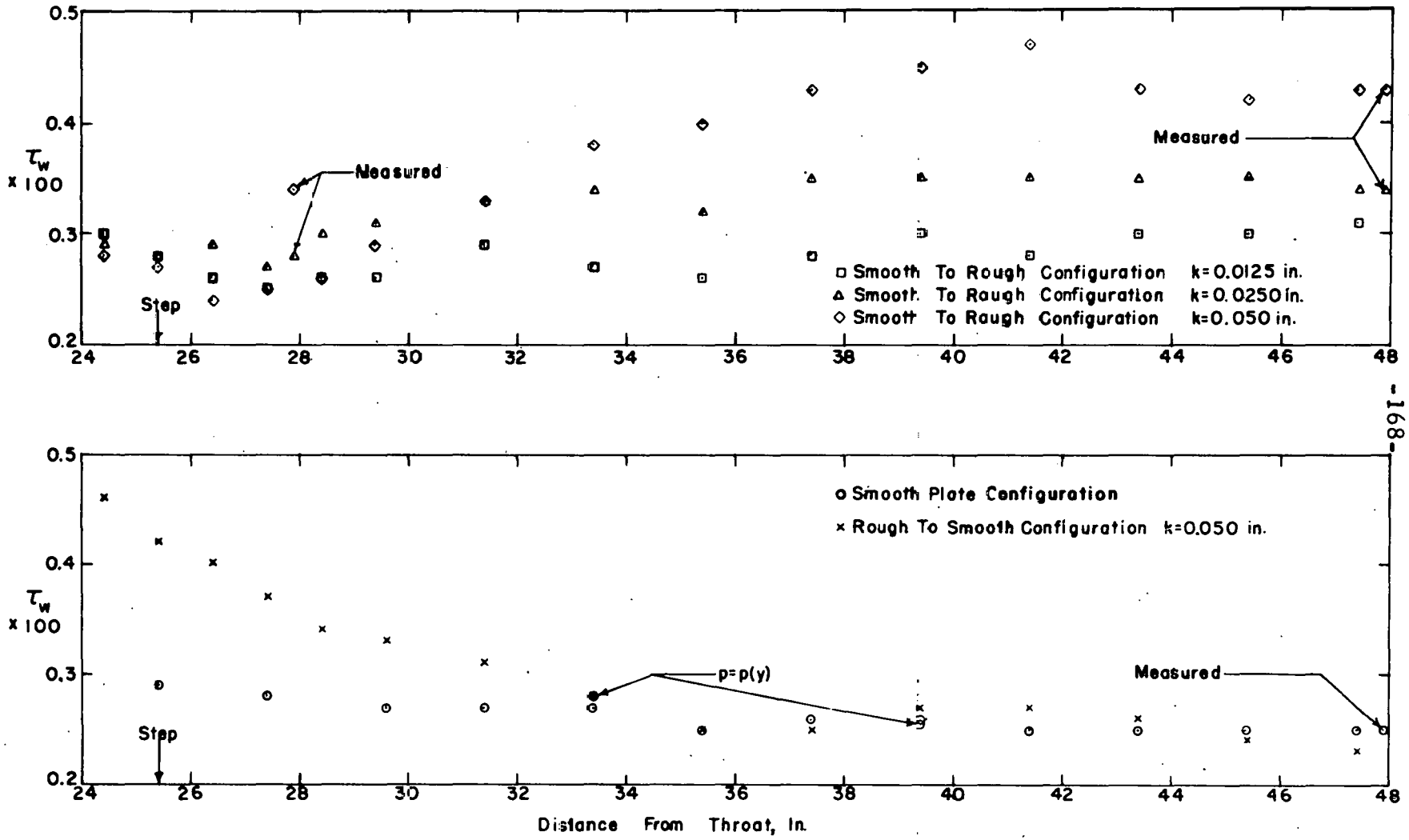

FIG. 32 AXIAL DISTRIBUTION OF SKIN FRICTION

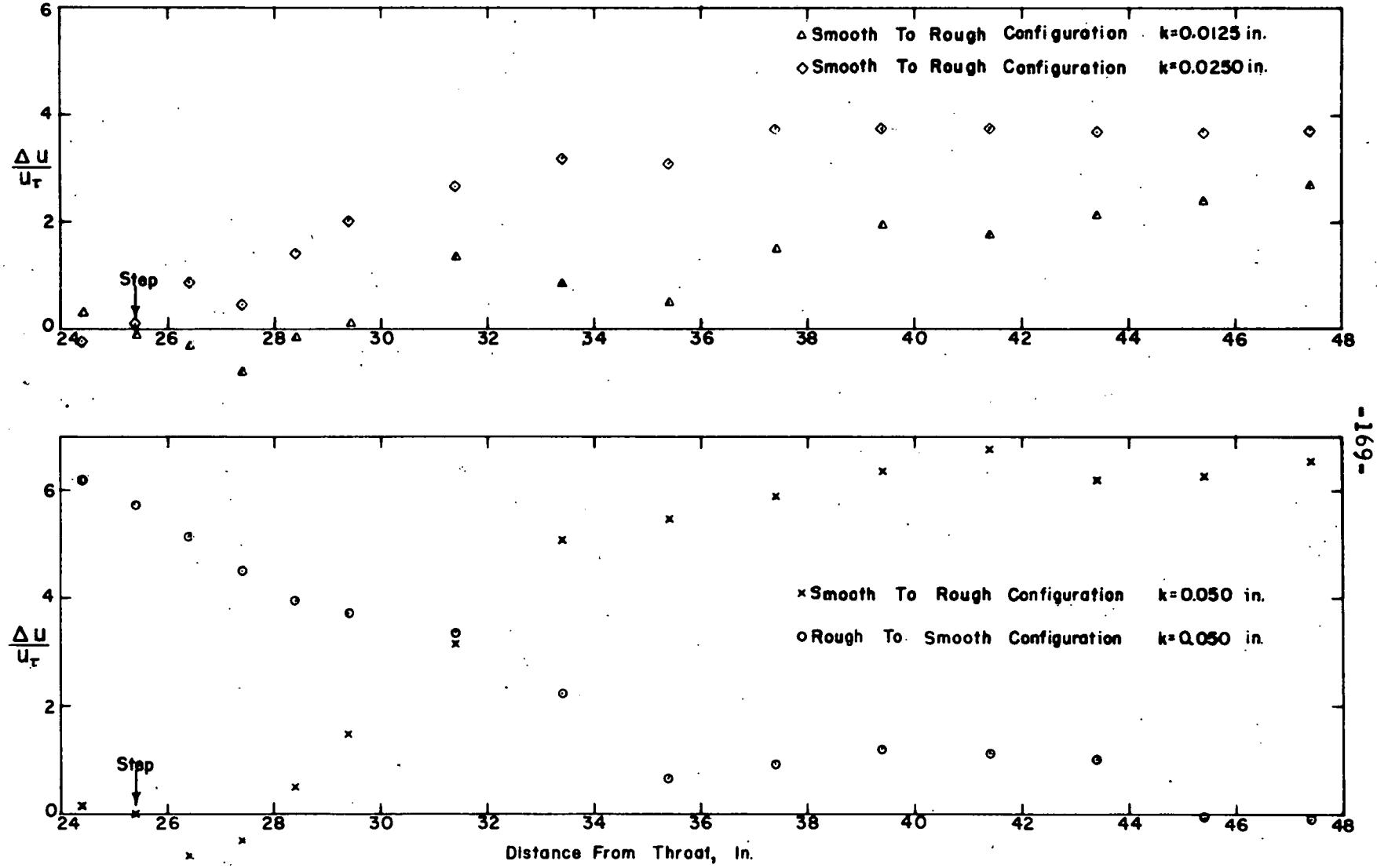

FIG. 33 AXIAL DEVELOPMENT OF ROUGH WALL VELOCITY DEFECT

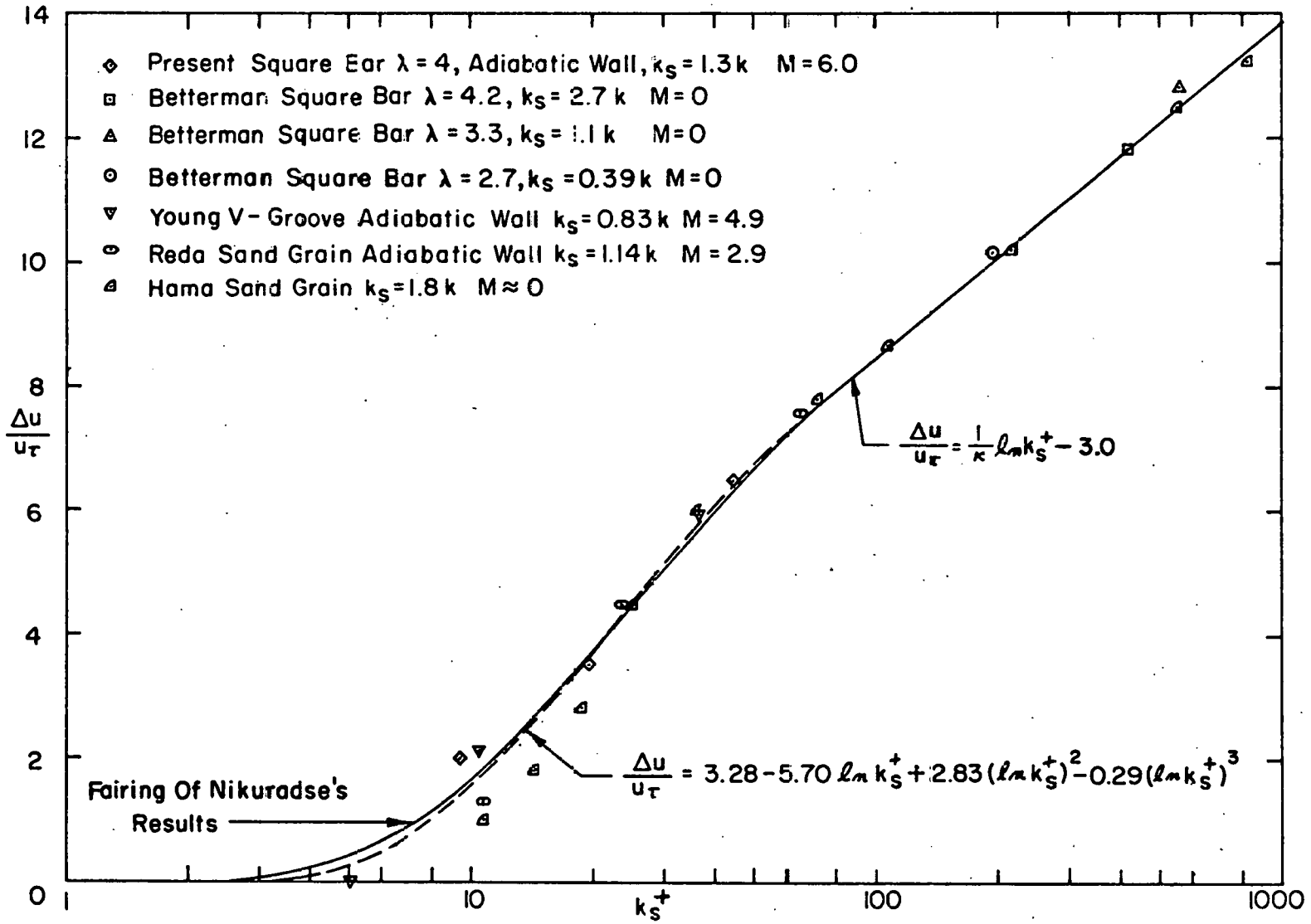

FIG. 34 ROUGH WALL VELOCITY DEFECT CORRELATION

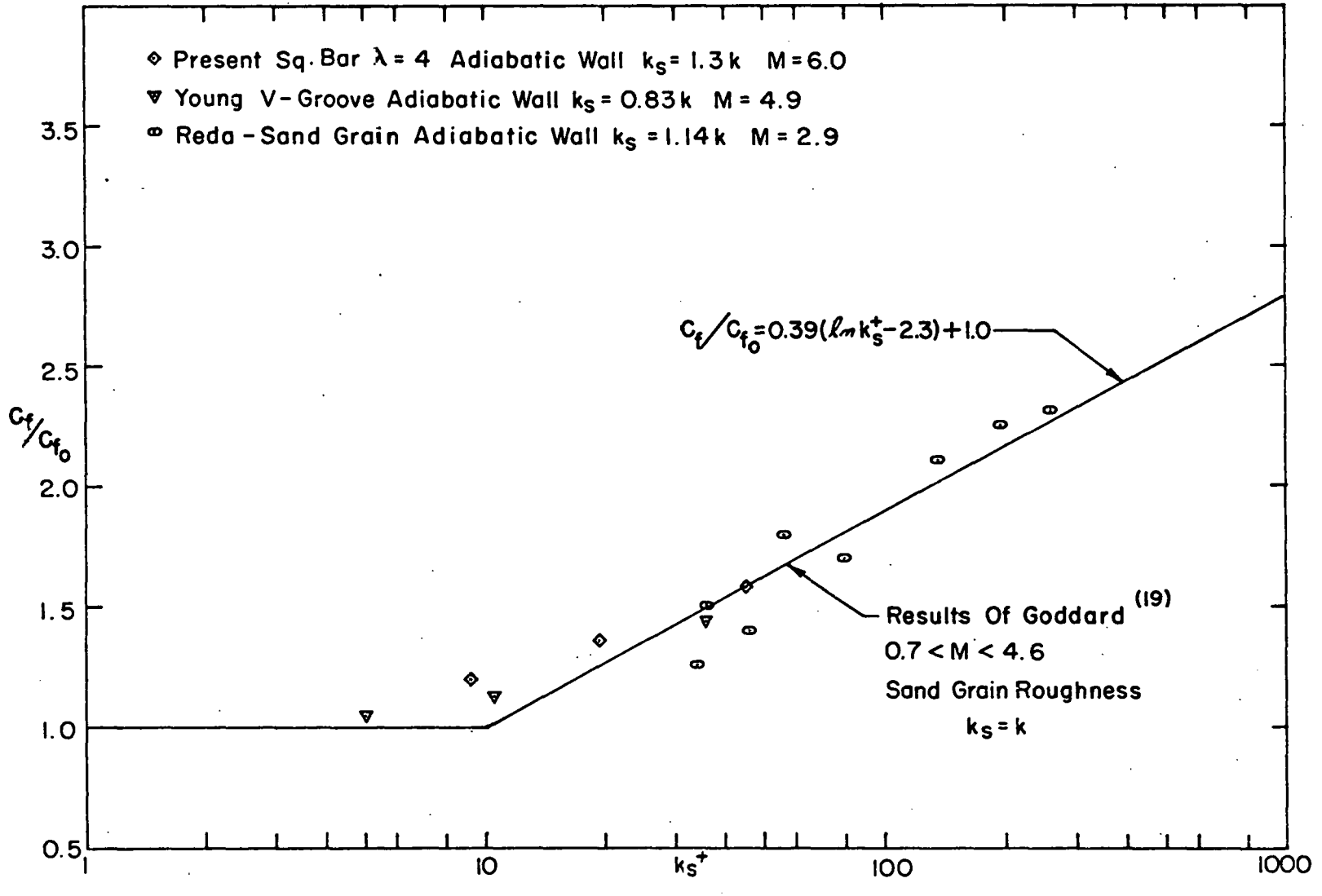

FIG. 35 ROUGH WALL SKIN FRICTION CORRELATION

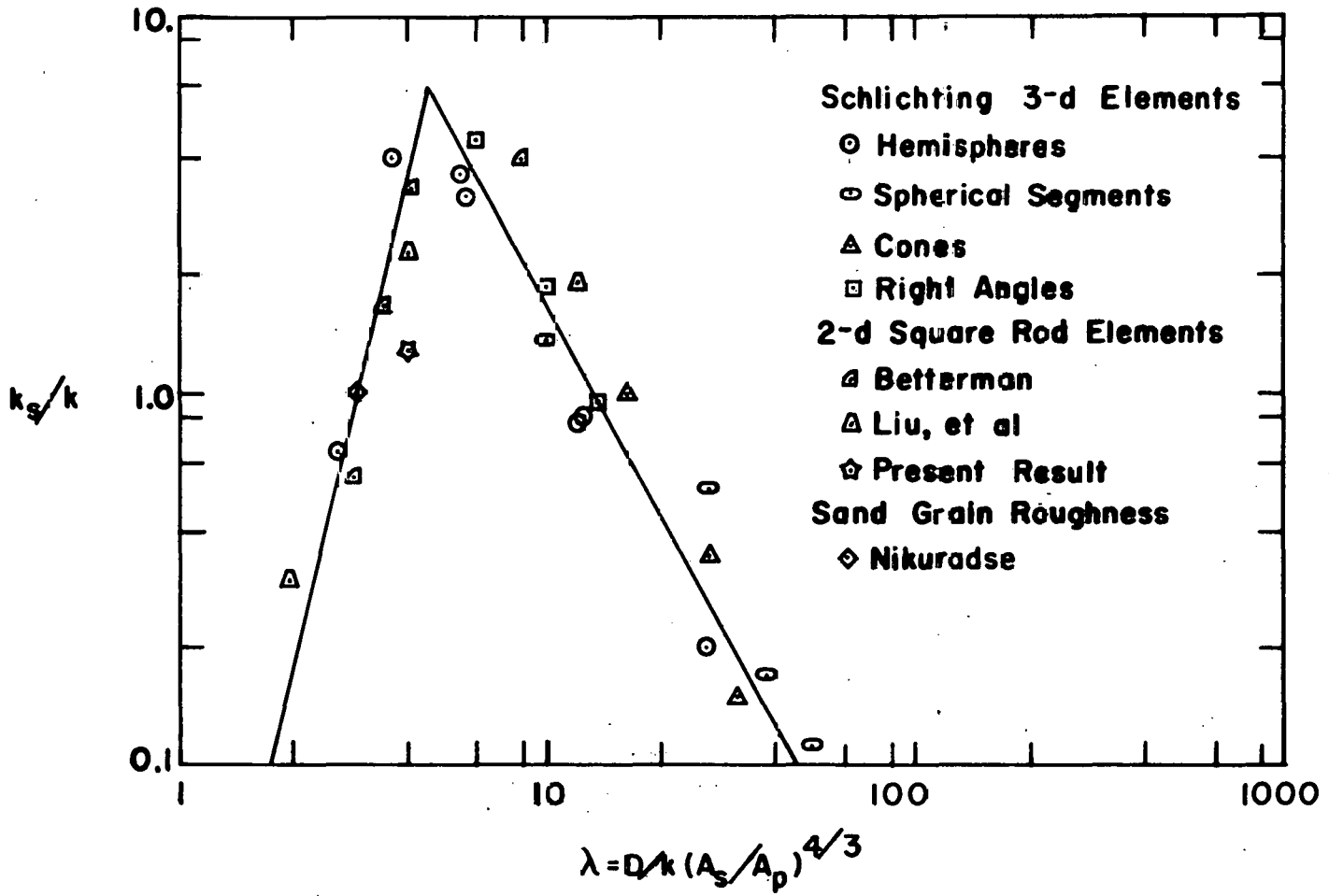

FIG. 36 COMPARISON OF PRESENT RESULTS WITH LOW SPEED EFFECTIVE ROUGHNESS CORRELATION (From Dirling)

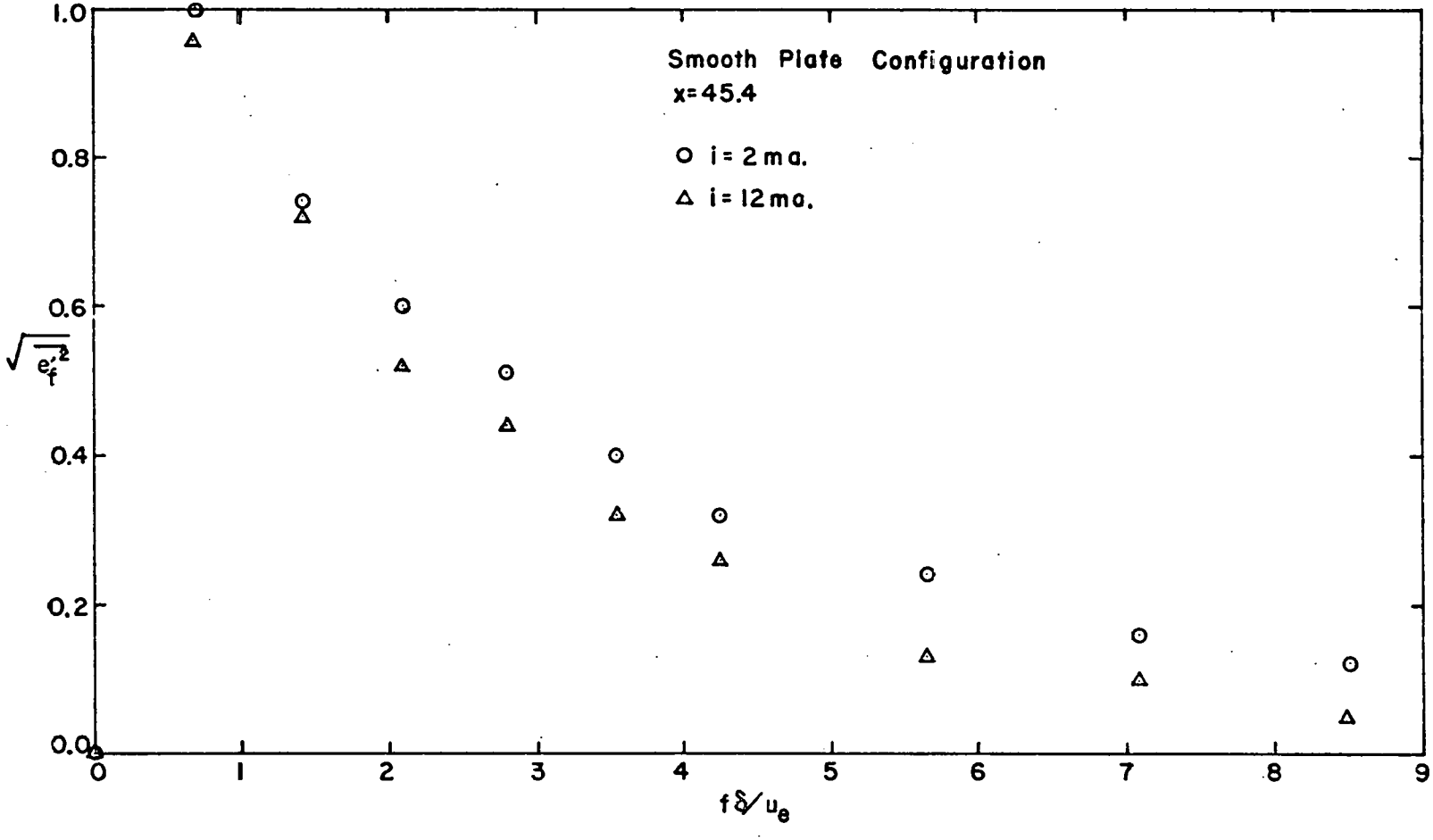

FIG. 37 TYPICAL HOT WIRE SPECTRA

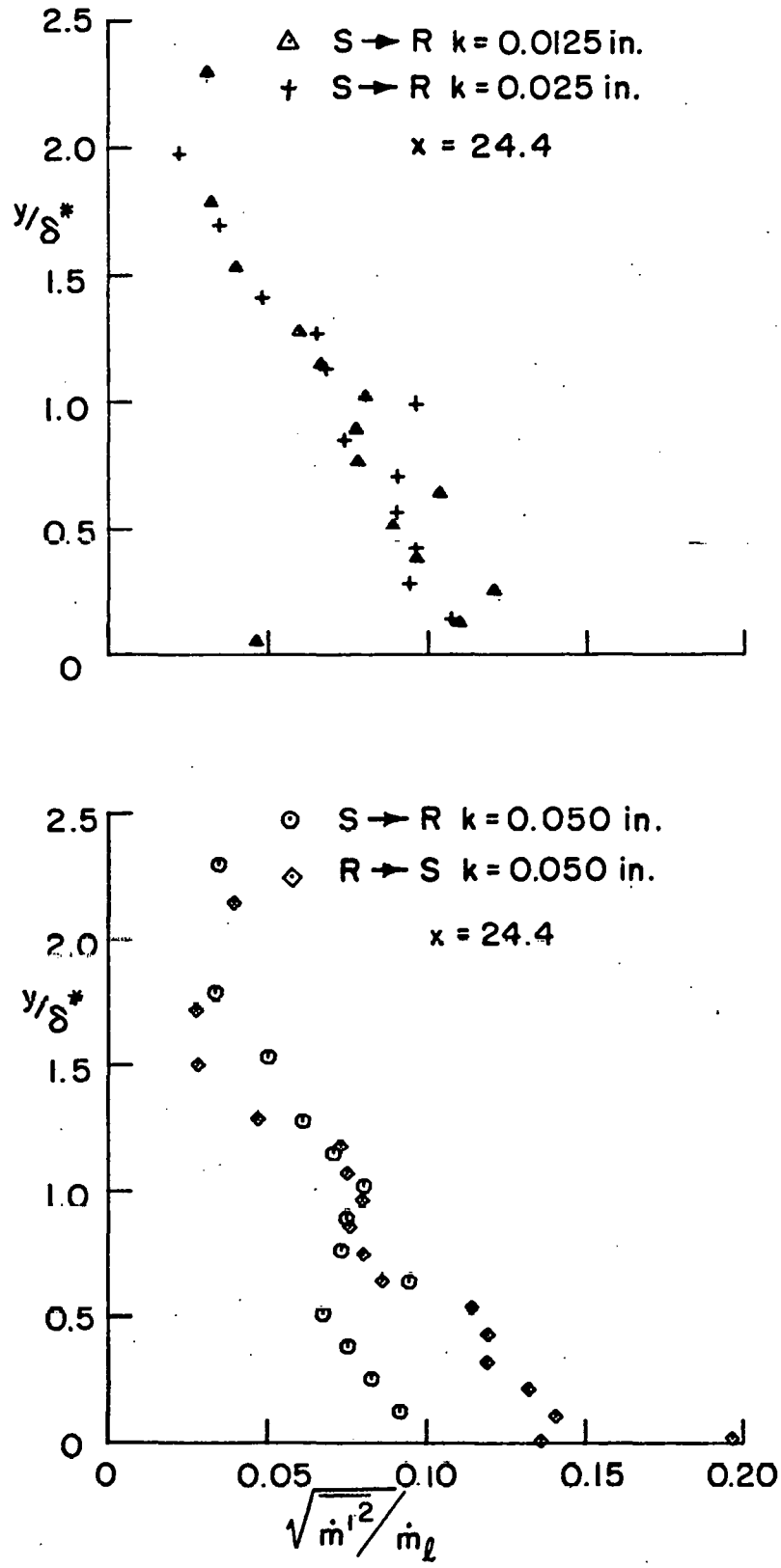

FIG. 38 MASS FLUX FLUCTUATIONS

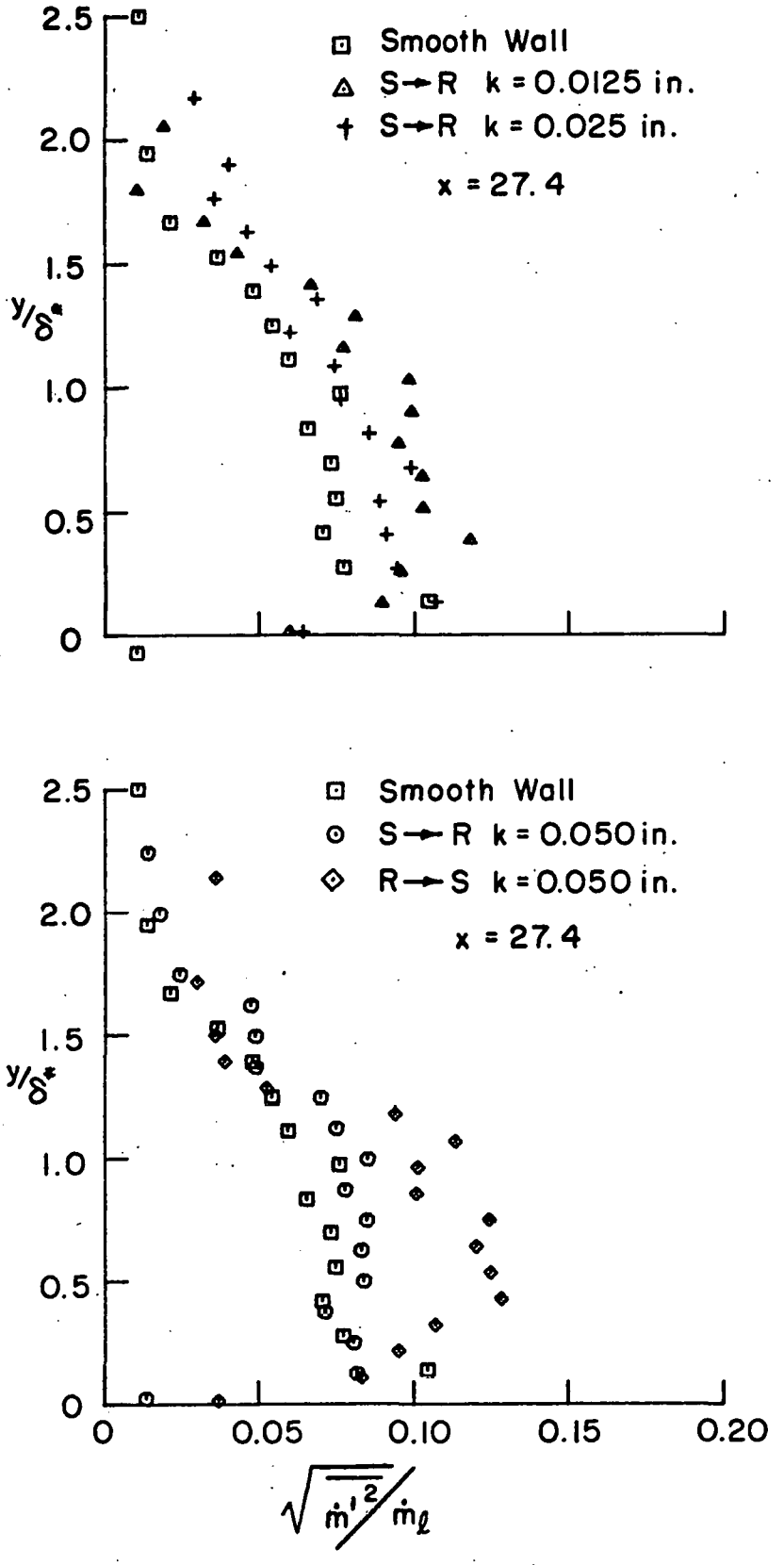

FIG. 38 (CONTINUED)

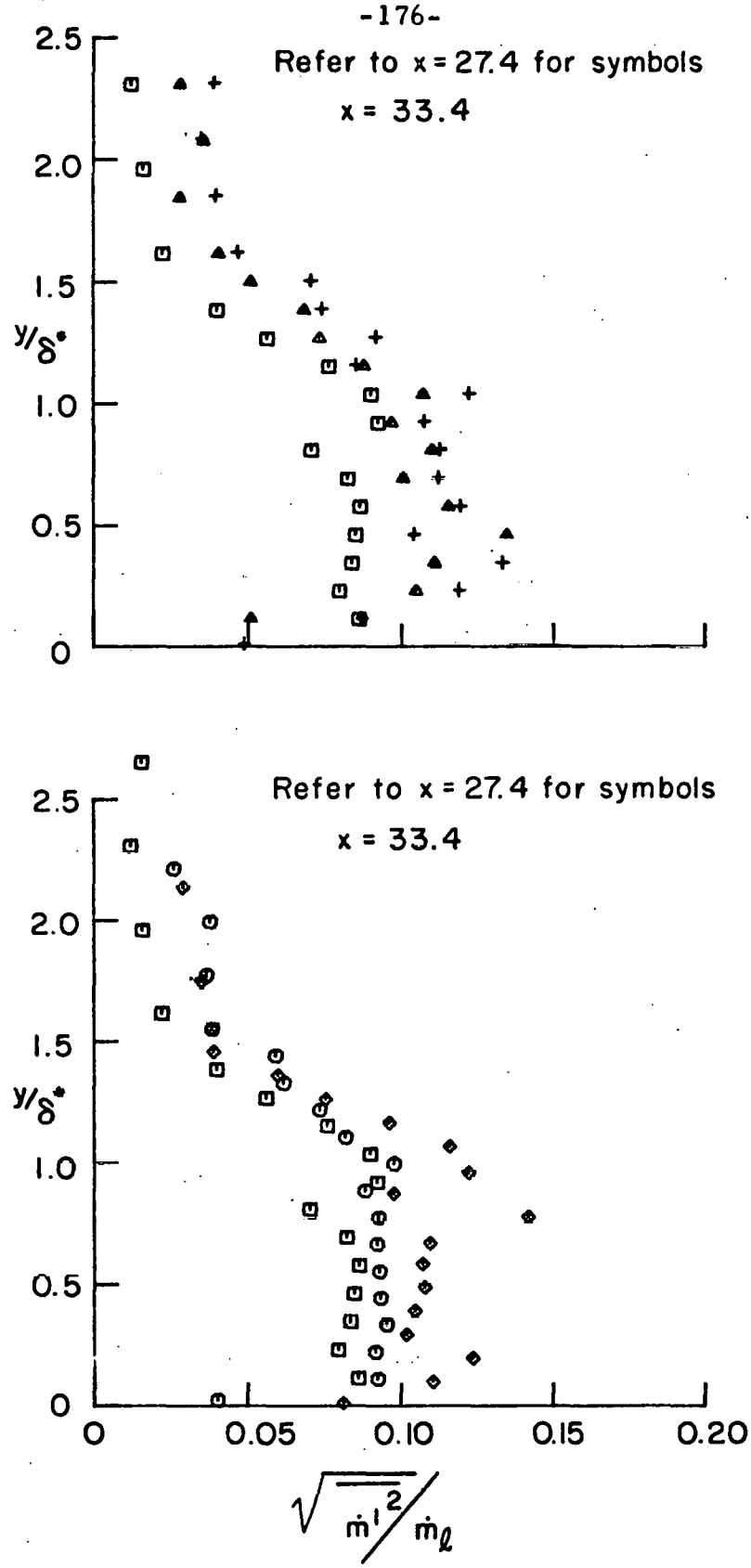

FIG. 38 (CONTINUED)

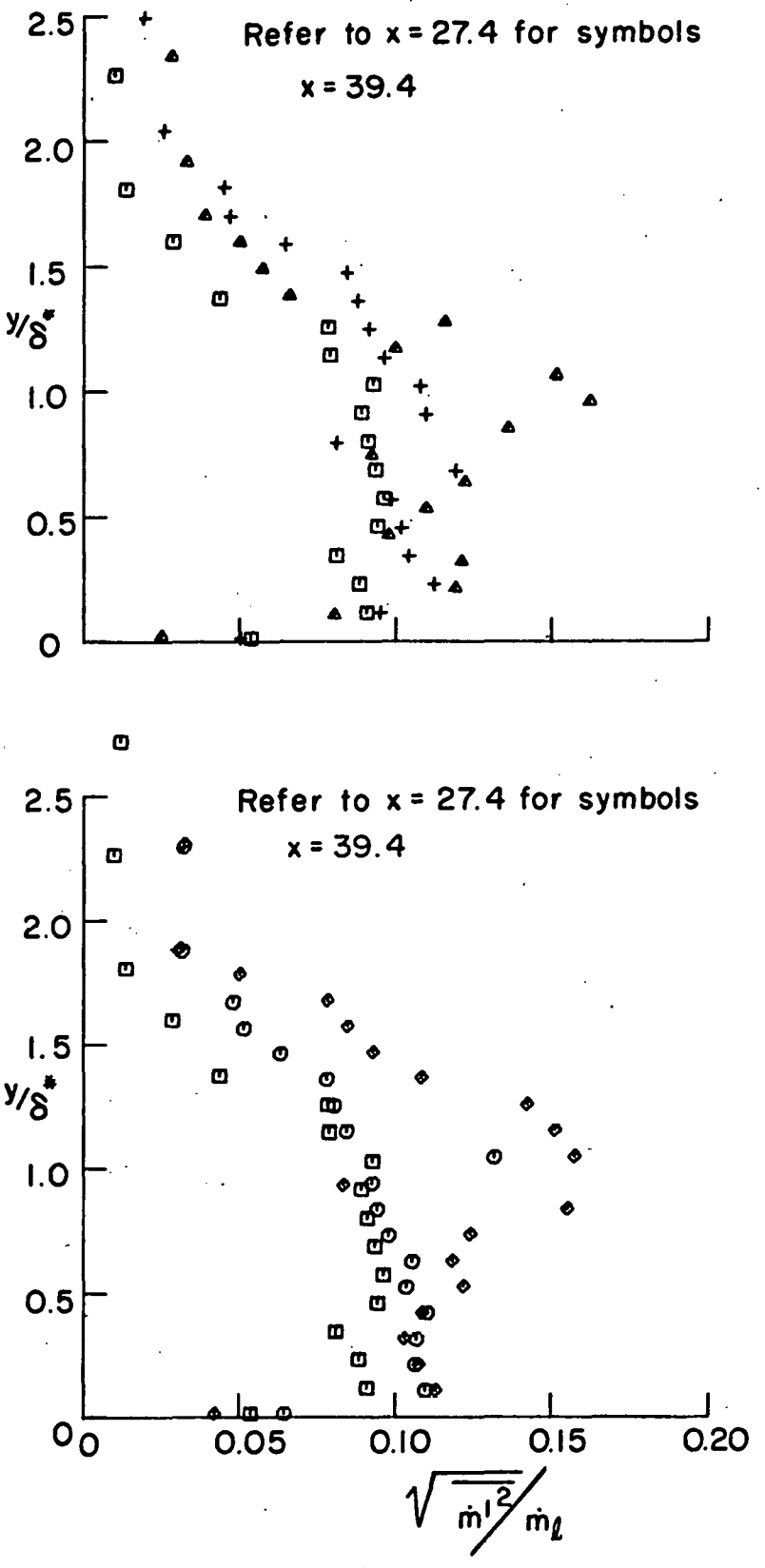

FIG. 38 (CONTINUED)

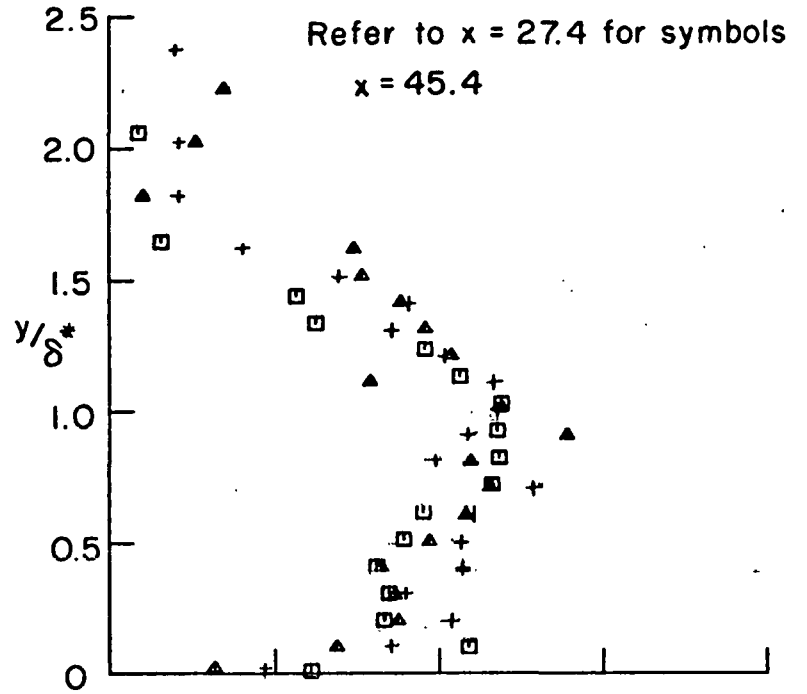

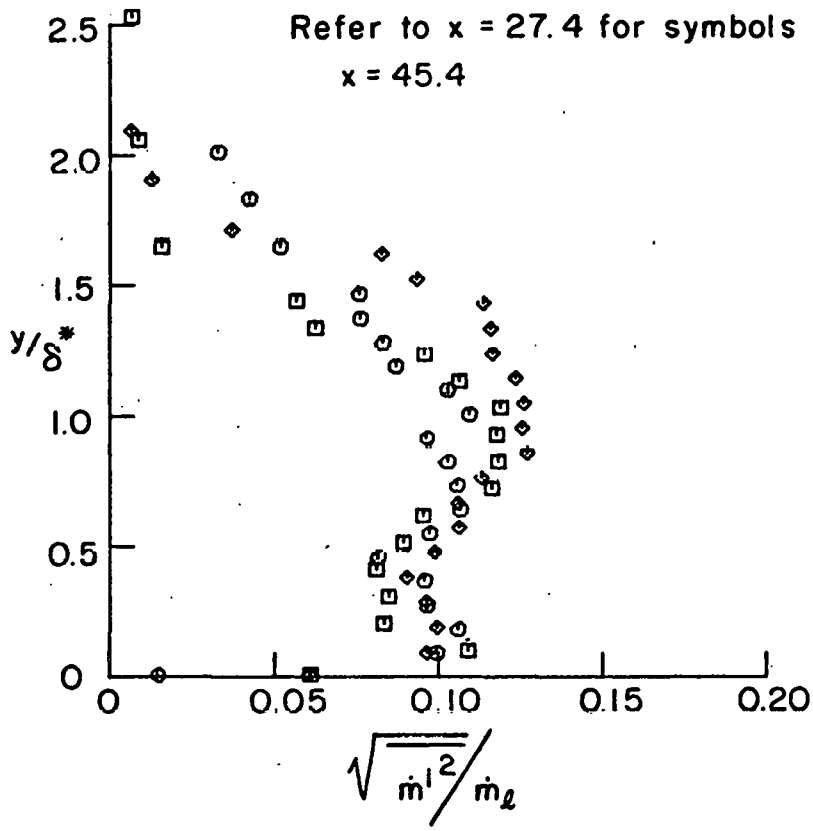

FIG. 38 (CONTINUED)

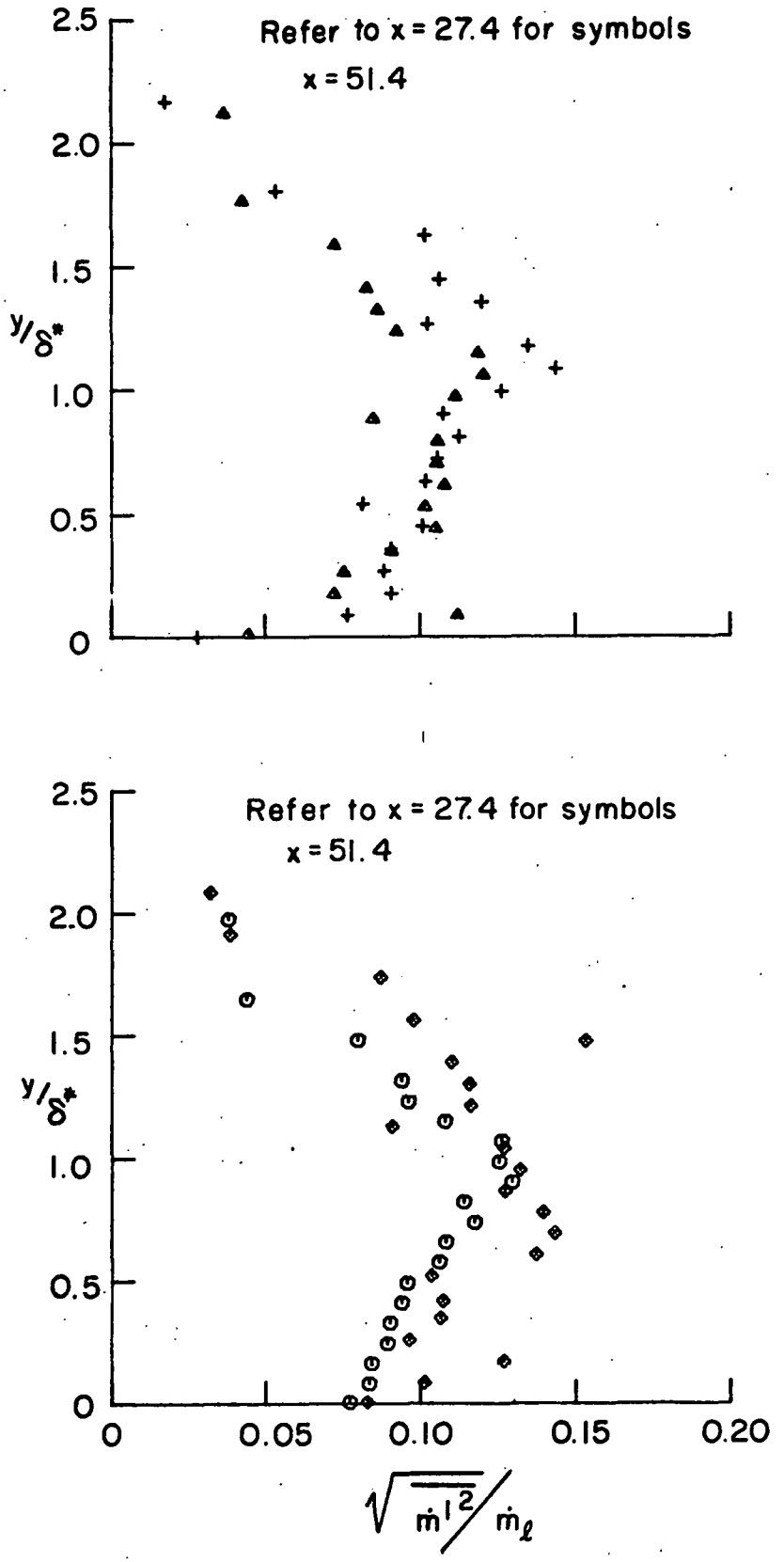

FIG. 38 (CONCLUDED)

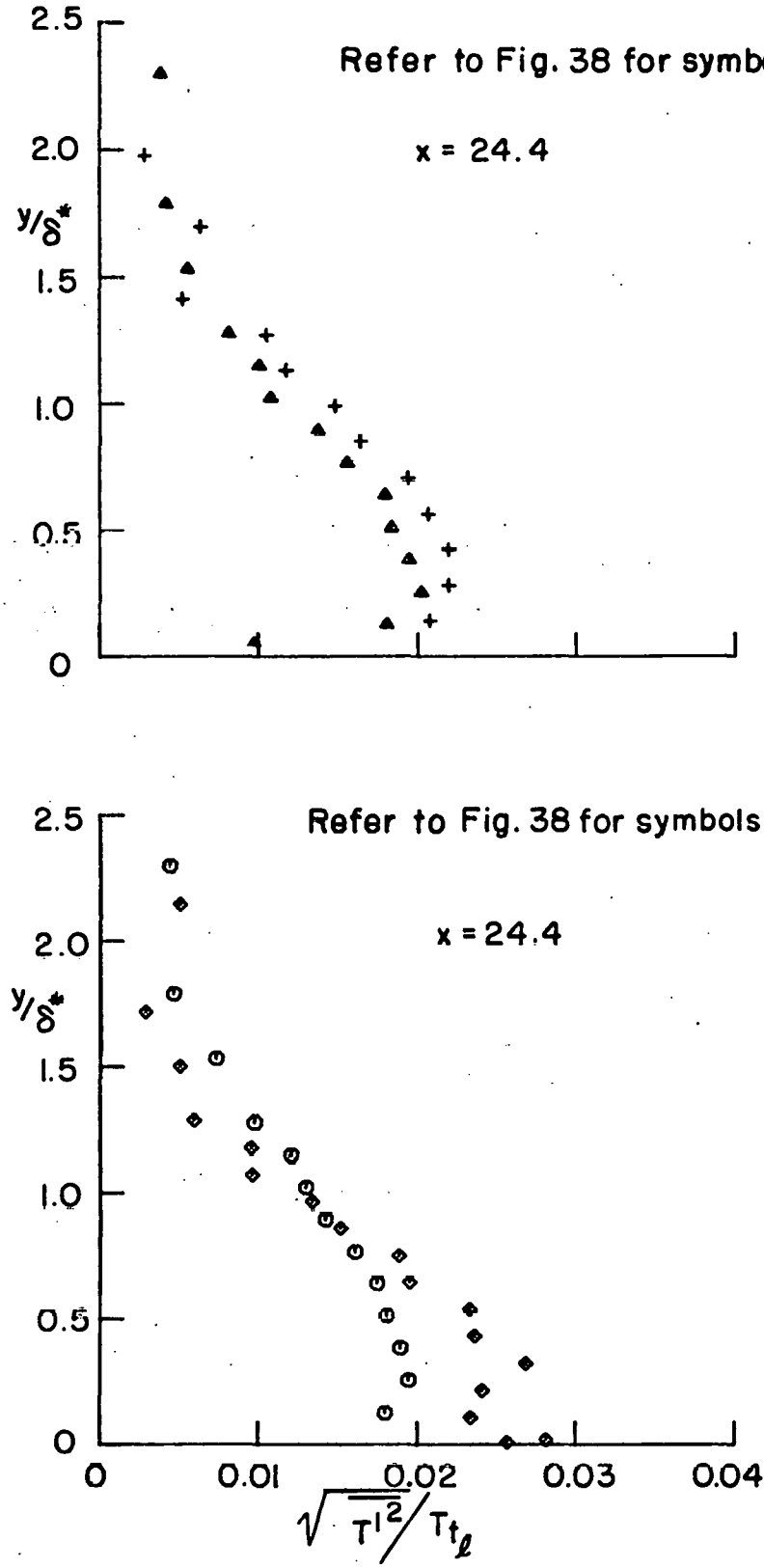

FIG. 39 TOTAL TEMPERATURE FLUCTUATIONS

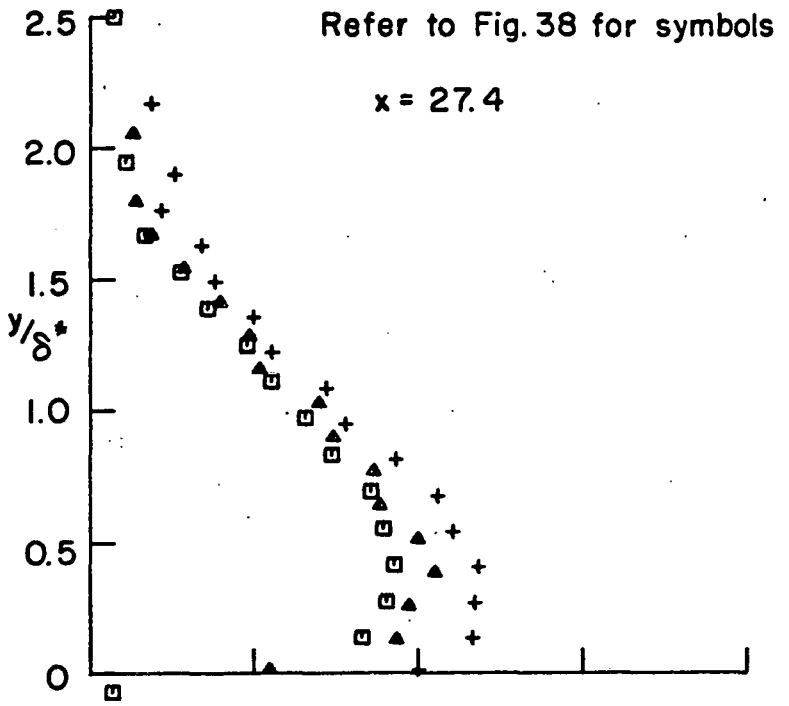

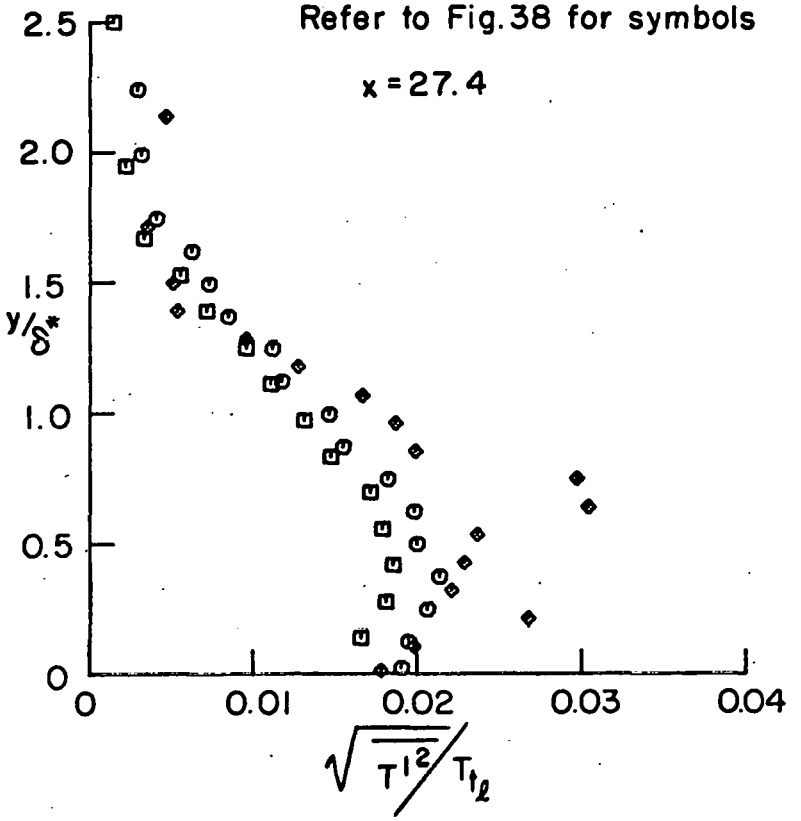

FIG. 39 (CONTINUED)

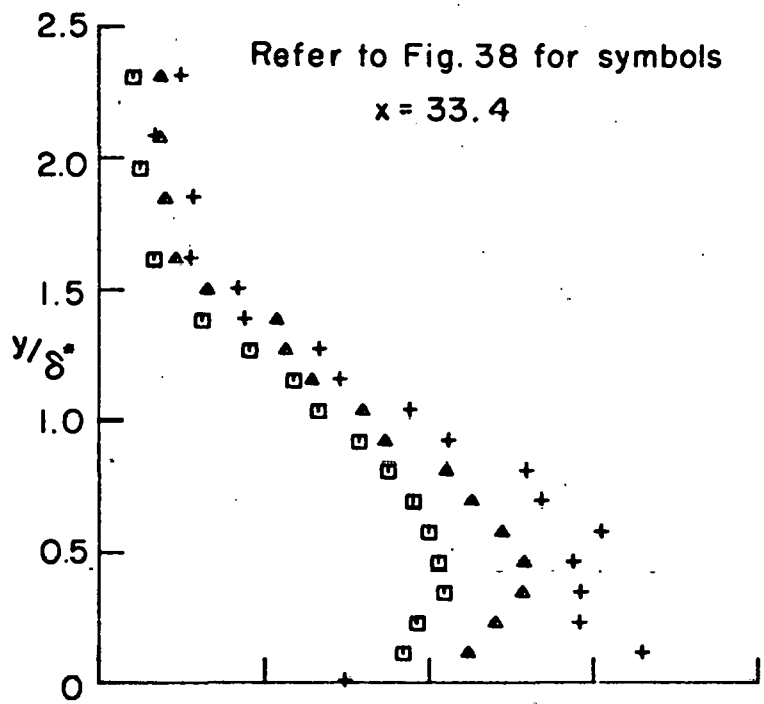

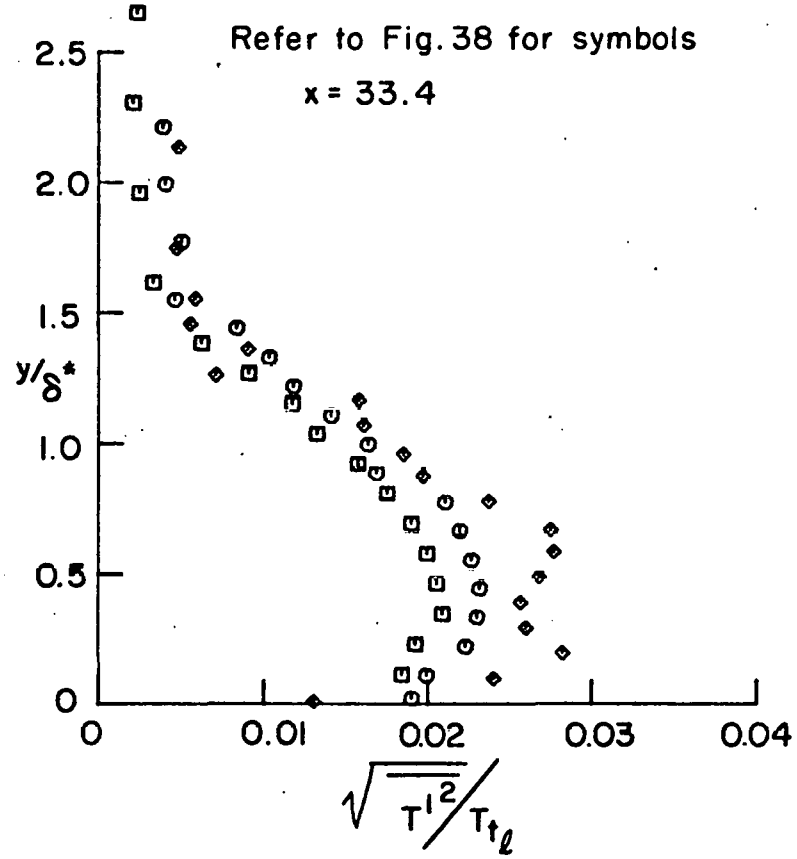

FIG. 39 (CONTINUED)

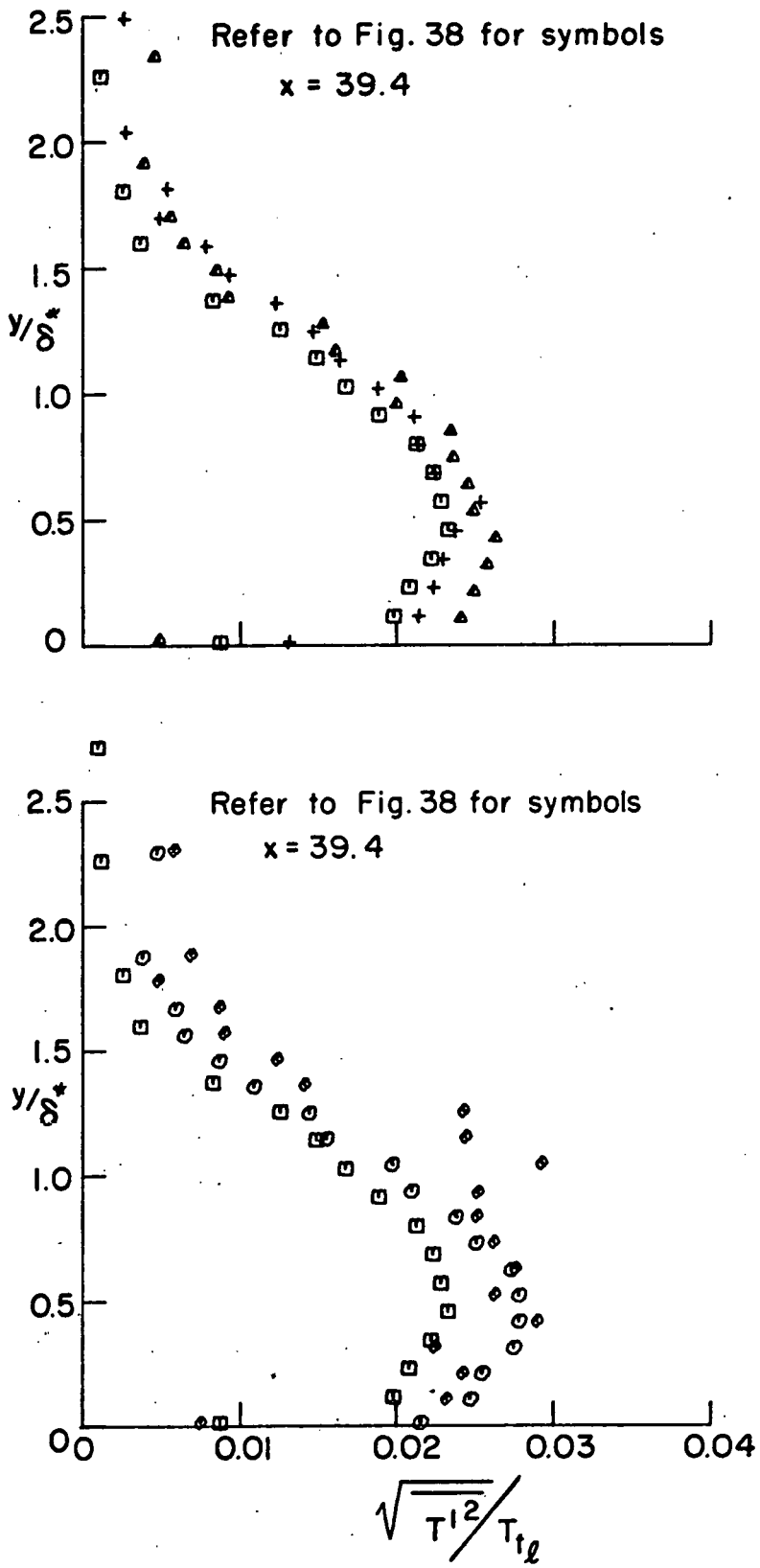

FIG. 39 (CONTINUED)

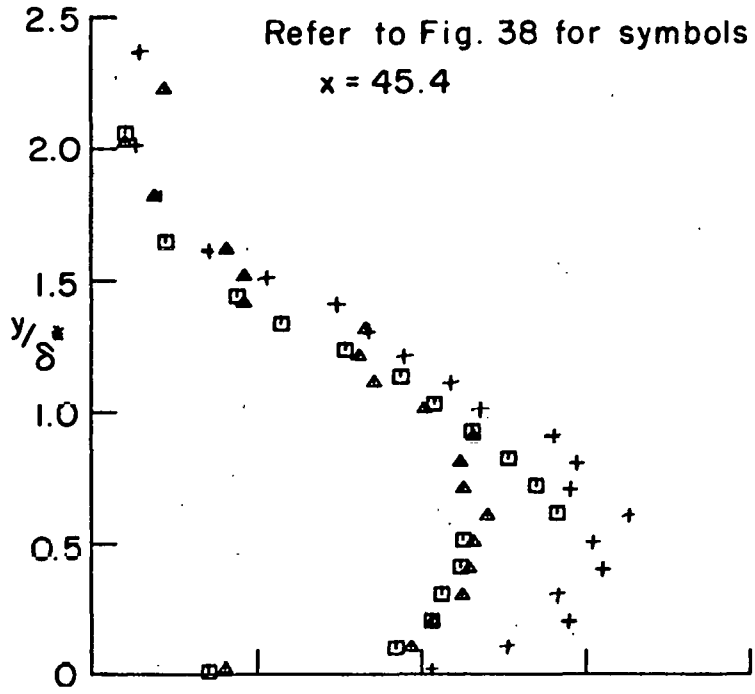

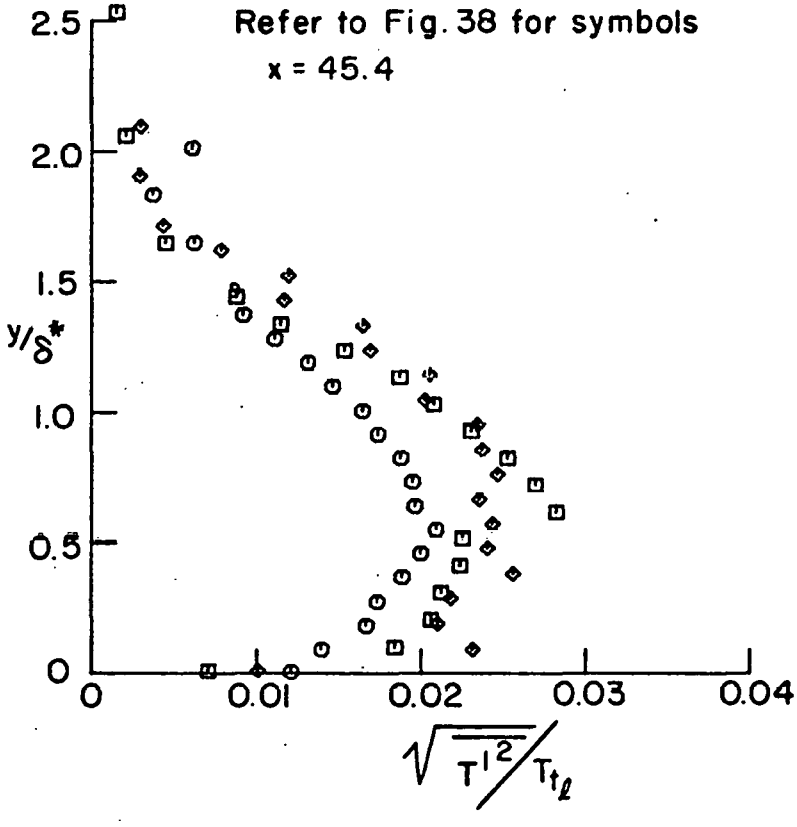

FIG. 39 (CONTINUED)

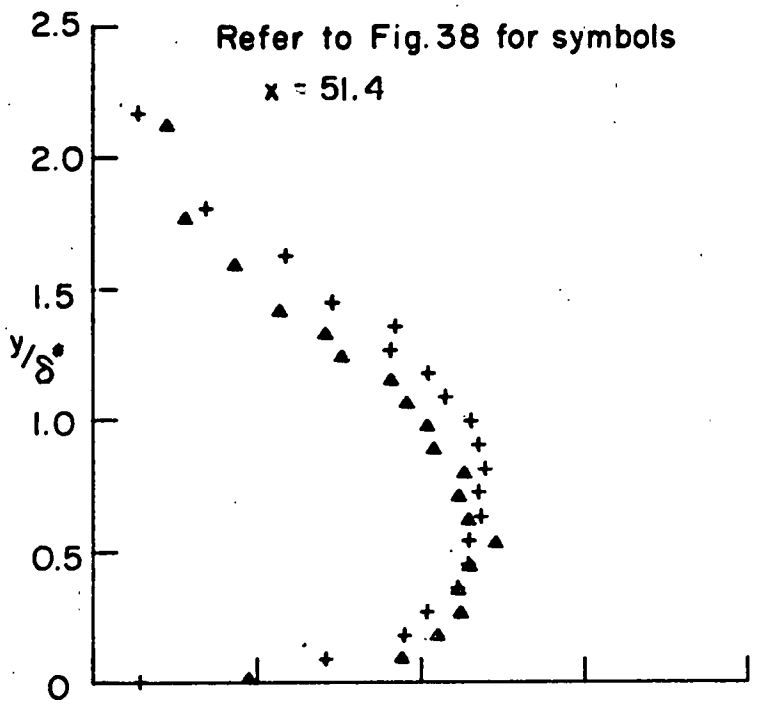

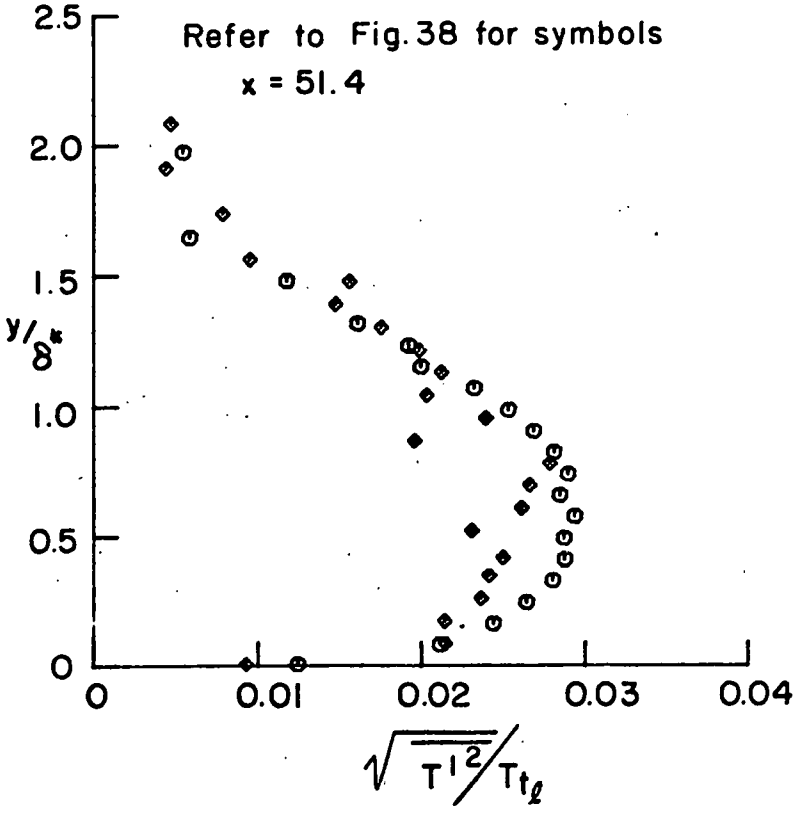

FIG. 39 (CONCLUDED)

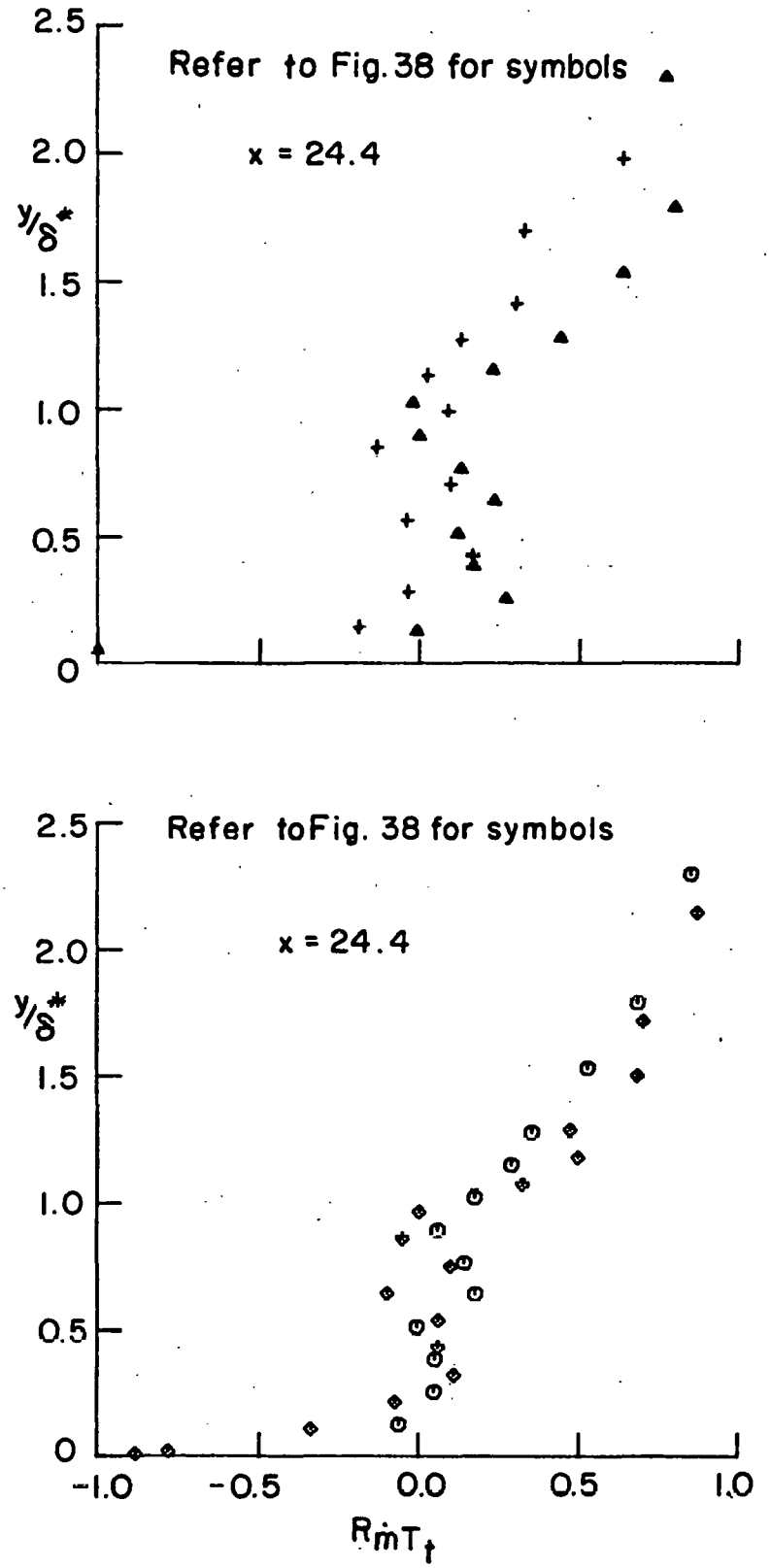

FIG. 40 MASS FLUX-TOTAL TEMPERATURE CORRELATION COEFFICIENT

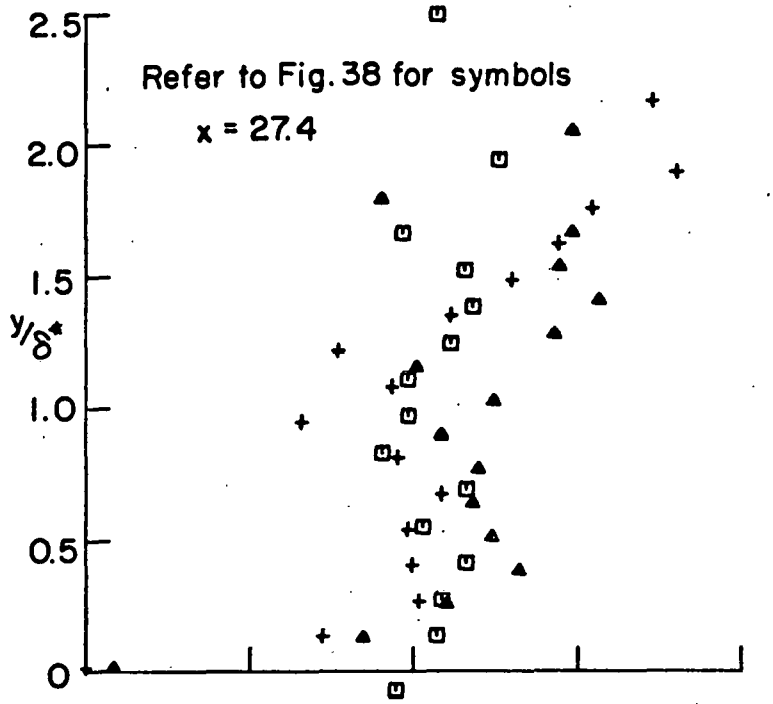

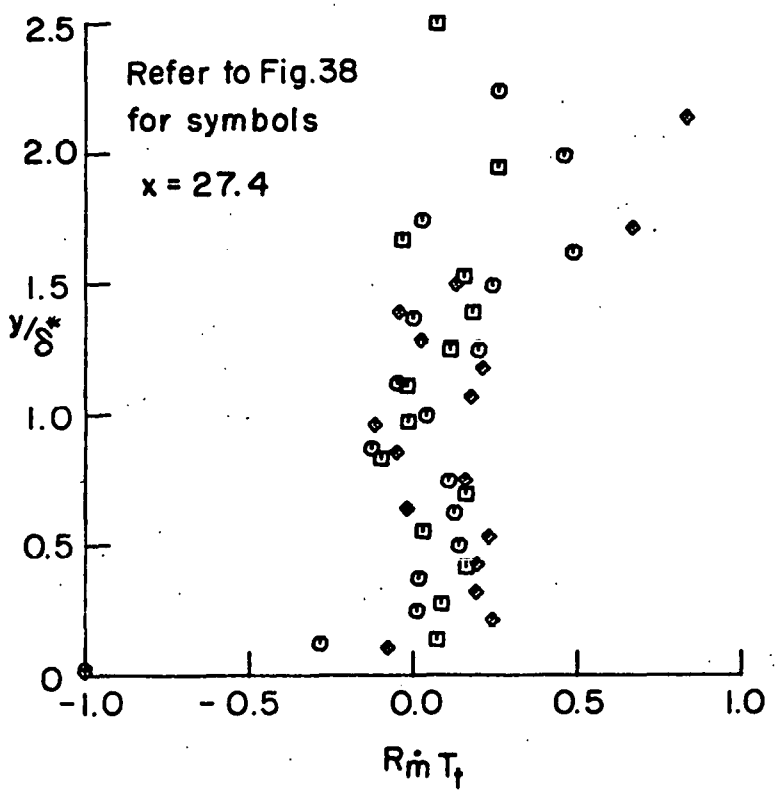

FIG. 40(CONTINUED)

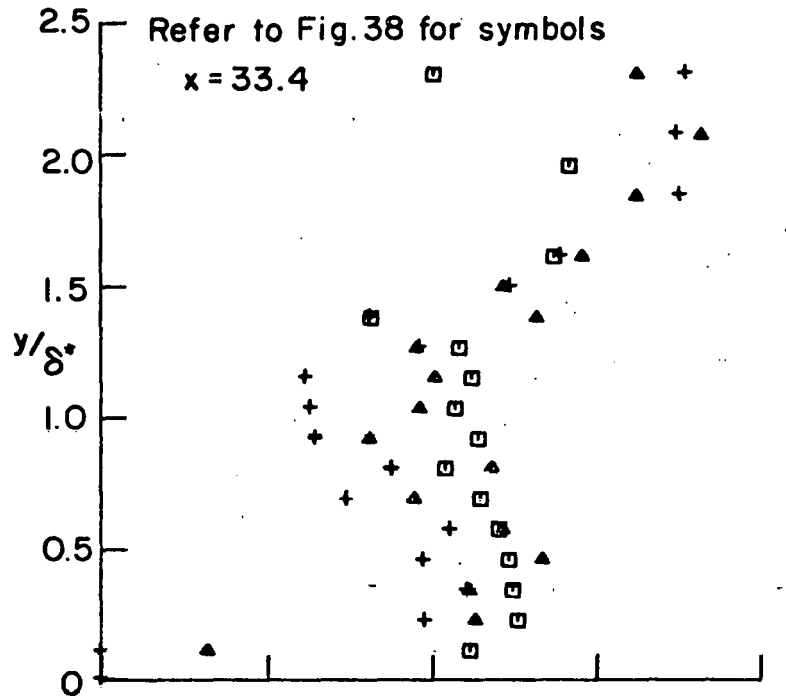

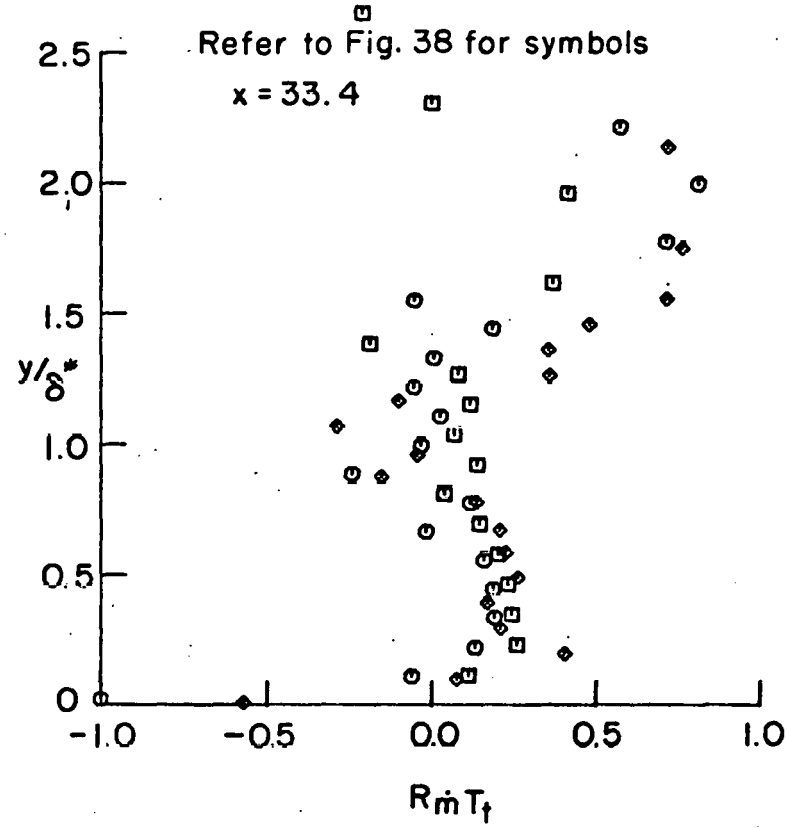

FIG. 40 (CONTINUED)

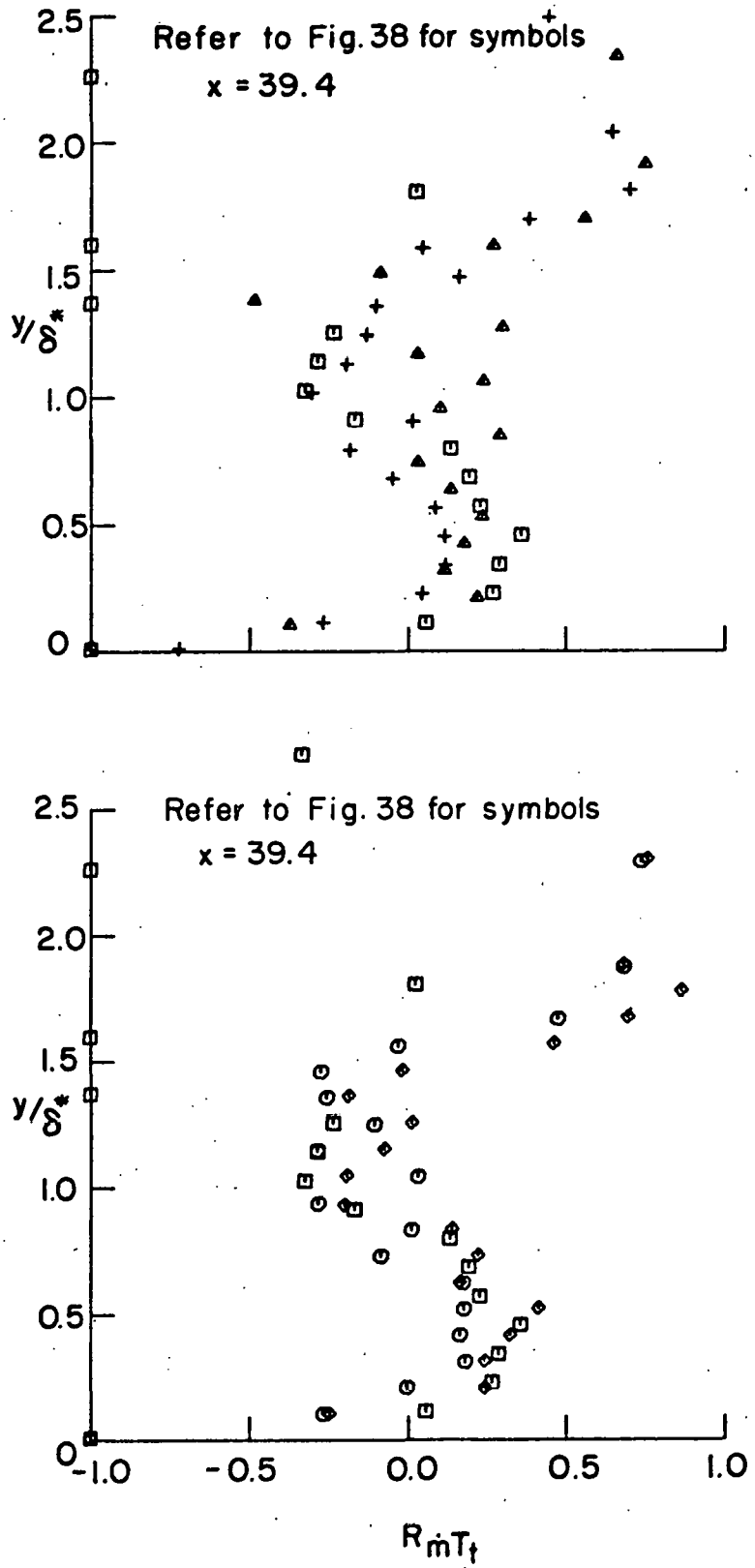

FIG. 40 (CONTINUED)

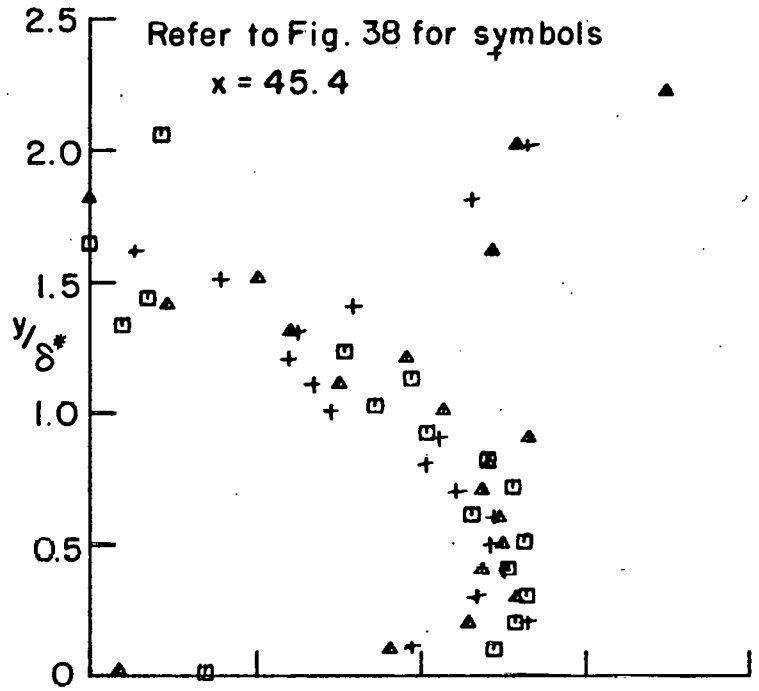

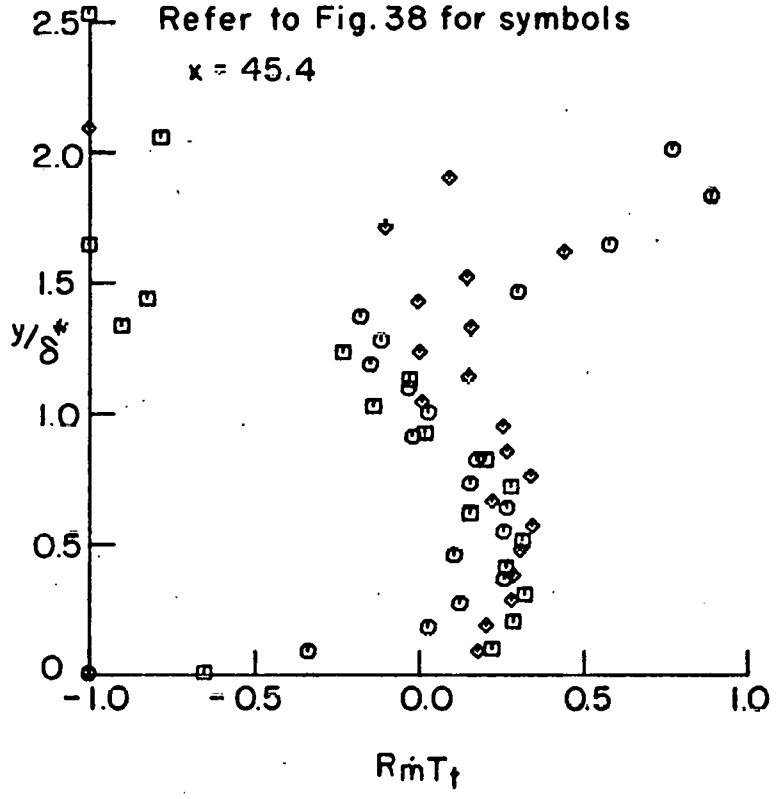

FIG. 40 (CONTINUED)

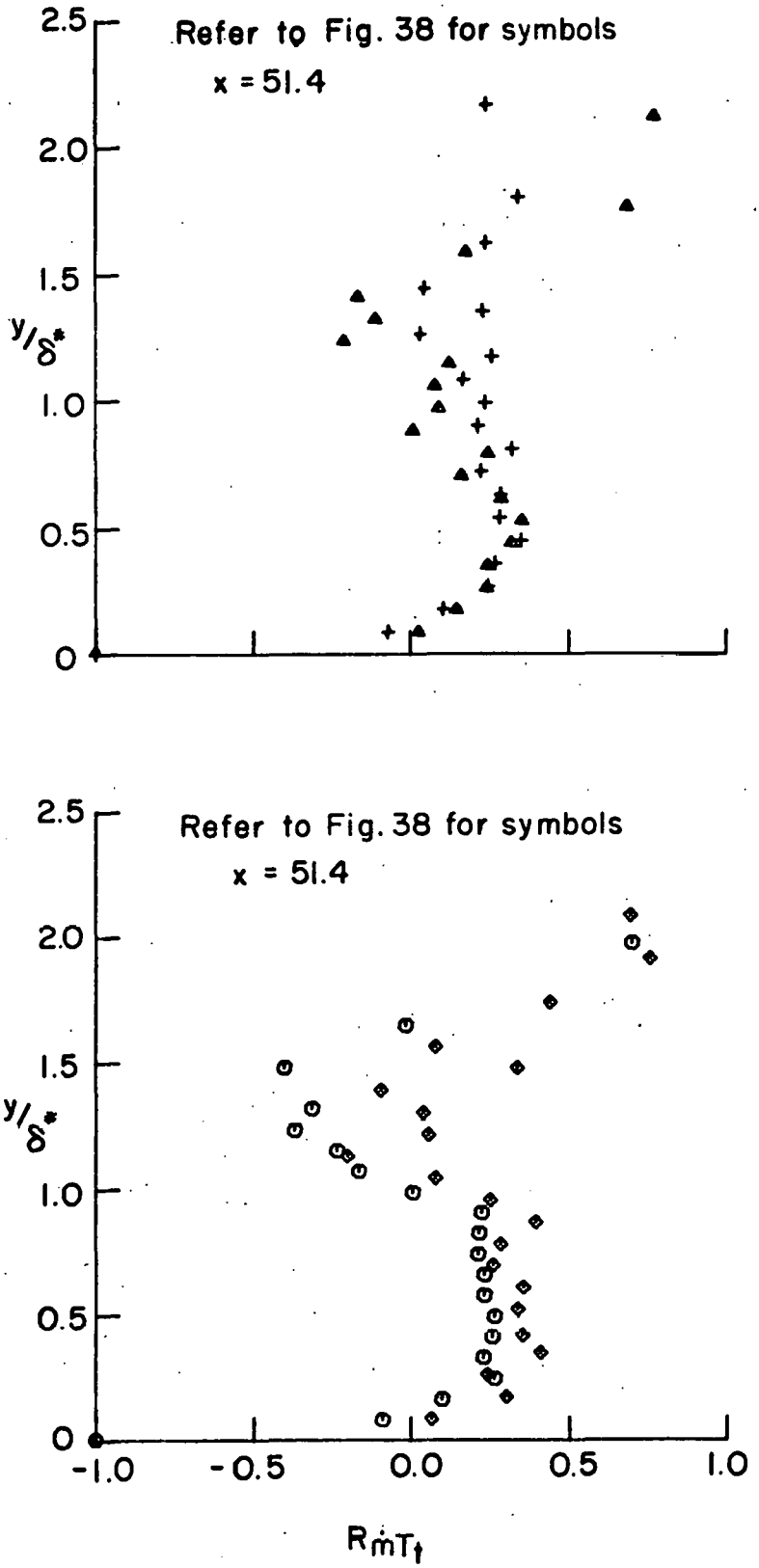

FIG. 40 (CONCLUDED)

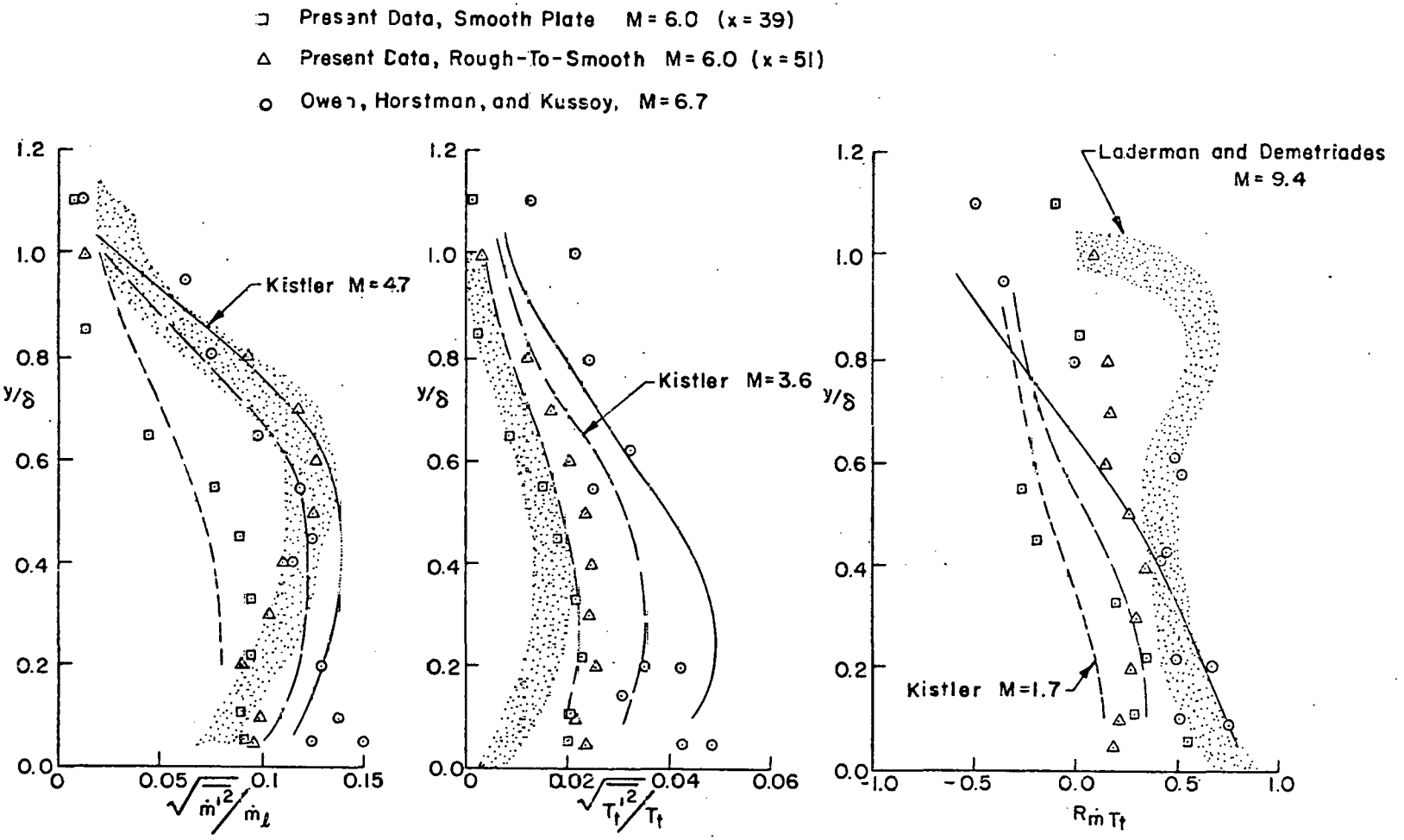

FIG. 41 COMPARISON OF EQUILIBRIUM SMOOTH WALL FLUCTUATION DATA WITH PREVIOUSLY PUBLISHED RESULTS

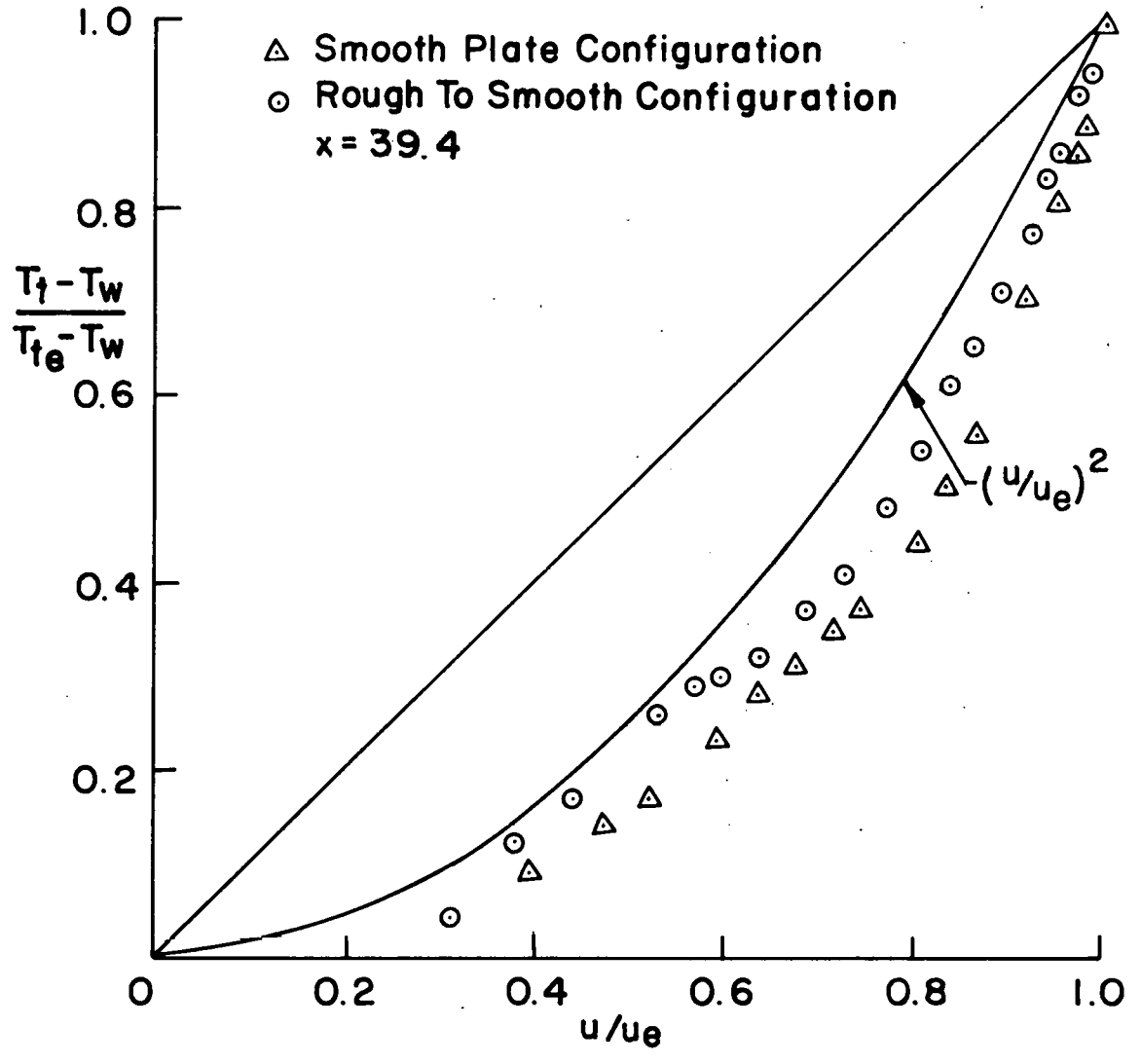

FIG. 42 HISTORY EFFECTS ON THE TOTAL TEMPERATURE-VELOCITY RELATION

DISTRIBUTION:

Spectron Development Laboratories, Inc. (2)
3303 Harbor Boulevard, Suite G-3
Costa Mesa, California 92626
Attn: A. F. Mills
J. F. Courtney

Naval Ordnance Laboratory
White Oak
Silver Spring, Maryland 20910
Attn: D. C. Reda

McDonnell Douglas Astronautics Company
McDonnell Douglas Corporation
5301 Bolsa Avenue
Huntington Beach, California 92647
Attn: R. B. Dirling, Jr.

Analytical Methods
100 116th Avenue SE
Bellevue, Washington 98004
Attn: F. A. Dvorak

Southern Methodist University
Dallas, Texas 75275
Attn: Dr. Roger L. Simpson

Aeronutronic Division
Aeronutronic Ford Corporation
Ford Road
Newport Beach, California 92663
Attn: A. Demetriades

1000 G. A. Fowler
Attn: C. D. Broyles - 1100
W. A. Gardner - 1200
O. E. Jones - 1700
1260 K. J. Touryan
1300 D. B. Shuster
Attn: A. A. Lieber - 1310
M. L. Kramm - 1320
R. G. Clem - 1350
1330 R. C. Maydew
1331 H. R. Vaughn
1332 C. W. Peterson
1333 S. McAlees
1333 G. F. Wright
1334 D. D. McBride
1334 D. E. Berg (10)
1335 W. R. Barton

Distribution (continued):

1335 W. E. Williamson
1336 J. K. Cole
8266 E. A. Aas (2)
3141 C. A. Pepmueller (Actg.) (5)
3151 W. L. Garner (3)
For ERDA/TIC (Unlimited Release)
ERDA/TIC (25)
(R. P. Campbell, 3171-1)